

Towards Photoactive Manganese(IV) and Nickel(II) Complexes

Dissertation zur Erlangung des Grades
„Doktor der Naturwissenschaften“
im Promotionsfach Chemie

am Fachbereich Chemie, Pharmazie, Geographie
und Geowissenschaften
der Johannes Gutenberg-Universität Mainz

Nathan R. East
geboren in Swansea

Mainz, 2023

The present work was carried out in the period from November 2019 to June 2023 in the Department of Chemistry (formerly Institute for Inorganic Chemistry and Analytical Chemistry) at the Johannes Gutenberg University in Mainz under the supervision of [REDACTED]
[REDACTED]

Dean [REDACTED]

1st Supervisor: [REDACTED]

2nd Supervisor: [REDACTED]

Day of oral examination: _____

I, Nathan Roy East, hereby certify that I have written this work independently and have not used any sources or aids other than those indicated. I have marked all explanations that were taken from others literally or analogously.

(Date)

(Signature)

Abstract

With increased emphasis on sustainability, photochemistry with earth abundant 3d transition metal complexes has become increasingly important. Primary focus over the last decades has centered on optimising and developing charge transfer phosphorescence. However, in recent years octahedral 3d transition metal complexes containing low energy metal-centered states have received a great deal of attention, particularly with the $[\text{Cr}(\text{ddpd})_2]^{3+}$ (ddpd = *N,N'*-dimethyl-*N,N'*-dipyridin-2-ylpyridine-2,6-diamine) as prime example. Such successes have guided very recent research with $[\text{V}(\text{ddpd})_2]^{3+}$ as the first octahedral vanadium(III) complex to display room temperature phosphorescence. With the prospect of d^2 , d^3 , d^4 and d^8 electron configurations possessing low energy metal-centered states potentially capable of phosphorescence, research with other 3d metals in relevant oxidation states is of particular interest. To date only one d^3 manganese(IV) and no d^8 nickel(II) complexes show luminescence from metal-centered states.

Part one of this work details the synthesis and characterization of an octahedral Mn^{IV} complex $[\text{Mn}(\text{dgpy})_2]^{4+}$ (dgpy = 2,6-diguanidylpyridine) with a d^3 electron configuration analogous to chromium(III). This begins with the synthesis of a manganese(II) precursor $[\text{Mn}(\text{dgpy})_2]^{2+}$, and oxidation to the Mn^{IV} complex via a Mn^{III} intermediate. Structural, magnetic, spectroscopic and computational studies for the complete series of oxidation states +II to +IV provides important information to aid in synthesis and design of potentially photoactive manganese(IV) complexes. It is shown that six-membered chelating ligands with mixture of strongly donating and accepting moieties are required to stabilise such a labile electron-rich d^5 Mn^{II} , Jahn-Teller distorted d^4 Mn^{III} and electron-poor d^3 Mn^{IV} complexes.

The photophysics and photochemistry of $[\text{Mn}(\text{dgpy})_2]^{4+}$ are subsequently described and documented in part two. The photophysics of such Mn^{IV} complexes are poorly understood due to extreme rarity. The present investigation reveals only the second example of Mn^{IV} phosphorescence, with luminescence in the low energy NIR-II region (1435 nm). The excited $^2\text{LMCT}/^2\text{MC}$ state (0.86 eV) of this complex was found to be long lived enough (1.6 ns) to participate in bimolecular chemistry. $[\text{Mn}(\text{dgpy})_2]^{4+}$ was discovered to be strongly dual state photooxidative following NIR irradiation and is able to oxidise naphthalene dynamically via a $^2\text{LMCT}/^2\text{MC}$ state and also more difficult substrates like benzene statically via a $^4\text{LMCT}$ state (1.46 eV). Bimolecular quenching of this photoreactive complex gives valuable insight into further photophysical dynamics and potential design of future photoactive Mn^{IV} transition metal complexes capable of bimolecular reactivity following low energy excitation (850 nm).

The third part is an investigation into understanding the requirements necessary for a metal-centered emission from octahedral d^8 nickel(II) complexes. To date metal-centered emission from octahedral nickel(II) is undocumented; and here an investigation is made to discover why. A strong ligand field is required to get the correct excited state ordering i.e. the intraconfigurational singlet states being lowest in energy. However, there is a limit to the

ligand field strength that can be imposed on d^8 systems and still maintain an octahedral coordination, with advantageous excited state ordering. To further examine the effect of ligand field strength on excited state ordering the series of complexes $[\text{Ni}(\text{dgpy})_2]^{2+}$, $[\text{Ni}(\text{terpy})_2]^{2+}$ (terpy = 2,2';6',2''-terpyridine), $[\text{Ni}(\text{phen})_3]^{2+}$ (phen = 1,10-phenanthroline), $[\text{Ni}(\text{ddpd})_2]^{2+}$ and $[\text{Ni}(\text{tpe})_2]^{2+}$ (tpe = 1,1,1-tris(pyrid-2-yl)ethane) are synthesized and structural and electronic properties examined. Additionally, the influence of increased hydrostatic pressure on ligand field states of $[\text{Ni}(\text{ddpd})_2]^{2+}$ is also investigated, to evaluate if the inter- and intraconfigurational states can be further separated. This investigation gives valuable information in the pursuit of metal-centered spin-flip emissive octahedral Ni^{II} complexes.

Part four builds on part three by looking at the impact of increasing ligand field strength on Ni^{II} ligand field states. This is done by firstly increasing σ -donation to destabilize the e_g^* orbitals, with synthesis of the carbene complex $[\text{Ni}(\text{CNC})(\text{NCN})]^{2+}$ (CNC = 1,1'-(pyridin-2,6-diyl)bis(3-methyl-1H-imidazol-3-ylidene)) and NCN = (1,3-bis(2-pyridyl)imidazolyidene). With increased σ -donation it is also conceivable that the complex will adopt square planar geometry, thus structural confirmation of an octahedral environment is the first step, and further characterization will follow. An alternative method of increasing ligand field strength is using π -acceptor ligands to stabilize the t_{2g} orbitals. This method will also be shown with the synthesis of $[\text{Ni}(\text{dcpp})_2]^{2+}$ (dcpp = (2,6-bis(2-carboxypyridyl)pyridine)). The dcpp ligand contains two π -accepting carbonyl groups which enhance the π -accepting ability of the ligand. A Lewis acid ($\text{Sc}[\text{OTf}]_3$) will then be coordinated to the ligand carbonyl groups, and a second coordination sphere will give further insight into the influence of increasing ligand π -acceptance on ligand field states of $[\text{Ni}(\text{dcpp})_2]^{2+}$. This investigation aims to further understand the ligand requirements for Ni^{II} in the pursuit of spin-flip emission.

Kurzzusammenfassung

Mit zunehmendem Fokus auf den Aspekt der Nachhaltigkeit hat Photochemie mit auf gut verfügbaren 3d-Metallen basierenden Übergangsmetallkomplexen an Bedeutung gewonnen. In den letzten Jahrzehnten lag der Schwerpunkt auf der Optimierung und Entwicklung von *charge-transfer*-Photosensibilisatoren. In jüngeren Jahren haben jedoch oktaedrische 3d-Übergangsmetallkomplexe, die niederenergetische metallzentrierte Zustände aufweisen, viel Aufmerksamkeit erhalten, insbesondere $[\text{Cr}(\text{ddpd})_2]^{3+}$ (ddpd = *N,N'*-Dimethyl-*N,N'*-dipyridin-2-ylpyridin-2,6-diamin) als Paradebeispiel. Im Rahmen nachfolgender Forschungen konnte $[\text{V}(\text{ddpd})_2]^{3+}$ als erster oktaedrischer Vanadium(III)-Komplex, der bei Raumtemperatur Phosphoreszenz zeigt, synthetisiert werden. Im Hinblick auf d^2 -, d^3 -, d^4 - und d^8 -Elektronenkonfigurationen, die niederenergetische metallzentrierte Zustände besitzen, die potenziell zur Phosphoreszenz fähig sind, ist die Forschung mit anderen 3d-Metallen in relevanten Oxidationszuständen von besonderem Interesse. Bislang sind nur ein d^3 -Mangan(IV)- und keine d^8 -Nickel(II)-Komplexe bekannt, die Lumineszenz aus metallzentrierten Zuständen zeigen.

Der erste Teil dieser Arbeit beschreibt die Synthese und Charakterisierung eines oktaedrischen Mn^{IV} -Komplexes $[\text{Mn}(\text{dgpy})_2]^{4+}$ (dgpy = 2,6-diguanidylpyridin) mit einer d^3 -Elektronenkonfiguration analog zu Chrom(III). Dies beginnt mit der Synthese eines Mangan(II)-Vorläufers $[\text{Mn}(\text{dgpy})_2]^{2+}$ und der Oxidation zum Mn^{IV} -Komplex über ein Mn^{III} -Zwischenprodukt. Strukturelle, magnetische, spektroskopische und theoretische Studien für die gesamte Reihe der Oxidationsstufen +II bis +IV liefern wichtige Informationen für die Synthese und das Design potenziell photoaktiver Mangan(IV)-Komplexe. Es wird gezeigt, dass sechsgliedrige Chelatliganden mit einer Mischung aus starken Akzeptor- und Donoreigenschaften erforderlich sind, um die unterschiedlichen Oxidationsstufen des Mangans zu stabilisieren.

Die Photophysik und Photochemie von $[\text{Mn}(\text{dgpy})_2]^{4+}$ wird anschließend im zweiten Teil beschrieben. Über die Photophysik solcher Mn^{IV} -Komplexe ist aufgrund der geringen Anzahl von Beispielen nur wenig bekannt. Die vorliegende Untersuchung zeigt erst das zweite Beispiel für Mn^{IV} -Phosphoreszenz, mit Lumineszenz im niederenergetischen NIR-II-Bereich (1435 nm). Der angeregte $^2\text{LMCT}/^2\text{MC}$ -Zustand (0,86 eV) dieses Komplexes erwies sich als langlebig genug (1,6 ns), um bimolekulare Reaktionen zu ermöglichen. Es wurde festgestellt, dass $[\text{Mn}(\text{dgpy})_2]^{4+}$ nach NIR-Bestrahlung stark photooxidativ ist und Naphthalin dynamisch über den $^2\text{LMCT}/^2\text{MC}$ -Zustand und auch reaktionsträgere Substrate wie Benzol statisch über einen $^4\text{LMCT}$ -Zustand (1,46 eV) oxidieren kann. Das bimolekulare Quenchen dieses photoreaktiven Komplexes gibt wertvolle Einblicke in die weitere photophysikalische Dynamik und das potenzielle Design zukünftiger photoaktiver Mn^{IV} -Übergangsmetallkomplexe, die nach einer niederenergetischen Anregung (850 nm) bimolekulare Reaktivität zeigen.

Im dritten Teil wird untersucht, welche Voraussetzungen für eine metallzentrierte Emission aus oktaedrischen d^8 -Nickel(II)-Komplexen erforderlich sind. Bislang ist die metallzentrierte Emission von oktaedrisch koordiniertem Nickel(II) nicht dokumentiert. Ein starkes Ligandenfeld ist erforderlich, um die für Spin-Flip Emission notwendige energetische Abfolge der angeregten Zustände zu erhalten, d. h. energiearme intrakonfigurationale Singulett-

Zustände. Es gibt jedoch eine Grenze für die Stärke des Ligandenfeldes, die d^8 -Systemen auferlegt werden kann, um eine oktaedrische Koordination mit einer vorteilhaften Anordnung der angeregten Zustände aufrechtzuerhalten. Die Reihe der Komplexe $[\text{Ni}(\text{dgpy})_2]^{2+}$, $[\text{Ni}(\text{terpy})_2]^{2+}$ (terpy = 2,2'; 6',2"-terpyridin), $[\text{Ni}(\text{phen})_3]^{2+}$ (phen = 1,10-phenanthrolin), $[\text{Ni}(\text{ddpd})_2]^{2+}$ und $[\text{Ni}(\text{tpe})_2]^{2+}$ (tpe = 1,1,1-tris(pyrid-2-yl)ethan) sind Beispiele für Ni^{II} im oktaedrischen Ligandenfeld mittlerer Stärke und die daraus resultierenden Auswirkungen auf die inter- und intrakonfigurativen Zustände. Darüber hinaus wird auch der Einfluss von erhöhtem hydrostatischem Druck auf die Ligandenfeldzustände untersucht, um festzustellen, ob die inter- und intrakonfigurationsalen Zustände weiter voneinander separiert werden können. Diese Untersuchung liefert wertvolle Informationen für die Suche nach metallzentrierten oktaedrischen Ni^{II} -Komplexen mit Spin-Flip-Emissionen.

Teil vier baut auf Teil drei auf, indem die Auswirkungen einer Erhöhung der Ligandenfeldstärke auf die Ni^{II} -Ligandenfeldzustände untersucht werden. Dazu werden die Carbenliganden $\text{CNC} = (1,1'-(\text{pyridin-2,6-diyl})\text{bis}(3\text{-methyl-1H-imidazol-3-ium)})$ und $\text{NCN} = (1,3\text{-bis}(2\text{-pyridyl})\text{imidazolium})$ mit ausgeprägterer σ -Donorfähigkeit an Ni^{II} koordiniert, um die e_g^* -Orbitale zu destabilisieren. Durch die stärkere Ligandenfeldaufspaltung ist es denkbar, dass der Komplex eine quadratisch-planare Geometrie annimmt. Somit stellt die strukturelle Bestätigung einer oktaedrischen Komplexgeometrie den ersten Schritt vor weiteren Charakterisierungsmethoden dar. Ein alternativer Ansatz zur Erhöhung der Ligandenfeldstärke ist die Verwendung von π -Akzeptorliganden, um die t_{2g} -Orbitale zu stabilisieren. Diese Methode wird anhand der Synthese von $[\text{Ni}(\text{dcpp})_2]^{2+}$ (dcpp = (2,6-bis(2-carboxypyridyl)pyridin)) näher erläutert. Der dcpp-Ligand enthält zwei elektronenziehende Carbonylgruppen wodurch bei Koordination an das Metall ein stark π -akzeptierendes Ligandenfeld erzeugt wird. Eine Lewis-Säure ($\text{Sc}[\text{OTf}]_3$) wird dann an die Carbonylgruppen des Liganden koordiniert. Der Einfluss dieser zweiten Koordinationssphäre soll die π -Akzeptorfähigkeit des Liganden erhöhen. Dies soll tiefere Einblicke in die gezielte Beeinflussung der relativen energetischen Lagen der Ligandenfeldzustände des Komplexes geben. Diese Untersuchung zielt darauf ab, die Ligandenanforderungen für Ni^{II} bei der Verwirklichung der Spin-Flip-Emission besser zu verstehen.

Table of Contents

Abstract	I
Abbreviations and Physical Quantities	VII
1. Introduction	1
1.1 Excited State Properties of Transition Metal Complexes.....	4
1.1.1 Fluorescence and Phosphorescence	5
1.1.2 Non-Radiative Decay Processes	6
1.1.3 Excited-State Bimolecular Processes.....	9
1.2 Emission from 3d Transition Metal Complexes.....	14
1.2.1 Luminescence Enhancement.....	19
1.3 Manganese	21
1.3.1 Manganese(II).....	21
1.3.2 Manganese(III).....	24
1.3.3 Manganese(IV)	26
1.4 Nickel(II).....	30
2. Aims of Work	32
3. Results and Discussion	34
3.1 The Full d^3-d^5 Redox Series of Mononuclear Manganese Complexes: Geometries and Electronic Structures of $[\text{Mn}(\text{d}g\text{py})_2]^{n+}$	38
3.2 Oxidative Two-State Photoreactivity of a Manganese(IV) Complex using NIR Light	49
3.3 Coupled Potential Energy Surfaces Strongly Impact the Lowest-Energy Spin-Flip Transition in Six-Coordinate Nickel(II) Complexes	66
3.4 Influencing Ligand Field States of Nickel(II) Complexes with Strongly σ -Donating and π -Accepting Ligands.....	77
3.4.1 Increasing σ -Donation	79
3.4.2 Increasing π -Accepting	81
3.4.3 Conclusion	86
4. Summary and Outlook	87
5. References	89
6. Appendix	97
4	97
6.1 Supporting Information to Chapter 3.1. (“The Full d^3-d^5 Redox Series of Mononuclear Manganese Complexes: Geometries and Electronic Structures of $[\text{Mn}(\text{d}g\text{py})_2]^{n+}$ ”)	97
6.2 Supporting Information to Chapter 3.2. (“Oxidative Two-State Photoreactivity of a Manganese(IV) Complex using NIR Light”).....	123

6.3	Supporting Information to Chapter 3.3. (“Coupled Potential Energy Surfaces Strongly Impact the Lowest-Energy Spin-Flip Transition in Six-Coordinate Nickel(II) Complexes”)	165
6.4	Supporting Information to Chapter 3.4. (“Influencing Ligand field states of Nickel(II) Complexes with Strongly σ -Donating and π -Accepting Ligands”).....	192
7.	Acknowledgements.....	197
8.	Curriculum Vitae	198

Abbreviations and Physical Quantities

(Ph)OLED	(Phosphorescent) organic light-emitting diode
(^{phen}N,N'[^]C)₂	2-(3-(<i>tert</i> -butyl)phenyl)-1,10-phenanthroline
\hat{H}	Hamiltonian
H_{ab}^2	Electronic coupling matrix element
μS	Microsecond
4, 4'-bpy(NO₂)₂	4, 4'-dinitro-2,2'-bipyridine
Abs	Absorption
als	3-((2-hydroxybenzylidene)amino)propanoic acid
B, C	Racah parameters
big	Biguanide
bISC	Back-intersystem crossing
Bn-TPEN	<i>N</i> -benzyl- <i>N,N',N'</i> -tris(2-pyridylmethyl)-1,2-diamino-ethane)
bpmp	2,6-bis(2-pyridyl-methyl)pyridine
bpy	2,2'-bipyridine
btz	3,3'-dimethyl-1,1'-bis(<i>p</i> -tolyl)-4,4'-bis(1,2,3-triazol-5-ylidene)
Cbz	Carbazole
CNAr₅^(th)NC	1,3-bis(<i>N</i> -formyl-4-methyl-6-phenylanilin-2-yl)benzene
CNAr₅NC	1,3-bis(<i>N</i> -formyl-4-methyl-6-phenylanilin-2-yl)thiophene
CNC	1,1'-(pyridin-2,6-diyl)bis(3-methyl-1 <i>H</i> -imidazol-3-ylidene)
CO	Carbon monoxide
CT	Charge transfer
<i>D</i>	Axial zero-field splitting parameter
dcpp	2,6-bis(2-carboxypyridyl)pyridine
ddpd	<i>N,N'</i> -dimethyl- <i>N,N'</i> -dipyridin-2-ylpyridine-2,6-diamine
dgpy	2,6-diguanidylpyridine
dmp	2,9-dimethyl-1,10-phenanthroline
dpb	1,3-bis(<i>N</i> -alkylbenzimidazol-2'-yl)benzene
dpc	3,6-di- <i>tert</i> -butyl-1,8-di(pyridine-2-yl)-carbazolato
DSSCs	Dye-sensitized solar cell
E_{00}	One electron potential at zero vibrational transition
$E_{1/2}$	Half-wave potential
EnT	Energy transfer
E_{ox}	Ground state oxidation potential
eq	Equivalentents
E_{red}	Ground state reduction potential
ES	Excited state
eV	Electron volt

FCWD	Franck-Condon weighed density
FI	Fluorescence
fs	Femtosecond
GS	Ground state
HB(3, 5-Mepz)	3, 5-dimethyl pyrazolyl borate
L-6H	Hydrazine clathrochelate
Hbig	H-biguanide
HOMO	Highest occupied molecular orbital
HS	High-spin
ILCT	Intraligand charge transfer
Imp	1,1'-(1,3-phenylene)bis(3-methyl-1-imidazol-2-ylidene)
ISC	Intersystem crossing
k_B	Boltzman constant
k_{ENT}	Rate constant for energy transfer
k_{fl}	Fluorescence rate constant
k_{ISC}	Rate constant for intersystem crossing
k_{nr}	Non-radiative decay rate constant
k_{ph}	Phosphorescence rate constant
k_{ET}	Rate constant for electron transfer
k_r	Radiative decay rate constant
λ_S	Solvent reorganization energy
L^{bi}	2,5-bis(3,5-di- <i>tert</i> -butyl-2-isocyanophenyl)thiophene
LC	Ligand-centered
L^{CNC}	<i>Tert</i> -butyl-carbazole dicyclohexylmesoionic carbene
LF	Ligand field
LLCT	Ligand-to-ligand transfer
LMCT	Ligand-to-metal charge transfer
L^{me}	1,3-dimethyl-2-phenyl-1,3-diazaphospholidine-2-oxide
L^{py}	bispidine pyridine
LS	Low-spin
LUMO	Lowest occupied molecular orbital
MC	Metal-centered
M-L	Metal-to-ligand
MLCT	Metal-to-ligand charge transfer
ms	Millisecond
NCN	1,3-bis(2-pyridyl)imidazolylidene
NIR	Near infrared (760 -1000 nm)
NIR-II	Near infrared II (1000-1700 nm)
nm	Nanometers
nr	Non-radiative decay

ns	Nanosecond
OLED	Organic light-emitting diode
P_{SEN}	Photosensitizer
PES	Potential energy surface
PET	Photoelectron transfer
Ph₄P	Tetraphenylphosphonium cation
phen	1,10-phenanthroline
Ph	Phosphorescence
Phtmeimb	Phenyl[tris(3-methylimidazol-1-ylidene)]
ppy	Deprotonated 2-phenylpyridine
ps	Picosecond
RT	Room temperature
S₀	Singlet ground state
S₁	1 st excited singlet state
S₂	2 nd excited singlet state
sal	Salicylic acid
SCO	Spin crossover
SF	Spin-flip
SMM	Single molecule magnet
SOC	Spin-orbit coupling
SOMO	Singly occupied molecular orbital
Sub	Substrate
T₁	Lowest energy triplet excited state
^tBu-terpy	<i>Tert</i> -butyl 2,2';6',2"-terpyridine
terpy	2,2';6',2"-terpyridine
ThiaSO₂	<i>P-tert</i> -butylsulphonylcalix[4]arene
TM	Transition metal
TMCs	Transition metal complexes
tpe	1,1,1-tris(pyrid-2-yl)ethane
tppb	Hydro-tris(3-phenylpyrazol-1-yl)borate
Tripp	2,4,6-triisopropylphenyl
V	Volt
VR	Vibrational relaxation
Z_{eff}	Effective nuclear charge
ZFS	Zero field splitting
Δ_o	Octahedral ligand field splitting
λ_{em}	Emission wavelength
π_L	Ligand π-orbitals
π_L[*]	Ligand π-antibonding orbitals
σ_{ML}	Metal-ligand sigma bonding orbitals

ΔE_a	Activation energy
Φ	Quantum Yield
τ	Lifetime
ζ	Spin-orbit coupling constant

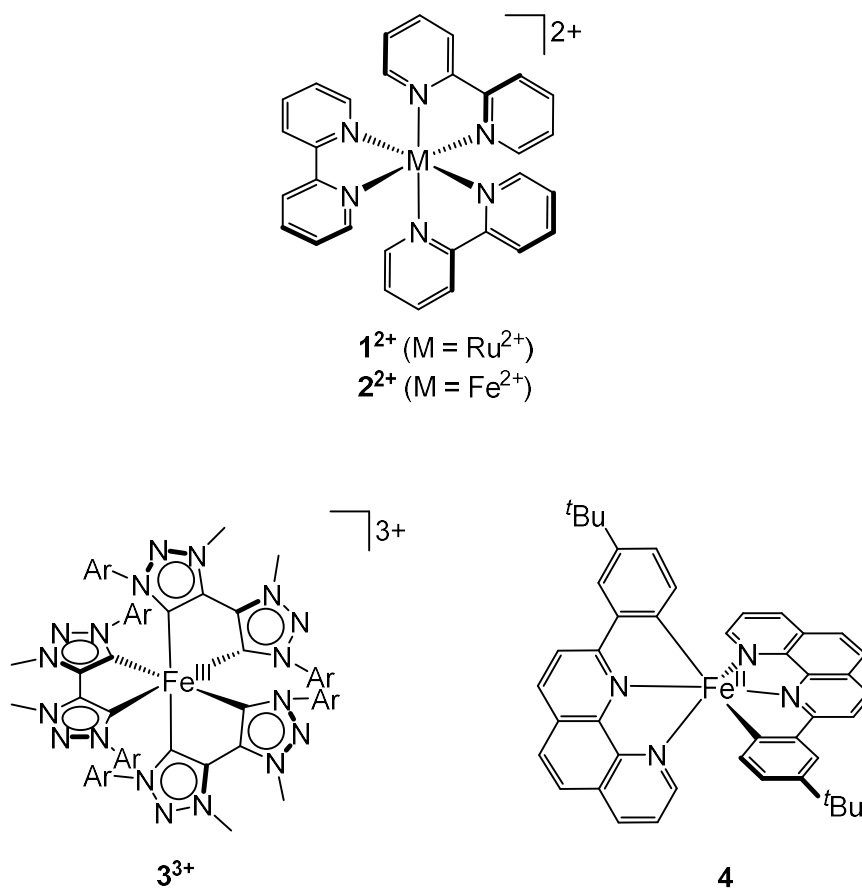


1. Introduction

Photochemistry using transition metals (TMs) has become increasingly important in recent decades as a means to achieve more sustainable energy usage. Current world energy consumption is heavily reliant on fossil fuels, which contribute largely to greenhouse gas emissions and have finite availability.^[1] A significant challenge is transitioning from these types of energy sources to more sustainable, less polluting alternatives.

Photochemistry is the concept of chemically harnessing sunlight and converting into energy that can be exploited for use in various ways including – but not limited to – catalytic chemical transformations,^[2] use as light harvesters in dye sensitized solar cells (DSSCs)^[3,4] or for use in other energy efficient applications such as organic light emitting diodes (OLEDs) or phosphorescent organic light emitting diodes ((Ph)OLEDs).^[5] TM photochemistry typically uses transition metal complexes (TMCs) to perform such light-harvesting, as they possess favorable excited state (ES) dynamics. TMs such as Ru, Ir or Pt are primarily used in such applications, as their ES dynamics are particularly advantageous. A typical example is $[\text{Ru}(\text{bpy})_3]^{2+}$ (bpy = 2,2'-bipyridine) (**1**²⁺, scheme 1.1) as used in DSSCs^[6] or in photoredox catalysis,^[7] due to high stability and ES lifetime, excellent redox properties and broad absorption in the visible region of the spectrum.

Although heavier 4d and 5d TMs are typically better suited for photochemistry, there are some inherent drawbacks associated with their use that are largely related to their abundance. For instance, first row 3d TMs are several orders of magnitude more abundant in the earth's crust than their heavier analogues e.g. Ru is $\approx 10^{-6}$ % abundant, while Fe is ≈ 5 % abundant as mass percentage of the earth's crust.^[8,9] In addition extraction of these metals is challenging which inflates cost further.^[10] A cheaper and more sustainable alternative is the use of 3d metals instead.^[8,9,11]

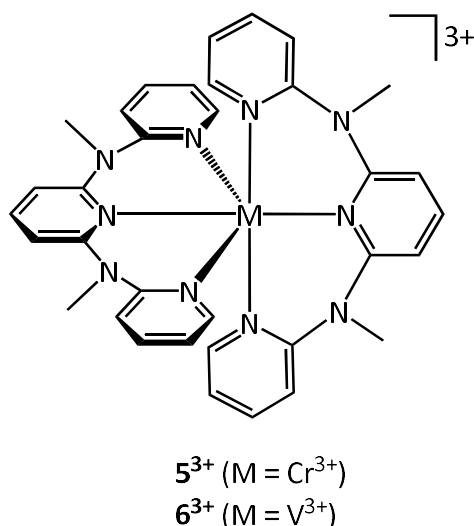


Scheme 1.1: Molecular structures of Ru^{II} and Fe^{III,II} complexes **1²⁺**, **2²⁺**, **3³⁺** and **4**.

While more sustainable there are some inherent challenges associated with using 3d TMs over 4d and 5d. This is evident when comparing [Fe(bpy)₃]²⁺ (lifetime (τ) = 150 fs) (**2²⁺**, scheme 1.1) ^[12] and [Ru(bpy)₃]²⁺ (λ_{em} = 620 nm, τ = 0.80 μ s, quantum yield (Φ) = 9.5 % in deoxygenated CH₃CN at RT). [Fe(bpy)₃]²⁺ is not phosphorescent and cannot be used in the same applications as its Ru analogue.^[13] This is largely a result of the intrinsically strong ligand field (LF) splitting of 4d and 5d metals. 3d metals suffer from much weaker intrinsic LF splitting as a result of the primogenic effect,^[14] and from much smaller spin-orbit coupling (SOC), which scales with Z_{eff} ('heavy-atom effect'), and might slow down intersystem crossing (ISC).^[15]

Thus, in recent decades there has been increased research into 3d luminescent metal complexes and there has been significant progress made.^[16] Including such examples as the [Fe(btz)₃]³⁺ (btz = 3,3'-dimethyl-1,1'-bis(p-tolyl)-4,4'-bis(1,2,3-triazol-5-ylidene)) (**3³⁺**, scheme 1.1) complex,^[17] which shows room temperature (RT) ²LMCT based fluorescence at 600 nm (τ = 0.1 ns, Φ = 0.03 %); and the more recent [Fe(phenN,N'[^]C)₂] (phenN,N'[^]C = 2-(3-(tert-butyl)phenyl)-1,10-phenanthroline) (**4**, scheme 1.1) complex,^[18] which shows MLCT phosphorescence at 1200 nm (τ = 14 ns at 77K in frozen toluene/THF solution). Such progress is a consequence of sophisticated ligand design and has helped lead to further efforts using other 3d TMs.

To date considerable research has focused on manipulation of 3d metal charge transfer (CT) ESs. However, metal-centered (MC) ESs can also be photoactive, and according to work by Y. Tanabe and S. Sugano achieving such depends on LF strength,^[19,20] illustrating that certain electronic configurations can be emissive in strong octahedral LFs.^[21] Their work has led to substantial developments in the area of MC based emission, particularly with chromium(III) with a d^3 electronic configuration.^[22–24] Such exemplary progress can be seen with the more recent example of $[\text{Cr}(\text{ddpd})_2]^{3+}$ (ddpd = *N,N'*-dimethyl-*N,N'*-dipyridin-2-ylpyridine-2,6-diamine) (**5**³⁺, scheme 1.2) showing MC spin-flip (SF) luminescence at 738/775 nm with exceptional quantum yield and lifetime in CH_3CN under deoxygenated conditions ($\tau = 1122 \mu\text{s}$, $\Phi = 13.7 \%$).^[25] The photophysical characteristics of **5**³⁺ are largely attributed to ligand design, and this work has led to other outstanding contributions in this area including the NIR-II SF emissive *mer*- $[\text{V}(\text{ddpd})_2]^{3+}$ complex ($\lambda_{\text{em}} = 1109/1123 \text{ nm}$, $\tau = 1.35 \mu\text{s}$, $\Phi = 1.8 \times 10^{-4} \%$ in deoxygenated CH_3CN at RT) (**6**³⁺, scheme 1.2),^[26] with these aforementioned developments in 3d luminophores it heralds work with other 3d metals.



Scheme 1.2: $[\text{Cr}(\text{ddpd})_2]^{3+}$ (**5**³⁺) and $[\text{V}(\text{ddpd})_2]^{3+}$ (**6**³⁺) exhibiting NIR and NIR-II luminescence respectively.

Manganese(IV) is also capable of SF emission as it possesses a d^3 electronic configuration and so is isoelectronic with chromium(III). Moreover, in a strong field ligand environment it can also possess low energy MC states capable of phosphorescence. Molecular octahedral Mn^{IV} complexes are rare^[27–34] – particularly with only nitrogen donor ligands – and there is only one previously known emissive octahedral Mn^{IV} complex. Thus, their photophysical and chemical properties are poorly understood.

Nickel(II) octahedral TMCs have other associated challenges. There are many more documented examples of molecular octahedral nickel(II) d^8 compounds even in strong ligand fields (e.g. $[\text{Ni}(\text{ddpd})_2]^{3+}$). However, there is no report to date of SF emission from these complexes.^[35] There is a need for further fundamental understanding to help overcome these challenges. Thus, work with these alternative 3d TMs is necessary on a fundamental level to increase understanding and open the way for eventual use in applications.

1.1 Excited State Properties of Transition Metal Complexes

Photoexcitation of a TMC creates an ES species, which has many possible routes to return to the ground state (GS) (figure 1.1). With the correct ES ordering a TMC can be emissive, and it is also possible that such a low energy ES can be quenched in photochemical applications e.g. bimolecular redox (ET) or energy transfer (EnT) processes. It is important to understand the various routes of decay in order to design photoactive TMCs for use in application.^[15]

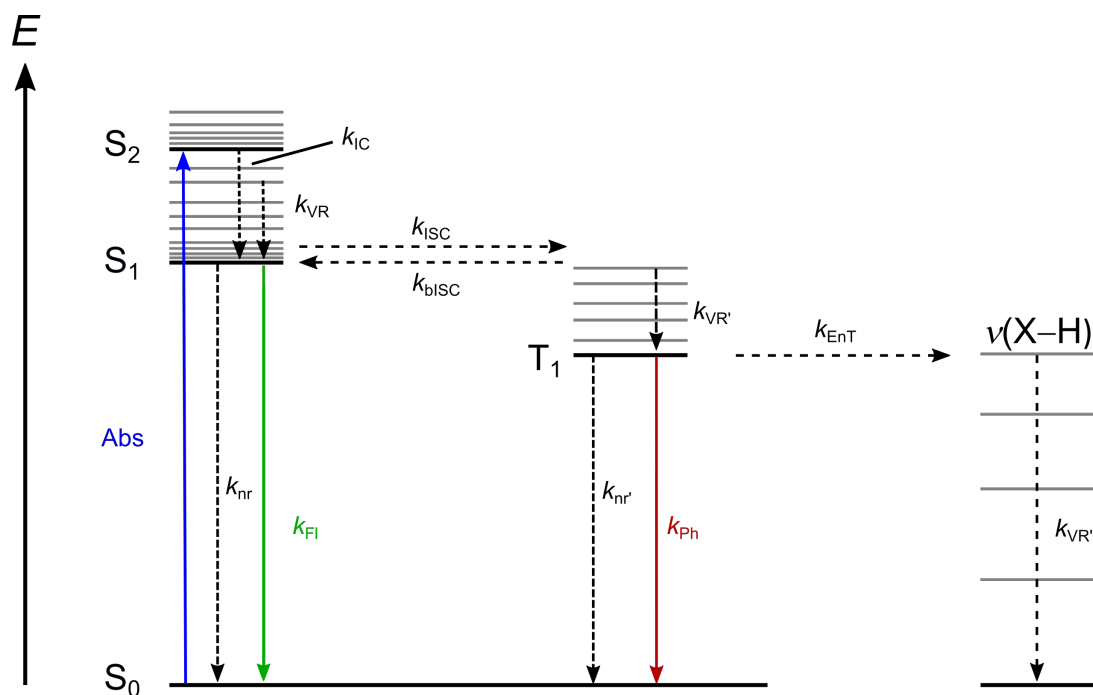


Figure 1.1: Simplified Jablonski energy diagram showing processes that follow absorption of a photon by a singlet GS (S_0) molecule. Absorption (Abs), 1st singlet ES (S_1), 2nd singlet ES (S_2), lowest energy triplet ES (T_1), vibrationally excited oscillators $\nu(X-H)$ ($X = C, N, O$). Rate constants (k) for: vibrational relaxation (VR), internal conversion (IC), intersystem crossing (ISC), back-intersystem crossing (bISC), fluorescence (FI), non-radiative decay (nr), phosphorescence (Ph).

It is possible for an ES complex to relax to the GS radiatively (fluorescence/ phosphorescence), non-radiatively or via bimolecular quenching. Each of these processes will be described and discussed in subsequent sections.

1.1.1 Fluorescence and Phosphorescence

Following photoexcitation of a TMC to the first ES (S_1) (also be described as a Franck-Condon state), the ES can radiatively relax back to the GS. Decay can occur from S_1 to S_0 (i.e. fluorescence) or from a T_1 to S_0 (i.e. phosphorescence). Each process leads to emission of radiative energy (figure 1.1). Fluorescence is a spin-allowed process where the spin multiplicity is conserved. The resulting fluorescence is relatively fast, occurring on a timescale of approximately 10^{-9} to 10^{-7} s. Phosphorescence however is spin-forbidden involving a change in multiplicity, more specifically a ‘flip’ in the excited electrons spin. This spin forbidden process of triplet state relaxation to a singlet GS typically occurs on a much longer scale 10^{-6} to 10^{-3} s. The lowest energy T_1 is lower in energy than the lowest energy S_1 , due to Hunds rule of maximum multiplicity and so decay from these states is energetically preferred, occurring at longer wavelengths. The process that governs the change of an electrons spin (transition from a singlet ES to a triplet ES) is the relative rate of intersystem crossing (k_{ISC}). Phosphorescence is preferential for many applications as the state is longer lived and can be further exploited.^[15]

Lifetimes and Quantum Yields

To further describe an ES molecule, the parameters of lifetime (τ) and quantum yield (Φ) are used. The lifetime of an ES is expressed as the reciprocal sum of radiative (k_r) and non-radiative (k_{nr}) rate constants (figure 1.1, equation. 1.1).^[36]

$$\tau = \frac{1}{\sum k_r + \sum k_{nr}} \quad (\text{equation. 1.1})$$

The term k_r includes the terms k_{fl} and k_{ph} , and k_{nr} consists of the various non-radiative rate terms.

The quantum yield (Φ) of a process describes the efficiency of a radiative process in terms of the ratio of photons absorbed ($\sum k_r + \sum k_{nr}$) to photons emitted (k_r)(equation. 1.2).^[36-38]

$$\Phi = \frac{k_r}{\sum k_r + \sum k_{nr}} \quad (\text{equation. 1.2})$$

The smaller the non-radiative decay term the closer to 1 the quantum yield will be. It is evident from these two equations that the lifetime and quantum yield of an emissive process is heavily dependent on competitive non-radiative processes.

1.1.2 Non-Radiative Decay Processes

An ES can also depopulate without emission, where the energy of the absorbed photon is dissipated via another process. Deactivation of an ES via vibrational relaxation (k_{VR}) and internal conversion (k_{IC}) are dominant non-radiative mechanisms that are ultrafast (10^{-14} to 10^{-11} s) and so very likely to occur immediately following excitation. The non-radiative mechanistic description is further enhanced with two general mechanisms, known as strong and weak coupling limits. Strong coupling describes non-radiative decay that typically accompanies distorted ESs; weak coupling describes non-radiative decay processes associated with a nested ES.

Strong Coupling Limit

Strong coupling limit (figure 1.2) describes non-radiative decay (k_{nr}) that occurs due to strong ES distortion (equation. 1.3).^[39-42]

$$k_{nr} = \frac{k_B T}{\hbar} H_{ab}^2 \sqrt{\frac{2\pi}{E_m (k_B T)^3}} \times \exp\left(-\frac{\Delta E_a}{k_B T}\right) \quad (\text{equation. 1.3})$$

The electronic coupling matrix element (H_{ab}^2) describes the transition from GS to ES. E_m describes the half Stokes shift of emission from excitation, and ΔE_a represents the energy gap between the lowest excited vibronic state and the crossing point between the ES and GS PESs. In this case, the k_{nr} displays temperature dependent Arrhenius behavior; ΔE_a is the energy barrier governing non-radiative decay. In situations where ES distortion is large (figure 1.2), the activation energy required for non-radiative decay approaches zero; the resultant non-radiative decay in this case is almost barrier-free at RT. Such strong coupling effects can be reduced by carrying out emission measurements at cryogenic temperatures or with ligand rigidification, both reducing ES distortion.^[43,44]

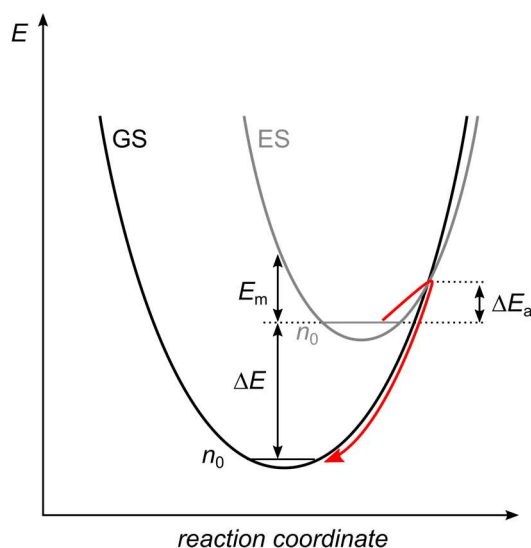


Figure 1.2: Ground (GS) and excited state (ES) PESs at the strong coupling limit, the red arrow indicates the non-radiative decay route. Half Stokes shift (E_m), GS vibrational energy level (n_o), gap (ΔE) between GS (n_o) and ES (n_o) and activation energy (ΔE_a).

Weak Coupling Limit

Weak coupling limit (figure 1.3) can occur when the ES PES is nested with the GS PES. First tunneling from an ES into a vibrationally excited GS occurs, followed by vibrational relaxation (equation. 1.4 and figure 1.3).^[40,41,45]

$$k_{nr} = \frac{2\pi}{\hbar} \cdot \frac{H_{ab}^2}{\sqrt{4\pi\lambda_s k_B T}} \cdot \sum_{n_M} \left[\frac{S_M^{n_M}}{n_M!} \cdot \exp(-S_M) \cdot \exp\left(-\frac{(\Delta E - n_M \hbar \omega_M - \lambda_s)^2}{4\lambda_s k_B T}\right) \right] \quad (\text{equation. 1.4})$$

Here k_{nr} dependence includes the electronic coupling matrix (H_{ab}^2); solvent reorganizational energy (λ_s); the Huang-Rhys factor (S_M) which describes geometric distortion between GS and ES; the energy difference between the GS and ES vibrational levels (ΔE) and the quantum number for intraligand vibrational modes of the GS (n_M). This relationship is also known as the 'energy gap law' i.e. the exponential dependence of k_{nr} on ΔE , k_{nr} is inversely proportional to ΔE therefore the larger the energy gap between ES and GS the smaller k_{nr} .^[38,41]

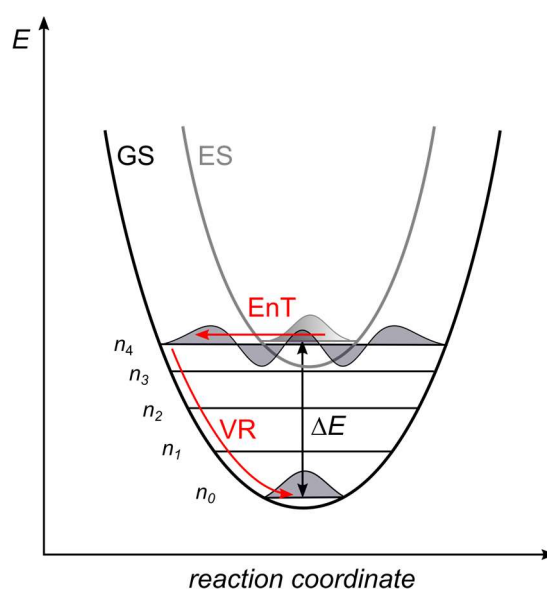


Figure 1.3: Ground (GS) and excited state (ES) PESs at the weak coupling limit, the red arrow horizontal arrow indicates the energy transfer via tunneling (EnT) and the vertical red arrow indicates vibrational relaxation (VR). Vibrational energy level (n) and the gap (ΔE) between GS (n_o) and ES (n_o).

Deactivation occurs via a horizontal EnT transition followed by vibrational relaxation to the GS. Equation 1.4 shows that k_{nr} increases with geometric ES displacement S_m , and with vibrational energy levels with the lowest quantum numbers n_m . Vibrational modes (with low quantum number overtones) that contribute most include high energy C–H, O–H and N–H

($\omega_M(X-H) = 3000-3600 \text{ cm}^{-1}$) stretching vibrations, and will affect ES energies of $8000-14500 \text{ cm}^{-1}$.^[41,46] Transfer of energy can occur to high energy oscillators present on the ligands of a TMC, or alternatively to surrounding solvent molecules.

Intersystem Crossing

The rate at which intersystem crossing (k_{ISC}) occurs relative to other competing processes will primarily determine whether phosphorescence will occur. This process has many competing processes which prevent population of a triplet state (mainly k_{VR} and k_{IC}) however, k_f will also compete with k_{ISC} . For phosphorescence to occur a change of spin multiplicity happens during a transition. This process is spin selection rule forbidden ($\Delta S = 0$), and so has a low probability of occurring. Facilitation of this change in multiplicity can occur because of SOC which is a relativistic effect where the spin and orbital angular momentum magnetically mix and interact. The total angular momentum of a system (J) should remain unchanged and can remain unchanged with change in spin angular momentum (S), but only if a simultaneous change of orbital angular momentum (L) occurs (equation. 1.5, El Sayed's rules). This mixing of orbital and spin angular momentum allows electronic states of different multiplicity to couple and mix, assisting with overcoming the selection rule restriction and thus increasing the probability of an electron 'flip'.^[15,37,39]

$$J = L + S \quad (\text{equation. 1.5})$$

The quantified SOC constant (ζ), is shown by the simplified Hamiltonian (\hat{H}_{SOC}) (equation. 1.6), and it includes several variables. The operator is the sum of the angular momentum operator (\hat{l}_i), spin angular momentum operator (\hat{s}_i) and SOC constant (ζ). The SOC constant importantly depends on the specific electronic configuration of an atom, and approximately scales with Z_{eff}^4 . 'The heavy atom effect' describes this increase in SOC in 4d and 5d TMs (e.g. $\zeta(\text{Ru}^{2+})_{\text{exp}} = 1159 \text{ cm}^{-1}$) compared with 3d TMs (e.g. $\zeta(\text{Fe}^{2+})_{\text{exp}} = 436 \text{ cm}^{-1}$) which can significantly increase k_{ISC} and the probability of phosphorescence.^[24]

$$\hat{H}_{SOC} = \sum_i \hat{l}_i \hat{s}_i \zeta \quad (\text{equation. 1.6})$$

The effect of SOC on k_{ISC} is apparent when applying Fermi's golden rule approximation (equation. 1.7);^[47] this approximation also includes the relation of the T_1 Franck-Condon weighted density of accepting states (FCWD) available for coupling with the S_1 state.

$$k_{ISC} = \frac{2\pi}{\hbar} \langle S_1 | \hat{H}_{SOC} | T_1 \rangle^2 \cdot \text{FCWD} \quad (\text{equation. 1.7})$$

Spin-vibronic coupling is another mechanism that can facilitate high ISC rates. This type of coupling assumes a breakdown of the Born-Oppenheimer approximation instead assuming nuclear and electron motion are on a similar timescale. Coupling or mixing of electronic states with vibronic progressions, resulting from molecular geometric distortions can then occur.^[39] Smaller SOC can present an intrinsic problem when attempting to achieve phosphorescence in 3d TMCs. ISC for TMCs typically occurs on a short timescales (fs) (e.g. ruthenium(II) (**1**²⁺) and chromium(III) (**5**³⁺)),^[48,49] though slower (ns-ps) timescales have been observed in some other complexes.^[26,39,50–52] Such examples include [FeO₄]²⁻ (**7**²⁻) with slower ISC being attributed to nested high energetic barriers for surface crossing,^[53] and [Cu(dmp)₂]⁺ (dmp = 2,9-dimethyl-1,10-phenanthroline) (**8**⁺) with slower ISC described as a result of weakened SOC due to geometric distortion and ‘flattening’ of the complex.^[54,55]

1.1.3 Excited-State Bimolecular Processes

Bimolecular quenching is an alternative non-radiative process that can follow excitation of a TMC, and can occur as EnT (Förster and Dexter) and ET (oxidative and reductive). It is essential that the energy of an ES photosensitized donor (D^{*}) can excite an acceptor molecule (A) for EnT to occur.^[56] Whereas for ET to occur the excited state redox potential of a photosensitizer (P_{SEN}) and GS redox potential of a substrate (sub) must be compatible.^[2,57] Bimolecular quenching can be further classified by timescale. Dynamic (collisional) bimolecular quenching requires a sufficiently long ES lifetime to be quenched on a diffusion controlled timescale, as described by the Stern-Volmer relation i.e. > 1 ns (equation. 1.8).^[38]

$$\frac{\Phi_0}{\Phi} = \frac{\tau_0}{\tau} = 1 + K_D \tau_0 [Q] = 1 + K_{SV} [Q] \quad (\text{equation. 1.8})$$

Here, Φ_0 and Φ represent luminescence intensities without and with quencher; τ_0 and τ the lifetime of emitter without and with quencher present; $[Q]$ the concentration of quenching species and K_D the dynamic quenching constant. The Stern-Volmer constant K_{SV} for a specific system can be extracted from concentration dependent experiments i.e. plotting Φ_0/Φ or τ_0/τ vs $[Q]$, where the slope is equal to K_{SV} . Additional factors such as medium viscosity, temperature and sterics (sensitizer and quencher) can affect diffusion and thus collision kinetics.^[38] Conversely, static bimolecular quenching is not diffusion controlled and has a pseudo Stern-Volmer relationship. It can therefore occur on shorter timescales (< 1 ns), as there is already close pre-association between ES sensitizer and quencher (equation. 1.9).^[58–60]

$$\frac{\Phi_0}{\Phi} = 1 + K_s [Q] \quad (\text{equation. 1.9})$$

Where, K_s represents the association constant of the complex formation, and Φ_0/Φ vs $[Q]$, will yield a straight line with slope equal to the static quenching constant K_s . Transient absorption spectroscopy (TA) can also help to assign static quenching, as this type of quenching typically does not have an effect on the lifetime of a sensitizer. Such time resolved spectroscopy can also be used in the case of non-emissive bimolecular processes to extract information bimolecular quenching kinetics.^[2,61,62] Although Stern-Volmer analysis and ultrafast spectroscopy can distinguish between static or dynamic quenching, they cannot reveal whether ET and EnT has occurred. Further analysis of product formation will confirm if ET or EnT has occurred (i.e. looking for presence of oxidized or reduced photosensitizer/quencher confirms that ET has occurred).^[24,60]

Energy transfer

Photophysical EnT occurs from a D^* molecule to an A molecule in a lower energy state. This EnT leads to dissipation of D^* and excitation of A. The thermodynamic potential is connected to the E_{00} of both D^* and A i.e. $\Delta G^0 = E_{00}^A - E_{00}^D$ (with entropic and λ_s effects assumed negligible). This enables the possibility of a Marcus-type treatment (equation. 1.10) for such processes.^[24,36]

$$k_{EnT} = \frac{4\pi^2}{h} (H^{EnT})^2 FCWD \quad (\text{equation. 1.10})$$

Here k_{EnT} depends on the electronic coupling between D^* and A (H^{EnT}) and is composed of electronic Coulombic and exchange elements that regulate EnT. The Franck-Condon weighted density of states ($FCWD$) corresponds with the spectral overlap integral between the absorption and emission spectra. The two mechanisms for EnT i.e. electronic Coulombic (Förster) and exchange (Dexter), are described in the following section.^[38]

Förster Resonance Mechanism

The mechanism of Förster EnT is dipole-dipole induced, distance dependent, and can follow when sufficient spectral overlap between the emission of D^* and the absorption of A occurs. (equation. 1.11, figure 1.4).

$$k_{EnT}^F = 8.8 \times 10^{-25} \frac{K^2 \Phi}{n^4 r^6 \tau} J_F \quad (\text{equation. 1.11})$$

Here n is the solvent refractive index and r is distance between D^* and A; τ and Φ are the lifetime and quantum yield of D^* respectively; J_F signifies the normalized spectral overlap between the emission of D^* and absorption of A, while K^2 describes directional dipole-dipole

interactions. Importantly this mechanism can occur over a relatively long range (r^{-6}). Förster EnT does not involve a change in multiplicity i.e. singlet to singlet EnT.^[38]

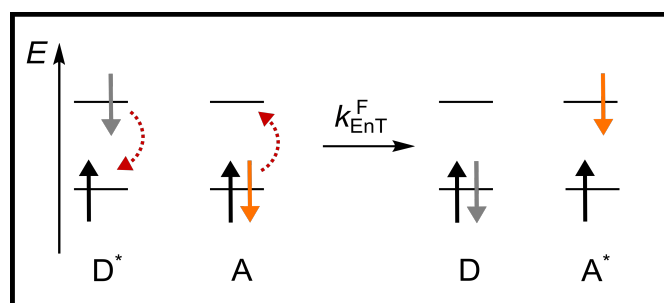


Figure 1.4: Schematic representation of Förster (Coloumbic) EnT from excited singlet donor molecule (D^*) to a singlet acceptor molecule (A).

Dexter Mechanism

Dexter, unlike Förster EnT, is a double electron transfer and can occur between D^* and A states of different multiplicities. The multiplicity of D^* and A can change during the exchange and the overall multiplicity of the process can remain conserved. This mechanism describes how an electron transfers from D^* to the LUMO of A, while simultaneous movement of a second electron from the HOMO of A to the SOMO of D^* (figure 1.5).^[24,36]

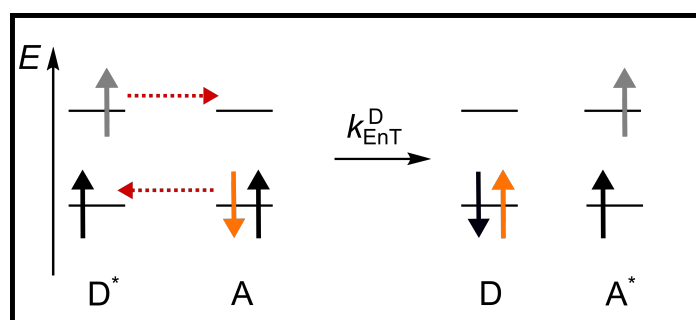


Figure 1.5: Schematic representation of Dexter (exchange) EnT from an excited triplet donor molecule (D^*) to the HOMO of an acceptor molecule (A) and concurrent transfer of a second electron from HOMO on A to SOMO on D^* .

Dexter EnT is strongly distance dependent as it requires orbital/wavefunction overlap of D^* and A ($r < 10 \text{ \AA}$); its rate decreases exponentially with increased distance (equation. 1.12).

$$k_{\text{EnT}}^{\text{D}} = \frac{4\pi^2}{h} \left(H^{\text{EnT}}(0) \cdot \exp \left[-\frac{\beta^{\text{EnT}}}{2} (r - r_0) \right] \right)^2 J_{\text{D}} \quad (\text{equation. 1.12})$$

Here, the electronic coupling factor H^{EnT} includes the interaction contact distance $H^{\text{EnT}}(0)$, along with attenuation factor for the exchange energy β^{EnT} . J_{D} describes normalized overlap of the emission of D^* and absorption of A. One common example of Dexter EnT is quenching of a triplet emission by triplet oxygen, producing singlet oxygen. Although detrimental for

emission, this can be harnessed for use in optical oxygen sensing or production of $^1\text{O}_2$ for use in further reactions.^[25,63,64]

Electron Transfer

Photoexcited species can act as stronger oxidants or reductants compared to their GS counterparts. When in contact with molecules that have suitable potentials, photo-induced electron transfer (PET) can happen to quench the ES. This can occur when an electron is transferred from substrate to the now strongly oxidizing ES photosensitizer (figure 1.6a) or where ET occurs from the strongly reducing ES photosensitizer to a substrate molecule that is lower in energy (figure 1.6b).

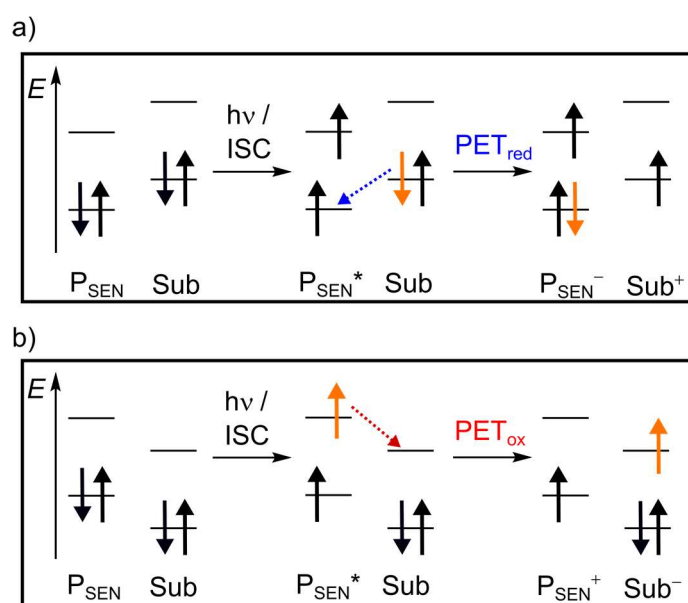


Figure 1.6: Schematic representation of reductive (a) and oxidative (b) photo-induced electron transfer (PET).

The ES photoredox potentials of a species can be estimated using equations 1.13 and 1.14.^[2,62]

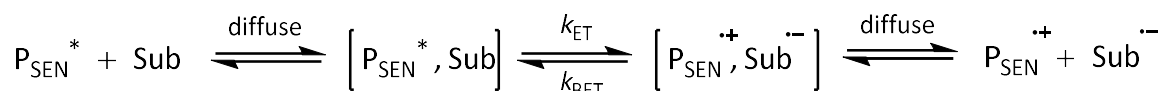
$$E_{ox}^* = E_{ox} - E_{00} \quad (\text{equation. 1.13})$$

$$E_{red}^* = E_{red} + E_{00} \quad (\text{equation. 1.14})$$

E_{00} represents the energy gap between the ES and GS at zero vibrational levels (0–0 transition); E_{ox} the one electron GS oxidation potential and E_{red} the one electron GS reduction potential. Kinetically ET is described by expanded Marcus theory (equation. 1.15).^[65–67]

$$k_{ET} = \frac{4\pi^2}{h} \left(H^{ET}(0) \cdot \exp \left[-\frac{\beta^{ET}}{2} (r - r_0) \right] \right)^2 \frac{1}{\sqrt{4\pi k_b T}} \cdot \exp \left(-\frac{(\Delta G^0 + \lambda)^2}{4\lambda k_b T} \right) \quad (\text{equation. 1.15})$$

The rate constant k_{ET} has a P_{SEN}/Sub distance-dependent electronic coupling factor H^{ET} , which includes the interaction contact distance $H^{ET}(0)$, along with an attenuation factor β^{ET} . The Franck-Condon factor contains the reorganizational energy λ , which reflects the energetics associated with structural or solvent redistribution tied to ET, the Boltzmann constant k_b and the thermodynamic driving force ΔG^0 .

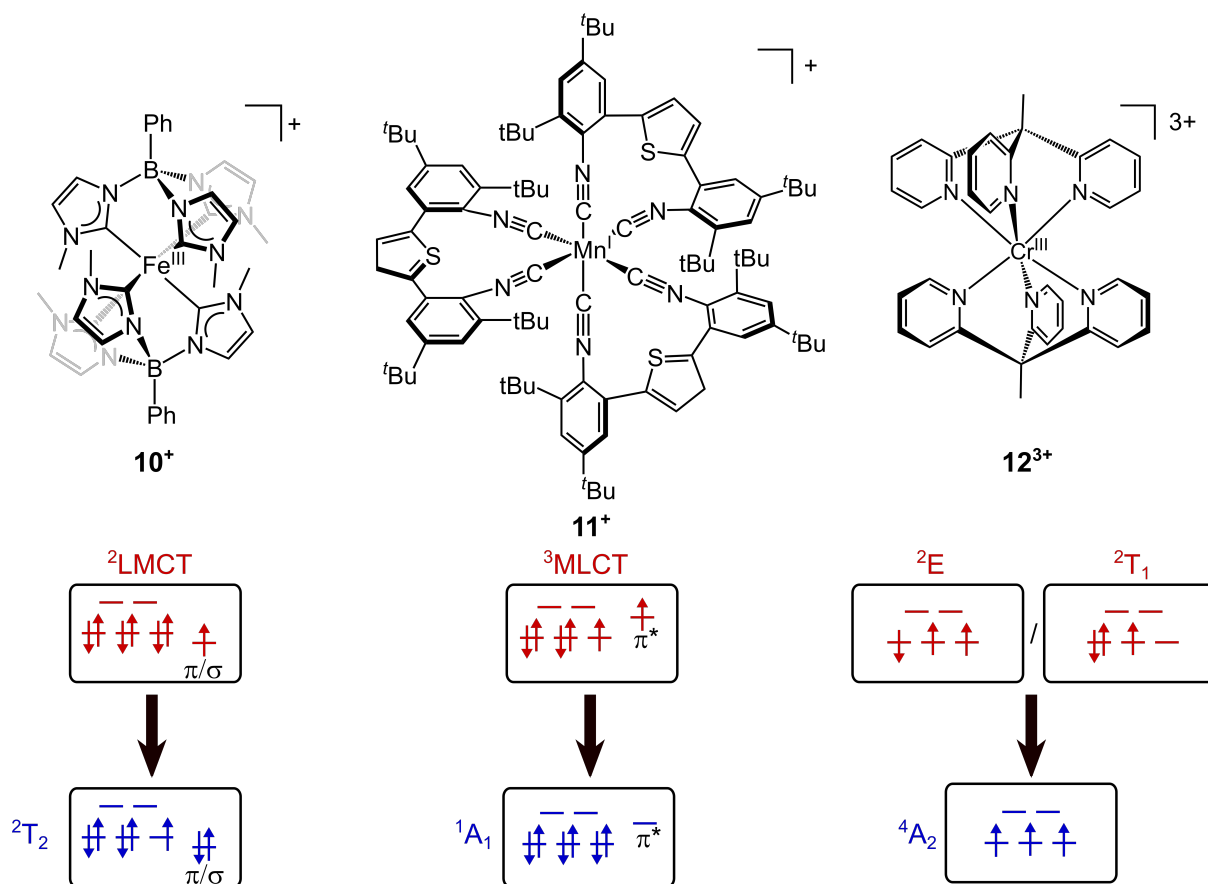


Scheme 1.3: Schematic representation of the stages of ET (oxidative quenching) between photosensitizer (P_{SEN}) and substrate (sub).

For an outer sphere ET (i.e. ET between two moieties that do not undergo ligand substitution) (scheme 1.3), P_{SEN} and Sub diffuse together to form an encounter complex. This encounter complex is surrounded by a cage of solvent molecules wherein ET can occur if there is sufficient driving force and electronic coupling. Following ET, products can then escape the solvent cage and diffuse apart. The cage escape yield of an electron transfer process, i.e. the yield with which products charge separate and escape a solvent cage, and the rate of back ET will have an effect on the overall process rate and outcome.^[62] Examples of factors that can affect such cage escape and back electron transfer include solvent polarity/viscosity, temperature, spin-parity and SOC.^[62,68–71] If a photosensitizer can be reversibly recovered, it is possible to use them in a photocatalytic cycle.^[57] Regeneration of the photoactive species can be carried out using a sacrificial oxidant/reductant or electrolysis^[72–74] to give a closed catalytic cycle, and subsequent turnovers following absorption of light.^[7,71] An example of photocatalysis can be seen with the trisaminocyclopropenium radical dication.^[74] This photocatalyst was found to be strongly photooxidative ($E_{ox}^* = 2.95$ vs ferrocene/ferrocenium) and capable of catalyzing Nicewicz-type coupling of benzene to a deactivated pyrazole (1H-pyrazole-4-carboxylic acid ethyl ester) with 65% yield following irradiation (compact fluorescent light (CFL), 23 W) for 60 hrs. Re-oxidation of the catalyst was carried out using electrolysis,^[72–74] due to its high GS potential ($E_{1/2} = +0.88$ V ferrocene/ferrocenium) and significant absorption in the visible region (up to 600 nm).^[74]

1.2 Emission from 3d Transition Metal Complexes

Phosphorescence from 3d TMCs can have different character depending on the electronic nature and structures of the TMCs. The main types are charge-transfer (CT), metal-centered (MC/SF) and ligand-based (Intraligand-charge transfer (ILCT), ligand-to-ligand charge transfer (LLCT)).^[16] Examples of some CT and MC emissive TMCs include $[\text{Fe}(\text{phtmeimb})_2]^+$ (phtmeimb = phenyl[tris(3-methylimidazol-1-ylidene)] (**10**⁺, scheme 1.4) which shows ²LMCT emission ($\lambda_{\text{em}} = 655 \text{ nm}$, $\tau = 2 \text{ ns}$, $\Phi = 2.1 \%$ at RT in CH_3CN),^[75] $[\text{Mn}(\text{L}^{\text{bi}})_3]^+$ ($\text{L}^{\text{bi}} = 2,5\text{-bis}(3,5\text{-di-}t\text{-tert-butyl-2-isocyanophenyl)thiophene}$) (**11**⁺, scheme 1.4) which shows ³MLCT emission ($\lambda_{\text{em}} = 485 \text{ nm}$, $\tau = 0.74 \text{ ns}$, $\Phi = 0.05 \%$ at RT in deaerated CH_3CN)^[76] and $[\text{Cr}(\text{tpe})_2]^{3+}$ (tpe = 1,1,1-tris(pyrid-2-yl)ethane) (**12**³⁺, scheme 1.4) which shows ²MC emission ($\lambda_{\text{em}} = 748 \text{ nm}$, $\tau = 4500 \mu\text{s}$, $\Phi = 8.2 \%$ at RT in deaerated $\text{D}_2\text{O}/\text{DCIO}_4$).^[77]



Scheme 1.4: Example TMC complexes showing emission originating from various types of phosphorescence. Shown here a LMCT transition (left) which involves transfer of charge from occupied π_{L} orbitals or σ_{ML} bonding orbitals to the metal; an MLCT transition (middle) which involves transfer of charge from the π -metal t_{2g} orbitals to unoccupied π_{L}^* orbitals; and a MC/SF transition (right) involving only metal d orbitals.

Spin-Flip

Spin-flip emission is described as phosphorescence from a TMC intraconfigurational MC state, and to understand the requirements for MC/SF emission (scheme 1.4, right), a further the electronic description using potential energy surfaces (PESs) and Tanabe-Sugano diagrams can be used.^[19,20] Both can be used to understand which d electron configurations are suitable for SF emission. Configurations d^2 , d^3 , d^4 and d^8 are candidates for such emission as they contain nested intraconfigurational states i.e. SF states share the same overall electronic configuration as the GS. This means that the ES is not geometrically distorted (e.g. M-L bond elongation) due to no bonding orbitals being depopulated or anti-bonding orbitals being populated following excitation and SF transition (figure 1.7, bottom). This is not the case for other configurations such d^6 low-spin (LS) that contains distorted interconfigurational states (figure 1.7, top).^[21] This nesting of SF states gives a sharp emission band profile that is typically low in energy (NIR). The benefit of having nested states means that k_{nr} is less competitive with k_{ph} , leading to phosphorescence in spite of the transition being Laporte and spin selection rule forbidden.^[78,79]

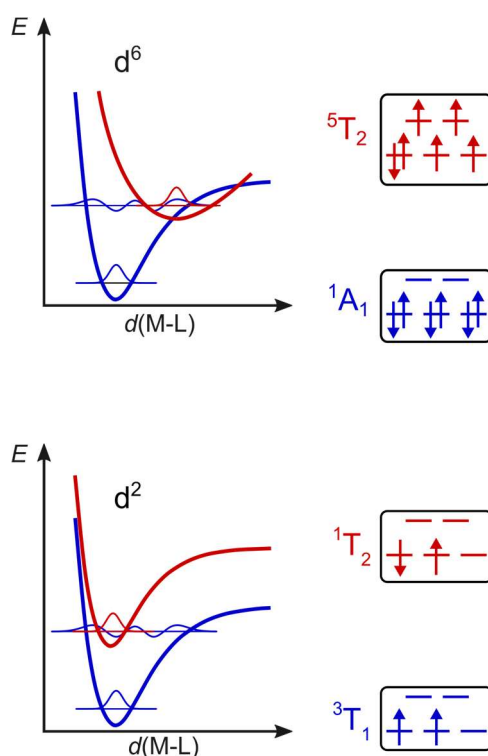


Figure 1.7: Example GS (blue) and lowest SF/MC (red) potential energy curves for d^2 electronic configuration (bottom) and d^6 LS (top), illustrating a geometrically distorted (5T_2 d^6 LS) compared with a nested ES (1T_2 d^2).

Tanabe-Sugano diagrams are important descriptors of intra- and interconfigurational states of TMCs. In an octahedral ligand environment LF terms are plotted as a function of LF strength, and both terms are scaled by the Racah parameters. The Racah parameters (B and C) describe the d-d interelectronic repulsion in octahedral TMCs where the relative state energies are proportional to the C/B ratio and so will vary with varied TMCs.^[21] The Tanabe-Sugano diagram for the d^2 electronic configuration shows this relation (figure 1.8); As LF

strength increases, so does the energy of the distorted 1st excited state (3T_2) beyond the point where it crosses (black circle) with the LF independent SF states (${}^1E/{}^1T_2$). This leaves SF states as the lowest energy states and allows for potential SF emission. Larger LF strength is advantageous because a larger energy gap between intra- and interconfigurational states ($\Delta_0/B > 40$) helps suppresses thermally activated bISC.^[78]

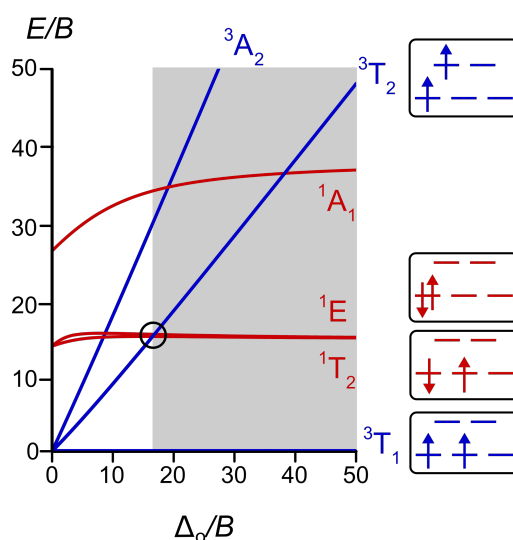
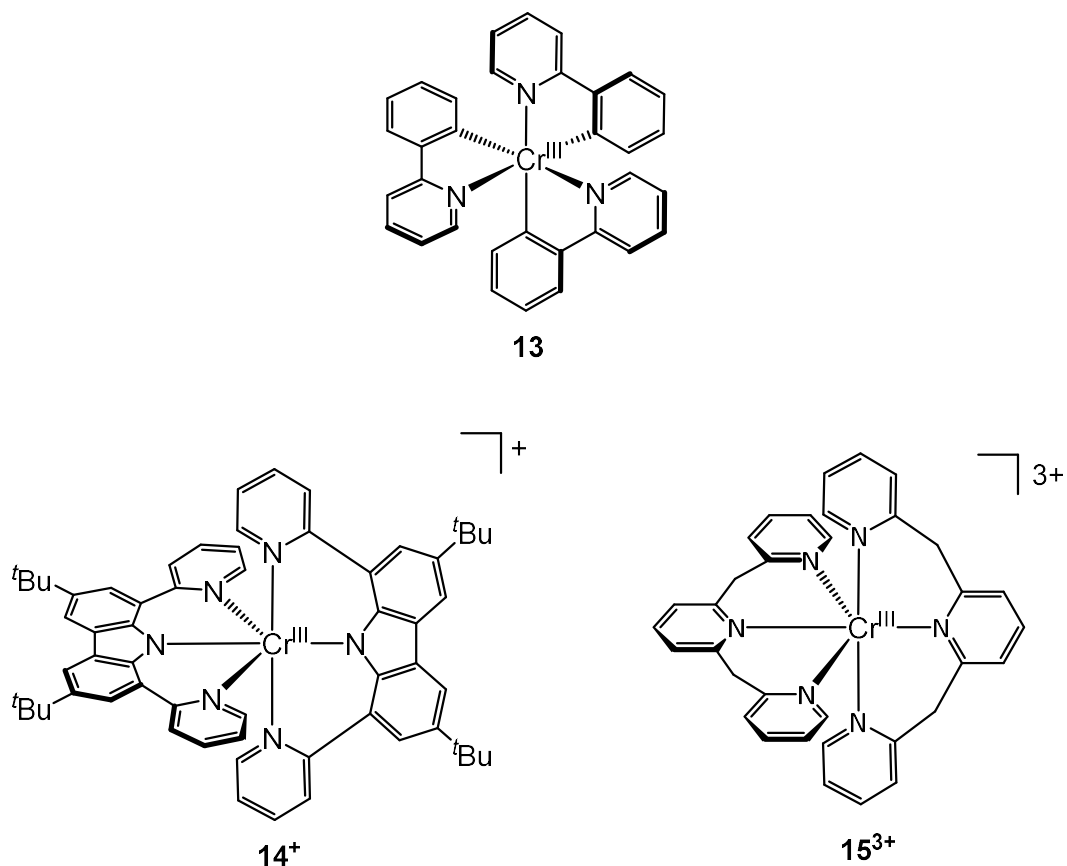


Figure 1.8: Simplified Tanabe-Sugano diagram for octahedral d^2 electronic configuration in octahedral symmetry ($C/B = 4$, scaled by Racah B parameter) with microstates of the triplet, spin allowed states (blue) and singlet MC states (red). Configurations d^3 , d^8 and d^4 will be further discussed in sections 1.3 and 1.4.^[80]

Tanabe-Sugano diagrams apply for strict octahedrons; deviations from this symmetry in the GS or ES mean deviations from these descriptions. These diagrams do not factor in SOC, which also can lead to state mixing and deviations (not as significant for 3d metals compared with 4d and 5d). They also neglect CT states which can have an effect on SF emission.^[21]

When it comes to adjusting emission energies for SF emitters, it is challenging; the energies of SF states are difficult to predict because of d-d interelectronic repulsion. Furthermore, a clear relationship between various ligands, metal identity and charge does not exist beyond the nephelauxetic relationship^[81,82] i.e. the relation of d-d interelectronic repulsion as described by the Racah parameters B and C and the effect on M-L bond covalency. An increase in M-L bond strength and larger degree of covalency correlates with a decrease in Racah parameter B , and a lowering in energy of SF states, and a red shift in emission energies. This effect is seen when comparing complex 5^{3+} to other octahedral chromium(III) complexes such as *fac*-[Cr(ppy)₃] (ppy = deprotonated 2-phenylpyridine) (**13**, scheme 1.5) ($\lambda_{em} = 910$ nm at 77K in frozen 2-MeTHF)^[83] and [Cr(dpc)₂]⁺ (dpc = 3,6-di-*tert*-butyl-1,8-di(pyridine-2-yl)-carbazolato) (**14**⁺, scheme 1.5) ($\lambda_{em} = 1067$ nm at 77K in frozen CH₃CN).^[84] Increasing the Racah B parameter has the opposite effect, with the increase of interelectronic repulsion and blue shift of emission compared to 5^{3+} , demonstrated in [Cr(bpmp)₂]³⁺ (bpmp = 2,6-bis(2-pyridylmethyl)pyridine) (**15**³⁺, scheme 1.5) ($\lambda_{em} = 709$ nm at RT in H₂O).^[63] This effect can also be linked to the charge of the metal center where the Racah B and C parameters increase with charge.^[85]



Scheme 1.5: Molecular structures of emissive chromium(III) complexes **13–15³⁺**.

SF emission (energy, lifetime and quantum yield) are affected by various external factors, such as temperature and pressure. While increased temperature can have the effect of leading to thermal deactivation processes, it can also affect the Boltzmann population of various energetically close SF states. In turn, this can affect the emission band shape and number of bands, which is the case of complex **5³⁺** (scheme 1.2). **5³⁺** has dual band luminescence at RT, however the relative intensity of these band changes with temperature allowing for further use as an optical ratiometric thermometer.^[86] External pressure has been seen to also have an effect on SF emission with complex **5³⁺** which shows a shift in emission of $-14.8 \text{ cm}^{-1} \text{ kbar}^{-1}$ in H_2O . Increase in hydrostatic pressure leads to small structural changes in the complex and consequently the M-L bonding changes, changing the nephelauxetic effect and leading to a red shift in emission. This effect can be harnessed for use as an optical pressure sensor.^[87] SF emission can also be switched off by altering the pH as seen with **15³⁺** (scheme 1.5). Increasing the pH leads to deprotonation of the ligand methylene bridge and the complex becomes non-luminescent, as this leads to de-aromatization of one of the coordinating pyridine moieties and thus alteration of ligand donor properties. Such reversible deprotonation allows for ratiometric optical pH sensing.^[63]

Charge Transfer

Charge transfer emission involves movement of charge within a molecule. LMCT requires an electron deficient metal centre (e.g. Iron(III), scheme 1.4, left); MLCT requires an electron rich metal centre (manganese(I), scheme 1.4, middle). This electronic transition involves bonding orbital depopulation or anti-bonding orbital population, leading to ES distortion (similar to d^6 LS PESs (figure 1.7, top)). CT transitions are not Laporte-forbidden, unlike SF transitions and so generally give intense, broad emission profiles.^[44]

The emission energy for CT bands is conceptually more straightforward to adjust than with SF emitters, by adjusting the energy gap between the metal d-orbitals and the π_L^* orbitals (MLCT) or π_L/σ_{ML} orbitals (LMCT). The narrowing of this energy gap would cause a red shift emission; an MLCT example would be to use more σ -donating ligands to de-stabilise the t_{2g} orbitals relative to the π_L^* , or to introduce electron withdrawing substituents onto a ligand lowering the π_L^* orbital energy relative to the t_{2g} orbitals.^[88] This can be seen with the example of $\mathbf{1}^{2+}$ ($\lambda_{em} = 620$ nm) vs. $[\text{Ru}(4,4'\text{-bpy}(\text{NO}_2)_2)_3]^{2+}$ ($4,4'\text{-bpy}(\text{NO}_2)_2 = 4, 4'\text{-dinitro-2,2'-bipyridine}$) ($\mathbf{16}^{2+}$) ($\lambda_{em} = 700$ nm).^[2,36,89-94] The MLCT emission energy can also be lowered by changing the metal centre e.g. Ru to Os (4d vs. 5d orbitals) shown by complex $\mathbf{1}^{2+}$ ($\lambda_{em} = 620$ nm) vs. $[\text{Os}(\text{bpy})_3]^{2+}$ ($\mathbf{17}^{2+}$) ($\lambda_{em} = 735$ nm).^[44,95,96]

CT emitters are also subject to local environment changes; they have a larger transition dipole moment than SF emitters and so are more subject to changes in solvent polarity (solvatochromism) or changes in counter cation/anion.^[97] Cryogenic temperatures and high pressure have the effect of suppressing deactivation via solvent vibrational modes of ligand vibrational modes.^[98] Temperature changes can also lead to state occupation differences like with MC emitters, affecting emission profiles, with each effect previously reported to occur with complex $\mathbf{1}^{2+}$ (scheme 1.1).^[44,99]

Both SF and CT emissive states are sometimes not composed of 'pure' MC or CT character. Typically such states can be close in energy and so can mix, having properties of both types including LC admixtures.^[100] Emissive state mixing can additionally offer additional benefits. Increased MC character could offer an increase in lifetime (transition becomes more parity forbidden) and additional CT character can offer an increase in absorption of a complex. Alternatively, mixed character of states can offer challenges such as ES distortion and vibrational deactivation as seen with $\mathbf{14}^+$, noted as an admixture of $^2\text{LMCT}$ and ^2MC states.^[84]

1.2.1 Luminescence Enhancement

There are a number of ways to enhance emission for 3d TMCs, beginning with ligand design. The initial challenge is a result of the primogenic effect which describes how 3d TMs have the inherent problem of smaller LF splitting due to the absence of radial nodes in the 1st d shell electronic functions. This results in radial contraction of the 3d orbitals in contrast to the 4d and 5d orbitals. This contraction leads to poor overlap of 3d orbitals with ligand orbitals leading to smaller LF splitting (figure 1.9).^[101,102]

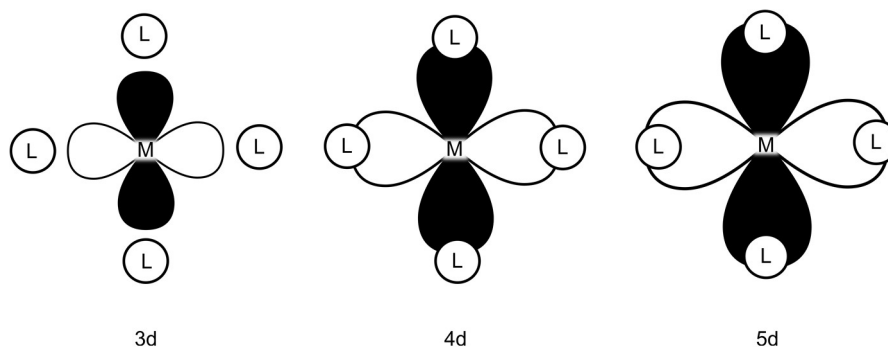


Figure 1.9: Schematic representation of the primogenic effect, illustrating the contraction of 3d orbitals, relative to the 4d and 5d homologues.

There are a few noteworthy ways to overcome this challenge, including the use of strong field ligands and/or maximizing metal-to-ligand (M-L) bond overlap. The use of strong field ligands is a clear way to overcome such issues i.e. increasing the σ -donating character of the ligand will destabilize the σ -bonding metal e_g^* orbitals (e.g. use of carbenes);^[103] increasing the π -accepting ability of a ligands will stabilize the π -metal non-bonding t_{2g} orbitals (e.g. use of CO).^[104] Another way is by maximising M-L bite angle (L-M-L) and bond overlap; this is the idea of increasing the bonding angle of the ligand to overlap more efficiently with the orthogonal 3d bonding d_z^2 and $d_{x^2-y^2}$ orbitals. This can be clearly seen when comparing the 3d $d_{x^2-y^2}$ orbital overlap with the ddpd ligand and the terpy ligand (figure 1.10).^[79,105]

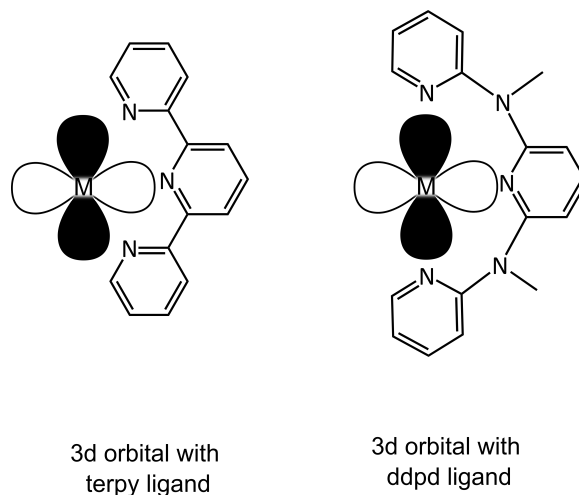


Figure 1.10: Comparison of 3d orbital overlap with a terpy (left) and ddpd (right) ligand; N-M-N bond angles for the 5-membered terpy ligand are *ca.* 78°, whereas angles with the 6-membered ddpd ligand are close to 90° enabling much more efficient M-L orbital overlap and leading to a stronger LF.

These strategies of course can be – and usually are – combined, as many ligand types are both accepting and donating. Effective ligand design has also been shown to help suppress quenching with confined SF states (Dexter EnT) via triplet oxygen. For example making a ligand more sterically bulky, as seen with substituted 5^{3+} (scheme 1.2). Bulky Tripp groups (Tripp = 2, 4, 6-triisopropylphenyl) were added at the 5-position of the terminal pyridines of ddpd ligand. This enhanced the lifetime and quantum yield in oxygenated CH_3CN from 52 μs and 0.8 % to 518 μs and 5.1 %.^[25]

In addition to effective ligand design other methods can be employed to increase the lifetime and quantum yield of 3d TMCs. For instance, as previously mentioned cryogenic temperatures along with the rigidification of the complex can reduce geometric distortion and intramolecular vibrations.^[106] Increasing the energy separation between the emissive states and deactivating states is another method to reduce deactivation.^[79] Another example for SF emitters is the introduction of an inversion center to a TMC, increasing the Laporte-forbidden nature of a MC/SF transition and prolonging the lifetime as seen with 12^{3+} (scheme 1.4) showing a lifetime of 4500 μs ^[77] compared with 1122 μs for 5^{3+} (scheme 1.2).^[78] A particularly successful approach to suppress the multiphonon relaxation is the deuteration of ligand and/or solvent. This approach aims to significantly reduce the energy of the X–H oscillators, increasing their quantum number overtone and thus decreasing non-radiative decay via multiphonon relaxation (figure 1.1). This method is especially useful for NIR emitters whose energy is most at risk from deactivation via weak coupling. This was seen with 5^{3+} , where the lifetime and quantum yields were extended by changing H_2O to D_2O , which increases the quantum yield and lifetime from 11 % and 898 μs to 14.2 % and 1164 μs (in deoxygenated conditions). Further enhancement was achieved by the statistical deuteration of the ddpd ligand; the combined effect of D_2O and d_9 -ddpd enhances the quantum yield and lifetime to 30 % and 2300 μs (deoxygenated conditions).^[78,79,107,108] This can also be seen for complex 15^{3+} (scheme 1.5), with quantum yield and lifetime increasing from 15.8 % and 1550 μs to 24.6 % and 2500 μs (in acidic deoxygenated media) upon introduction of deuterated solvent and

ligand.^[63] A similar yet smaller effect is seen in the CT emitter **1**²⁺ (scheme 1.1), where the lifetime is prolonged by 75 ns upon deuteration.^[44,109]

1.3 Manganese

Manganese is one of the most abundant TMs on earth at $\approx 0.1\%$ of the earth's crust.^[9,110] It is commonly found in the Earth's crust as the minerals pyrolusite (MnO_2) and rhodochrosite (MnCO_3), and when isolated it is used in various industrial processes, particularly in making alloys such as steel to improve strength and hardness.^[111] It is used in catalysis,^[112] found in biological systems^[113] and is vital in photosynthesis, as part of the oxygen evolving cluster ($\text{Mn}_4\text{O}_5\text{Ca}$) that splits water as part of the photosystem II process.^[114,115] Manganese possesses rich redox chemistry and is relatively stable in eight oxidation states, with 0, I, II, IV and VII compounds being most prevalent. Common examples include MnCl_2 , $\text{MnBr}(\text{CO})_5$, MnO_2 and the well-known aqueous oxidant KMnO_4 .^[116] The oxidation states III, V, VI are less stable and compounds containing manganese in these oxidation states more rare; some examples include such as Mn_2O_3 or K_2MnO_4 .^[110] Notably, manganese has rich oxide chemistry, as the hard dianionic oxygen ligand can better stabilize the higher oxidation states of Mn.^[117]

With greater general emphasis on sustainability, there has been increased interest in the photophysical properties of Mn based sensitizers. There are various reports of emissive doped $\text{Mn}^{\text{II,IV,V}}$ solids and their potential in applications such as in OLEDs.^[118–120] Most examples of emissive molecular manganese TMCs are with the Mn^{II} cation, which is largely related to the ease of synthesis from readily available manganese(II) starting materials.^[121] Manganese(IV) is an attractive prospect as an analogue to chromium(III), with the rich well documented Cr^{III} SF photochemistry.^[16] However, TMCs containing Mn^{IV} are comparatively few and synthesis begins with Mn^{II} salts, requiring challenging oxidations to achieve Mn^{IV} ;^[122] thus, the photophysical properties are not well understood.^[8]

The unique properties and (photo)physical characteristics of molecular Mn^{II} compounds advancing through Mn^{III} to Mn^{IV} will be discussed, with focus on Mn^{IV} , to aid in the understanding, design and synthesis of photoactive Mn^{IV} containing TMCs.

1.3.1 Manganese(II)

Mn^{II} is the most common oxidation state of Mn and has a d^5 electronic configuration. When in an octahedral LF it can have a high-spin (HS) ($S = 5/2$) or LS ($S = 1/2$) configuration. Typically, Mn^{II} exists in a highly paramagnetic HS configuration, which is a consequence of the inherent stability of a half-filled d electron shell and Hund's rule of maximum multiplicity.^[81] Octahedral HS Mn^{II} is also characteristically substitutionally labile, resulting from the larger ionic radii and

lack of LF stabilization energy. This lability also means the barrier for isomerization is low, making isolation of single isomers a challenge.^[123] Suppressing such ligand substitution and isomerization proves challenging. It is possible with careful ligand design, for example using rigid chelate ligands or steric bulk e.g. $[\text{Mn}(\text{tppb})_2]^{2+}$ (tppb = hydro-tris(3-phenylpyrazol-1-yl)borate) (**18**²⁺, scheme 1.6)^[124] or $[\text{Mn}(\text{L}^{\text{py}})_2]^+$ (**19**⁺, scheme 1.6) (L^{py} = bispidine pyridine).^[125,126]

The Tanabe-Sugano diagram for octahedral Mn^{II} TMCs (figure 1.11) shows the photophysical MC landscape of these complexes.

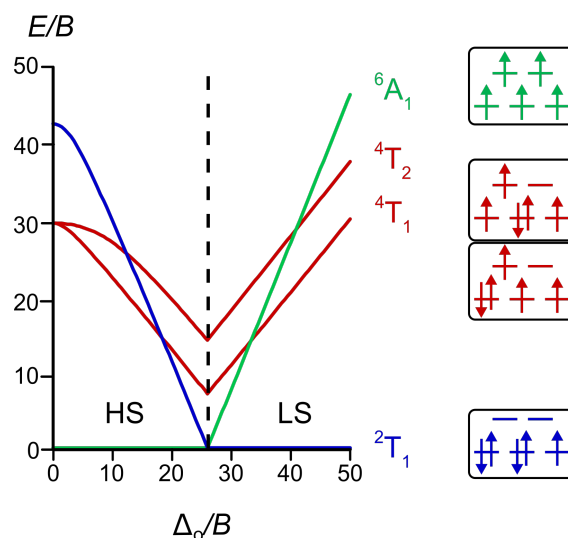
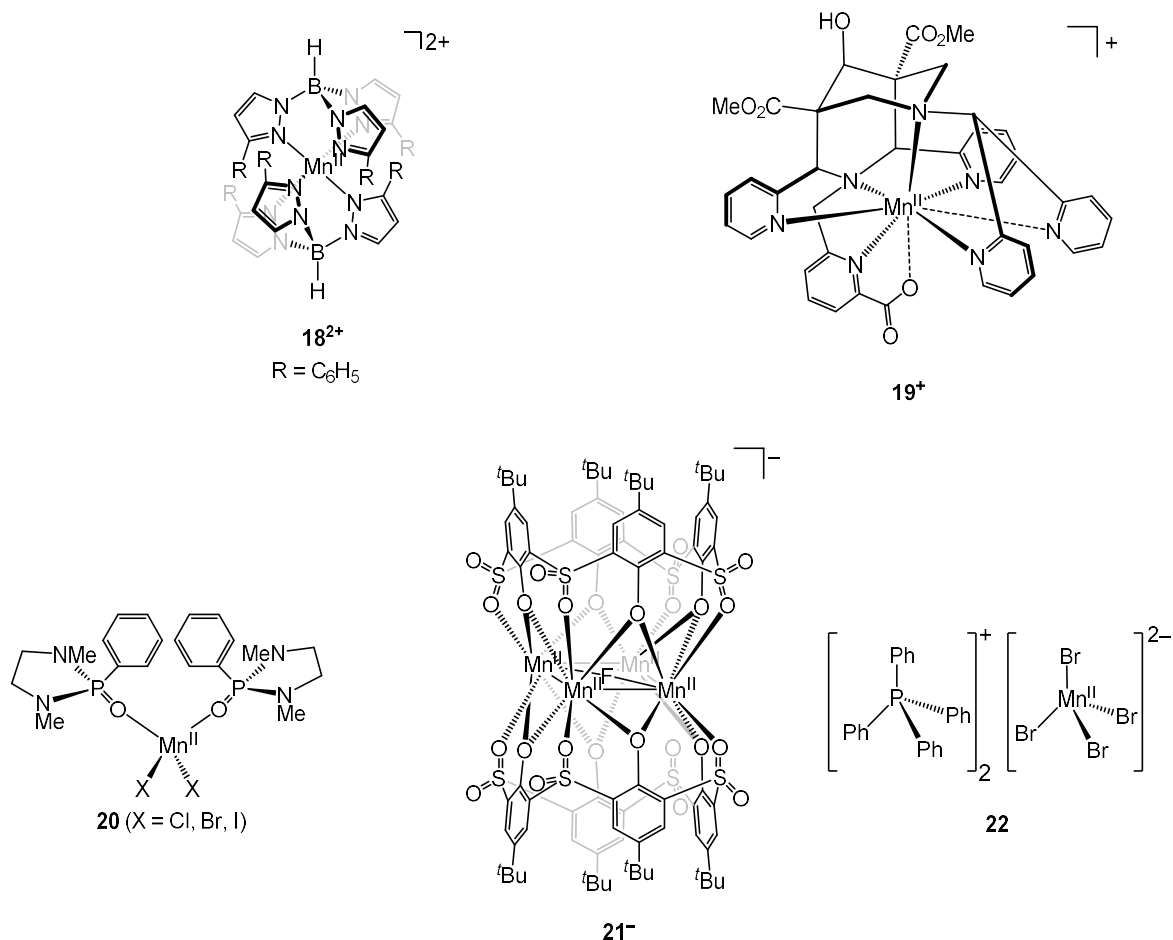


Figure 1.11: Simplified Tanabe-Sugano diagram for d^5 electronic configuration in octahedral symmetry ($C/B = 4$, scaled by Racah B parameter) with microstates of the doublet (blue), sextet (green) and quartet, MC states (red).^[80]

In HS configuration, LF transitions are Laporte-forbidden and spin-forbidden leading to weakly colored complexes.^[127,128] However, molecular (and solid state) luminescent Mn^{II} complexes are most common amongst Mn TMCs.^[121,129,130] An important difference between the d^5 Tanabe-Sugano diagram with those of d^2 - d^4 and d^8 , is that the quartet states ($4T_2$ and $4T_1$), are not nested (antibonding orbitals are populated) and structurally distorted. As the LF strength increases, a spin-crossover point is reached and HS converts to LS; such conversion with Mn^{II} requires strong field ligands, e.g. CN^- .^[131] LS Mn^{II} compounds are rare with only a few reported.^[132–136]



Scheme 1.6: Molecular structures of HS d^5 - Mn^{II} complexes **18²⁺**–**22**; complexes **20**–**22** show MC luminescence.

Due to the forbidden nature of the MC transitions in HS Mn^{II} complexes, strategies for luminescence aim at reducing the overall symmetry of the system. This is done by making transitions ‘more’ allowed, for example with $[MnX_2(L^{me})_2]$ ($X = Cl, Br, I$, $L^{me} = 1,3$ -dimethyl-2-phenyl-1,3-diazaphospholidine-2-oxide) (**20**, scheme 1.6) ($\lambda_{em}(Br) = 509$ nm, $\tau(Br) = 683$ μ s and $\Phi(Br) = 23$ % in solid state at RT), utilizing a tetrahedral environment that does not possess a center of inversion,^[137–139] or with the structurally restrained $[Mn_4(ThiaSO_2)_2F]^+$ (ThiaSO₂ = *p*-*tert*-butylsulphonylcalix[4]arene) (**21⁻**, scheme 1.6) ($\lambda_{em} = 666$ nm, $\tau = 1.08$ ms and $\Phi = 15$ % in deoxygenated DMF at RT under inert conditions).^[140] Another method involves introducing heavy halides to increase ISC rates via the heavy atom effect as with $[Ph_4P]_2[MnBr_4]$ (Ph_4P = tetraphenylphosphonium cation) (**22**, scheme 1.6) ($\lambda_{em} = 516$ nm, $\tau = 355$ μ s and $\Phi = 0.98$ % in solid state at RT).^[141,142] Most strategies typically combine the aforementioned approaches.^[139,143] Luminescence from these complexes is MC based and the strictly spin-forbidden nature of the relaxation leads to relatively long lifetimes (μ s–ms). HS Mn^{II} complexes present an interesting prospect for OLEDs^[141] and also as triboluminescent sensors that respond to mechanical stress.^[129,139,144]

In strong LFs, Mn^{II} is LS and has an electron hole in the t_{2g} orbitals analogous to Fe(III) complexes, which promotes a parity-allowed strongly colored LMCT transition. It is

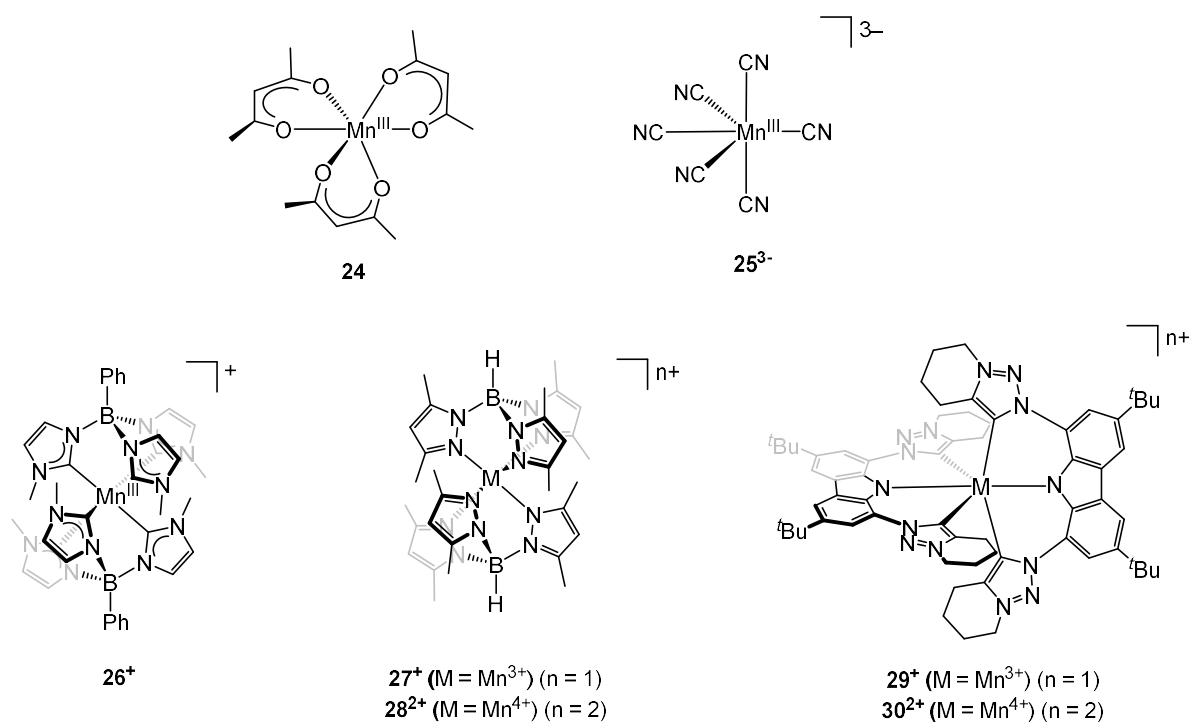
conceivable to achieve emission from LS d^5 compounds if the LF splitting is strong enough and low energy MC states are destabilized enough. Such $^2\text{LMCT}$ emission has been seen in very few Fe(III) complexes such as $\mathbf{3}^{3+}$, $\mathbf{10}^+$ (schemes 1.1 and 1.4) and $[\text{Fe}(\text{ImP})_2]^+$ (ImP = 1,1'-(1,3-phenylene)bis(3-methyl-1-imidazol-2-ylidene)) ($\mathbf{23}^+$) ($\lambda_{\text{em}} = 736 \text{ nm}$, $\tau = 0.2 \text{ ns}$, $\Phi = < 1 \%$ in CH_3CN at RT).^[103,145] There are no known emissive LS Mn^{II} complexes. Mn^{II} may require stronger field ligands to achieve $^2\text{LMCT}$ emission, originating from the lower intrinsic LF of the doubly-charged Mn ion vs. the triply-charged Fe ion.^[103]

To increase the oxidation state of Mn^{II} compounds a suitable chemical (or electrochemical) oxidant must be selected.^[72,122] The oxidation of Mn^{II} TMCs to Mn^{IV} is dependent on the II/III and III/IV redox couples;^[128,146] complexes with weakly donating ligands will have the intrinsic problem of having the III/IV oxidation couple being too high in potential to achieve and, if achieved, being too unstable and decomposing. This is seen with $[\text{Mn}(\text{terpy})_2]^{2+}$ (terpy = 2,2';6',2''-terpyridine) ($\mathbf{32}^{2+}$) that has a very high III/IV oxidation couple of 1.39 V (vs ferrocene/ferrocenium).^[32] Introduction of more strongly-donating ligands such as phtmeimb makes the oxidation couples more negative (II/IV = -2.09 V and III/IV = -0.77 V vs ferrocene/ferrocenium)^[30] and higher oxidation states more stable. Thus, higher oxidation states can be reached with various strong one electron chemical oxidations such as thianthrene radical cation $[\text{C}_{12}\text{H}_8\text{S}_2]^+$ (0.87 V vs ferrocene/ferrocenium in CH_3CN), nitrosonium salts $[\text{NO}]^+$ (0.87 V vs ferrocene/ferrocenium in CH_3CN), or silver salts (Ag^+) (0.65 V vs ferrocene/ferrocenium in DCM).^[32]

1.3.2 Manganese(III)

Octahedral Mn^{III} d^4 TMCs can exist in both HS ($S = 2$) or LS ($S = 1$) configurations. HS Mn^{III} TMCs are more common than LS^[127,147] but can have a tendency to disproportionate with weak field ligands to Mn^{II} and Mn^{IV} products,^[148] driven largely by the high stability and insolubility of MnO_2 .^[123] Another factor that can increase the instability of Mn^{III} is the Jahn-Teller distortion present in HS Mn^{III} TMCs.^[127,149,150] HS Mn^{III} TMCs have unsymmetrically filled e_g^* orbitals ($t_{2g}^3 e_g^1$) which leads to geometric distortion and tetragonal elongation along the z-axis as seen with the $[\text{Mn}(\text{acac})_3]$ (acac = acetylacetonate) ($\mathbf{24}$) complex.^[151,152] This Jahn-Teller axial distortion increases zero-field splitting (ZFS) of $^5\text{E}_g$ GS and, coupled with SOC mixing of states, leads to axial magnetic anisotropy (D). A larger D means the barrier for magnetization can be large; and magnetization can be retained by the TMC following removal of a magnetic field. This ability can enable use of a TMC as a single-molecule magnet (SMM), and has potential in various applications such as information storage.^[153] Relaxation to the magnetic GS is slow with large barriers, but there is always a possibility for fast decay via a different mechanism (e.g. quantum tunneling).^[154] There are a number of Mn^{III} TMCs that are used as SMMs as a result of Jahn-Teller induced axial anisotropy.^[153,155] LS Mn^{III} TMCs are more scarce, the LF strength required for Mn^{III} spin-crossover (SCO) is smaller than LF strength for Mn^{II} SCO due to its larger charge, thus (in the right ligand environment) the possibility for switchable SCO

i.e. using temperature or pressure.^[156,157] There are few reports of LS Mn^{III} TMCs with stronger field ligands including [Mn(CN)₆]³⁻ (**25³⁻**, scheme 1.7),^[131] [Mn(phtmeimb)₂]⁺ (**26⁺**, scheme 1.7),^[158] [Mn(HB(3, 5-Mepz)₃)₂]⁺ (HB(3, 5-Mepz) = 3, 5-dimethyl pyrazolyl borate) (**27⁺**, scheme 1.7)^[159] and [Mn(L^{CNC})₂]⁺ (L^{CNC} = *tert*-butyl-carbazole dicyclohexylmesoionic carbene) (**29⁺**, scheme 1.7).^[29]



Scheme 1.7: Molecular structures of HS d⁴- Mn^{III} complex **24** and LS d⁴- Mn^{III} complexes **25³⁻**–**27⁺** and **29⁺**.

Mn d⁴ compounds are more strongly colored than their d⁵ counterparts, as d-d transitions are no longer spin-forbidden, although still Laporte-forbidden. Photophysically the Tanabe-Sugano diagram shows that MC SF emission from Mn^{III} is conceivable in very strong LFs, where the ⁵E state is sufficiently destabilised and the SF states (¹E₂ and ¹T₂) become the lowest energy ESs (black circle, figure 1.12).^[21]

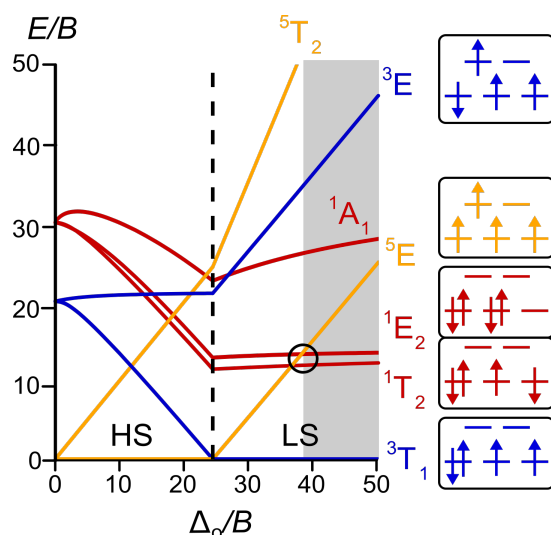


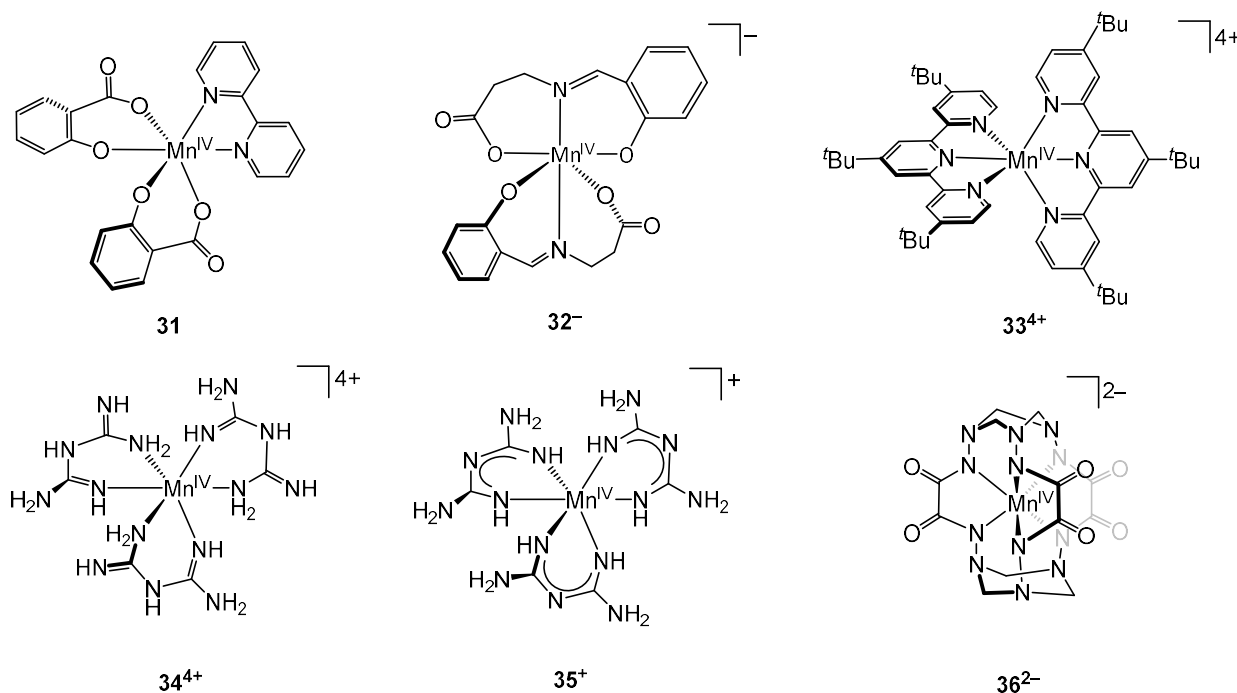
Figure 1.12: Simplified Tanabe-Sugano diagram for d^4 electronic configuration in octahedral symmetry ($C/B = 4$, scaled by Racah B parameter) with microstates of the pentet (orange), triplet (blue) and singlet SF states (red).^[80]

However SF MC luminescence from molecular Mn^{d4} TMCs, has yet to be reported for HS or LS, with only few reports of emission e.g. Mn^{III} clusters^[160] or LC emission.^[161]

1.3.3 Manganese(IV)

When oxidized mononuclear Mn^{III} and Mn^{II} TMCs can yield Mn^{IV} TMCs. These compounds are particularly uncommon with only a few octahedral complexes reported.^[127] Mn^{IV} is highly charged and has a small ionic radius, and so exists largely as its stable oxide (MnO_2) or with other strongly donating or anionic ligands capable of stabilizing the Mn^{IV} cation. Most reports of octahedral Mn^{IV} TMCs contain both nitrogen and oxygen donor ligands, e.g. $[Mn(sal)_2(bipy)]$ (sal = salicylic acid) (**31**, scheme 1.8)^[162,163] or $[Mn(als)_2]^-$ (als = 3-((2-hydroxybenzylidene)amino)propanoic acid)) (**32**⁻, scheme 1.8)^[164] with a Schiff base N, O type ligand.^[165,166] There are even fewer Mn^{IV} TMCs complexed solely with nitrogen donors due to the fact they are not as strongly donating and don't stabilise the higher Mn oxidation states as well. However, there are examples where ligands have been designed in such a way to increase stabilization e.g. $[Mn(tBu-terpy)_2]^{4+}$ (*t*Bu-terpy = *tert*-butyl 2,2';6',2''-terpyridine) (**33**⁴⁺, scheme 1.8)^[32] and $[Mn(bigH)_2]^{4+}$ (bigH = H-biguanide) (**34**⁴⁺, scheme 1.8)^[31] where stabilization is enhanced by the donating capability of the ligands. Other examples are seen with $[Mn(HB(3,5-Mepz)_3)_2]^{2+}$ (**28**²⁺, scheme 1.7),^[167] $[Mn(big)_3]^+$ (big = biguanide) (**35**⁺, scheme 1.8)^[27] and $[Mn(L-6H)]^{2-}$ (L-6H = hydrazine clathrochelate) (**36**²⁻, scheme 1.8)^[34,168] where stability is enhanced by using anionic ligands and/or steric bulk. As interest in synthesizing and isolating Mn^{IV} TMCs has increased to harness their unique properties and photophysics, more emphasis has been placed on ligand modification with strongly donating and/anionic ligands. This is apparent with recent examples using carbene-based anionic ligands e.g. $[Mn(L^{CNC})_2]^+$

($L^{\text{CNC}} = \textit{tert}$ -butylcarbazole dicyclohexylmesoionic carbene) ($\mathbf{30}^{2+}$, scheme 1.7)^[29] that stabilise the Mn^{IV} centre.^[123,127]



Scheme 1.8: Molecular structures of d^3 - Mn^{IV} complexes $\mathbf{31}$ – $\mathbf{36}^{2-}$.

As an analogue to Cr^{III} d^3 configuration, simplified octahedral Mn^{IV} photophysics (without ES distortion or CT state considerations) can be better understood with the Tanabe-Sugano diagram (figure 1.13).

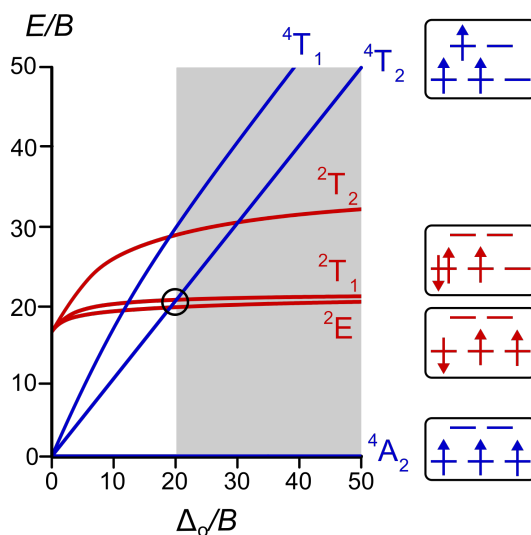
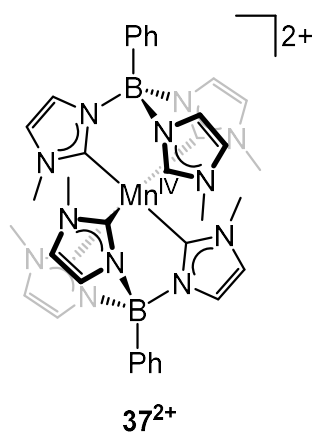


Figure 1.13: Simplified Tanabe-Sugano diagram for d^3 electronic configuration in octahedral symmetry ($C/B = 4$, scaled by Racah B parameter) with microstates of the quartet (blue) and doublet SF states (red).^[80]

Population of the lowest energy doublet states (${}^2\text{T}_1$ and ${}^2\text{E}$) requires a LF strength beyond the crossing point (black circle, figure 1.13). Back-intersystem crossing (i.e. ${}^2\text{T}_1/{}^2\text{E}$ to ${}^4\text{T}_2$) is still feasible when close to the crossing point. To avoid this, stronger LFs are used to increase the

energy separation between the quartet and doublets states. Such emission has been reported with Mn^{IV} in doped solid state materials, reporting red emission,^[119,169–172] whereas Cr^{III} SF emitters have been primarily reported as NIR emitters. Such a blue shift in emission is thought to be a result of the increased metal ion charge. The smaller Mn^{IV} cation ($\text{Mn}^{\text{IV}} = 0.53 \text{ \AA}$ vs $\text{Cr}^{\text{III}} = 0.62 \text{ \AA}$)^[81] leads to increased interelectronic repulsion, seen by the comparative Racah B and C parameters ($\text{Cr}^{\text{III}} B \approx 918 \text{ cm}^{-1}$ and $C \approx 3850 \text{ cm}^{-1}$ vs $\text{Mn}^{\text{IV}} B \approx 1160 \text{ cm}^{-1}$ and $C \approx 4303 \text{ cm}^{-1}$) for free ions.^[85] This leads to the increased energy of the ${}^2\text{T}_1$ and ${}^2\text{E}$ states (relative to $\text{Cr}(\text{III})$) and a blue shift in emission to the visible region).^[85,173] While important, the reason for emission blue shift is more multifaceted. For example in Mn^{IV} doped fluorides and oxides the effect of Mn-L bond length can be seen. In doped fluorides with shorter fixed bond lengths they have generally higher Racah B parameters and higher energy emission, compared with doped oxides.^[169] This larger degree of bond covalency within the doped oxides leads to an increased nephelauxetic effect (leading to lower interelectronic repulsion and lower emission energies). This effect translates to the only emissive molecular Mn^{IV} compound $[\text{Mn}(\text{phtmeimb})_2]^{2+}$ (**37**²⁺, scheme 1.9), which is subject to increased M-L covalency, with significantly red shifted emission to NIR region ($\lambda_{\text{em}} = 828 \text{ nm}$, $\tau = 1.5 \text{ }\mu\text{s}$ in solid state at 85 K).^[174]



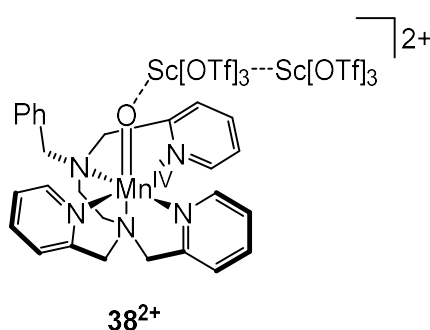
Scheme 1.9: Molecular structure of emissive $[\text{Mn}(\text{phtmeimb})_2]^{2+}$ **37**²⁺.

While weakly emissive, the red shift in emission is interesting considering the increase in charge compared with $\text{Cr}(\text{III})$. However, with only one molecular emissive octahedral Mn^{IV} complex reported, the photophysics and the nephelauxetic effect for these types of TMCs are not well understood.^[82] Nevertheless, it is clear from **37**²⁺ that ligand design is critical. Strongly donating ligands such as carbenes or even anionic ligands are required to ensure SF states are lowest in energy and to stabilise the high oxidation state. An additional challenge that is coupled with the +IV oxidation state is the presence of low energy CT (${}^4\text{LMCT}$ and ${}^2\text{LMCT}$) states, which can deactivate emission from SF states.^[174]

The ${}^4\text{LMCT}$ absorption band for **37**²⁺ peaks at 500 nm, with a tail up to 625 nm, and emission is reported at 828 nm. In this case, the ${}^4\text{LMCT}$ and associated ${}^2\text{LMCT}$ states are not causing deactivation of the SF state. However, with complex **30**²⁺ (scheme 1.7) the ${}^4\text{LMCT}$ band is

reported as panchromatic with the peak at 730 nm and tail up to 930 nm. Although no emission has been reported, SF emission within that range will probably be deactivated.^[29] If SF emission were to occur from complexes with such panchromatic LMCT absorption it would have to be significantly red shifted to avoid deactivation.

It is possible for Mn^{IV} complexes to be photoactive without being emissive. This is seen with the [(Bn-TPEN)Mn(O)]²⁺-[Sc(OTf)₃]₂ (Bn-TPEN = *N*-benzyl-*N,N',N'*-tris(2-pyridylmethyl)-1,2-diamino-ethane) (**38**²⁺, scheme 1.10); although not emissive, it is still able to photooxidize and hydroxylate challenging compounds including benzene with irreversible decomposition of the complex.

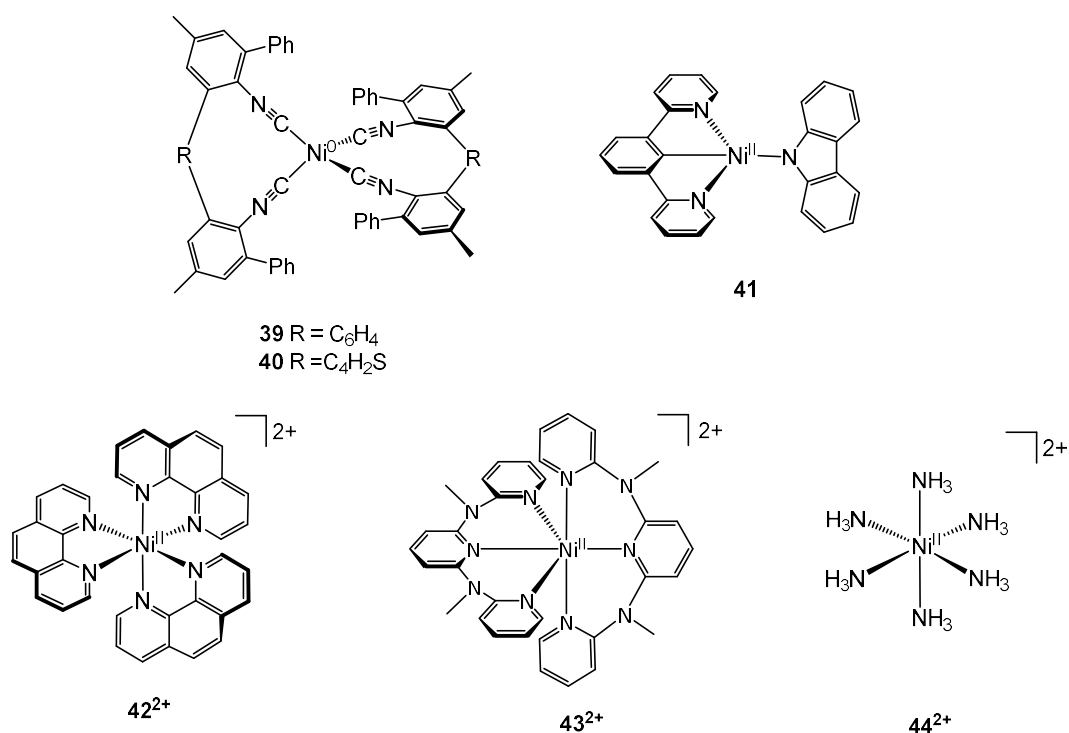


Scheme 1.10: Molecular structure of non-emissive strong photooxidant, together with Lewis acid activation from 2 eq of Sc[OTf]₃ **38**²⁺.^[61]

This bimolecular reactivity is attributed to a non-emissive long lived mixed ²MC/²LMCT state ($\tau = 6.4 \mu\text{s}$ in CH₃CN/TFE mixture) that, following irradiation at 440 nm, oxidises benzene and transfers an oxygen atom to the benzene radical cation forming phenol.^[33,61,175] Such reactivity is enabled by the second coordination sphere, i.e. the coordination of 2 eq of Sc[OTf]₃. This coordination significantly enhances the GS oxidation potentials of the [(Bn-TPEN)Mn(O)]²⁺ complex (0.38 V with no Sc[OTf]₃ to 0.96 V (vs ferrocene/ferrocenium) with 2 eq). As a result, the ES potential reaches 1.7 V (vs ferrocene/ferrocenium). Similar shifts also occurred with coordination of 2 eq of Sc(NO₃)₃ (ES_{ox} = 1.72 V, $\tau = 7.1 \mu\text{s}$ in CH₃CN/TFE mixture).^[176] This difference enables the oxidation of aryl substrates and significantly increases the ET transfer rates due to a large increase in driving force and a decrease in reorganizational energy, i.e. the Mn=O bond length change following ET is much smaller due to prior elongation at Sc[OTf]₃ coordination.^[177,178] This complex represents one of the very few examples of the unique photoredox capabilities of Mn^{IV} TMCs, particularly with challenging substrates.^[62,175,178–182]

1.4 Nickel(II)

The area of emissive molecular nickel TMCs is relatively underdeveloped, and there are only very few reports of emission. For example a $^3\text{MLCT}$ emission with Ni^0 d^{10} tetrahedral isocyanide complexes $[\text{Ni}(\text{CNAr}_5\text{NC})_2]$ ($\text{CNAr}_5\text{NC} = 1,3\text{-bis}(\text{N-formyl-4-methyl-6-phenylanilin-2-yl})\text{benzene}$) (**39**) ($\lambda_{\text{em}} = 510 \text{ nm}$, $\tau = 1.1 \mu\text{s}$ at 77 K in toluene) and $[\text{Ni}(\text{CNAr}_5^{(\text{th})}\text{NC})_2]$ ($\text{CNAr}_5^{(\text{th})}\text{NC} = 1,3\text{-bis}(\text{N-formyl-4-methyl-6-phenylanilin-2-yl})\text{thiophene}$) (**40**, scheme 1.11) ($\lambda_{\text{em}} = 560 \text{ nm}$, $\tau = 1.2 \mu\text{s}$ at 77 K in toluene).^[183,184] Emission from Ni^{II} has also been reported in the solid state^[35] and one recent report of an emissive square planar Ni^{II} d^8 complex, $[\text{Ni}(\text{dpb})(\text{Cbz})]$ ($\text{dpb} = 1,3\text{-bis}(\text{N-alkylbenzimidazol-2'-yl})\text{benzene}$) and $\text{Cbz} = \text{carbazole}$) (**41**, scheme 1.11) which shows metal perturbed $^3\text{ILCT}$ emission ($\lambda_{\text{em}} = 468 \text{ nm}$, $\tau = 0.11 \mu\text{s}$ at 77 K in solid state).^[9,16,185,186]



Scheme 1.11: Molecular structures of emissive Ni^0 TMCs **39** and **40**, emissive Ni^{II} complex **41** and non-emissive $[\text{Ni}(\text{ddpd})_2]^{2+}$ **42**²⁺, $[\text{Ni}(\text{phen})_3]^{2+}$ **43**²⁺ and hexammine Ni^{II} complexes **44**²⁺.

Based on the Tanabe-Sugano diagram it is theoretically possible to achieve MC SF emission from molecular Ni^{II} in an octahedral environment, but this has yet to be achieved. The Tanabe-Sugano diagram for d^8 configurations demonstrates like for d^2 , d^3 and d^4 configurations – that as LF strength increases, the intraconfigurational SF states become the lowest ES (black circle, figure 1.14), while the interconfigurational ES are linearly destabilized. The main difference here is that the SF transition involved the e_g^* orbitals, not the t_{2g} orbitals as with the other configurations.^[21] The impact of this difference on state splitting is not well understood due to the lack of emissive molecular Ni^{II} octahedral complexes.^[187]

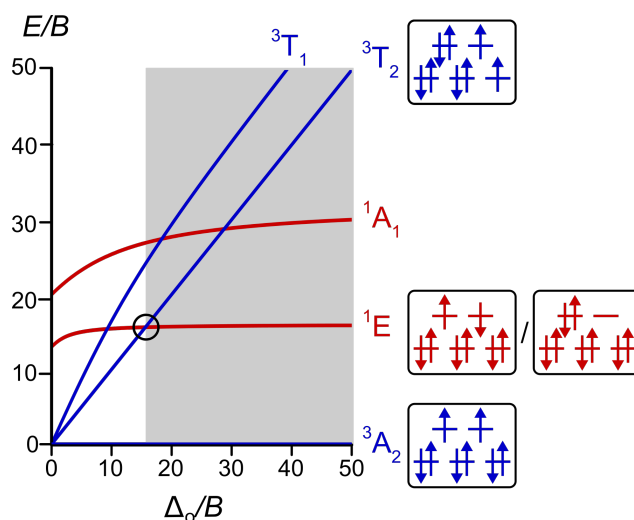


Figure 1.14: Simplified Tanabe-Sugano diagram for d^8 electronic configuration ($C/B = 4$, scaled by Racah B parameter) with microstates of the triplet (blue) and singlet SF states (red).^[80]

There are many octahedral Ni^{II} complexes known, with their synthesis being relatively uncomplicated from readily available precursors (e.g. $Ni[BF_4]_2 \cdot 6H_2O$), yet none show SF luminescence. This phenomenon has been explained by detrimental singlet/triplet state mixing and this effect is visible in the absorbance spectra due to intensity borrowing, i.e. when close to the crossing point of the 3T_2 and 1E states (black circle) the proximity of the states leads to mixing and singlet intensity borrowing from the spin allowed transition via SOC.^[187–189] With stronger LFs $[Ni(ddpd)_2]^{2+}$ and $[Ni(phen)_3]^{2+}$ (phen = 1,10-phenanthroline) (**42**²⁺ and **43**²⁺, scheme 1.11), the 1E state can be detected as a low energy shoulder on the 3T_2 band, weaker field ligands such as NH_3 in the complex $[Ni(NH_3)_6]^{2+}$ (**44**²⁺, scheme 1.11) have a spectrum where the 1E state manifests as a high energy shoulder or band.^[187,190,191]

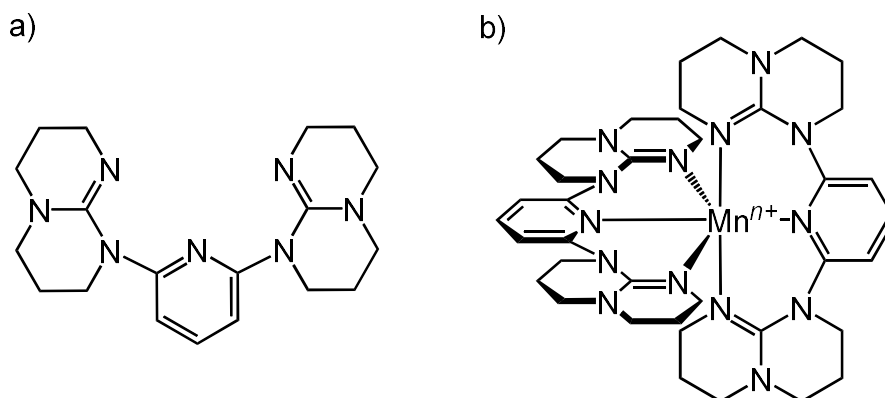
As states mix, the SF nested transition 1E gains more 3T_2 character and becomes more structurally distorted, leading to efficient non-radiative decay.^[192] It is possible to increase the energy separation between these states by hydrostatically increasing pressure (**5**³⁺, section 1.1), leading to less mixing and a more ‘pure’ SF state.^[193–195] However, it is clear that stronger LFs are required to split the triplet and singlet states and avoid state mixing/bISC. This is a challenge with d^8 configurations, as LF strength increases a square planar configuration is preferred over octahedral coordination.^[196] This can be seen with the heavier Ni^{II} analogues Pd^{II} and Pt^{II} that almost exclusively prefer square planar configurations.

Thus, a balance is required with the strength of LF imposed on Ni^{II} , enough to separate states but not too much as to promote square planar geometry. Another method could be to impose an octahedral geometry with a rigid strong field (σ -donation, π -accepting or a combination of both) or a cage ligand, thus ensuring octahedral geometry is maintained along with a strong LF.^[197–201]

2. Aims of Work

There are very few Mn^{IV} transition metal complexes and only one emissive complex,^[174] and so the photophysical properties of such complexes are poorly understood. Thus, the primary objective of this work is to design and synthesize photoactive octahedral Mn^{IV} complexes as analogues to MC emissive Cr^{III} complexes, and to further investigate their photophysical properties and applications.

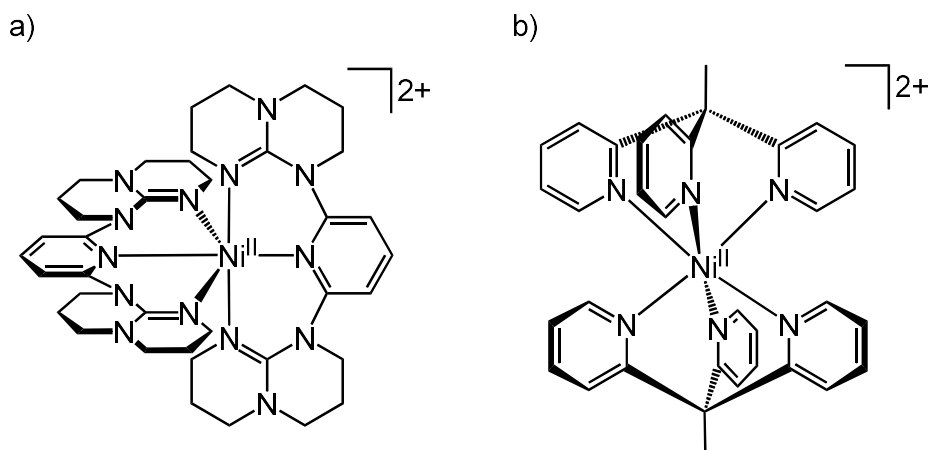
This work initially centers on the idea of using strongly donating tridentate ligands capable of 6-membered coordination, to stabilise the highly charged Mn^{IV} ion and ensure that the intraconfigurational states (${}^2\text{E}/{}^2\text{T}_1$) are lowest in energy. The literature known ligand 2,6-diguandylpyridine (dgpy) (scheme 1.12a) offers such characteristics, having already yielded ${}^3\text{LMCT}$ luminescence with cobalt(III).^[202] Synthesis will begin with a readily available Mn^{II} precursor ($\text{Mn}[\text{OTf}]_2$), following isolation and characterization of $[\text{Mn}(\text{dgpy})_2]^{2+}$ the primary aim is to find a viable synthetic route to $[\text{Mn}(\text{dgpy})_2]^{4+}$ (e.g. chemical oxidation via $[\text{Mn}(\text{dgpy})_2]^{3+}$) (scheme 1.12b). Full characterization (structurally, electronically, theoretically and magnetically) will follow isolation of $[\text{Mn}(\text{dgpy})_2]^{4+}$. Photophysical investigation will then be a significant focus; absorption, variable temperature emission and time resolved spectroscopy, along with detailed theoretical studies (DFT) will be utilized to better understand the ES dynamics. Application work will follow photophysical characterization, pending the discovery of advantageous ES ordering and lifetimes.



Scheme 1.12: Structures of a) 2,6-diguandylpyridine (dgpy) ligand and b) $[\text{Mn}(\text{dgpy})_2]^{n+}$ ($n = 2-4$) complex.

The other objective of this work is to more fully understand and investigate the nature of MC SF transitions in octahedral Ni^{II} complexes, and how they can be influenced to ultimately yield SF emission from molecular octahedral Ni^{II} complexes.

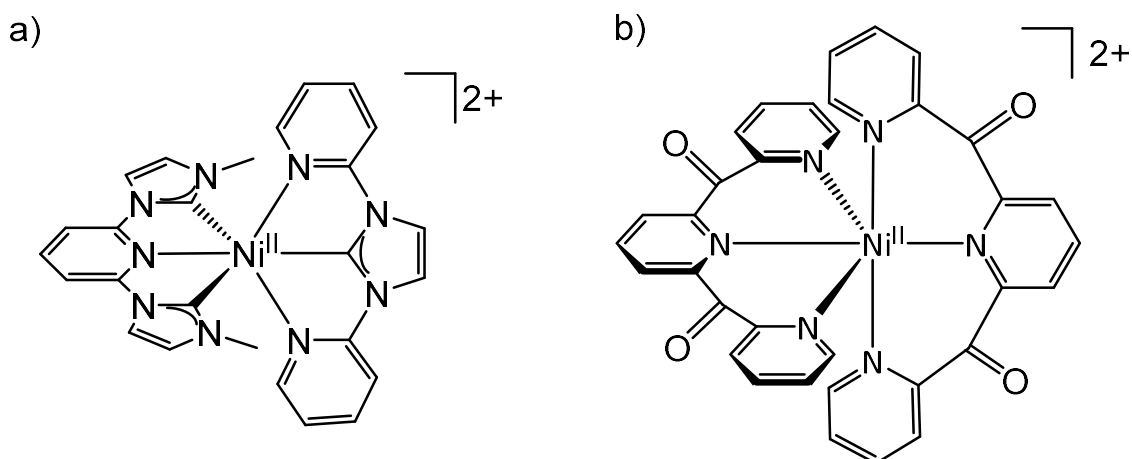
To achieve this, a series of three literature known complexes $[\text{Ni}(\text{terpy})_2]^{2+}$, **42**²⁺, **43**²⁺ and two novel octahedral homoleptic nickel(II) complexes (scheme 1.13) will be synthesised and fully characterized.



Scheme 1.13: Structures of a) $[\text{Ni}(\text{dgpy})_2]^{2+}$ and b) $[\text{Ni}(\text{tpe})_2]^{2+}$ complexes.

The photophysical properties will be described using absorption and emission spectroscopies, and theoretically using detailed LF theory analysis along with DFT, CASSCF and coupled potential energy surface analysis. These compounds will also be tested to see if increased hydrostatic pressure can separate the intra- and interconfigurational LF states.^[87]

To further this study the influence of increased σ -donating and π -accepting ligands will be looked at. The synthesis of $[\text{Ni}(\text{CNC})(\text{NCN})]^{2+}$ (CNC = 1,1'-(pyridin-2,6-diyl)bis(3-methyl-1H-imidazol-3-ylidene) and NCN = 1,3-bis(2-pyridyl)imidazolylidene) will explore the influence of increased σ -donation, and synthesis of $[\text{Ni}(\text{dcp})_2]^{2+}$ (dcp = 2,6-bis(2-carboxypyridyl)pyridine) will look at increased ligand π -acceptance (scheme 1.14).



Scheme 1.14: Structures of a) $[\text{Ni}(\text{CNC})(\text{NCN})]^{2+}$ and b) $[\text{Ni}(\text{dcp})_2]^{2+}$ complexes.

As mentioned in a strong enough ligand field it is possible for Ni^{II} to adopt square planar coordination. These complexes will first be characterized structurally to confirm an octahedral environment and then characterized optically to investigate the position of ligand field states and determine if SF emission is possible.

3. Results and Discussion

Most of the results and findings detailed and documented in this thesis have been submitted to and/or published as scientific articles in peer-reviewed chemistry journals. Each article discussed is reprinted with permission from respective publishers.

Synthesis, characterization and quantum chemical calculations of the novel $[\text{Mn}(\text{dgpy})_2]^{n+}$ complex in three different oxidation states (II, III, IV) is presented in section 3.1 “*The Full d^3-d^5 Redox Series of Mononuclear Manganese Complexes: Geometries and Electronic Structures of $[\text{Mn}(\text{dgpy})_2]^{n+}$* ”. The investigation and study of $[\text{Mn}(\text{dgpy})_2]^{n+}$ in three different oxidation states represents the first of its type for Mn, showing the direct geometric and electronic effects related to the challenging sequential removal of two electrons from e_g^* orbitals on the way to the Mn^{IV} complex. Synthesis of this series begins with $[\text{Mn}(\text{dgpy})_2][\text{OTf}]_2$ from $\text{Mn}[\text{OTf}]_2$ and dgpy ligand, the complex precipitated from dry THF. Both almost colorless *cis-fac* and *mer* isomers were isolated due to a result of the lack of ligand field stabilization and the inherent substitution lability of HS Mn^{II} complexes. Following isolation of $[\text{Mn}(\text{dgpy})_2][\text{OTf}]_2$, electrochemical characterization was carried out to reveal the oxidative potentials required to achieve +IV oxidation state from +II. Cyclic voltammograms revealed the +II/+III couple at -0.26 V (vs ferrocene/ferrocenium) and the +III/+IV couple at $+0.58$ V (vs ferrocene/ferrocenium). Thus, 1 eq of a suitable oxidant (AgPF_6 , $E_{1/2}(\text{Ag}^{+/0}) = +0.04$ V in CH_3CN) was selected and used to make orange $[\text{Mn}(\text{dgpy})_2]^{3+}$, which following removal of solid Ag was isolated as mainly the *mer* isomer, $[\text{Mn}(\text{dgpy})_2][\text{PF}_6]_3$. $[\text{Mn}(\text{dgpy})_2]^{4+}$ was synthesised in a similar fashion, but with 2 eq of a stronger chemical oxidant ($\text{C}_{12}\text{H}_8\text{S}_2^{+}$, $E_{1/2}([\text{C}_{12}\text{H}_8\text{S}_2]^{+/0}) = +0.86$ V in CH_3CN), yielding *mer*- $[\text{Mn}(\text{dgpy})_2][\text{PF}_6]_4$ as deep purple crystals. The geometric studies and analysis using computational methods (DFT) and X-ray diffraction (XRD) showed a clear relationship of decreased bond length with decreased antibonding orbital population. Superconducting quantum interference magnetic measurements (SQUID) confirmed the spin-only magnetic moments and thus the spin state of the complexes. Furthermore, the axial magnetic anisotropy (D) of $[\text{Mn}(\text{dgpy})_2]^{3+}$ was confirmed to be -3.84 cm^{-1} which agrees well with the CASSCF/NEVPT2 calculated axial anisotropy value of -4.54 cm^{-1} . Most importantly, absorbance spectroscopy of $[\text{Mn}(\text{dgpy})_2]^{4+}$ revealed an intense ($\epsilon > 2700$ $\text{M}^{-1} \text{cm}^{-1}$) panchromatic LMCT band up to 950 nm, which masks any (calculated with CASSCF/NEVPT2) d-d transitions. The $[\text{Mn}(\text{dgpy})_2]^{3+}$ and $[\text{Mn}(\text{dgpy})_2]^{4+}$ complexes represent rare examples of Mn^{III} and Mn^{IV} supported solely by nitrogen donors.

In Section 3.2, “Oxidative Two-State Photoreactivity of a Manganese(IV) Complex using NIR Light”, the photophysics and resulting applications of the $[\text{Mn}(\text{dgp})_2]^{4+}$ complex are detailed and listed.

$[\text{Mn}(\text{dgp})_2]^{4+}$ displays weak NIR-II phosphorescence at 1435 nm in solid state at 77K following laser excitation at 730 nm. Using DFT it was found that the emission originates from a mixed $^2\text{MC}/^2\text{LMCT}$ state. Following transient absorption spectroscopy this state was found to be long lived enough (1.6 ns) to participate in dynamic bimolecular chemistry. Using steady state absorption spectroscopy $[\text{Mn}(\text{dgp})_2]^{4+}$ was found to be strongly photooxidative following NIR irradiation (850 nm). The complex is able to participate in dynamic quenching via the lower energy $^2\text{MC}/^2\text{LMCT}$ state and oxidise naphthalene ($E_{\text{ox}} \approx 0.93 - 1.16$ V vs ferrocene/ferrocenium) forming a naphthalene radical cation and $[\text{Mn}(\text{dgp})_2]^{3+}$. The naphthalene radical cation was trapped using an electron-poor pyrazole (ethyl 1-phenyl-1H-pyrazole-4-carboxylate) in a Nicewicz-type oxidative coupling and characterized with ESI mass spectroscopy ($\text{C}_{16}\text{H}_{15}\text{N}_2\text{O}_2$ $m/z = 267$). Mechanistic aspects were examined using DFT and confirmed with time resolved spectroscopy. They showed following low energy excitation a $^4\text{LMCT}$ state forms and ISC occurs in 780 fs to a lower energy mixed $^2\text{LMCT}/^2\text{MC}$, this state then oxidises naphthalene forming a radical cation and LS $[\text{Mn}(\text{dgp})_2]^{3+}$. LS $[\text{Mn}(\text{dgp})_2]^{3+}$, then undergoes SCO to form HS $[\text{Mn}(\text{dgp})_2]^{3+}$.

$[\text{Mn}(\text{dgp})_2]^{4+}$ also displays surprising reactivity and is able to oxidise substrates with significantly higher potentials up to benzene ($E_{\text{ox}} \approx 1.98$ V vs ferrocene/ferrocenium) and even solvents such as CH_3CN and CH_3NO_2 . This reactivity is attributed to the more reactive short lived $^4\text{LMCT}$ (1.46 eV) state and enabled by slow ISC. Photooxidation occurs more slowly and statically via a close pre-organized CH_3CN molecule, which was confirmed with molecular dynamics simulations and with ESI mass spectroscopy (H/D isotopic) showing a benzene nitrilium ion ($m/z = 118$ for $\text{C}_8\text{H}_8\text{N}$ and $m/z = 123$ for $\text{C}_8\text{H}_3\text{D}_5\text{N}$). Steady state absorption measurements were carried out with mesitylene, toluene and benzene all showing similar reactivity. The radical cations of mesitylene ($\text{C}_{15}\text{H}_{19}\text{N}_2\text{O}_2$ $m/z = 259$) and benzene ($\text{C}_{12}\text{H}_{13}\text{N}_2\text{O}_2$ $m/z = 217$ and $\text{C}_{12}\text{H}_8\text{D}_5\text{N}_2\text{O}_2$ $m/z = 222$) were also trapped in the same Nicewicz-type oxidative coupling as the naphthalene radical cation. The formation of the benzene cross-coupled product 1H-pyrazole-4-carboxylic acid ethyl ester was also confirmed with HPLC (comparing peak area to a known standard) and the reaction yield was found to be 11%. Molecular dynamics simulations also showed close interaction of PF_6 anions and complex in solution suggested ion pairing. To further investigate if ion pairing has an effect on reactivity steady state absorption measurements were carried out with increased ionic strength (0, 50, 100 and 200 mM $[\text{nBu}_4\text{N}][\text{PF}_6]$). Results showed a slowing of rate with increased ionic strength which suggests slower photooxidation or slower cage escape. This coupled with no changes observed in transient spectroscopy at high ionic strength (100 mM) indicates that ion pairing likely affects cage escape rather than the initial static quenching step.

In Section 3.3, “*Coupled Potential Energy Surfaces Strongly Impact the Lowest-Energy Spin-Flip Transition in Six-Coordinate Nickel(II) Complexes*”, describes the synthesis and characterization of a series of five Ni^{II} octahedral complexes. Three literature known complexes [Ni(terpy)₂]²⁺, [Ni(phen)₂]²⁺ and [Ni(ddd)₂]²⁺ and two novel complexes [Ni(dgpy)₂]²⁺ and [Ni(tpe)₂]²⁺ to help understand the specific dynamics governing SF states in octahedral Ni^{II} d⁸ complexes. Unlike d², d³ and d⁴, the SF transition occurs in the antibonding e_g^{*} orbitals and there are no emissive molecular octahedral complexes Ni^{II} that exist to date.^[187] Each of the five complexes show increasing LF strength beginning with [Ni(dgpy)₂]²⁺ which was synthesized from Ni[BF₄]₂·6H₂O and 2 eq of dgpy ligand. LF states can be seen with absorption spectroscopy as a result of ¹E state intensity borrowing, and this complex shows weakest LF strength of the five, with the ¹E state manifest as a high energy shoulder (12 600 cm⁻¹) on the ³T₂ state (11 990 cm⁻¹). [Ni(terpy)₂]²⁺ shows increased LF strength with ³T₂ state being higher in energy (12 420 cm⁻¹), however the ¹E state (12 630 cm⁻¹) remains as a higher energy shoulder. As ligand field strength increases with the [Ni(phen)₂]²⁺ and [Ni(ddd)₂]²⁺ complexes the ¹E state moves to lower energy (phen = 11 650 cm⁻¹, ddpd = 11 300 cm⁻¹), compared with the ³T₂ state (phen = 12 680 cm⁻¹, ddpd = 12 700 cm⁻¹). [Ni(tpe)₂]²⁺ was synthesised in a similar way to [Ni(dgpy)₂]²⁺, with 2 eq of tpe ligand stirred with Ni[BF₄]₂·6H₂O. Separation of LF states reaches its largest with this complex (³T₂ = 13 380 cm⁻¹, ¹E = 11 650 cm⁻¹). None of these complexes are luminescent, even at high hydrostatic pressure as seen with [Ni(ddd)₂]²⁺ at 62 kbar.

With detailed DFT, LF studies and coupled potential energy surface studies, it is shown that singlet/triplet state mixing is the primary reason for this occurrence. This mixing via SOC leads to the ¹E state taking on more anharmonic distorted character, which leads to increased non-radiative decay. Even though LF strength increases with this series (also seen with CASSCF/NEVPT2 calculations) the singlet/triplet state proximity remains an issue which inhibits the possibility of SF emission.

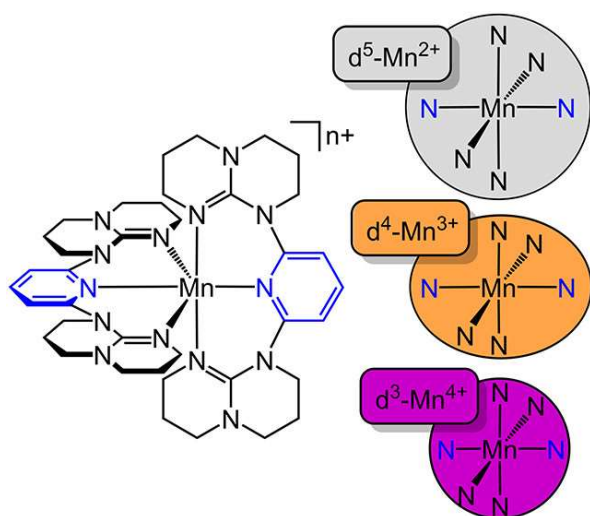
In Section 3.4, “*Influencing Ligand field states of Nickel(II) Complexes with Strongly σ -Donating and π -Accepting Ligands*”, further investigates increasing ligand field strength in Ni^{II} complexes by using strongly σ -donating and π -accepting ligands. This sheds further light on required ligand characteristics for SF emission from octahedral Ni^{II}. This chapter describes synthesis of a Ni^{II} carbene complex [Ni(CNC)(NCN)]²⁺, beginning with a [NiBr(CNC)]Br precursor the NCN ligand is deprotonated with a weak base (NaOAc) and heated for complexation to occur. Here the LF strength is higher resulting from the three strong σ -donor carbene ligands. Following XRD structural characterization it is seen that the LF is too strong and has lead Ni^{II} to adopt a square planar and 4+1 geometry, meaning an octahedral d⁸ photophysical description no longer applies.

The second complex [Ni(dcpp)₂]²⁺ synthesised looks at the effect of increasing LF strength with π -accepting ligands. This complex was synthesized by stirring Ni[BF₄]₂·6H₂O and 2 eq of dcpp ligand. Following isolation and XRD it can be seen that the complex exists in an octahedral geometry. Absorption spectroscopy reveals that even at this increased π -accepting LF the ³T₂ and ¹E LF states remain mixed and are not separate. The ¹E band is seen as a low energy should (11 480 cm⁻¹) on the ³T₂ band (12 750 cm⁻¹). Thus SF emission does not occur from this complex. Furthermore, the dcpp ligand contains two carbonyl groups, this provides the possibility to further increase the π -accepting ability of dcpp upon Lewis acid coordination. Sc[OTf]₃ (1–2 eq) were coordinated to [Ni(dcpp)₂]²⁺ as a second coordination sphere. Absorption spectroscopy showed unexpected results with the LF states ³T₂ and ³T₁ moving to lower energies with increased equivalence of Sc[OTf]₃ and movement of the ¹E state to higher energies. The movement of the ³T₂ and ³T₁ to lower energies could be a result of decreased the σ -donation of the dcpp ligand lowering Δ_o . Movement of the ¹E state to higher energies could be a result of changes in coordinated geometry upon addition of Sc[OTf]₃, which would change the nephelauxetic effect.

3.1 The Full d^3 – d^5 Redox Series of Mononuclear Manganese Complexes: Geometries and Electronic Structures of $[\text{Mn}(\text{dgpy})_2]^{n+}$

Nathan R. East, Christoph Förster, Luca M. Carrella, Eva Rentschler and Katja Heinze.

Inorg. Chem. **2022**, *61*, 37, 14616–14625



This article reports the novel $[\text{Mn}(\text{dgpy})_2]^{n+}$ complexes isolated in three oxidation states (II, III, IV). Aided by DFT and CASSCF studies, this complete series gives unique insight on how structural, electronic, optical and magnetic properties change with sequential removal of an electron from the e_g^* orbitals. In particular, $[\text{Mn}(\text{dgpy})_2]^{4+}$ is a rare example of an octahedral Mn^{IV} complex stabilized solely by nitrogen donor ligands, showing strong ($\epsilon > 2700 \text{ M}^{-1} \text{ cm}^{-1}$) panchromatic LMCT absorbance.

Author contributions

Synthesis and characterization of the title compounds, along with DFT studies, CASSCF calculations and optical studies were carried out by N. R. East. All crystal structures were solved and refined by Dr. C. Förster. SQUID magnetic measurements were performed by Dr. L. M. Carrella (group of Prof. Dr. E. Rentschler). The manuscript and supplementary information were written by Prof. Dr. Katja Heinze and N. R. East.

Supporting Information

Found on page 97

“N. R. East, C. Förster, L. M. Carrella, E. Rentschler, K. Heinze, *Inorg. Chem.* **2022**, *61*, 37, 14616–14625. Copyright 2022 American Chemical Society. Reproduced with permission”

The Full d^3 – d^5 Redox Series of Mononuclear Manganese Complexes: Geometries and Electronic Structures of $[\text{Mn}(\text{dgpy})_2]^{n+}$

Nathan R. East, Christoph Förster, Luca M. Carrella, Eva Rentschler, and Katja Heinze*

Cite This: *Inorg. Chem.* 2022, 61, 14616–14625

Read Online

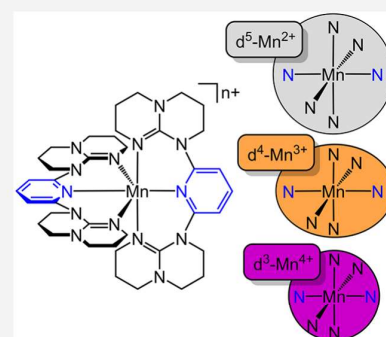
ACCESS |

Metrics & More

Article Recommendations

Supporting Information

ABSTRACT: Although manganese ions exhibit a rich redox chemistry, redox processes are often accompanied by structural reorganization and a high propensity for ligand substitution, so that no complete structurally characterized manganese(II,III,IV) complex series without significant ligand sphere reorganization akin to the manganese(II,III,IV) oxides exists. We present here the series of pseudo-octahedral homoleptic manganese complexes $[\text{Mn}(\text{dgpy})_2]^{n+}$ ($n = 2-4$) with the adaptable tridentate push–pull ligand 2,6-diguanidylpyridine (dgpy). Mn–N bond lengths and N–Mn–N bond angles change characteristically from $n = 2$ to $n = 4$, while the overall $[\text{MnN}_6]$ coordination sphere is preserved. The manganese(III) complex $[\text{Mn}(\text{dgpy})_2]^{3+}$ exhibits a Jahn–Teller elongated octahedron and a negative $D = -3.84 \text{ cm}^{-1}$. Concomitantly with the consecutive oxidation of $[\text{Mn}(\text{dgpy})_2]^{2+}$ to $[\text{Mn}(\text{dgpy})_2]^{4+}$, the optical properties evolve with increasing ligand-to-metal charge transfer character of the absorption bands culminating in the panchromatic absorption of the purple-black manganese(IV) complex $[\text{Mn}(\text{dgpy})_2]^{4+}$.



INTRODUCTION

Manganese possesses a very rich redox chemistry, which also defines its applications in batteries¹ and catalysis² as well as its important role in biology.^{3,4} Oxidation states of +II to +VII are prevalent in water, with oxido ligands stabilizing the higher oxidation states.⁵ Manganese(III) and manganese(IV) complexes lacking oxido ligands are comparably rare. Only six complex types are reported so far with a $[\text{MnN}_6]$ coordination sphere (Chart 1).^{6–14} While some of the manganese(II,III,IV) complexes have been structurally characterized, e.g., **A**^{3+/2+},⁷ **B**²⁺,⁸ or **D**¹¹ (Chart 1), no complete series of manganese(II,III,IV) complexes with a $[\text{MnN}_6]$ coordination is available so far.

Mn^{IV} complexes should be strong oxidants, but the oxidative power is often damped by strong σ/π donors with $E(\text{Mn}^{\text{IV/III}})$ potentials of $[\text{MnN}_6]$ complexes ranging from -1.48 to $+1.69$ V vs ferrocene (Chart 1).^{6–14} The highest potentials are achieved by pyridine and pyrazol donors,^{6–8} while strong donors such as guanidines or carbenes and anionic donors such as guanidates, hydrazides, amides, or azides lower the potential appreciably.^{9,14} (Chart 1). Six carbene donors or four carbene donors with two amides furnish $E(\text{Mn}^{\text{IV/III}})$ potentials as low as -0.71 and -0.55 V, respectively.^{15,16}

None of the reported manganese complexes with $[\text{MnN}_6]$ coordination were structurally characterized in both the +III and +IV oxidation states and certainly not in the three oxidation states +II, +III, and +IV. Consequently, only limited information is available on molecular $[\text{MnN}_6]$ complexes, while the full series of solid manganese oxides MnO (manganosite), Mn_2O_3 (bixbyite), and MnO_2 (pyrolusite)

represents standard textbook knowledge.⁵ MnO_2 is employed in batteries¹ and is utilized for the oxidation of organic substrates.^{2,17} Oxido manganese(IV/III) clusters Mn_4CaO_5 perform the oxidation of water to dioxygen in the oxygen-evolving complex (OEC) of photosystem II.^{18,19} Two different Jahn–Teller distortions (elongations) of the dangling six-coordinate manganese(III) site with high-spin d^4 electron configuration along two different axes explain two different EPR signatures of the OEC in its S_1 state of the Kok cycle (S_0-S_4).¹⁹ For the bis(terpyridine) manganese(III) complex $[\text{A}^{\text{H},4\text{-tolyl}}]^{3+}$ an unusual Jahn–Teller compression has been reported,⁷ which might be an effect of the rigid terpyridine.²⁰ Some mononuclear high-spin manganese(III) complexes display slow magnetic relaxation and thus single-ion magnetic behavior, e.g., in a $[\text{Mn}^{\text{III}}\text{N}_4\text{O}_2]$ coordination environment.²¹ In stronger octahedral ligand fields, the manganese(III) ion can undergo a spin-crossover transition to the low-spin state at low temperature, e.g., in a $[\text{Mn}^{\text{III}}\text{N}_6]$ coordination sphere.²² In the enantioselective Jacobsen–Katsuki epoxidation of alkenes, chiral salene manganese(III) complexes with a $[\text{MnN}_2\text{O}_2]$ coordination represent the resting state of the catalyst.^{23,24} Similarly, O_2 binding and activation requires a free

Received: May 16, 2022

Published: September 7, 2022

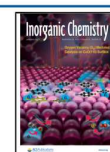
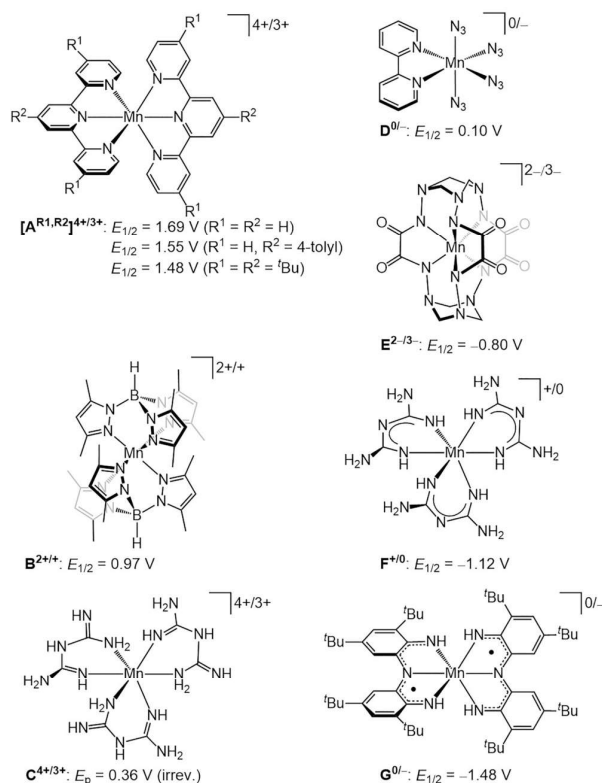


Chart 1. Manganese(IV/III) Complexes with a [MnN₆] Coordination^a

^aRedox potentials of the Mn^{IV/III} couple are given vs the ferrocene/ferrocenium couple.^{6–14}

coordination site at manganese(II,III,IV).²⁵ In manganese superoxide dismutases (SODs) the Mn^{II}/Mn^{III} redox shuttle, ligated by three histidines, an aspartate, and a water or hydroxide, serves to disproportionate superoxide into O₂ and H₂O₂.^{26,27} However, artificial manganese(II) complexes are among the most labile transition metal(II) complexes due to the comparably large ionic radius and importantly due to the lack of ligand field stabilization in the high-spin d⁵ electron configuration, as is well known from the Irving–Williams series.²⁸ To achieve less labile manganese(II) complexes, chelate or even macrocyclic ligands²⁹ are required.

Consequently, each oxidation state +IV, +III, and +II implies its own challenges, namely, the high oxophilicity of Mn^{IV} and Mn^{III}, the potentially high Mn^{IV/III} oxidation potential, the Jahn–Teller distortion of high-spin Mn^{III}, and the lability of high-spin Mn^{II}. This might explain why no complete series of molecular [Mn^{II,III,IV}N₆] complexes has been reported so far, although all these oxidation states are relevant in biological and artificial catalytic systems.

To tackle these challenges, we chose the tridentate chelate ligand 2,6-diguanyldipyridine (dgpy)^{30–33} with donors of different strength to allow for Jahn–Teller distortions along a single axis (Mn^{III}), with six-membered chelate rings to accommodate different bond lengths in the different oxidation states Mn^{II}–Mn^{IV} and with both electron-donating (guanidine) and -accepting (pyridine) properties (push–pull charge-balancing character) to stabilize both electron-poor Mn^{IV} and more electron-rich Mn^{II} central ions. This ligand has been

previously coordinated to iron(II/III), cobalt(III), and ruthenium(III) ions with d⁵–d⁶ electron configurations to form homoleptic complexes, namely, *cis-fac*-[Fe(dgpy)₂]²⁺, *mer*-[Fe(dgpy)₂]²⁺, *mer*-[Fe(dgpy)₂]³⁺, and *cis-fac*-[Ru(dgpy)₂]³⁺,^{30–32} and some heteroleptic complexes with M^{II} ions (M = Fe, Co, Ni, Cu, Zn),³³ while high-valent metal complexes with this ligand have not yet been reported. The observation of *mer* and *cis-fac* isomers in the reported [M(dgpy)₂]^{3+/2+} complexes supports the flexible coordination behavior of dgpy. With respect to this coordinative flexibility, dgpy resembles the all-pyridine ligand *N,N'*-dimethyl-*N,N'*-dipyridine-2-ylpyridine-2,6-diamine (ddpd).^{20,34,35}

The d⁵–d³ complexes [Mn(dgpy)₂]^{*n*+} (*n* = 2–4) discussed in this study represent the first complete series with fully reversible outer-sphere redox processes and detailed structural, magnetic, and spectroscopic characterization of all [MnN₆]^{*n*+} complexes, allowing a comparison with the manganese oxide series MnO, Mn₂O₃, and MnO₂.

EXPERIMENTAL SECTION

General Procedures. The ligand dgpy³⁰ and the thianthrene radical cation oxidant [C₁₂H₈S₂][PF₆]³⁶ were synthesized according to literature procedures. CH₃CN, Et₂O, and THF were distilled from calcium hydride, sodium, and potassium, respectively. Reagents were used as received from commercial suppliers (ABCR, Acros Organics, Alfa Aesar, Fisher Scientific, Fluka, and Sigma-Aldrich). Gloveboxes (UniLab/MBraun, Ar 4.8, O₂ < 1 ppm, H₂O < 0.1 ppm) were used to store and weigh sensitive compounds as well as to prepare samples that require the absence of oxygen and water. ESI mass spectra were recorded on an Agilent 6545 QTOF-MS spectrometer. ATR-IR spectra were recorded with a Bruker ALPHA II FT-IR spectrometer with a platinum Di-ATR module inside an argon-filled glovebox. Elemental analyses were performed by the microanalytical laboratory of the Department of Chemistry of the University of Mainz using an Elementar Vario EL Cube. Electrochemical experiments were carried out on a BioLogic SP-200 voltammeter using platinum wires as counter and working electrodes and a silver wire treated with hydrochloric acid as pseudo Ag/AgCl reference electrode. The measurements were carried out at a scan rate of 100 mV s⁻¹ for cyclic voltammetry experiments and at 50 mV s⁻¹ for square wave voltammetry experiments using 0.001 M of the sample in 0.1 M [^{*n*}Bu₄N][B(C₆F₅)₄] as the supporting electrolyte in CH₃CN. Potentials are referenced to the ferrocene/ferrocenium couple ($E_{1/2} = 235 \pm 5$ mV under the experimental conditions). UV/vis/NIR spectra were recorded on a Jasco V-770 spectrometer using 1.0 cm cells (Hellma, Suprasil) equipped with a Schott valve. Emission spectra were recorded with a FLS1000 spectrometer from Edinburgh Instruments equipped with the cooled red and NIR-sensitive photomultiplier detectors PMT-980 and N-G09 PMT-1700, together covering the spectral range between 200 and 1700 nm. A xenon arc lamp Xe2 (450 W) was used for excitation. Temperature-dependent optical spectra were recorded on a freshly prepared butyronitrile³⁷ solution using an Oxford cryostat (Oxford Instruments OptistatDN). DC magnetic studies for all compounds were performed with a Quantum Design MPMS-XL-7 SQUID magnetometer on powdered microcrystalline samples. Experimental susceptibility data were corrected for the underlying diamagnetism using Pascal's constants. The temperature-dependent magnetic contribution of the holder was determined experimentally and subtracted from the measured susceptibility data. Variable-temperature susceptibility data were collected in a temperature range of 2–300 K under an applied field of 0.1 T, while magnetization data were collected between 2 and 10 K and magnetic fields up to 7 T. The magnetic data were fitted with the program PHI.³⁸

Intensity data for crystal structure determinations were collected with a STOE IPDS-2T diffractometer from STOE & CIE GmbH with an Oxford cooling system using Mo K α radiation ($\lambda = 0.71073$ Å).

The diffraction frames were integrated using the STOE X-Area³⁹ software package and were corrected for absorption with MULABS⁴⁰ of the PLATON software package.⁴¹ The structures were solved with SHELXT⁴² and refined by the full-matrix method based on F^2 using SHELXL⁴³ of the SHELX⁴⁴ software package and the ShelXle⁴⁵ graphical interface. All non-hydrogen atoms were refined anisotropically, while the positions of all hydrogen atoms were generated with appropriate geometric constraints and allowed to ride on their respective parent atoms with fixed isotropic thermal parameters. Crystallographic data for the structures reported in this paper have been deposited with the Cambridge Crystallographic Data Centre as supplementary publication no. CCDC-2171814 for *cis-fac-1*-[PF₆]₂×0.5C₂H₅OC₂H₅×CH₃CN, no. CCDC-2171813 for *mer-1*[BF₄]₂, CCDC-2171815 for *mer-1*[PF₆]₃×1.5CH₃CN, and CCDC-2171816 for *mer-1*[PF₆]₄×3CH₃CN.

Density functional theory (DFT) calculations were carried out using the ORCA program package⁴⁶ (version 4.1.1). Tight convergence criteria were chosen for all calculations (keywords *tightscf* and *tightopt*). All calculations were performed using the B3LYP functional^{47–49} employing the RJCOSX approximation (keyword *RJCOSX*).^{50,51} Relativistic effects were calculated at the zeroth-order regular approximation (keyword *ZORA*) level.⁵² The *ZORA* keyword automatically invokes relativistically adjusted basis sets. To account for solvent effects, a conductor-like screening model (keyword *CPCM*) modeling acetonitrile was used in all calculations.^{53,54} Geometry optimizations were performed using Ahlrichs' polarized valence triple- ζ basis set (def2-TZVPP).^{55,56} An atom-pairwise dispersion correction was performed with the Becke–Johnson damping scheme (D3BJ).^{57,58} The energy of the electronic states and presence of energy minima were checked by numerical frequency calculations. Explicit counterions and/or solvent molecules were not taken into account. The charge transfer number analyses of the time-dependent DFT (TDDFT)-calculated transitions were done using TheoDRE 2.2.^{59,60}

SOC-CASSCF-SC-NEVPT2. Calculations of ground- and excited-state properties with respect to metal-centered (MC) states for complex cations *mer-1*²⁺, *mer-1*³⁺, and *mer-1*⁴⁺ were performed using the complete-active-space self-consistent-field method including spin-orbit coupling (SOC-CASSCF)^{61,62} for calculation of the zero-field splitting D in conjunction with the strongly contracted N -electron valence perturbation theory to second order (SC-NEVPT2)^{63,64} in order to recover missing dynamic electron correlations. SOC was treated through the mean-field (SOMF) approximation,^{65,66} and the effective Hamiltonian approach^{67–69} was used to compute the spin-Hamiltonian parameters. In order to model the ligand field, the respective active space was selected to include the dominating σ -bonding orbitals formed between manganese and the ligands (e_g), the 3d orbitals (t_{2g} and e_g^*), and a second d shell. An active space of (9,12) along with 1 sextet root, 16 quartet roots, and 10 doublet roots was selected for *mer-1*²⁺, an active space of (8,12) along with 5 quintet roots, 11 triplet roots, and 11 singlet roots was selected for *mer-1*³⁺, and an active space of (7,12) along with 10 triplet roots and 10 singlet roots was selected for *mer-1*⁴⁺.

Synthesis of 1[OTf]₂. A solution of 100 mg (0.283 mmol, 2.0 equiv) of dgpy in dry THF (5 mL) was added to a solution of 50 mg (0.141 mmol, 1.0 equiv) of Mn(OTf)₂ in dry THF (10 mL). The solution was stirred at ambient temperature for 24 h, and a white precipitate formed. The product was collected by filtration under inert conditions and purified by crystallization via slow diffusion of dry diethyl ether into a concentrated solution in acetonitrile to yield 115 mg (0.108 mmol, 77%) of *mer-1*[OTf]₂ likely in a mixture with *cis-fac-1*[OTf]₂ as clear crystals. Anal. Calcd for C₄₀H₅₄F₆MnN₁₄O₆S₂ (1060.01): C, 45.32; H, 5.14; N, 18.50. Found: C, 45.53; H, 5.43; N, 18.48. MS (CH₃CN, ES⁺): m/z (%) = 380.70 (13, [Mn(dgpy)₂]²⁺), 910.36 (62, [Mn(dgpy)₂+OTf]⁺), 354.24 (100, [dgpy+H]⁺). IR (ATR): $\tilde{\nu}/\text{cm}^{-1}$ = 3097 (vw), 2949 (vw), 2867 (vw), 1588 (s), 1501 (m), 1430 (m), 1373 (m), 1325 (w), 1374 (w), 1260 (s, SO₃), 1219 (m), 1198 (m), 1140 (s, CF₃), 1105 (w, sh), 1069 (vw), 1021 (s, SO₃), 992 (vw, sh), 911 (vw), 847 (vw), 810 (w), 752 (w), 729 (w), 711 (vw, sh), 637 (s), 573 (w), 553 (w), 514 (m), 448 (vw). UV/vis/

NIR (CH₃CN, 298 K): $\lambda_{\text{max}}/\text{nm}$ ($\epsilon/M^{-1} \text{cm}^{-1}$) = 220 (75 800), 255 (40 700), 309 (20 100). CV (CH₃CN, 0.1 M [ⁿBu₄N][B(C₆F₅)₄], vs ferrocene): $E_{1/2}/V$ = −0.26 (qrev, *mer-1*^{3+/2+}), −0.06 (qrev, *cis-fac-1*^{3+/2+}), 0.58 (qrev, *mer-1*^{4+/3+}). Magnetism (solid, 295 K): $\chi_M T/\text{cm}^3 \text{K mol}^{-1}$ = 4.53 (μ_{eff} = 6.02 μ_B); g = 2.056(2).

Synthesis of *mer-1*[BF₄]₂ for Single-Crystal XRD Analysis. A solution of 36 mg (0.10 mmol, 2.2 equiv) of dgpy in dry CH₃CN (2.5 mL) was added to 10 mg (0.047 mmol, 1.0 equiv) of MnBr₂ and stirred. A solution of 20 mg of AgBF₄ (0.10 mmol, 2.2 equiv) in dry CH₃CN (2.5 mL) was added to yield an immediate off-white precipitate of AgBr, which was removed via filtration, leaving a colorless solution. Crystallization via slow diffusion of dry diethyl ether into a concentrated solution in CH₃CN gave clear crystals of *mer-1*[BF₄]₂, suitable for single-crystal XRD analysis.

Synthesis of *cis-fac-1*[PF₆]₂ for Single-Crystal XRD Analysis. A solution of 131 mg (0.372 mmol, 2.0 equiv) of dgpy in dry CH₃CN (2.5 mL) was added to 40 mg (0.186 mmol, 1.0 equiv) of MnBr₂ and stirred. A solution of 94 mg of AgPF₆ (0.372 mmol, 2 equiv) in dry CH₃CN (2.5 mL) was added to yield an immediate off-white precipitate of AgBr, which was removed via filtration, leaving a colorless solution. Crystallization via slow diffusion of dry diethyl ether into a concentrated solution in CH₃CN gave clear crystals of *cis-fac-1*(PF₆)₂, suitable for single-crystal XRD analysis.

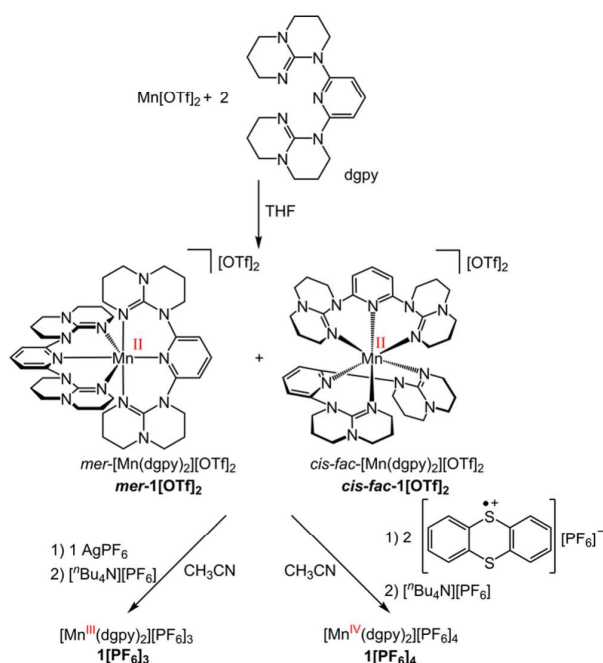
Synthesis of 1[PF₆]₃. A solution of 4.77 mg (0.0188 mmol, 1.0 equiv) of AgPF₆ in dry CH₃CN (2 mL) was added to a solution of 20 mg (0.0188 mmol, 1.0 equiv) of 1[OTf]₂ in dry CH₃CN (2 mL). The reaction was covered with foil and stirred at ambient temperature for 1 h. The mixture was filtered under inert conditions, and the orange filtrate was collected. A solution of 91 mg of [ⁿBu₄N][PF₆] (0.24 mmol, 13 equiv) in dry CH₃CN (1 mL) was added to the filtrate. The product was purified by crystallization via slow diffusion of dry diethyl ether into a concentrated solution in acetonitrile to yield 15.2 mg (0.0127 mmol, 67%) of *mer-1*[PF₆]₃ in a mixture with *cis-fac-1*[PF₆]₃ as orange crystals. Anal. Calcd for C₃₈H₅₄F₁₈MnN₁₄P₃×1.5CH₃CN (1258.38): C, 39.13; H, 4.69; N, 17.25. Found: C, 38.95; H, 4.55; N, 17.63. MS (CH₃CN, ES⁺): m/z (%) = 390.20 (6, [Mn(dgpy)₂+F]²⁺), 1051.33 (31, [Mn(dgpy)₂+2PF₆]⁺). IR (ATR): $\tilde{\nu}/\text{cm}^{-1}$ = 1593 (m), 1578 (m), 1496 (w), 1460 (vw), 1445 (vw, sh), 1420 (vw), 1381 (w), 1276 (vw), 1207 (w), 1161 (vw), 1120 (vw, sh), 1031 (vw), 916 (vw), 831 (s), 740 (w), 637 (w), 555 (s), 420 (w). UV/vis/NIR (CH₃CN, 298 K): $\lambda_{\text{max}}/\text{nm}$ ($\epsilon/M^{-1} \text{cm}^{-1}$) = 215 (90 000), 255 (55 300), 309 (27 000), 354 (12 600), 450 (1200). CV (CH₃CN, 0.1 M [ⁿBu₄N][B(C₆F₅)₄], vs ferrocene): $E_{1/2}/V$ = −0.06 (qrev, *mer-1*^{3+/2+}), 0.56 (qrev, *mer-1*^{4+/3+}). Magnetism (solid, 295 K): $\chi_M T/\text{cm}^3 \text{K mol}^{-1}$ = 3.04 (μ_{eff} = 4.82 μ_B); g = 2.049(2); D/cm^{-1} = −3.84(1).

Synthesis of *mer-1*[PF₆]₄. A solution of 13.6 mg (0.04 mmol, 2.0 equiv) of [thianthrene][PF₆] in dry CH₃CN (2 mL) was added to a solution of 20 mg (0.019 mmol, 1.0 equiv) of 1[OTf]₂ in dry CH₃CN (2 mL). The reaction was stirred at ambient temperature for 5 min. The mixture was filtered under inert conditions, and the deep purple filtrate was collected. A solution of 91 mg of [ⁿBu₄N][PF₆] (0.24 mmol, 13 equiv) in dry CH₃CN (1 mL) was added to the filtrate. The product was purified by crystallization via slow diffusion of dry diethyl ether into a concentrated solution in CH₃CN to yield 26.5 mg (0.02 mmol, 52%) of *mer-1*[PF₆]₄ as dark crystals. Anal. Calcd for C₃₈H₅₄F₂₄MnN₁₄P₄×3CH₃CN (1464.93): C, 36.08; H, 4.34; N, 16.25. Found: C, 36.15; H, 4.90; N, 16.85. MS (CH₃CN, ES⁺): m/z (%) = 525.66 (30, [Mn(dgpy)₂+2PF₆]²⁺), 1196.29 (80, [Mn(dgpy)₂+3PF₆]⁺). IR (ATR): $\tilde{\nu}/\text{cm}^{-1}$ = 1581 (m), 1491 (m), 1463 (w, sh), 1386 (w), 1312 (w), 1269 (vw), 1210 (w), 1154 (vw), 1016 (vw), 944 (vw), 913 (vw), 831 (s), 760 (m, sh), 711 (w, sh), 640 (w), 558 (s), 445 (vw). UV/vis/NIR (CH₃CN, 298 K): $\lambda_{\text{max}}/\text{nm}$ ($\epsilon/M^{-1} \text{cm}^{-1}$) = 215 (82 300), 255 (50 400), 308 (27 000), 354 (7160, sh), 514 (6860), 775 (3320, sh). Magnetism (solid, 295 K): $\chi_M T/\text{cm}^3 \text{K mol}^{-1}$ = 1.88 (μ_{eff} = 3.73 μ_B); g = 2.025(1).

RESULTS AND DISCUSSION

Syntheses of Manganese Complexes. Colorless crystals precipitate from a stoichiometric mixture of dgpy and $\text{Mn}(\text{OTf})_2$ (Scheme 1). These crystals analyze for $1[\text{OTf}]_2$

Scheme 1. Syntheses of Manganese(II/III/IV) Complexes with the Ligand dgpy



by elemental analysis (Experimental Section). IR spectroscopy reveals vibrations of $[\text{OTf}]^-$ at 1140 and 1260 cm^{-1} , and ESI⁺ mass spectrometry shows a peak for the cluster ion $[\text{Mn}(\text{dgpy})_2 + \text{OTf}]^+$ at $m/z = 910.36$ (Supporting Information, Figures S1 and S2). Starting from MnBr_2 and AgBF_4 or AgPF_6 as bromide acceptors delivered crystals of $\text{mer-}1[\text{BF}_4]_2$ and $\text{cis-fac-}1[\text{PF}_6]_2$, respectively, suitable for XRD analyses (see below). The flexibility of dgpy, the absence of crystal field stabilization, and the resulting lability of manganese(II) accounts for the formation of isomers. Analogous *mer/cis-fac* isomers were found for the $[\text{Fe}(\text{dgpy})_2]^{2+}$ complex.³²

To access the higher oxidation states +III and +IV, suitable oxidants were identified from the oxidation potentials of $1[\text{OTf}]_2$. A $\text{CH}_3\text{CN}/[\text{tBu}_4\text{N}][\text{B}(\text{C}_6\text{F}_5)_4]$ solution of $1[\text{OTf}]_2$ displays two dominant one-electron (quasi)reversible oxidative redox waves at -0.26 V ($\text{mer-}1^{3+/2+}$) and $+0.58$ V ($\text{mer-}1^{4+/3+}$) in the cyclic voltammogram (Figure 1). In addition, a weaker wave at -0.06 V is observed, which is assigned to the $\text{Mn}^{\text{III/II}}$ oxidation of the *cis-fac* isomer $\text{cis-fac-}1^{3+/2+}$. The purified manganese(IV) complex $\text{mer-}1^{4+}$ on the other hand (see below) shows no reductive wave in the square wave voltammogram (SWV) for the *cis-fac-}1^{3+/2+} isomer (Supporting Information, Figure S3c,d), which allows assigning the waves to the individual isomers. Upon reduction of $\text{mer-}1^{3+}$, isomerization of the formed substitutionally labile $\text{mer-}1^{2+}$ cannot be excluded in CV experiments. The reductive SWV of $\text{mer-}1^{3+}$ starting at 1^{4+} indicates the presence of *cis-fac-}1^{3+} as a minor component (Supporting Information, Figure S3a,b). The large potential difference between the $\text{Mn}^{\text{III/II}}$ and $\text{Mn}^{\text{IV/III}}$ oxidation events of the *mer* isomers of 0.83 V gives a**

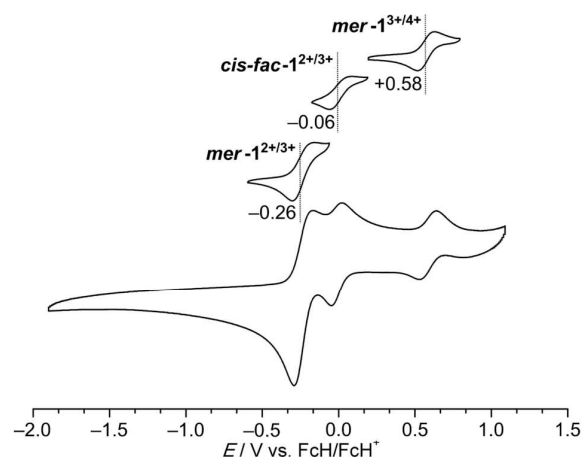


Figure 1. Cyclic voltammograms of $1[\text{OTf}]_2$, 1 mM in acetonitrile containing 0.1 M $[\text{tBu}_4\text{N}][\text{B}(\text{C}_6\text{F}_5)_4]$ as supporting electrolyte.

comproportionation constant $K_C = 10^{\Delta E/0.059 \text{ V}} = 1.2 \times 10^{14}$ for the meridional manganese(III) complex, demonstrating its stability toward disproportionation.⁷⁰ The $1^{4+/3+}$ redox potential of $+0.58$ V lies in-between that of all-pyridine and all-guanidine $[\text{MnN}_6]$ complexes, reflecting the mixed push-pull ligand sphere of $[\text{Mn}(\text{dgpy})_2]^{4+/3+}$ (Chart 1).

As a suitable oxidant to access the manganese(III) complex 1^{3+} , we chose one equivalent of AgPF_6 in CH_3CN ($E_{1/2}(\text{Ag}^{+/0}) = +0.04$ V in CH_3CN).⁷¹ The resulting silver is easily separated from the cationic complex 1^{3+} by filtration. Salt metathesis with $[\text{tBu}_4\text{N}][\text{PF}_6]$ delivered orange crystals of $\text{mer-}1[\text{PF}_6]_3$ as the major isomer. The successful counterion exchange was confirmed by IR spectroscopy, showing the characteristic T_{1u} bands of the $[\text{PF}_6]^-$ counterion at 831 and 555 cm^{-1} and by ESI⁺ mass spectrometry (Supporting Information, Figures S4 and S5). The ESI⁺ mass spectrum furthermore substantiates the triple charge of 1^{3+} showing a peak at $m/z = 1051.33$, which is assigned to the cluster ion $[\text{Mn}(\text{dgpy})_2 + (\text{PF}_6)_2]^+$.

Oxidation of 1^{2+} to the manganese(IV) complex 1^{4+} requires a strong oxidant. In principle, Ag^+ would be sufficiently oxidizing in CH_2Cl_2 ($E_{1/2}(\text{Ag}^{+/0}) = +0.65$ V in CH_2Cl_2).⁷¹ However, the solubility of the cations 1^{n+} in CH_2Cl_2 is too low, precluding this reaction. Finally, we were successful employing a stoichiometric amount of the thianthrene radical cation salt $[\text{C}_{12}\text{H}_8\text{S}_2][\text{PF}_6]$ as oxidant ($E_{1/2}([\text{C}_{12}\text{H}_8\text{S}_2]^{+/0}) = +0.86$ V) in CH_3CN .^{34,71} The resulting purple cationic complex 1^{4+} is separated straightforwardly by precipitation as $\text{mer-}1[\text{PF}_6]_4$ from the neutral thianthrene byproduct. The exclusive presence of the meridional isomer is supported by the reductive SWV, lacking the $1^{3+/2+}$ redox event of the *cis-facial* isomer (Supporting Information, Figure S3c,d) and the presence of the meridional isomer in the crystals of $1[\text{PF}_6]_4$. The presence of the $[\text{PF}_6]^-$ counterion is confirmed by its IR spectroscopic signature at 831 and 558 cm^{-1} and by ESI⁺ mass spectrometry (Supporting Information, Figures S6 and S7). The ESI⁺ mass spectrum furthermore corroborates the +4 charge of 1^{4+} showing a peak at $m/z = 1196.29$, which is assigned to $[\text{Mn}(\text{dgpy})_2 + 3(\text{PF}_6)_3]^+$.

Structures of *cis-fac-}1^{2+}, *mer-}1^{2+}, *mer-}1^{3+}, and *mer-}1^{4+}.**** All complex cations 1^{n+} feature a $[\text{MnN}_6]$ coordination sphere, however with significantly different Mn–N bond lengths and N–Mn–N bond angles (Figure 2, Table 1). In the

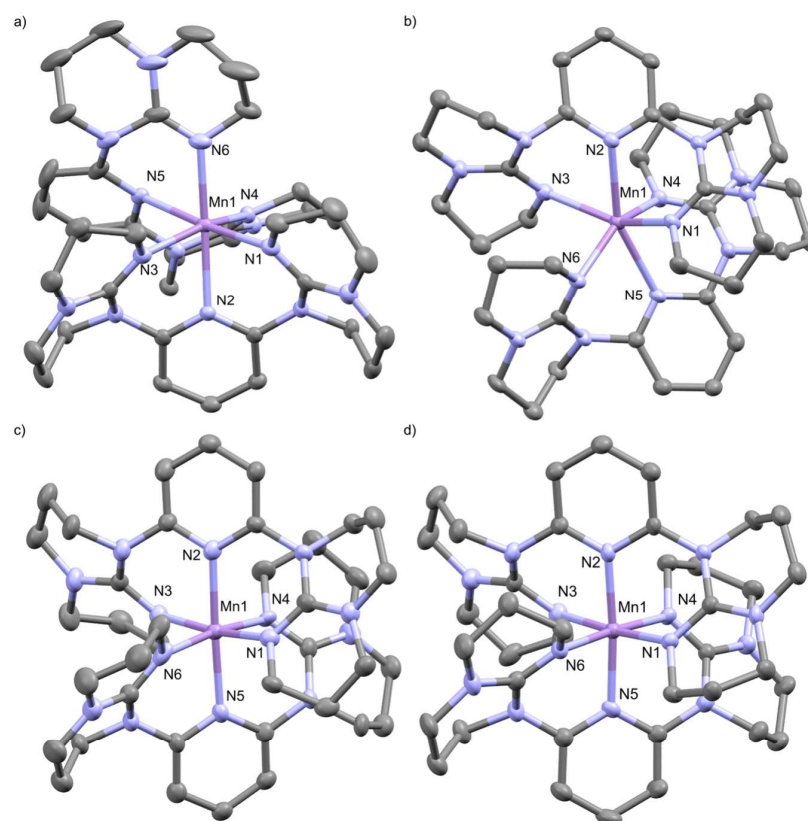


Figure 2. Molecular structures of the cations of (a) *cis-fac-1*[PF₆]₂ × 0.5C₂H₅OC₂H₅ × CH₃CN, (b) *mer-1*[BF₄]₂, (c) *mer-1*[PF₆]₃ × 1.5CH₃CN (only cation A of the two independent cations A/B in the unit cell shown), and (d) *mer-1*[PF₆]₄ × 3CH₃CN determined by XRD. Thermal ellipsoids are displayed at 50% probability. Hydrogen atoms are omitted for clarity.

Table 1. Selected Bond Lengths/Å and Angles/deg of the Cations of *cis-fac-1*[PF₆]₂ × 0.5C₂H₅OC₂H₅ × CH₃CN, *mer-1*[BF₄]₂, *mer-1*[PF₆]₃ × 1.5CH₃CN (Two Independent Cations A/B in the Unit Cell), and *mer-1*[PF₆]₄ × 3CH₃CN

	<i>cis-fac-1</i> [PF ₆] ₂	<i>mer-1</i> [BF ₄] ₂	<i>mer-1</i> [PF ₆] ₃ (A)	<i>mer-1</i> [PF ₆] ₃ (B)	<i>mer-1</i> [PF ₆] ₄
Mn1–N1	2.1839(17)	2.177(2)	2.009(7)	1.993(7)	1.958(4)
Mn1–N2(py)	2.2837(16)	2.276(2)	2.143(8)	2.176(8)	1.979(4)
Mn1–N3	2.2016(17)	2.217(2)	2.008(7)	2.006(7)	1.967(5)
Mn1–N4	2.1977(17)	2.155(2)	2.008(7)	2.022(7)	1.966(4)
Mn1–N5(py)	2.2986(17)	2.309(2)	2.156(7)	2.191(8)	2.002(4)
Mn1–N6	2.1888(18)	2.083(2)	2.003(7)	2.021(7)	1.949(4)
(Mn–N) _{av}	2.226	2.203	2.055	2.068	1.970
N1–Mn1–N2	78.97(6)	76.04(8)	85.1(3)	86.2(3)	89.25(18)
N2–Mn1–N3	76.98(6)	76.80(8)	87.2(3)	83.1(3)	87.12(18)
N4–Mn1–N5	77.36(6)	73.10(8)	85.0(3)	83.9(3)	89.49(18)
N5–Mn1–N6	78.54(7)	78.96(9)	87.1(3)	86.2(3)	86.86(18)
(N–Mn–N) _{av}	78.0	76.2	86.1	84.9	88.2
S(OC-6)	1.982	6.717	0.473	0.803	0.200

meridional series *mer-1*ⁿ⁺, the average Mn–N bond lengths decrease from 2.203 and 2.062 Å to 1.970 Å as expected for the increasing formal charge of the manganese center. The *cis-fac-1*²⁺ isomer possesses only slightly larger Mn–N distances as compared to the isoelectronic meridional isomer *mer-1*²⁺ (Table 1). In all complexes *1*ⁿ⁺, the Mn–N distances to the pyridine (py) donor of the dgpy ligand are longer than the distances to the guanidine (gua) donors (0.017–0.177 Å), suggesting only very weak π -back bonding between 3d^{5,4,3}-Mn^{II,III,IV} and pyridine. In contrast, the M–N_{py} distances in the

low-spin 3d⁶ complexes *mer*-[Co(dgpy)₂]³⁺ and *mer*-[Fe(dgpy)₂]²⁺ are slightly shorter than the M–N_{gua} distances due to the π -accepting nature of pyridine and a filled t_{2g} orbital set.^{31,32} The manganese(III) complex *mer-1*[PF₆]₃ with two independent cations in the unit cell possesses the largest difference between M–N_{py} and M–N_{gua} distances (0.135–0.177 Å). This larger elongation supports a Jahn–Teller elongation of a high-spin d⁴ electron configuration. In contrast, the high-spin 3d⁴-bis(terpyridine) complex [A^{H,Tol}][PF₆]₃

(Chart 1) exhibits a compressed tetragonal distortion, which might be enforced by the rigid terpyridine ligand.²⁰

The structural changes in the series high-spin Mn^{II} (3d⁵-1²⁺) → high-spin Mn^{III} (3d⁴-1³⁺) → Mn^{IV} (3d³-1⁴⁺), namely, compression in the *xy* plane and then compression along the *z* axis (according to the populations of the e_g* orbitals) parallel the metrics in the manganese oxides manganosite MnO [*d*(Mn–O) = 2.222 Å (6×)],⁷² bixbyite Mn₂O₃ [*d*(Mn–O) = 2.242 Å (2×), 1.987 Å (4×)],⁷³ and pyrolysate MnO₂ [*d*(Mn–O) = 1.877 Å (2×), 1.891 Å (4×)].⁷⁴ The rock salt and rutile structure types of manganosite MnO and pyrolysate MnO₂, respectively, crystallographically impose O–Mn–O angles of 180°,^{72,74} while the [MnO₆] polyhedron in bixbyite Mn₂O₃ is severely distorted with O–Mn–O angles of 167°, 167°, and 138°. For *mer*-1²⁺, *mer*-1³⁺, and *mer*-1⁴⁺, the average N–Mn–N bond angles increase from 76.2° and 85.8° to 88.2°, resulting in a “more octahedral” geometry for the Mn³⁺ and Mn⁴⁺ complexes according to the decreased shape parameter *S*(OC-6) (Table 1). The high-spin 3d⁵ electron configuration of 1²⁺ and the resulting absence of ligand field stabilization allow for different isomers and more distorted geometries as compared to the 3d⁴ and 3d³ electron configurations. Expectedly, the symmetric 3d³ electron configuration of 1⁴⁺ enables a coordination polyhedron very close to an ideal octahedron (*S*(OC-6) = 0.109).

The cations *cis*-*fac*-1²⁺, *mer*-1²⁺, *mer*-1³⁺, and *mer*-1⁴⁺ were optimized by density functional theory methods (CPCM-(acetonitrile)-R1JCOSX-UB3LYP-D3BJ-ZORA/def2-TZVPP); Table 2; for Cartesian coordinates see Supporting

Table 2. Selected Bond Lengths/Å and Angles/deg of *cis*-*fac*-1²⁺, *mer*-1²⁺, *mer*-1³⁺, and *mer*-1⁴⁺ Obtained by DFT Calculations

	<i>cis</i> - <i>fac</i> -1 ²⁺	<i>mer</i> -1 ²⁺	<i>mer</i> -1 ³⁺	<i>mer</i> -1 ⁴⁺
Mn1–N1	2.190	2.198	2.019	1.967
Mn1–N2(py)	2.309	2.266	2.199	1.978
Mn1–N3	2.194	2.199	2.022	1.958
Mn1–N4	2.211	2.224	2.013	1.943
Mn1–N5(py)	2.346	2.256	2.191	1.977
Mn1–N6	2.195	2.211	2.007	1.960
(Mn–N) _{av}	2.241	2.226	2.075	1.964
N1–Mn1–N2	78.85	78.87	84.37	88.03
N2–Mn1–N3	77.05	80.46	83.87	89.53
N4–Mn1–N5	77.51	77.31	83.21	87.83
N5–Mn1–N6	78.14	78.29	84.51	88.44
(Mn–N) _{av}	77.9	78.7	84.0	88.5
<i>S</i> (OC-6)	1.903	2.766	0.900	0.109

Information). Average distances and angles of the experimental structure determinations are well reproduced by the DFT calculations, as are the bond length differences between M–N_{py} and M–N_{gua}. This suggests that the geometries of the complex cations are dictated by the electron configuration of the manganese ion and the tridentate ligand and only negligibly by the environment (counterions, solvents). The DFT-optimized geometries are furthermore employed in complete active space self-consistent field (CASSCF) calculations augmented by a NEVPT2 treatment of the 3dⁿ cations to probe the magnetic and electronic properties.

Magnetic Properties and SOC-CASSCF-NEVPT2 Calculations. The magnetic properties of 1[OTf]₂ and 1[PF₆]_n (*n* = 3, 4) were experimentally determined on polycrystalline

powder samples and plotted in the form of $\chi_M T$ as a function of temperature. Expectedly, the manganese(II) complex shows a *T*-independent $\chi_M T$ product $\chi_M T = 4.53 \text{ cm}^3 \text{ K mol}^{-1}$ ($\mu_{\text{eff}} = 6.02 \mu_B$) close to the spin-only value of an *S* = 5/2 ground state ($\chi_{M,\text{so}} T = 4.38 \text{ cm}^3 \text{ K mol}^{-1}$ ($\mu_{\text{eff}} = 5.92 \mu_B$); $g_{\text{fit}} = 2.056(2)$); Supporting Information, Figure S8). Similarly, the 3d³ complex *mer*-1[PF₆]₄ possesses a *T*-independent product $\chi_M T = 1.88 \text{ cm}^3 \text{ K mol}^{-1}$ ($\mu_{\text{eff}} = 3.73 \mu_B$) close to the spin-only value of an *S* = 3/2 ground state with *g* = 2.0 ($\chi_{M,\text{so}} T = 1.87 \text{ cm}^3 \text{ K mol}^{-1}$ ($\mu_{\text{eff}} = 3.87 \mu_B$)). A $g_{\text{fit}} = 2.025(1)$ was fitted to the data (Supporting Information, Figure S9). Below 4 K, $\chi_M T$ decreases probably due to weak zero-field splitting (*zfs*), saturation, or very weak intermolecular exchange interactions.

The $\chi_M T$ versus *T* plot of 1[PF₆]₃ is typical for an isolated manganese(III) complex (*S* = 2) with $\chi_M T = 3.04 \text{ cm}^3 \text{ K mol}^{-1}$ ($\mu_{\text{eff}} = 4.82 \mu_B$) at 295 K ($\chi_{M,\text{so}} T = 3.00 \text{ cm}^3 \text{ K mol}^{-1}$ ($\mu_{\text{eff}} = 4.90 \mu_B$)). Below 30 K, $\chi_M T$ decreases due to *zfs*. To estimate the *zfs* and to determine the sign of *D*, the magnetization was measured as a function of the applied magnetic field at different temperatures (Figure 3). The experimental data were

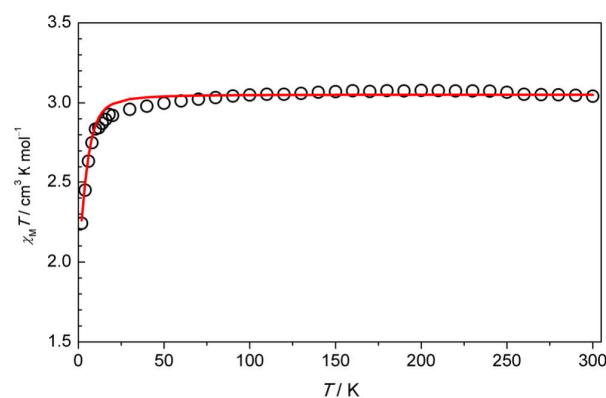


Figure 3. Temperature dependence of the magnetic susceptibility in $\chi_M T$ vs *T* for *mer*-1[PF₆]₃ (black circles). The red line corresponds to the fit obtained with $g = 2.049(2)$ and $D = -3.84(1) \text{ cm}^{-1}$.

fitted using a full-matrix-diagonalization procedure of the spin Hamiltonian $H = g\beta SH + D[S_z^2 - S(S + 1)]$. The best fit was obtained with $g_{\text{fit}} = 2.049(2)$ and $D = -3.84(1) \text{ cm}^{-1}$ (Figure 4a), while a fit with a positive value of $D = +4.28(8) \text{ cm}^{-1}$ (Figure 4b) was less accurate. The negative sign of *D* agrees with the tetrahedral elongated geometry of 1³⁺. Similarly, a negative $D = -3.29 \text{ cm}^{-1}$ was measured for Mn(N₃)₃(tpy) (tpy = 2,2':6',2''-terpyridine) due to a Jahn–Teller elongation,⁷⁵ while a positive $D = +4.82 \text{ cm}^{-1}$ had been assigned to the compressed bis(terpyridine) complex [A^{H,Tol}][PF₆]₃⁷ (Chart 1).

The *zfs* parameter *D* was calculated by ab initio calculations on the geometry-optimized *mer*-1³⁺ cation based on a SOC-CASSCF(8,12) calculation with five quintet, 11 triplet, and 11 singlet roots. Spin–spin interaction was neglected. The second-order spin–orbit coupling contribution and the effective Hamiltonian spin–orbital coupling as implemented in ORCA 4.1.1 yield $D = -3.05 \text{ cm}^{-1}$ and $D = -3.17 \text{ cm}^{-1}$, respectively. These values change to $D = -4.30 \text{ cm}^{-1}$ and $D = -4.54 \text{ cm}^{-1}$, respectively, after the NEVPT2 treatment. All CASSCF-derived values (neglecting spin–spin interactions) confirm the negative sign of *D* as suggested by the fitting of the experimental data. The positive sign of *D* for the compressed

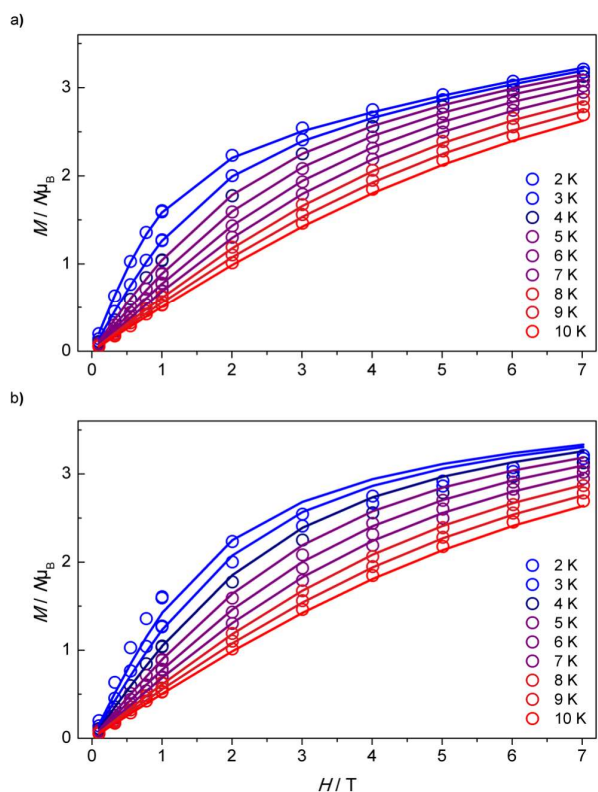


Figure 4. Field dependence of the magnetization of $1[\text{PF}_6]_3$ (open circles) at different temperatures. (a) Best fit with $D = -3.84(1) \text{ cm}^{-1}$ (constrained to be negative) and (b) fit with $D = +4.28(8) \text{ cm}^{-1}$ (constrained to be positive).

bis(terpyridine) complex $[\text{A}^{\text{H,Tol}}][\text{PF}_6]_3$ (Chart 1) had also been correctly predicted by CASSCF calculations neglecting spin–spin interactions, suggesting that this approach is well suited to predict the sign of D in manganese(III) complexes.⁷

Optical Spectroscopy. The optical properties of the $1[\text{OTf}]_2$ and $1[\text{PF}_6]_n$ ($n = 3, 4$) series were experimentally determined by absorption spectroscopy (Figure 5) and theoretically accessed by TDDFT and CASSCF-NEVPT2 calculations to describe charge transfer and ligand field transitions, respectively (Supporting Information, Figures S10–S15, Tables S1–S3).

Expectedly, the colorless manganese(II) complexes 1^{2+} possesses no strong absorption bands in the visible spectral region (Figure 5a). Bands with small oscillator strengths and metal-to-ligand charge transfer character at very similar energies and character are calculated by TDDFT on *mer-1*²⁺ and *cis-fac-1*²⁺, supported by charge transfer number analyses at 489–273 nm and 442–261 nm, respectively (Figure 5a; Supporting Information, Figures S10 and S11). Ligand field transitions in octahedral high-spin d^5 -complexes are spin- and Laporte-forbidden. CASSCF(9,12)-NEVPT2 calculations (Supporting Information, Figure S12, Table S1) estimate the ${}^6\text{A}_1 \rightarrow {}^4\text{T}_1(\text{G})$ and ${}^6\text{A}_1 \rightarrow {}^4\text{T}_2(\text{G})$ transitions (in octahedral symmetry) at 570 and 455 nm (intercombination bands), respectively.

Weak ligand-to-metal charge transfer (LMCT) transitions are calculated for *mer-1*³⁺ at 531, 499, and 458 nm by TDDFT and charge transfer number analyses (Supporting Information,

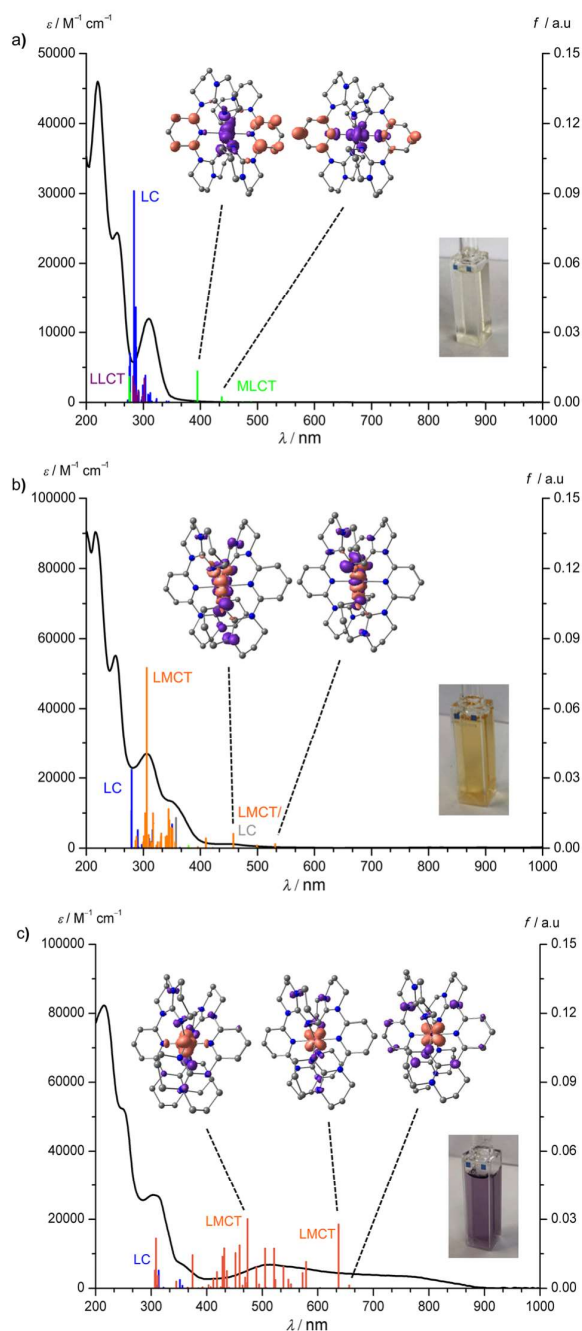


Figure 5. UV/vis/NIR spectra of (a) $1[\text{OTf}]_2$, (b) $1[\text{PF}_6]_3$, and (c) *mer-1* $[\text{PF}_6]_4$ in CH_3CN and TDDFT calculated transitions with the color code indicating the character of the transition according to charge transfer analyses (green: MLCT, purple: LLCT, orange: LMCT, blue: LC, gray: MC). Exemplary difference electron densities of significant low-energy spin-allowed transitions are displayed at an isosurface value of 0.03 au (purple = electron loss; orange = electron gain). The insets show photographs of the respective dilute solutions.

Figure S13). These match the experimental absorption band at 450 nm and account for the orange color of 1^{3+} . The ${}^5\text{E}$ ground state is strongly split by 8475 cm^{-1} due to the lower symmetry. The first spin-allowed ligand field transition ${}^5\text{E}(1) \rightarrow {}^5\text{T}_2(1)$ is calculated at ca. 370 nm according to

CASSCF(8,12)-NEVPT2 calculations (Supporting Information, Figure S14, Table S2).

The cation $mer-1^{4+}$ is deeply purple-black, which is accounted for by a panchromatic absorption throughout the visible spectral region ($\epsilon > 2700 \text{ M}^{-1} \text{ cm}^{-1}$ between 400 and 700 nm). All bands arise from LMCT transitions mainly from the guanidine units to the manganese center according to TDDFT calculations and charge transfer number analyses (Supporting Information, Figure S15). These strong LMCT absorptions find their solid material counterpart in the strongly colored MnO_2 ("Baunstein", "magnesia nigra"). The weaker Laporte-forbidden ligand field transitions cannot be discerned experimentally. CASSCF(7,12)-NEVPT2 calculations find the spin-allowed $^4A_2 \rightarrow ^4T_2$ transition at around 302 nm (Supporting Information, Figure S16, Table S3). This suggests a very large ligand field splitting induced by the high positive charge and the strong guanidine donors. The spin-forbidden transitions $^4A_{2g} \rightarrow ^2E_g$ and $^4A_{2g} \rightarrow ^2T_{1g}$ (in octahedral symmetry) are calculated at 572 and 540 nm, respectively. No ruby-like spin-flip emission is observed at room temperature or 77 K after excitation at 360 or 500 nm. This behavior is expected due to the presence of low-energy LMCT states (Figure 5c), which enable efficient nonradiative decay. In contrast, various red-emissive Mn^{4+} activated luminescent oxide or fluoride materials ($\lambda_{em} = 621\text{--}775 \text{ nm}$)⁷⁶ and a luminescent hexacarbene manganese(IV) complex ($\lambda_{em} = 828 \text{ nm}$) exist, which obviously lack detrimental low-energy LMCT states.^{15,77}

CONCLUSION

The coordination sphere of the pseudo-octahedral homoleptic manganese complexes $[\text{Mn}(\text{dgy})_2]^{n+}$ ($n = 2\text{--}4$) with the adaptable tridentate push–pull ligand dgy is preserved during the $\text{Mn}^{\text{III/II}}$ and $\text{Mn}^{\text{IV/III}}$ redox processes at -0.26 and $+0.58 \text{ V}$ versus ferrocene, respectively. The M–N distances contract in a specific manner from $[\text{Mn}(\text{dgy})_2]^{2+}$ via the tetragonal Jahn–Teller elongated $[\text{Mn}(\text{dgy})_2]^{3+}$ to the symmetrically compressed nearly octahedral $[\text{Mn}(\text{dgy})_2]^{4+}$ cation. The elongated $[\text{Mn}(\text{dgy})_2]^{3+}$ ion shows zero-field splitting with $D = -3.84 \text{ cm}^{-1}$. The colors evolve from the essentially colorless high-spin $3d^5$ - $[\text{Mn}(\text{dgy})_2]^{2+}$ over the orange-colored high-spin $3d^4$ - $[\text{Mn}(\text{dgy})_2]^{3+}$ to the purple-black $3d^3$ - $[\text{Mn}(\text{dgy})_2]^{4+}$. The intense absorption bands of $[\text{Mn}(\text{dgy})_2]^{3+}$ and $[\text{Mn}(\text{dgy})_2]^{4+}$ arise from transitions with ligand-to-metal charge transfer character. $[\text{Mn}(\text{dgy})_2]^{4+}$ absorbs light throughout the visible spectral region with $\epsilon > 2700 \text{ M}^{-1} \text{ cm}^{-1}$ between 400 and 700 nm. With these properties, $[\text{Mn}(\text{dgy})_2]^{n+}$ ($n = 2\text{--}4$) represent molecular analogs of the solid oxides MnO , Mn_2O_3 , and MnO_2 .

ASSOCIATED CONTENT

Supporting Information

The Supporting Information is available free of charge at <https://pubs.acs.org/doi/10.1021/acs.inorgchem.2c01680>.

Detailed IR, ESI⁺, magnetic, and electrochemical data, information on computational studies including charge transfer number analyses, difference densities, orbitals of the active space, and Cartesian coordinates of optimized geometries (PDF)

Accession Codes

CCDC 2171813–2171816 contain the supplementary crystallographic data for this paper. These data can be obtained

free of charge via www.ccdc.cam.ac.uk/data_request/cif, or by emailing data_request@ccdc.cam.ac.uk, or by contacting The Cambridge Crystallographic Data Centre, 12 Union Road, Cambridge CB2 1EZ, UK; fax: +44 1223 336033.

AUTHOR INFORMATION

Corresponding Author

Katja Heinze – Department of Chemistry, Johannes Gutenberg University, 55128 Mainz, Germany; orcid.org/0000-0003-1483-4156; Email: katja.heinze@uni-mainz.de

Authors

Nathan R. East – Department of Chemistry, Johannes Gutenberg University, 55128 Mainz, Germany

Christoph Förster – Department of Chemistry, Johannes Gutenberg University, 55128 Mainz, Germany

Luca M. Carrella – Department of Chemistry, Johannes Gutenberg University, 55128 Mainz, Germany

Eva Rentschler – Department of Chemistry, Johannes Gutenberg University, 55128 Mainz, Germany; orcid.org/0000-0003-1431-3641

Complete contact information is available at:

<https://pubs.acs.org/10.1021/acs.inorgchem.2c01680>

Author Contributions

The manuscript was written through contributions of all authors. All authors have given approval to the final version of the manuscript.

Notes

The authors declare no competing financial interest.

ACKNOWLEDGMENTS

This work has been financially supported by the Deutsche Forschungsgemeinschaft (DFG) under grant INST 247/1018-1 (K.H.). This work was supported by the Max Planck Graduate Center with the Johannes Gutenberg-Universität Mainz (MPGC). N.R.E. is a recipient of a position through the DFG Excellence Initiative by the Graduate School Materials Science in Mainz (GSC 266). Parts of this research were conducted using the supercomputer MOGON and advisory services offered by Johannes Gutenberg University Mainz (<http://www.hpc.uni-mainz.de>) and the supercomputer Elwetritsch and advisory services offered by the TU Kaiserslautern (<https://elwe.rhrk.uni-kl.de>), which are members of the AHRP and the Gauss Alliance e.V. We thank Dr. Dieter Schollmeyer for collecting the XRD data.

REFERENCES

- (1) Dell, R. M. Batteries fifty years of materials development. *Solid State Ionics* **2000**, *134*, 139–158.
- (2) *Manganese Catalysis in Organic Synthesis*; Sortais, J.-B., Ed.; Wiley-VCH Weinheim: Germany, 2022.
- (3) Erikson, K. M.; Ascher, M. In *Essential Metals in Medicine: Therapeutic Use and Toxicity of Metal Ions in the Clinic. Metal Ions in Life Sciences*; Sigel, A.; Freisinger, E.; Sigel, R. K. O.; Carver, P. L. Eds.; de Gruyter GmbH: Berlin, 2019; Vol. 19, Chapter 10, pp 253–266.
- (4) Umena, Y.; Kawakami, K.; Shen, J.-R.; Kamiya, N. Crystal structure of oxygen-evolving photosystem II at a resolution of 1.9 Å. *Nature* **2011**, *473*, 55–60.
- (5) Hollemann, A. F.; Wiberg, N. *Anorganische Chemie, Band 2, Nebengruppenelemente, Lanthanoide, Actinoide, Transactinoide*, 103; Auflage, Walter de Gruyter GmbH: Berlin/Boston, 2017.
- (6) Romain, S.; Baffert, C.; Duboc, C.; Leprêtre, J.-C.; Deronzier, S.; Collomb, M.-N. Mononuclear Mn^{III} and Mn^{IV} Bis-terpyridine

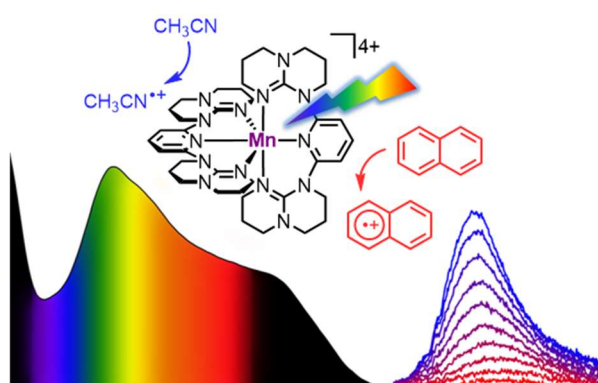
- Complexes: Electrochemical Formation and Spectroscopic Characterizations. *Inorg. Chem.* **2009**, *48*, 3125–3131.
- (7) Romain, S.; Duboc, C.; Neese, F.; Rivière, E.; Hanton, L.; Blackman, A.; Philouze, C.; Leprière, J.-C.; Deronzier, A.; Collomb, M.-N. An Unusual Stable Mononuclear Mn^{III} Bis-terpyridine Complex Exhibiting Jahn-Teller Compression: Electrochemical Synthesis, Physical Characterisation and Theoretical Study. *Chem.—Eur. J.* **2009**, *15*, 980–988.
- (8) Chan, M. K.; Armstrong, W. H. A high-potential mononuclear manganese(IV) complex. Synthesis, structure, and properties, including EPR spectroscopy and electrochemistry, of [Mn(HB(3,5-Me₂pz)₃)](ClO₄)₂ (pz = pyrazolyl). *Inorg. Chem.* **1989**, *28*, 3777–3779.
- (9) Das, G.; Bharadwaj, P. K.; Ghosh, D.; Chaudhuri, B.; Banerjee, R. Synthesis and structure of the [Mn^{IV}(biguanide)₃]⁴⁺ ion: the simplest source for water-stable manganese(IV). *Chem. Commun.* **2001**, 323–324.
- (10) Dhar, B. B.; Mukherjee, R.; Mukhopadhyay, S.; Banerjee, R. Mechanistic Investigation of the Oxidation of Glyoxylic and Pyruvic Acids by Tris(biguanide)manganese(IV) in Weakly Acidic Aqueous Media. *Eur. J. Inorg. Chem.* **2004**, *2004*, 4854–4858.
- (11) Dave, B. C.; Czernuszewicz, R. S. The nature of metal-azide interactions in a high-valent tetraazido-manganese(IV) complex. Isolation, structure and properties, including UV-VIS, EPR and resonance Raman spectroscopy of [Mn(bpy)(N₃)₄] (bpy = 2,2'-bipyridine). *J. Coord. Chem.* **1994**, *33*, 247–269.
- (12) Shylin, S. I.; Pogrebetsky, J. L.; Husak, A. O.; Bykov, D.; Mokhir, A.; Hampel, F.; Shova, S.; Ozarowski, A.; Gumienna-Kontecka, E.; Fritsky, I. O. Expanding manganese(IV) aqueous chemistry: unusually stable water-soluble hexahydrazide clathrochelate complexes. *Chem. Commun.* **2021**, *57*, 11060–11063.
- (13) Hart, R. O. C.; Bott, S. G.; Atwood, J. L.; Cooper, S. R. Higher valent manganese chemistry. [Mn(biguanide)₃]⁴⁺, a structurally characterized Mn^{IV} complex with all-nitrogen coordination. *J. Chem. Soc., Chem. Commun.* **1992**, 894–895.
- (14) Leconte, N.; Moutet, J.; Herasymchuk, K.; Clarke, R. M.; Philouze, C.; Luneau, D.; Storr, T.; Thomas, F. Mn(IV) and Mn(V)-radical species supported by the redox non-innocent bis(2-amino-3,5-di-tert-butylphenyl)amine pincer ligand. *Chem. Commun.* **2017**, *53*, 2764–2767.
- (15) Forshaw, A. P.; Bontchev, R. P.; Smith, J. M. Oxidation of the Tris(carbene)borate Complex PhB(MeIm)₃MnI(CO)₃ to Mn^{IV}[PhB(MeIm)₃]₂(OTf)₂. *Inorg. Chem.* **2007**, *46*, 3792–3794.
- (16) Wittwer, B.; Dickmann, N.; Berg, S.; Leitner, D.; Tesi, L.; Hunger, D.; Gratzl, R.; van Slageren, J.; Neuman, N. I.; Munz, D.; Hohloch, S. A mesoionic carbene complex of manganese in five oxidation states. *Chem. Commun.* **2022**, *58*, 6096.
- (17) Coutard, N.; Musgrave III, C. B.; Moon, J.; Liebov, N. S.; Nielsen, R. M.; Goldberg, J. M.; Li, M.; Jia, X.; Lee, S.; Dickie, D. A.; Schinski, W. L.; Wu, Z.; Groves, J. T.; Goddard, W. A., III; Gunnoe, T. B. Manganese Catalyzed Partial Oxidation of Light Alkanes. *ACS Catal.* **2022**, *12*, 5356–5370.
- (18) Suga, M.; Akita, F.; Hirata, K.; Ueno, G.; Murakami, H.; Nakajima, Y.; Shimizu, T.; Yamashita, K.; Yamamoto, M.; Ago, H.; Shen, J.-R. Native structure of photosystem II at 1.95 Å resolution viewed by femtosecond X-ray pulses. *Nature* **2015**, *517*, 99–103.
- (19) Drosou, M.; Zahariou, G.; Pantazis, D. A. Orientational Jahn-Teller Isomerism in the Dark-Stable State of Nature's Water Oxidase. *Angew. Chem., Int. Ed.* **2021**, *60*, 13493–13499.
- (20) Förster, C.; Dorn, M.; Reuter, T.; Otto, S.; Davarci, G.; Reich, T.; Carrella, L.; Rentschler, E.; Heinze, K. Ddpd as expanded terpyridine: dramatic effects of symmetry and electronic properties in first row transition metal complexes. *Inorganics* **2018**, *6*, 86.
- (21) Vallejo, J.; Pascual-Álvarez, A.; Cano, J.; Castro, I.; Julve, M.; Lloret, F.; Krzystek, J.; De Munno, G.; Armentano, D.; Wernsdorfer, W.; Ruiz-García, R.; Pardo, E. Field-Induced Hysteresis and Quantum Tunneling of the Magnetization in a Mononuclear Manganese(III) Complex. *Angew. Chem., Int. Ed.* **2013**, *52*, 14075–14079.
- (22) Sim, P. G.; Sinn, E. First Manganese(III) Spin Crossover and First d⁴ Crossover. Comment on Cytochrome Oxidase. *J. Am. Chem. Soc.* **1981**, *103*, 241–243.
- (23) Zhang, W.; Loebach, J. L.; Wilson, S. R.; Jacobsen, E. N. Enantioselective Epoxidation of Unfunctionalized Olefins Catalyzed by (Salen)manganese Complexes. *J. Am. Chem. Soc.* **1990**, *112*, 2801–2803.
- (24) Irie, R.; Noda, K.; Ito, Y.; Matsumoto, N.; Katsuki, T. Catalytic Asymmetric Epoxidation of Unfunctionalized Olefins Using Chiral (Salen)manganese(III) Complexes. *Tetrahedron Asymmetry* **1991**, *7*, 481–494.
- (25) Cook, E. N.; Machan, C. W. Bioinspired mononuclear Mn complexes for O₂ activation and biologically relevant reactions. *Dalton Trans.* **2021**, *50*, 16871–16886.
- (26) Atzenhofer, W.; Regelsberger, G.; Jacob, U.; Peschek, G. A.; Furtmüller, P. G.; Huber, R.; Obinger, C. The 2.0 Å Resolution Structure of the Catalytic Portion of a Cyanobacterial Membrane-bound Manganese Superoxide Dismutase. *J. Mol. Biol.* **2002**, *321*, 479–489.
- (27) Fukai, T.; Ushio-Fukai, M. Superoxide dismutases: role in redox signaling, vascular function, and diseases. *Antioxid Redox Signal.* **2011**, *15*, 1583–1606.
- (28) Irving, H.; Williams, R. J. P. The Stability of Transition-metal Complexes. *J. Chem. Soc.* **1953**, 3192–3210.
- (29) Chandra, S.; Gupta, K. Chromium(III), manganese(II), iron(III), cobalt(II), nickel(II) and copper(II) complexes with a pentadentate, 15-membered new macrocyclic ligand. *Transit. Met. Chem.* **2002**, *27*, 196–199.
- (30) Pal, A. K.; Zaccheroni, N.; Campagna, S.; Hanan, G. S. Near infra-red emission from a mer-Ru(II) complex: consequences of strong σ-donation from a neutral, flexible ligand with dual binding modes. *Chem. Commun.* **2014**, *50*, 6846–6849.
- (31) Pal, A. K.; Li, C.; Hanan, G. S.; Zysman-Colman, E. Blue-Emissive Cobalt(III) Complexes and Their Use in the Photocatalytic Trifluoromethylation of Polycyclic Aromatic Hydrocarbons. *Angew. Chem., Int. Ed.* **2018**, *57*, 8027–8031.
- (32) Moll, J.; Förster, C.; König, A.; Carrella, L.; Wagner, M.; Panthöfer, M.; Möller, A.; Rentschler, E.; Heinze, K. Panchromatic Absorption and Oxidation of an Iron(II) Spin Crossover Complex. *Inorg. Chem.* **2022**, *61*, 1659–1671.
- (33) Allen, J. E.; Kassel, S. W.; Piro, N. A. Synthesis, structures and characterization of complexes containing a 2,6-bis(guanidinyl)pyridine ligand on iron(II), cobalt(II), nickel(II), copper(I), copper(II) and zinc(II). *Polyhedron* **2018**, *155*, 77–84.
- (34) Förster, C.; Mack, K.; Carrella, L. M.; Ksenofontov, V.; Rentschler, E.; Heinze, K. Coordination of expanded terpyridine ligands to cobalt. *Polyhedron* **2013**, *52*, 576–581.
- (35) Förster, C.; Gorelik, T. E.; Kolb, U.; Ksenofontov, V.; Heinze, K. Crystalline Non-Equilibrium Phase of a Cobalt(II) Complex with Tridentate Ligands. *Eur. J. Inorg. Chem.* **2015**, *2015*, 920–924.
- (36) Boduszek, B.; Shine, H. J. Preparation of solid thianthrene cation radical tetrafluoroborate. *J. Org. Chem.* **1988**, *53*, 5142–5143.
- (37) Schoeller, W. W.; Niemann, J. Some aspects of the electronic hypersurface of bis(methylene) phosphorane. An experimental and theoretical approach. *J. Am. Chem. Soc.* **1986**, *108*, 22–26.
- (38) Chilton, N. F.; Anderson, R. P.; Turner, L. D.; Soncini, A.; Murray, K. S. PHI: A Powerful New Program for the Analysis of Anisotropic Monomeric and Exchange-Coupled Polynuclear d- and f-Block Complexes. *J. Comput. Chem.* **2013**, *34*, 1164–1175.
- (39) STOE & Cie, X-Area; STOE & Cie GmbH: Darmstadt, Germany.
- (40) Blessing, R. H. An empirical correction for absorption anisotropy. *Acta Crystallogr., Sect. A* **1995**, *51*, 33–38.
- (41) Spek, A. L. Structure validation in chemical crystallography. *Acta Crystallogr., Sect. D* **2009**, *65*, 148–155.
- (42) Sheldrick, G. M. SHELXT - integrated space-group and crystal-structure determination. *Acta Crystallogr., Sect. A* **2015**, *71*, 3–8.
- (43) Sheldrick, G. M. Crystal structure refinement with SHELXL. *Acta Crystallogr., Sect. C* **2015**, *71*, 3–8.

- (44) Sheldrick, G. M. A short history of SHELX. *Acta Crystallogr. Sect. A* **2008**, *64*, 112–122.
- (45) Hübschle, C. B.; Sheldrick, G. M.; Dittrich, B. ShelXle: a Qt graphical user interface for SHELXL. *J. Appl. Crystallogr.* **2011**, *44*, 1281–1284.
- (46) Neese, F. Software update: The ORCA program system, version 4.0. *WIREs Comput. Mol. Sci.* **2018**, *8*, e1327.
- (47) Becke, A. D. Density-functional thermochemistry. III. The role of exact exchange. *J. Chem. Phys.* **1993**, *98*, 5648–5652.
- (48) Miehlich, B.; Savin, A.; Stoll, H.; Preuss, H. Results obtained with the correlation energy density functionals of Becke and Lee, Yang and Parr. *Chem. Phys. Lett.* **1989**, *157*, 200–206.
- (49) Lee, C.; Yang, W.; Parr, R. G. Development of the Colle-Salvetti correlation-energy formula into a functional of the electron density. *Phys. Rev. B* **1988**, *37*, 785–789.
- (50) Neese, F.; Wennmohs, F.; Hansen, A.; Becker, U. Efficient, approximate and parallel Hartree-Fock and hybrid DFT calculations. A 'chain-of-spheres' algorithm for the Hartree-Fock exchange. *Chem. Phys.* **2009**, *356*, 98–109.
- (51) Izsák, R.; Neese, F. An overlap fitted chain of spheres exchange method. *J. Chem. Phys.* **2011**, *135*, 144105.
- (52) Pantazis, D. A.; Chen, X.-Y.; Landis, C. R.; Neese, F. All-Electron Scalar Relativistic Basis Sets for Third-Row Transition Metal Atoms. *J. Chem. Theory Comput.* **2008**, *4*, 908–919.
- (53) Miertus, S.; Scrocco, E.; Tomasi, J. Electrostatic interaction of a solute with a continuum: A direct utilization of ab initio molecular potentials for the prevision of solvent effects. *Chem. Phys.* **1981**, *55*, 117–129.
- (54) Barone, V.; Cossi, M. Quantum Calculation of Molecular Energies and Energy Gradients in Solution by a Conductor Solvent Model. *J. Phys. Chem. A* **1998**, *102*, 1995–2001.
- (55) Weigend, F. Accurate Coulomb-fitting basis sets for H to Rn. *Phys. Chem. Chem. Phys.* **2006**, *8*, 1057–1065.
- (56) Weigend, F.; Ahlrichs, R. Balanced basis sets of split valence, triple zeta valence and quadruple zeta valence quality for H to Rn: Design and assessment of accuracy. *Phys. Chem. Chem. Phys.* **2005**, *7*, 3297–3305.
- (57) Grimme, S.; Antony, J.; Ehrlich, S.; Krieg, H. A consistent and accurate ab initio parametrization of density functional dispersion correction (DFT-D) for the 94 elements H-Pu. *J. Chem. Phys.* **2010**, *132*, 154104.
- (58) Grimme, S.; Ehrlich, S.; Goerigk, L. Effect of the damping function in dispersion corrected density functional theory. *J. Comput. Chem.* **2011**, *32*, 1456–1465.
- (59) Plasser, F. TheoDORE; at <http://theodore-qc.sourceforge.net>.
- (60) Plasser, F. TheoDORE: A toolbox for a detailed and automated analysis of electronic excited state computations. *J. Chem. Phys.* **2020**, *152*, 84108.
- (61) Roos, B. O.; Taylor, R. P.; Siegbahn, P. E. M. A complete active space SCF method (CASSCF) using a density matrix formulated super-CI approach. *Chem. Phys.* **1980**, *48*, 157–173.
- (62) Siegbahn, P. E. M.; Almlöf, J.; Heiberg, A.; Roos, B. O. The complete active space SCF (CASSCF) method in a Newton-Raphson formulation with application to the HNO molecule. *J. Chem. Phys.* **1981**, *74*, 2384–2396.
- (63) Angeli, C.; Cimiraglia, R.; Evangelisti, S.; Leininger, T.; Malrieu, J.-P. Introduction of n-electron valence states for multi-reference perturbation theory. *J. Chem. Phys.* **2001**, *114*, 10252–10264.
- (64) Angeli, C.; Cimiraglia, R. Multireference perturbation configuration interaction V. Third-order energy contributions in the Møller-Plesset and Epstein-Nesbet partitions. *Theor. Chim. Acta.* **2002**, *107*, 313–317.
- (65) Neese, F. Efficient and accurate approximations to the molecular spin-orbit coupling operator and their use in molecular g-tensor calculations. *J. Chem. Phys.* **2005**, *122*, 034107.
- (66) Hess, B. A.; Marian, C. M. In *Computational Molecular Spectroscopy*; Jensen, P. B., Ed.; Wiley: New York, 2000; p 169.
- (67) Cahier, B.; Maurice, R.; Bolvin, H.; Mallah, T.; Guihéry, N. Tools for Predicting the Nature and Magnitude of Magnetic Anisotropy in Transition Metal Complexes: Application to Co(II) Complexes. *Magnetochemistry*. **2016**, *2*, 31.
- (68) Roos, B. O.; Malmqvist, P. A. Relativistic quantum chemistry: the multiconfigurational approach. *Phys. Chem. Chem. Phys.* **2004**, *6*, 2919–2927.
- (69) Durand, P.; Malrieu, J.-P. In *Advances in Chemical Physics: Ab Initio Methods in Quantum Chemistry*; Lawley, K. P., Ed.; John Wiley & Sons Ltd.: Hoboken, NJ, 1987; Vol. 67, Part 1, pp 321–412.
- (70) Kaim, W.; Klein, A.; Glöckle, M. Exploration of Mixed-Valence Chemistry: Inventing New Analogues of the Creutz-Taube Ion. *Acc. Chem. Res.* **2000**, *33*, 755–763.
- (71) Connelly, N. G.; Geiger, W. E. Chemical Redox Agents for Organometallic Chemistry. *Chem. Rev.* **1996**, *96*, 877–910.
- (72) Pacalo, R. E.; Graham, E. K. Pressure and temperature dependence of the elastic properties of synthetic MnO. *Phys. Chem. Minerals* **1991**, *18*, 69–80.
- (73) Geller, S. Structure of α -Mn₂O₃, (Mn_{0.983}Fe_{0.017})₂O₃ and (Mn_{0.37}Fe_{0.63})₂O₃ and relation to magnetic ordering. *Acta Crystallogr.* **1971**, *B27*, 821–828.
- (74) Wyckoff, R. W. G. *Crystal Structures*, 2nd ed.; Interscience Publishers: New York, 1963; Vol. 1, p 239.
- (75) Limburg, J.; Vrettos, J. S.; Crabtree, R. H.; Brudvig, G. W.; de Paula, J. C.; Hassan, A.; Barra, A.-L.; Duboc-Toia, C.; Collomb, M.-N. High-Frequency EPR Study of a New Mononuclear Manganese(III) Complex: [(terpy)Mn(N₃)₃] (terpy 2,2':6',2''-Terpyridine). *Inorg. Chem.* **2001**, *40*, 1698–1703.
- (76) Zhou, Z.; Zhou, N.; Xia, M.; Yokoyama, M.; Hintzen, H. T. Research progress and application prospects of transition metal Mn⁴⁺-activated luminescent materials. *J. Mater. Chem. C* **2016**, *4*, 9143–9161.
- (77) Harris, J. P.; Reber, C.; Colmer, H. E.; Jackson, T. A.; Forshaw, A. P.; Smith, J. M.; Kinney, R. A.; Telser, J. Near-infrared ²E_g - ⁴A_{2g} and visible LMCT luminescence from a molecular bis-(tris(carbene)-borate) manganese(IV) complex. *Can. J. Chem.* **2017**, *95*, 547–552.

3.2 Oxidative Two-State Photoreactivity of a Manganese(IV) Complex using NIR Light

Nathan R. East, Robert Naumann, Christoph Förster, Charusheela Ramanan, Gregor Diezemann and Katja Heinze.

Preprint [DOI: 10.26434/chemrxiv-2023-bhl82] (submitted)



This article reports the photophysical properties of the [Mn(dgpy)₂]⁴⁺ complex, possessing unique dual state photoreactivity using NIR excitation, acting as a luminescent strong photooxidant capable of oxidising challenging aryl substrates such as benzene via two mechanisms. At 730 nm excitation, a low energy NIR-II phosphorescent (1435 nm at 77 K) state is dynamically quenched by

naphthalene, with transient absorption spectroscopy confirming a lifetime of 1.6 ns, and DFT studies confirming the states identity as a mixed ²MC/²LMCT. Unconventionally, a high energy ⁴LMCT state (1.42 V vs ferrocene/ferrocenium) is statically quenched by benzene via a CH₃CN solvent molecule intermediate. Radical cations of these substrates were also trapped via Nicewicz-type oxidative coupling and products characterized with ESI mass spectrometry and HPLC, confirming reactivity. This is the first example of an emissive molecular Mn^{IV} complex capable of dual state photooxidative reactivity upon NIR excitation, and is a significant step in the pursuit of earth-abundant photoactive transition metal complexes.

Author contributions

N. R. East performed syntheses, reactivity studies, irradiation experiments and computational studies. Dr. R. Naumann performed and analyzed the luminescence and ultrafast time-resolved experiments and provided data interpretation. Dr. C. Förster performed and assisted with the computational studies. Dr. C. Ramanan assisted with the time-resolved experiments. Prof. Dr. G. Diezemann performed and analyzed the molecular dynamics simulations. The manuscript and supplementary information were written by Prof. Dr. Katja Heinze, Dr. R. Naumann and N. R. East.

Supporting Information

Found on page 123

“N. R East, R. Naumann, C. Förster, C. Ramanan, G. Diezemann, K. Heinze, *Preprint* [DOI: 10.26434/chemrxiv-2023-bhl82] Copyright 2023, Reproduced with permission”

Oxidative Two-State Photoreactivity of a Manganese(IV) Complex using NIR Light

Nathan R. East¹, Robert Naumann¹, Christoph Förster¹, Charusheela Ramanan^{2,3}, Gregor Diezemann¹ and Katja Heinze^{1*}

¹ Department of Chemistry, Johannes Gutenberg University, Duesbergweg 10-14, 55128 Mainz, Germany. Email: katja.heinze@uni-mainz.de

² Department of Physics and Astronomy, Vrije Universiteit Amsterdam, Amsterdam, Netherlands

³ Max-Planck-Institute for Polymer Research, Mainz, Germany

ORCIDiDs

Robert Naumann 0000-0002-0912-7644

Christoph Förster 0000-0003-4971-5368

Charusheela Ramanan 0000-0001-8603-6853

Gregor Diezemann 0000-0002-6347-8672

Katja Heinze 0000-0003-1483-4156

Highly reducing or oxidizing photocatalysts are a fundamental challenge in the field of inorganic and organic photochemistry. Only a few transition metal complexes with earth-abundant metal ions have so far advanced to excited state oxidants, including chromium, iron and cobalt. All these photocatalysts require high energy light for excitation and their oxidizing power has not been fully exploited due to significant energy dissipation before reaching the photoactive state. Herein we demonstrate that the complex $[\text{Mn}(\text{dgp})_2]^{4+}$ based on earth-abundant manganese can be excited with low-energy NIR light (850 nm, 1.46 eV) to yield a luminescent mixed $^2\text{LMCT}/^2\text{MC}$ excited state (1435 nm, 0.86 eV) with a lifetime of 1.6 ns. The dissipated energy amounts to 0.60 eV. In spite of this energy loss, $^*[\text{Mn}(\text{dgp})_2]^{4+}$ with its excited state redox potential E_{red}^* of 1.80 V vs SCE outcompetes the strongest reported precious metal photooxidant (iridium(III)). $^*[\text{Mn}(\text{dgp})_2]^{4+}$ oxidizes naphthalene ($E_{\text{ox}} \approx 1.31 - 1.54$ V vs. SCE) to its radical cation giving the manganese(III) complex $[\text{Mn}(\text{dgp})_2]^{3+}$ in a clean outer-sphere electron transfer process. Unexpectedly, mesitylene, toluene, benzene and nitriles with even extremely high oxidation potentials up to $E_{\text{ox}} = 2.4$ V provoke the $[\text{Mn}(\text{dgp})_2]^{4+/3+}$ reduction under photolysis. A higher energy short-lived $^4\text{LMCT}$ excited state with a lifetime of 0.78 ps is made responsible for these demanding oxidations, which proceed by static rather than dynamic quenching. This dual excited state reactivity from $^2\text{LMCT}/^2\text{MC}$ and $^4\text{LMCT}$ states is linked to the $^4\text{LMCT} \rightarrow ^2\text{LMCT}/^2\text{MC}$ intersystem crossing process. These unique findings demonstrate how the design of manganese complexes (i) expands the absorption cross section to 400 – 850 nm, (ii) increases the $^2\text{LMCT}/^2\text{MC}$ state lifetime to the nanosecond range allowing luminescence and classical dynamic photoredox processes and (iii) enables non-classical static quenching of an extremely oxidizing $^4\text{LMCT}$ excited state by the solvent. This conceptually novel approach of static quenching by the solvent minimizes free energy losses, harnesses the full photooxidizing power and thus allows even oxidation of nitriles and benzene using earth-abundant elements and low-energy light.

The costs of light-harvesting materials represent a bottleneck for widespread implementation, so that the search for novel organic and inorganic materials based on abundant elements is a highly active research field.¹⁻¹¹ Accepted key requirements for materials in large-scale photochemical applications are a sufficient abundance on earth, the efficient absorption of visible or even near-IR light, a suitably long excited state lifetime for dynamic quenching, a high photostability and a high stability in different oxidation states both for charge injection at semiconductors or for generating reduced or oxidized substrates in solution reactions.

Complexes of the precious metals fulfil most of these requirements, in particular high excited state lifetimes and reversible redox chemistry. Consequently, photochemical and photovoltaic applications are presently dominated by complexes of ruthenium(II) and iridium(III).^{1,11} With respect to photooxidizing properties, many strongly photooxidizing complexes operate as inner-sphere oxidants in hydrogen atom transfer and M–X bond homolysis reactions, such as high valent oxido and halido complexes of manganese(IV), tungsten(VI), cerium(IV), uranium(VI) and copper(II),¹²⁻¹⁹ while strong genuine single-electron outer-sphere photooxidants, which fully retain their coordination sphere, are rare. Recent advances in the field of earth-abundant photocatalysts operating as strong single-electron oxidants include zirconium(IV),^{20,21} cobalt(III),²² iron(III)²³⁻²⁷ and chromium(III) complexes²⁸⁻³¹ in their respective excited states, which are of ligand-to-metal charge transfer character (LMCT)³² for the former and of spin-flip character for chromium(III) complexes.^{10,33}

Photosensitizers possessing excited states with potentials more positive than +0.80 V vs. SCE (+0.42 V vs. ferrocene)³⁴ are considered as photosensitizers with extreme redox potentials.³⁵ The strongest iridium(III) containing photooxidant is [Ir(ppyF₂(CF₃)₂(bpy(CF₃)₂)]⁺ with E_{red}^{*} = 1.65 – 1.68 V vs. SCE (1.27 – 1.30 V vs. ferrocene), yet blue LEDs are required for excitation.^{35,36} The hexacarbene iron(III) complex [Fe(phtmeimb)₂]⁺ and various polypyridine chromium(III) complexes realize potentials of E_{red}^{*} = 1.25 – 1.84 V vs. SCE (0.87–1.46 V vs. ferrocene) (phtmeimb = [phenyl(tris(3-methylimidazolin-2-ylidene))borate][−]) with blue-green light excitation.²³⁻³¹ The formally strongest reported photooxidant based on a first row transition metal is [Co(dgpz)₂]³⁺ with E_{red}^{*} = 2.75 V vs. SCE (2.37 V vs. ferrocene), yet its strong oxidizing power towards challenging substrates has not yet been exploited (dgpz = 2,6-diguanyldipyrazine).²² Strong organic photooxidants encompass substituted acridinium salts,³⁷ 2,3-dichloro-5,6-dicyano-1,4-benzoquinone^{38,39} and the electrochemically generated trisamino-cyclopropenium radical dication with E_{red}^{*} = 2.06–3.33 V vs. SCE (1.68–2.95 V vs. ferrocene).^{40,41}

To fully harness the photon energy for a redox process, i.e. to reduce the free energy losses after excitation,⁴² high energy photoactive states are required for the electron transfer process. Excited states with the same multiplicity as the ground state are typically short-lived, for example organic sensitizers or the iron(III) complex [Fe(phtmeimb)₂]⁺.^{37-41,23,24} Excited states with a multiplicity differing from the ground state multiplicity, for example triplet metal-to-ligand charge transfer states (³MLCT), possess higher excited state lifetimes but are typically at lower energies than the corresponding singlet states (¹MLCT) leading to energy dissipation and consequently a loss of oxidizing/reducing power. Furthermore, an intersystem crossing (ISC) process⁴³ is required to reach the long-lived ³MLCT states, which is often fast and efficient for transition metal complexes, even for first row metals,⁴⁴⁻⁴⁶ yet in certain cases also slow and inefficient ISC processes have been reported.⁴⁷⁻⁵³

In the present study we demonstrate that a mixed pyridine/guanidine complex with manganese(IV) as earth-abundant metal ion can be excited with low-energy NIR light to give two photoactive states, namely an unconventional, luminescent and long-lived mixed doublet ligand-to-metal charge transfer/metal-centered (²LMCT/²MC) excited state with some spin-flip admixture at lower energy capable of oxidizing moderately challenging substrates and a short-lived ⁴LMCT excited state at high energy capable of oxidizing even extremely challenging substrates.

Results and discussion

Ground state properties of $[\text{Mn}(\text{dgpy})_2]^{4+}$

The purple-black manganese(IV) complex $[\text{Mn}(\text{dgpy})_2][\text{PF}_6]_4$ (Fig. 1a) with a d^3 electron configuration yielding a ${}^4\text{A}_2$ ground state (term symbol given for octahedral symmetry) is a strong oxidant in the ground state with $E_{1/2}(\text{Mn}^{\text{IV}}/\text{Mn}^{\text{III}}) = +0.94$ V vs. SCE (0.56 V vs. ferrocene) in acetonitrile (dgpy = 2,6-diguanidylpyridine).⁵⁴ One-electron reduction gives the yellow colored high-spin manganese(III) complex $[\text{Mn}(\text{dgpy})_2]^{3+}$ (Supplementary Fig. 5).⁵⁴ $[\text{Mn}(\text{dgpy})_2]^{4+}$ even oxidizes chloride ions in CH_3CN in the dark (Supplementary Fig. 6), similar to the solid state material MnO_2 ,⁵⁵ while light-induced chloride oxidation had been reported using designed ruthenium(II) and organic photooxidants using one- and two-photon excitation mechanisms.⁵⁶⁻⁵⁸ Clearly, $[\text{Mn}(\text{dgpy})_2]^{4+}$ is highly oxidizing already in its ground state and light excitation might even further enhance this oxidizing power.

$[\text{Mn}(\text{dgpy})_2][\text{PF}_6]_4$ shows panchromatic light absorption throughout the visible spectral region ($\epsilon_{400-700} > 2700 \text{ M}^{-1} \text{ cm}^{-1}$; Fig. 1a) peaking at 514 nm ($6860 \text{ M}^{-1} \text{ cm}^{-1}$) and 775 nm (sh, $3320 \text{ M}^{-1} \text{ cm}^{-1}$) and extending into the near-infrared spectral region.⁵⁴ On the other hand, the manganese(III) complex $[\text{Mn}(\text{dgpy})_2]^{3+}$ absorbs only weakly in the visible spectral region with a weak absorption band at 450 nm ($\epsilon = 600 \text{ M}^{-1} \text{ cm}^{-1}$, Supplementary Fig. 5).⁵⁴ According to time-dependent Density Functional Theory (TD-DFT) calculations and charge transfer number analysis, the strong absorption bands of $[\text{Mn}(\text{dgpy})_2]^{4+}$ arise from symmetry and spin allowed ${}^4\text{LMCT}$ transitions in particular from the guanidine moieties of the ligands to the high-valent manganese center.⁵⁴

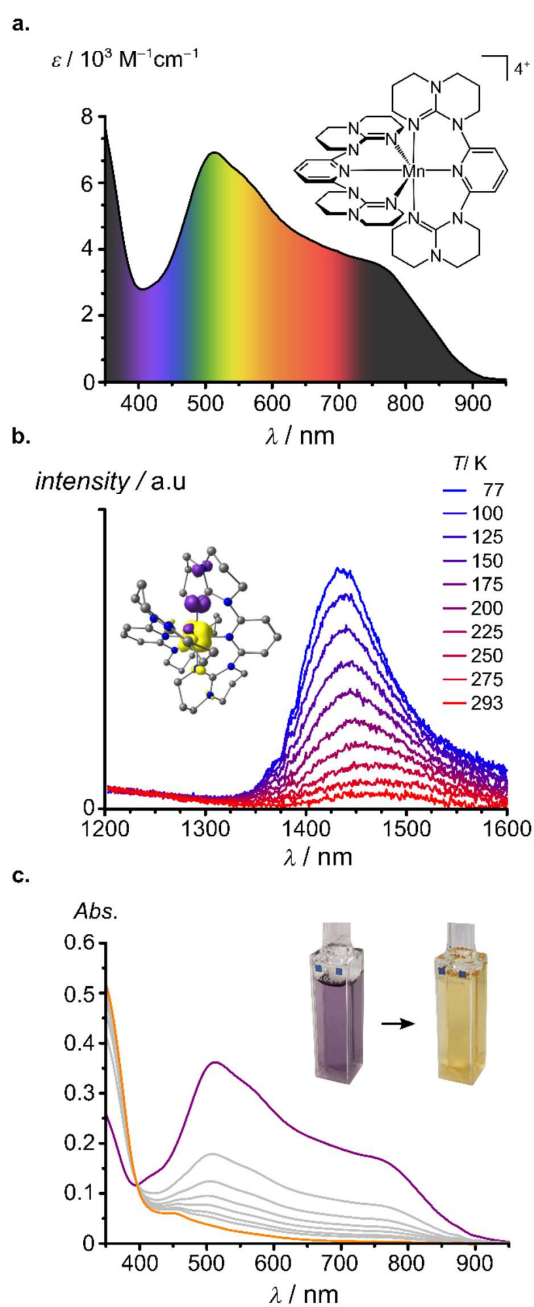


Fig. 1 | Steady-state UV/Vis/near-IR and emission spectroscopy of $[\text{Mn}(\text{dgpy})_2][\text{PF}_6]_4$. **a**, Absorption spectrum of $[\text{Mn}(\text{dgpy})_2][\text{PF}_6]_4$ in CH_3CN with the formula of $[\text{Mn}(\text{dgpy})_2]^{4+}$ indicated. **b**, Variable temperature luminescence spectra of solid $[\text{Mn}(\text{dgpy})_2][\text{PF}_6]_4$ after 730 nm excitation and DFT calculated spin density of the lowest $^2\text{LMCT}/^2\text{MC}$ state of $[\text{Mn}(\text{dgpy})_2]^{4+}$ at an isosurface value of 0.007 a.u. indicated; α and β spin density in yellow and purple, respectively; hydrogen atoms omitted. **c**, Absorption spectra of $[\text{Mn}(\text{dgpy})_2][\text{PF}_6]_4$ (50 μM) in CH_3CN in the presence of naphthalene (0.3 M) during 730 nm irradiation over 45 min; the final orange spectrum corresponds to $[\text{Mn}(\text{dgpy})_2]^{3+}$ and photographs of the cuvettes before and after irradiation.

Luminescence and excited state reactivity of the doublet state

Laser excitation (635 and 730 nm) of solid $[\text{Mn}(\text{dgy})_2][\text{PF}_6]_4$ resulted in a weak luminescence band around 1470 nm (Fig. 1b, Supplementary Figs. 7,8). Cooling to 77 K lead to a hypsochromic shift of the band of ca. $0.8 \text{ cm}^{-1} \text{ K}^{-1}$ to ca. 1435 nm (0.86 eV) and an approximately tenfold increase in intensity (Fig. 1b). The band is quite sharp with a full width at half maximum (FWHM) of ca. 460 cm^{-1} at 77 K. The only other known luminescent manganese(IV) complex $[\text{Mn}(\text{phtmeimb})]^{2+}$ displayed an emission around 828 nm at 85 K with FWHM = 800 cm^{-1} and a hypsochromic of ca. $0.8 \text{ cm}^{-1} \text{ K}^{-1}$ shift from 300 to 85 K.⁵⁹ This emission was assigned to the ${}^2\text{E} \rightarrow {}^4\text{A}_2$ spin-flip luminescence,⁵⁹ although low-energy charge transfer states prevail in the visible spectral region and although the FWHM of the emission band is comparably large.⁵⁹ Genuine spin-flip emitters based on chromium(III) exhibit FWHM of the emission bands around 280 and 420 cm^{-1} at room temperature.^{60,61}

In contrast to the spin-flip assignment of the $[\text{Mn}(\text{phtmeimb})]^{2+}$ luminescence and the similarity of the band characteristics, DFT calculations on the lowest energy doublet state of $[\text{Mn}(\text{dgy})_2]^{4+}$ support a strong ${}^2\text{LMCT}$ character with an admixture of metal-centered character (${}^2\text{MC}$, spin-flip) (Fig. 1b). This mixed ${}^2\text{LMCT}/{}^2\text{MC}$ state is calculated at an energy of 0.78 eV above the ground state excellently matching the emission energy of 0.86 eV at 77 K. In the mixed ${}^2\text{LMCT}/{}^2\text{MC}$ state, charge has transferred from a coordinated guanidine nitrogen atom to the Mn center (Fig. 1b). Possibly, the admixture of the ${}^2\text{MC}$ state into the ${}^2\text{LMCT}$ state gives rise to a more nested, i.e. less distorted, state and thus a rather sharp emission band. This ${}^2\text{MC}$ admixture giving a weakly distorted excited state might also prolong the doublet state lifetime as has been suggested previously for an oxido manganese(IV) complex.¹²

With the excited doublet state energy of $E_{00} = 0.86 \text{ eV}$, the excited state redox potential can be estimated as $E_{\text{red}}^*({}^*\text{Mn}^{\text{IV}}/\text{Mn}^{\text{III}}) = 1.80 \text{ V vs. SCE}$ (1.42 V vs. ferrocene). This is significantly higher than the excited state redox potential of the strongest reported iridium(III) photooxidant ($E_{\text{red}}^*({}^*\text{Ir}^{\text{III}}/\text{Ir}^{\text{II}}) = 1.54 \text{ V vs. SCE}$, 1.16 vs. ferrocene)^{35,36} and suffices to oxidize naphthalene with $E_{\text{ox}} \approx 1.31 - 1.54 \text{ V vs. SCE}$.^{12,62} Indeed irradiation of $[\text{Mn}(\text{dgy})_2][\text{PF}_6]_4$ (50 μM) in CH_3CN with 730 nm light in the presence of naphthalene (0.3 M) gives the manganese(III) complex according to UV/Vis/NIR spectroscopy (Fig. 1c). The series of spectra during photolysis displays isosbestic points at 334 and 398 nm indicating a clean Mn^{4+} to Mn^{3+} reduction (Fig. 1c). The naphthalene radical cation is too short-lived to be observed under these steady-state conditions. However, the naphthalene radical cation could be trapped by a deactivated pyrazole (1H-pyrazole-4-carboxylic acid ethyl ester) in a Nicewicz-type oxidative coupling.^{63,64} The naphthalenyl pyrazole C–H amination product was identified by mass spectrometry (with a signal at $m/z = 267$ for $\text{C}_{16}\text{H}_{15}\text{N}_2\text{O}_2$; Supplementary Fig. 9).

Ultrafast spectroscopy and the excited state reactivity of a quartet excited state

Unexpectedly, irradiation of the complex in the presence of mesitylene, toluene or benzene with much higher oxidation potentials up to $E_{\text{ox}} = 2.36 \text{ V vs. SCE}$ ^{12,62} and even in pure acetonitrile ($E_{\text{ox}} \approx 2.4 \text{ V vs. SCE}$)^{62,65} leads to clean photoreduction, albeit with much slower rates (Supplementary Figs. 10–14). Irradiation of $[\text{Mn}(\text{dgy})_2][\text{PF}_6]_4$ at 730 nm in butyronitrile, nitromethane, 1,2-butylene carbonate or γ -valerolactone with similarly high oxidation potentials⁶² as acetonitrile cleanly gives $[\text{Mn}(\text{dgy})_2]^{3+}$ as well (Supplementary Figs. 15–18) confirming an extraordinary high oxidation power of ${}^*[\text{Mn}(\text{dgy})_2]^{4+}$. The excited state redox potential can be estimated as at least $E_{\text{red}}^*({}^*\text{Mn}^{\text{IV}}/\text{Mn}^{\text{III}}) \approx 2.4 \text{ V vs. SCE}$ ($\approx 2.0 \text{ V vs. ferrocene}$) based on the CH_3CN oxidation potential. With the ground state redox potential given (see above), the excited state energy must be around 1.46 eV. This energy estimation fits to the low-energy tail of the absorption band around 850 nm (1.46 eV, Fig. 1a) and suggests a ${}^4\text{LMCT}$ excited state at $E_{00} = 1.46 \text{ eV}$ as photoactive state. Indeed, analogous Mn^{4+} to Mn^{3+} photoreductions by CH_3CN are observed with 850 nm LED illumination proving that this photoactive excited state of $[\text{Mn}(\text{dgy})_2]^{4+}$ is populated even with low energy light (Supplementary Fig. 19).

The proposed initially formed nitrile radical cation $\text{CH}_3\text{CN}^{*\cdot}$ in acetonitrile can be trapped by an arene, e.g. benzene C_6H_6 . Loss of a proton and a further electron yields the corresponding aryl nitrilium ion⁶⁶ as shown by ESI mass spectrometry ($m/z = 118$ for $\text{C}_8\text{H}_8\text{N}$; Supplementary Fig. 20). Isotopic labeling using C_6D_6 confirms the composition of the generated nitrilium ion ($m/z = 123$ for $\text{C}_8\text{H}_3\text{D}_3\text{N}$; Supplementary Fig. 21). Reaction of activated benzylic C–H bonds with CH_3CN via nitrilium ions had been reported by Lambert to give acetamides after hydrolysis with water using the electrochemically generated photoexcited trisaminocyclopropenium radical dication as oxidant.⁶⁷

To probe the formation of arene radical cations either by direct oxidation with $^*[\text{Mn}(\text{dgp})_2]^{4+}$ or by oxidation with the initially formed $\text{CH}_3\text{CN}^{*\cdot}$ as redox mediator we trapped the arene radical cation by a deactivated electron-poor pyrazole in a Nicewicz-type oxidative coupling.^{63,64} Electron-rich arenes have been coupled using 9-mesityl-10-methylacridinium photocatalysts^{63,64} and the challenging benzene itself has been coupled using the trisaminocyclopropenium radical dication.⁴⁰ Given that transition metal photocatalysts have not been reported to provoke such a transformation, we were pleased to see that mesitylene and even benzene were oxidatively coupled with 1H-pyrazole-4-carboxylic acid ethyl ester using $[\text{Mn}(\text{dgp})_2]^{4+}$ under red-NIR light (730 nm) irradiation to give the respective aminated arenes as shown by ESI mass spectrometry ($m/z = 259$ for $\text{C}_{15}\text{H}_{19}\text{N}_2\text{O}_2$; $m/z = 217$ for $\text{C}_{12}\text{H}_{13}\text{N}_2\text{O}_2$; Supplementary Figs. 22–23). Deuterated benzene gave the isotopologous amination product ($m/z = 222$ for $\text{C}_{12}\text{H}_8\text{D}_5\text{N}_2\text{O}_2$, Supplementary Fig. 24). Photolysis (730 nm) of benzene (1.3 M) in CH_3CN with 1H-pyrazole-4-carboxylic acid ethyl ester (30 mM) with $[\text{Mn}(\text{dgp})_2][\text{PF}_6]_4$ (2 mM) as the limiting reagent gave 11 % of the coupling product by HPLC analysis (Supplementary Fig. 25).

Clearly, the lowest energy $^2\text{LMCT}/^2\text{MC}$ state at $E_{00}(^2\text{LMCT}/^2\text{MC}) = 0.86$ eV is thermodynamically incompetent to oxidize these arene and nitrile substrates due to its too low excited state redox potential. Consequently, a different excited state must be responsible for this extraordinary photoreactivity, likely a $^4\text{LMCT}$ state at an energy $E_{00}(^4\text{LMCT}) = 1.46$ eV, i.e. 0.60 eV higher in energy than the $^2\text{LMCT}/^2\text{MC}$ state. To elucidate the nature of this proposed photoactive $^4\text{LMCT}$ state and the excited state dynamics, we performed femtosecond transient absorption (TA) spectroscopy and further mechanistic experiments.

Laser excitation of $[\text{Mn}(\text{dgp})_2][\text{PF}_6]_4$ in CH_3CN at 730 nm yields positive excited state absorption (ESA) bands below 420 and above 800 nm and a broad negative band between 430 and 800 nm peaking at 500 nm (Fig. 2a). The spectral evolution of the entire data set was fitted with a global fit comprising of three components with lifetimes of $\tau_{1,2,3} = 0.78, 9.7$ and 1600 ps (for evolution-associated difference spectra EADS and decay associated difference spectra DADS see Supplementary Fig. 26).

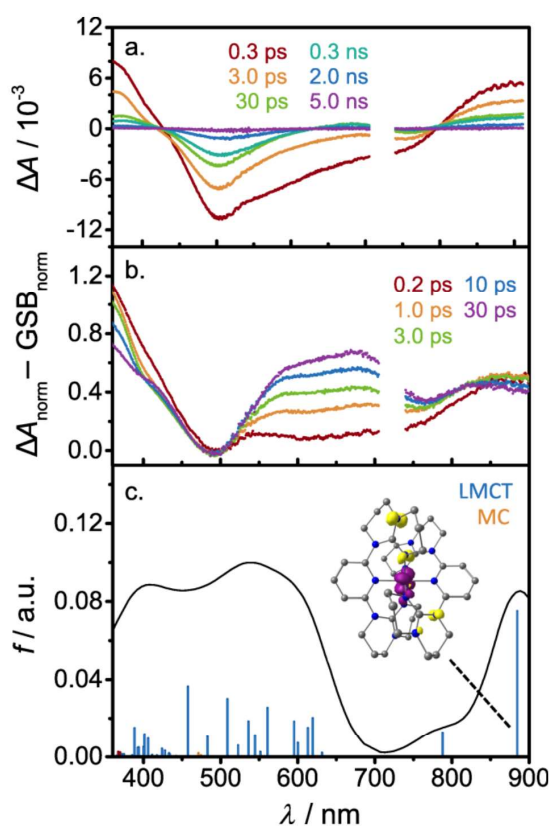


Fig. 2 | fs-Transient absorption investigations of $[\text{Mn}(\text{dgpy})_2][\text{PF}_6]_4$ in Ar saturated CH_3CN revealing the initial formation of the $^4\text{LMCT}$ state followed by the slow intersystem crossing to the $^2\text{LMCT}/^2\text{MC}$ state. **a**, Transient absorption spectra after excitation with 730 nm laser pulses of ca. 200 fs duration (800 nJ / pulse). **b**, Estimated ESA bands and evolution of an additional CT band in the visible range. **c**, Time-dependent DFT calculated low energy spin-allowed transitions of the $^2\text{LMCT}/^2\text{MC}$ state of $[\text{Mn}(\text{dgpy})_2]^{4+}$ (shifted by 145 cm^{-1} to lower energy) with the color code indicating the character of the transition according to charge transfer number analyses (blue: LMCT, orange: MC; isosurface value of electron difference density at 0.005 a.u., electron gain in purple, electron loss in yellow) and an envelope band shape composed of Gaussians with FWHM of 80 nm.

In general, negative bands can be assigned to the ground state bleach (GSB), although the band shape in most cases strongly deviates from the band shape of the corresponding part of the ground state spectrum due to superimposed ESA bands. For $[\text{Mn}(\text{dgpy})_2][\text{PF}_6]_4$, however, the initially observed negative band ($t < 300\text{ fs}$) almost perfectly matches the theoretical GSB spectrum in a large spectral range between 460 and 740 nm (Supplementary Fig. 27). Hence, the ESA of the initially populated $^4\text{LMCT}$ state does not contribute significantly to the overall signal in this spectral region. The pure excited state absorption can be estimated by subtracting the normalized theoretical GSB from the normalized difference absorption spectrum. In the spectral region between 460 and 520 nm, the band shape remains even unchanged at all time delays (Supplementary Fig. 27), such that the same method can be employed for all spectra. Fig. 2b displays the resulting ESA spectra revealing the formation of an additional positive band between 500 and 800 nm, which evolves within a few picoseconds and persists, apart from minor band shape changes, until complete relaxation to the ground state. This transition can also be observed in the decay trace at 680 nm, which shows a change of the sign in the

original TA data (Supplementary Fig. 28). The formation of this new band indicates a transition from the initially populated $^4\text{LMCT}$ state to a new electronically excited state, likely the $^2\text{LMCT}/^2\text{MC}$ state.

Time-dependent DFT calculations of the DFT geometry optimized lowest energy $^2\text{LMCT}/^2\text{MC}$ state (Fig. 1b) find several allowed transitions with predominant LMCT character between 400 and 600 nm as well as between 700 and 900 nm. The overall shape with two discernible absorption bands fits reasonably well to the two ESA bands observed in the TA spectra (Fig. 2c). Thus, we assign this process to the population of the $^2\text{LMCT}/^2\text{MC}$ state via slow ISC with $\tau_1 = 780$ fs. Although ISC is often ultrafast even for 3d transition metal complexes⁴⁴⁻⁴⁶, it can also be rather slow in the picosecond and even nanosecond range.⁴⁷⁻⁵³ After the population of the $^2\text{LMCT}/^2\text{MC}$ state is completed, the shape of the spectrum remains basically unchanged, besides minor shifts and a small increase of the intensity of the newly formed band ($\tau_2 = 9.7$ ps), which we attribute to thermal relaxation and reorganization of the solvent cage (VR, vibrational relaxation) due to the substantial change of the dipole moment during the LMCT transition. Hence, the slow final decay to the quartet ground state ($\tau_3 = 1.6$ ns) occurs from the thermally relaxed $^2\text{LMCT}/^2\text{MC}$ state. This assignment is also supported by the emission band found at 1435 nm (77 K), which matches the calculated energy of the lowest-energy $^2\text{LMCT}/^2\text{MC}$ state (Fig. 1b, vide supra). Excitation at 350 nm gives the same spectra and lifetime for the long-lived component ($\tau_1 = 1.6$ ns) as obtained with 730 nm excitation (Supplementary Fig. 29). Hence, the $^2\text{LMCT}/^2\text{MC}$ state is populated at both excitation wavelengths showing that no branching occurs at higher energies.

The evolution of the newly formed band could in principle also be rationalized by two other mechanisms, namely formation of low-spin $[\text{Mn}(\text{dgp})_2]^{3+}$ and $\text{CH}_3\text{CN}^{*+}$ via static hole transfer or by spin crossover (SCO) yielding a $^6\text{LMCT}$ state (Supplementary Fig. 30). Hole transfer can be excluded as neither low-spin $[\text{Mn}(\text{dgp})_2]^{3+}$ nor $\text{CH}_3\text{CN}^{*+}$ show transitions above 450 nm (Supplementary Fig. 31). Furthermore, excitation at 730 nm of $[\text{Mn}(\text{dgp})_2][\text{PF}_6]_4$ in CH_3NO_2 gives the same transient absorption spectra (Supplementary Fig. 32) and similar lifetimes ($\tau_{1,2,3} = 0.70, 9.1, 1700$ ps) illustrating that the spectral evolution is independent of the solvent that is oxidized. SCO to give a $^6\text{LMCT}$ state is also unlikely to compete with the ISC as the $^6\text{LMCT}$ state is calculated to display merely a single broad absorption band instead of two bands which are experimentally observed. Furthermore, the formation of the $^6\text{LMCT}$ state would be accompanied with an elongation of the Mn–N(pyridine) bonds by 0.15–0.26 Å due to the high-spin character of the formal Mn^{3+} center endowing substantial structural reorganization and large barriers.

The suggested sequential relaxation pathway $^4\text{LMCT} \rightarrow ^2\text{LMCT}/^2\text{MC}$ (hot) $\rightarrow ^2\text{LMCT}/^2\text{MC}$ (relaxed) $\rightarrow ^4\text{A}_2$ nicely fits to the observed reactivity. Challenging substrates like benzene or nitriles must be oxidized before ISC takes place as the $^2\text{LMCT}/^2\text{MC}$ state is not sufficiently oxidizing to enable these reactions (vide supra). Indeed, ISC was found to be comparably slow, such that the static hole transfer to the solvent can compete with the population of the $^2\text{LMCT}/^2\text{MC}$ state. On the other hand, ISC is fast enough to render the hole transfer rather inefficient, which explains the low reaction rate for these substrates. Moreover, the lifetime of the long-lived component remains unaltered when the solvent is changed from CH_3CN to CH_3NO_2 pinpointing the $^4\text{LMCT}$ state as the highly reactive excited state. However, the $^2\text{LMCT}/^2\text{MC}$ state combines sufficient oxidative power for less challenging substrates as naphthalene with a nanosecond lifetime that suffices for bimolecular reactivity. The switch from $^4\text{LMCT}$ to $^2\text{LMCT}/^2\text{MC}$ reactivity changes the mechanism from a solvent mediated process to direct substrate oxidation.

To confirm that neither dissociated dgpy ligand nor the $[\text{PF}_6]^-$ counter ions are potentially reacting with this $^4\text{LMCT}$ state we performed several test reactions. Partial ligand dissociation and consequently the presence of traces of dgpy in the solution as potential substrate could be excluded as $[\text{Mn}(\text{dgp})_2]^{4+}$ would oxidize uncoordinated dgpy already in its ground state in the dark (Supplementary Fig. 33). ^{19}F and ^{31}P NMR spectroscopy before and after photolysis confirm that the $[\text{PF}_6]^-$ counter ions are not

photooxidized as the NMR spectra remain unchanged after photolysis (Supplementary Figs. 34, 35). To further support the redox innocence of the $[\text{PF}_6]^-$ counter ions, the perchlorate salt $[\text{Mn}(\text{dgy})_2][\text{ClO}_4]_4$ has been prepared and investigated additionally (Supplementary Information). Irradiation of $[\text{Mn}(\text{dgy})_2][\text{ClO}_4]_4$ at 730 nm in CH_3CN leads to photoreduction of $[\text{Mn}(\text{dgy})_2]^{4+}$ as well, even slightly faster than with $[\text{PF}_6]^-$ counter ions (Supplementary Figs. 36, 37). The molar conductivity of $[\text{Mn}(\text{dgy})_2][\text{PF}_6]_4$ in CH_3CN is with $640 \text{ S cm}^{-1} \text{ M}^{-1}$ comparably high (Supplementary Fig. 38), although not many 1:4 electrolytes have been investigated so far hampering comparisons.^{68,69} A molecular dynamics simulation of $[\text{Mn}(\text{dgy})_2][\text{PF}_6]_4$ in CH_3CN over 1 μs resulted in shells of counterions with $\text{Mn}^{\cdot\cdot}[\text{PF}_6]$ (center-of-mass) distances peaking at 4.1, 6.1, 7.3 and 8.5 Å suggesting ion-pairing with $[\text{PF}_6]^-$ ions (Supplementary Fig. 39). Similarly, the molar conductivity of $[\text{Mn}(\text{dgy})_2][\text{PF}_6]_3$ in CH_3CN ($560 \text{ S cm}^{-1} \text{ M}^{-1}$) is high for a 1:3 electrolyte (Supplementary Fig. 38).^{68,69} To probe the effect of ion pairing on the photoreduction and cage escape,⁷⁰ $[\text{Mn}(\text{dgy})_2][\text{PF}_6]_4$ was photolyzed in CH_3CN in the presence of increasing amounts of $[\text{n-Bu}_4\text{N}][\text{PF}_6]$ (0, 50, 100 and 200 mM; Supplementary Figs. 40–42). The reaction is significantly slowed down with increasing $[\text{PF}_6]^-$ concentration suggesting a slower photooxidation of CH_3CN or a slower cage escape at high ionic strength (Supplementary Fig. 43). As the ultrafast dynamics observed by TA spectroscopy are unaffected by the presence of 100 mM $[\text{n-Bu}_4\text{N}][\text{PF}_6]$ (Supplementary Fig. 44), we suggest that the initial static quenching is not hampered but rather the cage escape reaction at high ionic strength. A similar retarding effect on the photoreduction, likely also affecting the cage escape rate, occurs when diluting the acetonitrile solution with redox-inert ortho-dichlorobenzene in 1:1 and 1:2 v/v ratios (Supplementary Figs. 45–47).

These combined experiments support the conclusion that the redox partner of the $^4\text{LMCT}$ excited Mn^{4+} complex is the solvent itself. Solvent molecules are already present in the vicinity of the Mn^{4+} complex. Two short $\text{Mn}^{\cdot\cdot}\text{N}(\text{CH}_3\text{CN})$ distances of 4.91 and 5.73 Å are present in the solid state structure (CCDC-2171816).⁵⁴ The molecular dynamics simulation of $[\text{Mn}(\text{dgy})_2][\text{PF}_6]_4$ in CH_3CN over 1 μs resulted in shells of CH_3CN molecules around the tetracation with $\text{Mn}^{\cdot\cdot}[\text{CH}_3\text{CN}]$ (center-of-mass) distances peaking at ca. 3.9, 6.0, 8.5, 12.3 and 16.8 Å (Supplementary Fig. 48). The first peak up to 4.25 Å corresponds to 0.9 CH_3CN molecules, i.e. approximately one CH_3CN molecule is present close to the Mn center. This allows for static quenching of the short-lived $^4\text{LMCT}$ state competitive with ISC, while a purely dynamic quenching on the short time scale of the $^4\text{LMCT}$ lifetime would be highly unlikely. Consequently, the reactivity of $[\text{Mn}(\text{dgy})_2]^{4+}$ in its excited $^4\text{LMCT}$ state relies on the extremely high excited state potential sufficient for solvent oxidation by a static quenching mechanism.

Quantum chemical calculations and mechanistic picture

Optical excitation of $[\text{Mn}(\text{dgy})_2]^{4+}$ from its $^4\text{A}_2$ ground state yields $^4\text{LMCT}$ excited Franck-Condon states at energies from 1.4 to 3.0 eV (Fig. 1a). The lowest-energy absorptions are assigned to the $^4\text{LMCT}$ transitions calculated at 656 and 637 nm shown in Fig. 3a with their electron difference densities. In these $^4\text{LMCT}$ states, electron density has been transferred from the guanidine ligands to a d_π orbital (t_{2g} in O_h notation) of the manganese center, i.e. forming a guanidine radical cation and a manganese(III) ion in its low-spin electron configuration.

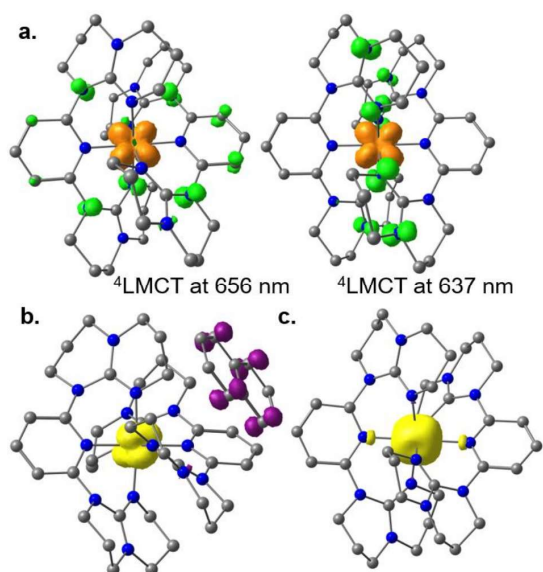


Fig. 3 | Quantum chemical calculations of excited states of $[\text{Mn}(\text{dgpy})_2]^{4+}$ and the products of the photoinduced electron transfer reaction. **a**, Difference electron density of the two lowest spin-allowed $^4\text{LMCT}$ transitions at 656 and 637 nm (green = electron density loss; orange = electron density gain) displayed at an isosurface value of 0.006 a.u.. **b**, DFT optimized geometry of the $^2\{[\text{Mn}(\text{dgpy})_2]^{3+}/\text{naphthalene}^{*+}\}^{4+}$ pair with spin densities after the electron transfer showing the low-spin $[\text{Mn}(\text{dgpy})_2]^{3+}$ complex and the naphthalene radical cation. **c**, DFT optimized geometry and spin density of the high-spin $[\text{Mn}(\text{dgpy})_2]^{3+}$ complex. Spin densities at an isosurface value of 0.012 a. u.; α and β spin density in yellow and purple, respectively. Hydrogen atoms omitted.

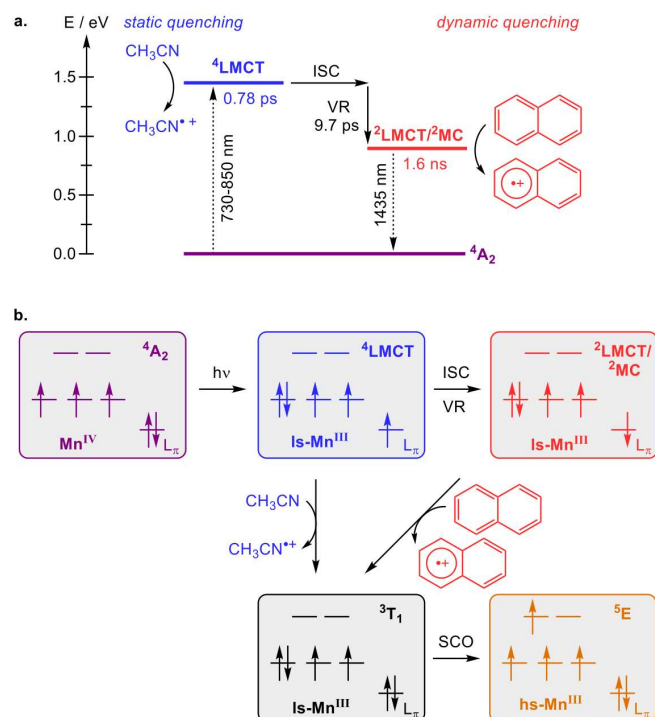


Fig. 4 | Jablonski diagram and electron configurations of the involved excited states and redox states.

a, Jablonski diagram including photoinduced redox processes from the $^4\text{LMCT}$ and $^2\text{LMCT}/^2\text{MC}$ excited states with acetonitrile and naphthalene, respectively, including data from luminescence and TA spectroscopy; ISC = intersystem crossing, VR = vibrational relaxation. **b**, Electron configurations of the $^4\text{A}_2$ ground state (purple), $^4\text{LMCT}$ (blue) and $^2\text{LMCT}/^2\text{MC}$ (red) excited states and the low-spin (black, $^3\text{T}_1$) and high-spin (orange, ^5E) manganese(III) complexes illustrated by the occupation of metal 3d orbitals and a ligand π orbital (L_π) (SCO = spin crossover).

The lifetime of the populated $^4\text{LMCT}$ state depends on the rates of the static quenching by a CH_3CN solvent molecule and of the ISC to the doublet manifold (Fig. 4a). With the above interpretations resulting from the TA spectra, the ISC process is rather slow in this Mn^{4+} complex. Still, only static quenching by the solvent accounts for the excited state reactivity of the $^4\text{LMCT}$ state. Hole transfer gives the acetonitrile radical cation and the low-spin manganese(III) complex ($^3\text{T}_1$, Fig. 4b). The latter is only weakly distorted compared to the manganese(IV) complex suggesting only a small kinetic barrier to hole transfer. The low-spin complex can then undergo spin-crossover (SCO) to the thermodynamically favored high-spin complex (^5E , Fig. 4b).⁵⁴ The here suggested oxidation of the solvent as initial photoredox step likely also occurs with other extremely strong photooxidants (which short excited state lifetimes) such as the electrochemically generated trisaminocyclopropenium radical dication in CH_3CN .^{40,41} Yet, this static quenching scenario of short-lived strongly oxidizing excited states by the solvent had not been considered so far.

The $^2\text{LMCT}/^2\text{MC}$ excited state resulting from ISC and vibrational relaxation is at lower energy by 0.60 V (Fig. 4a). Hypothetically pure ^2MC excited doublet states ($^2\text{E}/^2\text{T}_1$ spin-flip states) neglecting charge-transfer admixtures as assigned in the reported carbene manganese(IV) complex $[\text{Mn}(\text{phtmeimb})_2]^{2+}$ ⁵⁹ are expected around 572 and 540 nm for $[\text{Mn}(\text{dgp})_2]^{4+}$ according to CASSCF/NEVPT2 calculations comprising only the d orbitals.⁵⁴ Clearly, these putative pure spin-flip states are too high in energy to be the lowest energy doublet states in $[\text{Mn}(\text{dgp})_2]^{4+}$ but these spin-flip states can obviously mix with the $^2\text{LMCT}$ state. Hole transfer from the mixed $^2\text{LMCT}/^2\text{MC}$ state to a naphthalene substrate was modelled by DFT calculations generating the manganese(III) complex and the substrate radical cation (Figs. 3b, 4a). Spin conservation requests that the $\text{d}^4 \text{Mn}^{\text{III}}$ complex forms in its low-spin state ($S_{\text{Mn}} = 1$, $^3\text{T}_1$) with the radical cation spin ($S_{\text{radical}} = 1/2$) antiferromagnetically coupled to give a spin-correlated pair with $S_{\text{total}} = 1/2$ (Fig. 3b). The Mn–N bond lengths increase only slightly from 1.95 – 1.98 Å in the $^2\text{LMCT}/^2\text{MC}$ state to 2.00 Å in the highly symmetric low-spin $[\text{Mn}(\text{dgp})_2]^{3+}$ complex. This small elongation suggests only a minor reorganization energy stemming from the photooxidant for the hole transfer reaction. The initially formed low-spin manganese(III) complex finally undergoes SCO to yield the high-spin complex with $S_{\text{Mn}} = 2$ (^5E , Fig. 3c, 4b). The Mn–N(pyridine) bonds are significantly elongated to 2.20 Å in the high-spin configuration, and hence a larger structural reorganization likely occurs in the SCO step only after the actual hole transfer.

Conclusions

The high-valent manganese(IV) complex $[\text{Mn}(\text{dgp})_2]^{4+}$ constitutes the prototype of a new class of extremely potent outer-sphere photooxidants. The panchromatic absorption, the high ground state redox potential, the small reorganization energy of the $[\text{Mn}(\text{dgp})_2]^{4+}$ /low-spin $[\text{Mn}(\text{dgp})_2]^{3+}$ couple and the unique dual excited state reactivity of a 3d transition metal complex resulting from static quenching of a short-lived highly oxidizing $^4\text{LMCT}$ state and from dynamic quenching of a long-lived luminescent strongly oxidizing $^2\text{LMCT}/^2\text{MC}$ state allow for oxidations including challenging substrates such as nitriles and benzene, using low-energy red to near-infrared light (730 nm, 850 nm). The novel key aspects of this unique system are the exploitation of the earth-abundant, non-noble metal manganese instead of precious metals such as iridium, the usage of red to near-infrared light instead

of the typically used UV to green light for oxidative transformations, the minimal dissipative energy loss and the resulting extremely high excited state redox potential sufficient for solvent oxidation as the primary hole transfer step. Future studies will explore adapted and tuned Mn^{4+}/Mn^{3+} couples as photo(electro)catalysts in challenging transformations e.g. via ion pairing and as sensitizers for suitable p-type semiconductors close to the thermodynamic and kinetic limits.

Online content

Any methods, additional references, Nature Research reporting summaries, source data, extended data, supplementary information, acknowledgements, peer review information; and competing interests; and statements of data and code availability are available at xx.

Author contributions

N.R.E. performed the syntheses, the reactivity studies, the photolysis experiments and the computational studies. R.N. performed and analyzed the luminescence and ultrafast time-resolved experiments and provided data interpretation. C.F. performed and assisted with the computational studies. C.R. assisted with the time-resolved experiments. G.D. performed and analyzed the molecular dynamics simulations. K.H. conceptualized the research, conceived the experiments and performed data analyses and interpretation. All authors co-wrote the manuscript.

Conflict of interest

The authors declare no conflict of interest.

Methods

See the Supplementary Information for full details of the methods employed.

Data Availability

All data generated or analyzed during this study are included in this published article or its Supplementary Information files, which include Cartesian coordinates of DFT optimized geometries, photolyses under various conditions (light sources, substrates), luminescence and transient absorption spectroscopic data, conductivity data.

Acknowledgements

This work was supported by the Max Planck Graduate Center with the Johannes Gutenberg University Mainz (MPGC). N.R.E. is a recipient of a position through the DFG Excellence Initiative by the Graduate School Materials Science in Mainz (GSC 266). This work was further supported by the Deutsche Forschungsgemeinschaft through grant INST 247/1018-1 FUGG to KH. Parts of this research were conducted using the supercomputer Mogon and advisory services offered by Johannes Gutenberg University Mainz (<http://www.hpc.uni-mainz.de>) and the supercomputer Elwetritsch and advisory services offered by the Rheinland-Pfälzische Technische Universität Kaiserslautern-Landau (<https://hpc.rz.rptu.de>), which are members of the AHRP and the Gauss Alliance e.V.. We thank Dimitri Zorn for performing the HPLC analyses.

References

1. Prier, C. K., Rankic, D. A. & MacMillan, D. W. C. Visible light photoredox catalysis with transition metal complexes: applications in organic synthesis. *Chem. Rev.* **113**, 5322–5363 (2013).
2. Romero, N. A. & Nicewicz, D. A. Organic Photoredox Catalysis. *Chem. Rev.* **116**, 10075–10166 (2016).

-
- Liu, Y. Z., Persson, P., Sundström, V. & Wärnmark, K. Fe N-heterocyclic carbene complexes as promising photosensitizers. *Acc. Chem. Res.* **49**, 1477–1485 (2016).
 - Larsen, C. B. & Wenger, O. S. Photoredox catalysis with metal complexes made from earth-abundant elements. *Chem. Eur. J.* **24**, 2039–2058 (2018).
 - Wenger, O. S. Photoactive complexes with earth-abundant metals. *J. Am. Chem. Soc.* **140**, 13522–13533 (2018).
 - Otto, S., Dorn, M., Förster, C., Bauer, M., Seitz, M. & Heinze, K. Understanding and Exploiting Long-lived Near-infrared Emission of a Molecular Ruby. *Coord. Chem. Rev.* **359**, 102–111 (2018).
 - Förster, C. & Heinze, K. Photophysics and photochemistry with Earth-abundant metals – fundamentals and concepts. *Chem. Soc. Rev.* **49**, 1057–1070 (2020).
 - Dierks, P., Vukadinovic, Y. & Bauer, M. Photoactive iron complexes: more sustainable, but still a challenge. *Inorg. Chem. Front.* **9**, 206–220 (2022).
 - Kitzmann, W. R., Ramanan, C., Naumann, R. & Heinze, K. Molecular Ruby: Exploring the Excited State Landscape. *Dalton Trans.* **51**, 6519–6525 (2022).
 - Kitzmann, W. R., Moll, J. & Heinze, K. Spin-Flip Luminescence. *Photochem. Photobiol. Sci.* **21**, 1309–1331 (2022).
 - Sinha, N. & Wenger, O. S. Photoactive Metal-to-Ligand Charge Transfer Excited States in $3d^6$ Complexes with Cr^0 , Mn^I , Fe^{II} , and Co^{III} . *J. Am. Chem. Soc.* **45**, in press (2023). DOI: 10.1021/jacs.2c13432.
 - Sharma, N., Jung, J., Ohkubo, K., Lee, Y.-M., El-Khouly, M. E., Nam, W. & Fukuzumi, S. Long-Lived Photoexcited State of a Mn(IV)-Oxo Complex Binding Scandium Ions That is Capable of Hydroxylating Benzene. *J. Am. Chem. Soc.* **140**, 8405–8409 (2018).
 - Tzirakis, M. D., Lykakis, I. N. & Orfanopoulos, Decatungstate as an efficient photocatalyst in organic chemistry. *Chem. Soc. Rev.* **38**, 2609–2621 (2009).
 - Yu, D., To, W.-P., Tong, G. S. M., Wu, L.-L., Chan, K.-T., Du, L., Phillips, D. L., Liu, Y. & Che, C.-M. Luminescent tungsten(VI) complexes as photocatalysts for light-driven C–C and C–B bond formation reactions. *Chem. Sci.* **11**, 6370–6382 (2020).
 - Zhang, K., Chang, L., An, Q., Wang, X. & Zuo, Z. Dehydroxymethylation of Alcohols Enabled by Cerium Photocatalysis. *J. Am. Chem. Soc.* **141**, 26, 10556–10564 (2019).
 - Yang, Q., Wang, Y.-H., Qiao, Y., Gau, M., Carroll, P. J., Walsh, P. J. & Schelter, E. J. Photocatalytic C–H activation and the subtle role of chlorine radical complexation in reactivity. *Science* **372**, 847–852 (2021).
 - Yatham, V. R., Bellotti, P. & König, B. Decarboxylative hydrazination of unactivated carboxylic acids by cerium photocatalysis. *Chem. Commun.* **55**, 3489–3492 (2019).
 - West, J. G., Bedell, T. A. & Sorensen, E. J. The Uranyl Cation as a Visible-Light Photocatalyst for $C(sp^3)$ –H Fluorination. *Angew. Chem. Int. Ed.* **55**, 8923–8927 (2016).
 - Abderrazak, Y., Bhattacharyya, A. & Reiser, O. Visible-Light-Induced Homolysis of Earth-Abundant Metal-Substrate Complexes: A Complementary Activation Strategy in Photoredox Catalysis. *Angew. Chem. Int. Ed.* **60**, 21100–21115 (2021).
 - Zhang, Y., Petersen, J. L. & Milsman, C. A Luminescent Zirconium(IV) Complex as a Molecular Photosensitizer for Visible Light Photoredox Catalysis. *J. Am. Chem. Soc.* **138**, 13115–13118 (2016).
 - Zhang, Y., Lee, T. S., Petersen, J. L. & Milsman, C. A zirconium photosensitizer with a long-lived excited state: mechanistic insight into photoinduced single-electron transfer. *J. Am. Chem. Soc.* **140**, 5934–5947 (2018).
 - Pal, A. K., Li, C., Hanan, G. S. & Zysman-Colman, E. Blue-Emissive Cobalt(III) Complexes and Their Use in the Photocatalytic Trifluoromethylation of Polycyclic Aromatic Hydrocarbons. *Angew. Chem. Int. Ed.* **57**, 8027–8031 (2018).

-
23. Chábera, P. et al. A low-spin Fe(III) complex with 100-ps ligand-to-metal charge transfer photoluminescence. *Nature* **543**, 695–699 (2017).
 24. Kjær, K. S. et al. Luminescence and reactivity of a charge-transfer excited iron complex with nanosecond lifetime. *Science* **363**, 249–253 (2019).
 25. Rosemann, N. W., Chábera, P., Prakash, O., Kaufhold, S., Wärnmark, K., Yartsev, A. & Persson, P. Tracing the Full Bimolecular Photocycle of Iron(III)–Carbene Light Harvesters in Electron-Donating Solvents. *J. Am. Chem. Soc.* **142**, 8565–8569 (2020).
 26. Aydogan, A., Bangle, R. E., Cadranel, A., Turlington, M. D., Conroy, D. T., Cauët, E., Singleton, M. L., Meyer, G. J., Sampaio, R. N., Elias, B. & Troian-Gautier, L. Accessing Photoredox Transformations with an Iron(III) Photosensitizer and Green Light. *J. Am. Chem. Soc.* **143**, 15661–15673 (2021).
 27. Steube, J., Kruse, A., Bokareva, O. S., Reuter, T., Demeshko, S., Schoch, R., Cordereo, M. A. A., Krishna, A., Hohloch, S., Meyer, F., Heinze, K., Kühn, O., Lochbrunner, S. & Bauer, M. Janus-type emission of a Cyclometalated Iron(III) complex. *Nat. Chem.* (2023). DOI: 10.1038/s41557-023-01137-w.
 28. Stevenson, S. M., Shores, M. P. & Ferreira, E. M. Photooxidizing Chromium Catalysts for Promoting Radical Cation Cycloadditions. *Angew. Chem. Int. Ed.* **54**, 6506–6510 (2015).
 29. Sittel, S., Naumann, R. & Heinze, K. Molecular Rubies in Photoredox Catalysis. *Front. Chem.* **10**, 887439 (2022).
 30. Bürgin, T. H., Glaser, F. & Wenger, O. S. Shedding Light on the Oxidizing Properties of Spin-Flip Excited States in a Cr^{III} Polypyridine Complex and Their Use in Photoredox Catalysis. *J. Am. Chem. Soc.* **144**, 14181–14194 (2022).
 31. Sittel, S., Sell, A. C., Hofman, K., Wiedemann, C., Nau, J. P., Kerzig, C., Manolikakes, G. & Heinze, K. Visible-Light Induced Fixation of SO₂ into Organic Molecules with Polypyridine Chromium(III) Complexes. *Chem. Cat. Chem.* in press (2023). DOI: 10.1002/cctc.202201562.
 32. Li, C., Kong, X. Y., Tan, Z. H., Yang, C. T. & Soo, H. S. Emergence of ligand-to-metal charge transfer in homogeneous photocatalysis and photosensitization. *Chem. Phys. Rev.* **3**, 021303 (2022).
 33. Förster, C. & Heinze, K. Bimolecular Reactivity of 3d Metal-Centered Excited States (Cr, Mn, Fe, Co). *Chem. Phys. Rev.* **3**, 041302 (2022).
 34. Connelly, N. G. & Geiger, W. E. Chemical Redox Agents for Organometallic Chemistry. *Chem. Rev.* **96**, 877–910 (1996).
 35. Kim, D. & Teets, T. S. Strategies for accessing photosensitizers with extreme redox potentials. *Chem. Phys. Rev.* **3**, 021302 (2022).
 36. Choi, G. J., Zhu, Q., Miller, D. C., Gu, C. J. & Knowles, R. R. *Nature* **539**, 268 (2016).
 37. Tlili, A. & Lakhdar, S. Acridinium Salts and Cyanoarenes as Powerful Photocatalysts: Opportunities in Organic Synthesis. *Angew. Chem. Int. Ed.* **60**, 19526–19549 (2021).
 38. Natarajan, P. & König, B. Excited-State 2,3-Dichloro-5,6-dicyano-1,4-benzoquinone (DDQ*) Initiated Organic Synthetic Transformations under Visible-Light Irradiation. *Eur. J. Org. Chem.* 2145–2161 (2021).
 39. Huang, H. & Lambert, T. H. Electrophotocatalytic S_NAr Reactions of Unactivated Aryl Fluorides at Ambient Temperature and Without Base. *Angew. Chem. Int. Ed.* **59**, 658–662 (2020).
 40. Huang, H., Strater, Z. M., Rauch, M., Shee, J., Sisto, T. J., Nuckolls, C. & Lambert, T. H. Electrophotocatalysis with a Trisaminocyclopropenium Radical Dication. *Angew. Chem. Int. Ed.* **58**, 13318–13322 (2019).
 41. Huang, H. & Lambert, T. H. Electrophotocatalytic Acetoxyhydroxylation of Aryl Olefins. *J. Am. Chem. Soc.* **143**, 7247–7252 (2021).

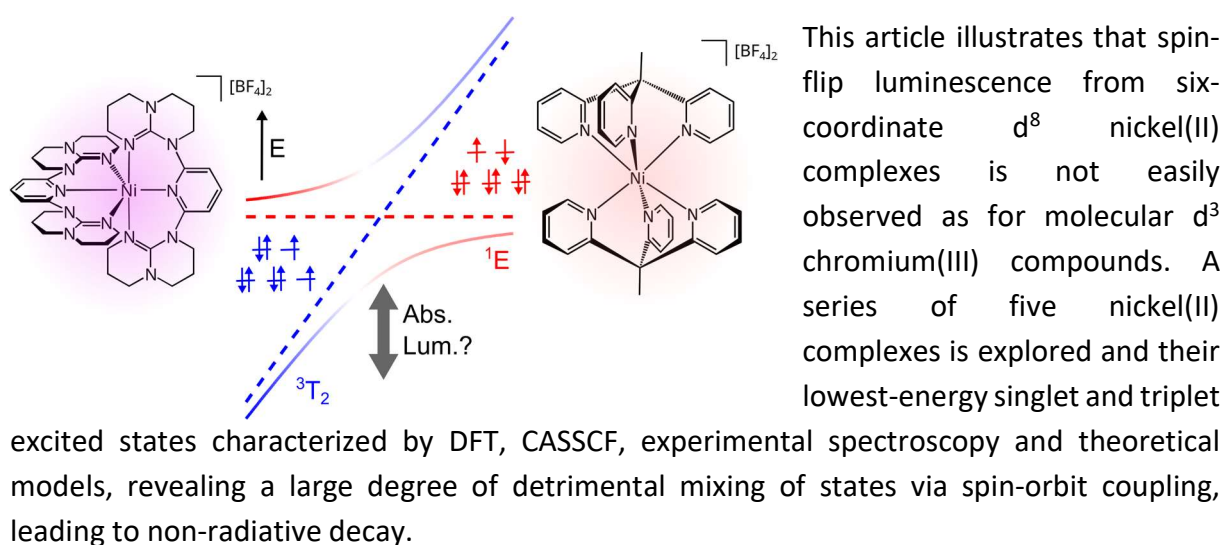
-
42. Cotic, A., Cerfontaine, S., Slep, L. D., Elias, B., Troian-Gautier, L. & Cadranel, A. Anti-Dissipative Strategies toward More Efficient Solar Energy Conversion. *J. Am. Chem. Soc.* (2023). DOI: 10.1021/jacs.2c11593.
43. Penfold, T. J., Gindensperger, E., Daniel, C. & Marian, C. M. Spin-Vibronic Mechanism for Intersystem Crossing. *Chem. Rev.* **118**, 6975–7025 (2018).
44. Auböck, G. & Chergui, M. Sub-50-fs photoinduced spin crossover in Fe(bpy)₃²⁺. *Nat. Chem.* **7**, 629–633 (2015).
45. Juban, E. A. & McCusker, J. K. Ultrafast Dynamics of ²E State Formation in Cr(acac)₃. *J. Am. Chem. Soc.* **127**, 6857–6865 (2005).
46. Wang, C., Reichenauer, F., Kitzmann, W. R., Kerzig, C., Heinze, K., Resch-Genger, U. Efficient Triplet-Triplet Annihilation Upconversion Sensitized by a Chromium(III) Complex via an Underexplored Energy Transfer Mechanism. *Angew. Chem. Int. Ed.* **61**, e202202238 (2022).
47. Dose, E.V., Hoselton, M. A., Sutin, N., Tweedle, M. F. & Wilson, L. J. Dynamics of Intersystem Crossing Processes in Solution for Six-Coordinate d⁵, d⁶, and d⁷ Spin-Equilibrium Metal Complexes of Iron(III), Iron(II), and Cobalt(II). *J. Am. Chem. Soc.* **100**, 1141–1147 (1978).
48. Siddique, Z. A., Yamamoto, Y., Ohno, T. & Nozaki, K. Structure-Dependent Photophysical Properties of Singlet and Triplet Metal-to-Ligand Charge Transfer States in Copper(I) Bis(diimine) Compounds. *Inorg. Chem.* **42**, 6366–6378 (2003).
49. Iwamura, M., Takeuchi, S. & Tahara, T. Real-Time Observation of the Photoinduced Structural Change of Bis(2,9-dimethyl-1,10-phenanthroline)copper(I) by Femtosecond Fluorescence Spectroscopy: A Realistic Potential Curve of the Jahn-Teller Distortion. *J. Am. Chem. Soc.* **129**, 5248–5256 (2007).
50. Shaw, G. B., Grant, C. D., Shirota, H., Castner Jr., E. W., Meyer, G. J. & Chen, L. X. Ultrafast Structural Rearrangements in the MLCT Excited State for Copper(I) bis-Phenanthrolines in Solution. *J. Am. Chem. Soc.* **129**, 2147–2160 (2007).
51. Gonçalves, P.J. De Boni, L., Borissevitch, I. E. & Zílio, S. C. Excited State Dynamics of meso-Tetra(sulphonatophenyl) Metalloporphyrins. *J. Phys. Chem. A* **112**, 6522–6526 (2008).
52. Dorn, M., Kalmbach, J., Boden, P., Pöpcke, A., Gómez, S., Förster, C., Kuczelinis, F., Carrella, L. M., Büldt, L., Bings, N., Rentschler, E., Lochbrunner, S., González, L., Gerhards, M., Seitz, M., & Heinze, K. A vanadium(III) complex with blue and NIR-II spin-flip luminescence in solution. *J. Am. Chem. Soc.* **142**, 7947–7955 (2020).
53. Antolini, C., Spellman, Jr., C. D., Otolski, C. J., Doumy, G., March, A. M., Walko, D. A., Liu, C., Zhang, X., Young, B. T., Goodwill, J. E. & Hayes, D. Photochemical and Photophysical Dynamics of the Aqueous Ferrate(VI) Ion. *J. Am. Chem. Soc.* **144**, 22514–22527 (2022).
54. East, N. R., Förster, C., Carrella, L. M., Rentschler, E. & Heinze, K. The full d³–d⁵ Redox Series of Mononuclear Manganese Complexes: Geometries and Electronic Structures of [Mn(dgpy)₂]^{nt}. *Inorg. Chem.* **61**, 14616–14625 (2022).
55. A. F. Holleman, F. Wiberg, Lehrbuch der anorganischen Chemie, 101. Ed., Walter de Gruyter Verlag, Berlin, New York, 1995
56. Troian-Gautier, L., Turlington, M. D., Wehlin, S. A. M., Maurer, A. B., Brady, M. D., Swords, W. D. & Meyer, G. J. Halide Photoredox Chemistry. *Chem. Rev.* **119**, 4628–4683 (2019).
57. Ward, W. M., Farnum, B. H., Siegler, M. & Meyer, G. J. Chloride Ion-Pairing with Ru(II) Polypyridyl Compounds in Dichloromethane. *J. Phys. Chem. A* **117**, 8883–8894 (2013).
58. Li, P., Deetz, A. M., Hu, J., Meyer, G. J. & Hu, K. Chloride Oxidation by One- or Two-Photon Excitation of N-Phenylphenothiazine. *J. Am. Chem. Soc.* **144**, 17604–17610 (2022).
59. Harris, J. P.; Reber, C.; Colmer, H. E.; Jackson, T. A.; Forshaw, A. P.; Smith, J. M.; Kinney, R. A. & Telser, J. Near-infrared ²E_g - ⁴A_g and visible LMCT luminescence from a molecular bis-(tris(carbene)borate) manganese(IV) complex. *Can. J. Chem.* **95**, 547–552 (2017).

-
60. Reichenauer, F., Wang, C., Förster, C., Boden, P., Ugur, N., Báez-Cruz, R., Kalmbach, J., Carrella, L. M., Rentschler, E., Ramanan, C., Niedner-Schatteburg, G., Gerhards, M., Seitz, M., Resch-Genger, U. & Heinze, K. Strongly Red-Emissive Molecular Ruby [Cr(bpmp)₂]³⁺ surpasses [Ru(bpy)₃]²⁺. *J. Am. Chem. Soc.* **143**, 11843–11855 (2021).
61. Otto, S., Grabolle, M., Förster, C., Kreitner, C., Resch-Genger, U. & Heinze, K. [Cr(ddpd)₂]³⁺: a molecular, water-soluble, highly NIR-emissive ruby analogue. *Angew. Chem. Int. Ed.* **54**, 11572–11576 (2015).
62. Fundamentals and Applications of Organic Electrochemistry (Eds. Fuchigami, T., Inagi, S., Atobe, M.), John Wiley & Sons, Ltd, 2015, Appendix B.
63. Romero, N. A., Margrey, K. A., Tay, N. E. & Nicewicz, D. A. Site-selective arene C-H amination via photoredox catalysis. *Science* 2015, **349**, 1326–1330.
64. Pistritto, V. A., Liu, S. & Nicewicz, D. A. Mechanistic Investigations into Amination of Unactivated Arenes via Cation Radical Accelerated Nucleophilic Aromatic Substitution. *J. Am. Chem. Soc.* **144**, 15118–15131 (2022).
65. Foley, J. K., Korzeniewski, C. & Pons, S. Anodic and cathodic reactions in acetonitrile/tetra-n-butylammonium tetrafluoroborate: an electrochemical and infrared spectroelectrochemical study. *Can. J. Chem.* **66**, 201–206 (1988).
66. Hammerich, O. & Parker, V. D. Reaction of the Anthracene Cation Radical with Acetonitrile. A Novel Anodic Acetamidation. *J. Chem. Soc., Chem. Commun.* 245–246, (1974).
67. Shen, T. & Lambert, T. H. C–H Amination via Electrophotocatalytic Ritter-type Reaction. *J. Am. Chem. Soc.* **143**, 8597–8602 (2021).
68. Geary, W. J. The use of conductivity measurements in organic solvents for the characterisation of coordination compounds. *Coord. Chem. Rev.* **7**, 81–122 (1971).
69. Basu, U., Otto, S., Heinze, K. & Gasser, G. Biological Evaluation of the NIR-Emissive Ruby Analogue [Cr(ddpd)₂][BF₄]₃ as a Photodynamic Therapy Photosensitizer. *Eur. J. Inorg. Chem.* 37–41 (2019).
70. Kavarnos, G. J. & Turro, N. Photosensitization by Reversible Electron Transfer: Theories, Experimental Evidence, and Examples. *Chem. Rev.* **86**, 401–449 (1986).

3.3 Coupled Potential Energy Surfaces Strongly Impact the Lowest-Energy Spin-Flip Transition in Six-Coordinate Nickel(II) Complexes

Nathan R. East, Chahinez dab, Christoph Förster, Katja Heinze and Christian Reber.

Inorg. Chem. **2023**, [DOI: 10.1021/acs.inorgchem.3c00779] (accepted)



Author contributions

N. R. East performed synthesis and characterization of the title compounds, along with DFT studies, CASSCF calculations and optical studies. Dr. Chahinez Dab (group of Prof. Dr. Christian Reber) measured all Raman and luminescence spectra on crystalline samples at variable temperature and pressure and analyzed the spectroscopic results. All crystal structures were solved and refined by Dr. Christoph Förster. The manuscript and supplementary information were written by Prof. Dr. Christian Reber, Prof. Dr. Katja Heinze and N. R. East.

Supporting Information

Found on page 165

“N. R. East, C. Dab, C. Förster, K. Heinze, C. Reber, *Inorg. Chem.* **2022**, [DOI: 10.1021/acs.inorgchem.3c00779]

Copyright 2022 American Chemical Society. Reproduced with permission”

Coupled Potential Energy Surfaces Strongly Impact the Lowest-Energy Spin-Flip Transition in Six-Coordinate Nickel(II) Complexes

Nathan R. East, Chahinez Dab, Christoph Förster, Katja Heinze,* and Christian Reber*

Cite This: <https://doi.org/10.1021/acs.inorgchem.3c00779>

Read Online

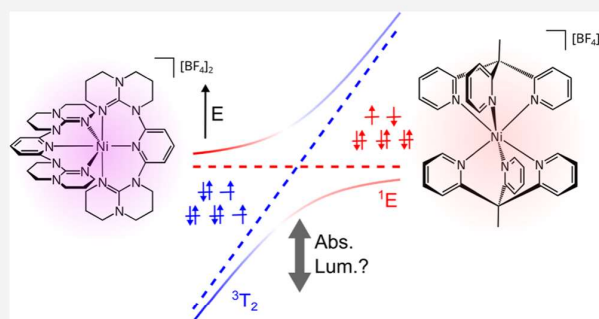
ACCESS |

Metrics & More

Article Recommendations

Supporting Information

ABSTRACT: Luminescent complexes of earth-abundant first-row transition metals are of renewed, broad interest due to their spectroscopic and photochemical properties as well as emerging applications. New strong-field polypyridine ligands have led to six-coordinate $3d^3$ chromium(III) complexes with intense spin-flip luminescence in solution at room temperature. The ground and emissive states both arise from the $(t_2)^3$ electron configuration involving the d_π levels (O point group symmetry labels). Pseudooctahedral $3d^8$ nickel(II) complexes with such strong ligands are *a priori* also promising candidates for spin-flip luminescence. In contrast, the relevant electron configurations involve the d_σ orbitals and $(e)^2$ configurations. We have prepared the known nickel(II) complexes $[\text{Ni}(\text{terpy})_2]^{2+}$, $[\text{Ni}(\text{phen})_3]^{2+}$, and $[\text{Ni}(\text{ddpd})_2]^{2+}$ as well as the novel complexes $[\text{Ni}(\text{dgpy})_2]^{2+}$ and $[\text{Ni}(\text{tpe})_2]^{2+}$ forming a series with increasing ligand field strengths (terpy = 2,2':6',2''-terpyridine; phen = 1,10-phenanthroline; ddpd = *N,N'*-dimethyl-*N,N'*-dipyridine-2-ylpyridine-2,6-diamine; dgpy = 2,6-diguanidylpyridine; tpe = 1,1,1-tris(pyrid-2-yl)ethane). The lowest-energy singlet and triplet excited states of these nickel(II) complexes are analyzed based on absorption spectra using ligand field theory and CASSCF-NEVPT2 calculations for vertical transition energies and a model based on coupled potential energy surfaces, leading to calculated absorption spectra in good agreement with the experimental data. No photoluminescence signal was observed in the wavelength ranges identified through the analyses of the absorption spectra. The models provide insight into key differences between the nickel(II) complexes and their strongly luminescent chromium(III) analogues.



INTRODUCTION

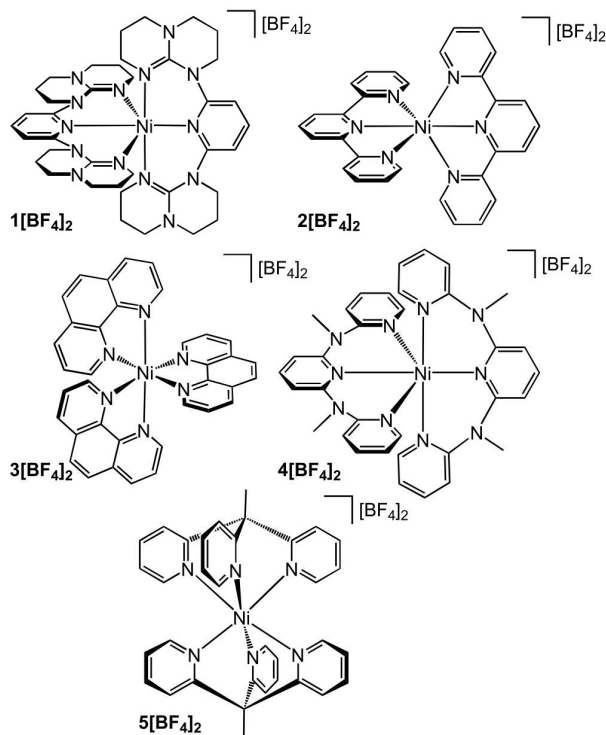
Long-lived excited states of complexes with earth-abundant metal centers are of renewed interest for a variety of photochemistry/material applications.^{1–7} Beyond the classical charge-transfer excited states of, for example, $[\text{Ru}(\text{bpy})_3]^{2+}$ and related complexes^{8,9}—including first complexes with $3d$ metal ions^{1–7}—photoactive spin-flip states are of particular interest.¹⁰ Mononuclear, six-coordinate complexes of d^2 vanadium(III),^{11,12} d^3 chromium(III),^{13–20} and d^3 manganese(IV)²¹ with long-lived photoluminescent states have been recently reported. Chemical and spectroscopic criteria leading to intense spin-flip luminescence of chromium(III) and vanadium(III)—a first for room temperature in solution—have been described in recent years, and the criteria guiding their design have been reviewed.^{22,23}

This report describes in detail the electronic situation and challenges for pseudooctahedral d^8 nickel(II) complexes of the same family, *a priori* an attractive target, due to the vast abundance and low toxicity of nickel and the rich variety of nickel(II) complexes. Luminescent nickel(II) complexes are, however, rare. Only a single square-planar cyclometallated carbazolato nickel(II) complex showing ligand-centered emission from triplet states has been reported recently.²⁴

The longest metal-to-ligand charge-transfer ($^3\text{MLCT}$) lifetimes of square-planar nickel(II) complexes up to 48 ps were achieved using cyclometallating, N-heterocyclic carbene and isonitrile ligands, while luminescence was not yet observed.²⁵ Weak, broad d–d emission for square-planar nickel(II) complexes has been reported,²⁶ yet, examples for luminescent spin-flip states comparable to those reported for Cr^{III} and V^{III} , presumably with long excited-state lifetimes, are unknown. We analyze a series of three known^{27–29} and two novel pseudooctahedral nickel(II) complexes with strong-field pyridine ligands (Chart 1) with respect to their excited-state landscape, namely, the order and mixing of relevant excited singlet (spin-flip) and triplet d–d states that arise from the $(t_2)^6(e)^2$ ground-state electron configuration.

Received: March 9, 2023

Chart 1. Schematic Structures of Nickel(II) Complexes
1[BF₄]₂, **2**[BF₄]₂, **3**[BF₄]₂, **4**[BF₄]₂, and **5**[BF₄]₂



All complexes feature six nitrogen ligand atoms (mostly pyridines), which induce strong ligand fields so that the lowest-energy spin-allowed and spin-forbidden d–d transitions are close in energy. We analyze absorption spectra in the region of these bands, which overlap in these systems, using three different types of theoretical models, namely, (i) ligand field theory, (ii) quantum chemical calculations (CASSCF-NEVPT2), and (iii) calculated absorption band profiles based on coupled potential energy curves,^{30,31} previously applied to absorption spectra of nickel(II) complexes.^{32–34} This approach provides insight into the properties of the two coupled excited states, in particular, regarding the possibility of spin-flip luminescence.

EXPERIMENTAL SECTION

General Procedures. All reactions and measurements were performed under an argon atmosphere unless otherwise noted. The ligands ddpd,³⁵ tpe,³⁶ and dgpy³⁷ and complexes [Ni(terpy)₂]²⁺,²⁷ [Ni(phen)₃]²⁺,²⁸ and [Ni(ddpd)₂]²⁺²⁹ were prepared according to slightly modified literature procedures. Gloveboxes (UniLab/MBraun—Ar 4.8, O₂ <1 ppm, H₂O <0.1 ppm) were used to store and weigh sensitive compounds for synthesis as well as to prepare any measurement sample that required the absence of oxygen and water. Acetonitrile and diethyl ether were dried from calcium hydride and sodium, respectively, and distilled prior to use. Dimethyl sulfoxide (DMSO) (>97%) was received from Sigma-Aldrich. The reagents were used as received from commercial suppliers (ABCR, Acros Organics, Alfa Aesar, Fischer Scientific, Fluka, and Sigma-Aldrich). Electrospray ionization mass spectra were recorded on an Agilent 6545 QTOF-MS spectrometer. ATR-IR spectra were recorded with a Bruker α II FT-IR spectrometer with a Platinum Di-ATR module inside an argon-filled glovebox. Elemental analyses were performed by the microanalytical laboratory of the Department of Chemistry of the University of Mainz using an Elementar vario EL Cube. Electro-

chemical experiments of **1**[BF₄]₂ and **5**[BF₄]₂ were carried out on a BioLogic SP-200 voltammetric analyzer using a platinum working electrode, a platinum wire as a counter electrode, and a Ag/AgCl wire (Ag wire immersed in 1 M HCl for 24 h and dried) as the reference electrode. The cyclic voltammetry experiments were carried out at a scan rate of 100 mV s⁻¹ using 0.1 M [ⁿBu₄N][PF₆] as the supporting electrolyte and 0.001 M of the sample in acetonitrile. Potentials are referenced relative to the ferrocene/ferrocenium couple. UV/Vis/NIR spectra were recorded on a Jasco V-770 spectrometer using 1.0 cm cells (Hellma, Suprasil). Emission spectra in frozen solution were recorded on a Varian Cary Eclipse spectrometer using an Oxford Instruments Optistat DN cryostat with cooling by liquid N₂. Raman spectra were measured with a Renishaw Via instrument equipped with a Linkam cryostat using cold nitrogen to cool the samples and a HPDO diamond anvil cell for measurements at variable pressure.

Intensity data for crystal structure determinations were collected with a STOE IPDS-2T diffractometer from STOE & CIE GmbH and an Oxford cooling system and corrected for absorption and other effects using Mo K α radiation ($\lambda = 0.71073$ Å). The diffraction frames were integrated using the STOE X-AREA³⁸ package, and most were corrected for absorption with MULABS³⁹ of the PLATON software package.⁴⁰ The structures were solved with SHELXT⁴¹ refined by the full-matrix method based on F^2 using SHELXL⁴² of the SHELX⁴³ software package and the ShelXle⁴⁴ graphical interface. All non-hydrogen atoms were refined anisotropically, while the positions of all hydrogen atoms were generated with appropriate geometric constraints and allowed to ride on their respective parent carbon atoms with fixed isotropic thermal parameters. Crystallographic data for the structures reported in this paper have been deposited with the Cambridge Crystallographic Data Centre as supplementary publication No. CCDC-2125075 for **1**[PF₆]₂ × CH₃CN and CCDC-2125074 for **5**[BF₄]₂ × 4CH₃CN. These data are provided free of charge by the Cambridge Crystallographic Data Centre.

Density Functional Theory Calculations. Density functional theory calculations on the nickel(II) complex cations (**1**²⁺–**5**²⁺) were carried out using the ORCA program package (version 4.1.1).⁴⁵ Tight convergence criteria were chosen for all calculations (keywords tightscf and tightopt). All calculations were performed using the B3LYP functional^{46–48} employing the RIJCOSX approximation.^{49,50} Relativistic effects were calculated at the zeroth order regular approximation (ZORA) level.⁵¹ The ZORA keyword automatically invokes relativistically adjusted basis sets. To account for solvent effects, a conductor-like screening model (CPCM) modeling acetonitrile was used in all calculations.⁵² Geometry optimizations were performed using Ahlrichs' polarized valence triple- ζ basis set (def2-TZVPP).^{53,54} Atom-pairwise dispersion correction was performed with the Becke-Johnson damping scheme (D3BJ). The energy of the electronic states and presence of energy minima were checked by numerical frequency calculations. Explicit counterions and/or solvent molecules were not taken into account.

SOC-CASSCF(12,7)-SC-NEVPT2. Calculations of ground- and excited-state properties with respect to metal-centered (MC) states for complex cations (**1**²⁺–**5**²⁺) were performed using the complete-active-space self-consistent field method in conjunction with the strongly contracted N-electron valence perturbation theory to second order (SC-NEVPT2)^{55,56} in order to recover missing dynamic electron correlation. In order to accurately model the ligand field, active spaces were chosen to encompass the dominant bonding/antibonding orbitals formed between nickel and the ligands. An active space of (12,7), along with 10 triplet roots and 15 singlet roots, was selected. An *ab initio* ligand field theory (AILFT)^{57,58} analysis was performed from CASSCF(8,5)-NEVPT results with 10 triplet and 15 singlet roots (keyword actorbbs dorbs).

Synthesis of **1[BF₄]₂.** A solution of 218 mg (0.616 mmol, 2.1 equiv) of dgpy in dry DMSO (5 mL) was added to a solution of 100 mg (0.294 mmol, 1.0 equiv) of Ni[BF₄]₂ × 6H₂O in dry DMSO (5 mL) under an inert atmosphere. The solution turned purple and was stirred at ambient temperature for 24 h. The DMSO was removed at 50 °C under reduced pressure, leaving a purple powder, which was purified by crystallization via slow diffusion of dry diethyl ether into a

concentrated solution in acetonitrile to yield 160 mg (0.170 mmol, 58%) of $1[\text{BF}_4]_2$ as purple crystals. Elem. anal. calcd. (%) for $\text{C}_{38}\text{H}_{54}\text{B}_2\text{NiF}_8\text{N}_{14}$ (939.25): C 48.59 H 5.80, N 20.88; found C 48.48, H 5.75 N 20.73. MS (ESI⁺, CH_3CN): m/z (%) = 382.20 (98, $[\text{Ni}(\text{dgp})_2]^{2+}$), 851.40 (100, $[\text{Ni}(\text{dgp})_2 + \text{BF}_4]^+$), 354.24 (84, $[\text{dgp} + \text{H}]^+$). IR (ATR): $\tilde{\nu}/\text{cm}^{-1}$ = 2950 (vw), 2865 (vw), 1617 (s), 1585 (s), 1500 (m), 1435 (s), 1365 (m), 1330 (w), 1310 (w, sh), 1200 (s), 1097 (m, sh), 1053 (s), 906 (w), 802 (s), 728 (w), 603 (sw), 550 (w), 516 (w). UV/Vis/NIR (CH_3CN): $\lambda_{\text{max}}/\text{nm}$ ($\epsilon/\text{M}^{-1}\text{cm}^{-1}$) = 540 (16.2), 793 (12.1), 834 (12.0). CV (CH_3CN , 0.1 M [ⁿBu₄N][PF₆], vs ferrocene): $E_{1/2}/\text{V}$ = + 0.39 V (rev.).

Synthesis of $1[\text{PF}_6]_2$ for Single-Crystal X-ray Diffraction (XRD) Analysis. A solution of 412 mg of [ⁿBu₄N][PF₆] (1.06 mmol, 10 equiv) in dry CH_3CN (1 mL) was added to 100 mg of $1[\text{BF}_4]_2$. Crystallization via slow diffusion of dry diethyl ether into this solution gave purple crystals of $1[\text{PF}_6]_2$, suitable for single-crystal XRD analysis.

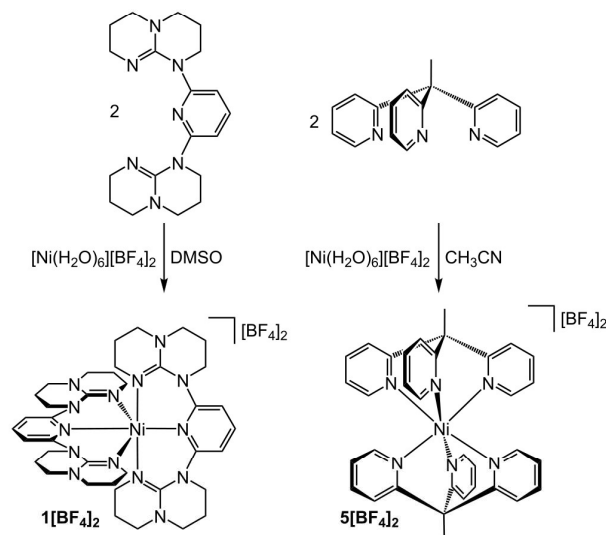
Synthesis of $5[\text{BF}_4]_2$. A solution of 540 mg (2.06 mmol, 2.0 equiv) of tpe in dry CH_3CN (5 mL) was added to a solution of 352 mg (1.034 mmol, 1.0 equiv) of $\text{Ni}[\text{BF}_4]_2 \times 6\text{H}_2\text{O}$ in dry CH_3CN (5 mL). The solution turned light red and was stirred at ambient temperature for 24 h. The CH_3CN was removed at ambient temperature under reduced pressure, leaving a light red powder, which was purified by crystallization via slow diffusion of dry diethyl ether into a concentrated solution in acetonitrile to yield 420 mg (0.556 mmol, 54%) of $5[\text{BF}_4]_2$ as clear, nearly colorless crystals. Elem. anal. calcd. (%) for $\text{C}_{38}\text{H}_{54}\text{B}_2\text{NiF}_8\text{N}_{14}$ (939.25): C 54.09 H 4.01, N 11.13; found C 53.89, H 3.96 N 11.12. MS (ESI⁺, CH_3CN): m/z (%) = 290.09 (74, $[\text{Ni}(\text{tpe})_2]^{2+}$), 667.19 (100, $[\text{Ni}(\text{tpe})_2 + \text{BF}_4]^+$). IR (ATR): $\tilde{\nu}/\text{cm}^{-1}$ = 2961 (vw), 1593 (w), 1470 (m), 1430 (w), 1370 (w), 1291 (vw), 1274 (vw), 1170 (vw), 1040 (s), 846 (w), 780 (w, sh), 750 (m), 652 (vw, sh), 560 (w), 515 (m). UV/Vis/NIR (CH_3CN): $\lambda_{\text{max}}/\text{nm}$ ($\epsilon/\text{M}^{-1}\text{cm}^{-1}$) = 473 (7.3), 531 (5.2), 747 (6.2), 862 (2.1). CV (CH_3CN , 0.1 M [ⁿBu₄N][PF₆], vs ferrocene): $E_{1/2}/\text{V}$ = -2.31 V (irrev.), -1.92 V (irrev.).

RESULTS AND DISCUSSION

Syntheses and Characterization of Nickel(II) Complexes. The complexes $[\text{Ni}(\text{terpy})_2]^{2+}$ 2^{2+} , $[\text{Ni}(\text{phen})_3]^{2+}$ 3^{2+} , and $[\text{Ni}(\text{ddpd})_2]^{2+}$ 4^{2+} were prepared according to the literature procedures (terpy = 2,2':6',2''-terpyridine; phen = 1,10-phenanthroline; ddpd = *N,N'*-dimethyl-*N,N'*-dipyridine-2-ylpyridine-2,6-diamine).^{27–29} The dgpy complex $1[\text{BF}_4]_2$ was obtained by adding a stoichiometric amount of dgpy to $\text{Ni}[\text{BF}_4]_2 \times 6\text{H}_2\text{O}$ in dimethyl sulfoxide (Scheme 1) and recrystallization from acetonitrile/diethyl ether as purple crystals of $1[\text{BF}_4]_2$ (dgpy = 2,6-diguanyldipyridine; Experimental Section). Its IR spectrum shows bands for vibrations of the $[\text{BF}_4]^-$ counterion around 1053 cm^{-1} , and the ESI⁺ mass spectrum confirms the composition of the cation showing peaks for the dication $[\text{Ni}(\text{dgp})_2]^{2+}$ at m/z = 382.20 and for $[\text{Ni}(\text{dgp})_2 + \text{BF}_4]^+$ at m/z = 851.40 (Supporting Information, Figures S1 and S2). Anion exchange from $[\text{BF}_4]^-$ to $[\text{PF}_6]^-$ was achieved via crystallization with [ⁿBu₄N][PF₆] in CH_3CN giving crystals of $1[\text{PF}_6]_2$ suitable for XRD analysis.

An analogous procedure was used for the synthesis of $5[\text{BF}_4]_2$ employing a stoichiometric amount of tpe in CH_3CN (tpe = 1,1,1-tris(pyrid-2-yl)ethane; Scheme 1). Recrystallization from acetonitrile/diethyl ether gave pink crystals of $5[\text{BF}_4]_2$ suitable for XRD analysis (Experimental Section). IR spectroscopy shows bands of $[\text{BF}_4]^-$ vibrations around 1040 cm^{-1} , and ESI⁺ mass spectrometry reveals peaks for the dication $[\text{Ni}(\text{tpe})_2]^{2+}$ and the ion pair $[\text{Ni}(\text{tpe})_2 + \text{BF}_4]^+$ at m/z = 290.09 and m/z = 667.19, respectively (Supporting Information, Figures S3 and S4).

Scheme 1. Syntheses of Nickel(II) Complexes $1[\text{BF}_4]_2$ and $5[\text{BF}_4]_2$



A $\text{CH}_3\text{CN}/[\text{Bu}_4\text{N}][\text{PF}_6]$ solution of the dgpy complex $1[\text{BF}_4]_2$ displays a single reversible redox wave at $E_{1/2} = + 0.39$ V vs ferrocene for the $[\text{Ni}(\text{dgp})_2]^{3+/2+}$ redox pair (Supporting Information, Figure S5). Similar to the ddpd complex $[\text{Ni}(\text{ddpd})_2][\text{BF}_4]_2$ ($E_{1/2} = 1.22$ V),²⁹ this oxidation is ligand- rather than metal-centered. The much lower potential reflects the much more electron-rich and electron-donating guanidine units of dgpy. No reduction of the pyridine unit is observed up to -2.5 V. On the other hand, the tpe complex $5[\text{BF}_4]_2$ displays two irreversible redox waves at -2.31 and -1.92 V in $\text{CH}_3\text{CN}/[\text{Bu}_4\text{N}][\text{PF}_6]$ (Supporting Information, Figure S6) attributed to ligand-centered reductions and no ligand-centered oxidation wave up to 1 V, reflecting the more electron-accepting character of the tpe ligand. Consequently, the dgpy and tpe ligands constitute largely π -donating and π -accepting ligands, respectively. Electrochemical data for all complexes are summarized in Table S1.

Structures of $1[\text{PF}_6]_2$, $2[\text{ClO}_4]_2$, $3[\text{BF}_4]_2$, $4[\text{BF}_4]_2$, and $5[\text{BF}_4]_2$. All nickel(II) complex cations exhibit a $[\text{NiN}_6]$ pseudooctahedral coordination sphere (see Figure 1 for 1^{2+} and 5^{2+} and the literature^{29,59,60} for 2^{2+} – 4^{2+} ; Supporting Information, Table S2) with Ni–N bond lengths varying only slightly from an average of 2.073 Å in $1[\text{PF}_6]_2$ to an average of 2.088 Å in $3[\text{BF}_4]_2$. Complex cations 1^{2+} , 3^{2+} , 4^{2+} , and 5^{2+} show average N–Ni–N angles ranging from 84.64 to 92.03°, while the terpyridine complex 2^{2+} has appreciably smaller average N–Ni–N bond angles of 77.74° due to the five-membered nature of the tridentate terpyridine ligand coordination.

Absorption Spectra and Ligand Field Analysis. Normalized ligand field spectra of 1^{2+} – 5^{2+} in CH_3CN are displayed in Figure 2 in the region of the lowest-energy electronic transitions. Full absorption spectra with both spin-allowed interconfigurational ${}^3\text{A}_2 \rightarrow {}^3\text{T}_2$ and ${}^3\text{A}_2 \rightarrow {}^3\text{T}_1({}^3\text{F})$ bands with extinction coefficients varying between 6 and 32 $\text{M}^{-1}\text{cm}^{-1}$ and a Tanabe–Sugano diagram for the d^8 electron configuration in perfect octahedral symmetry are given in the Supporting Information (Figures S7–S12). The energy of the ${}^3\text{A}_2 \rightarrow {}^3\text{T}_2$ band maximum increases from 11,990 to 13,380 cm^{-1} in the series 1^{2+} – 5^{2+} reflecting the increasing ligand field

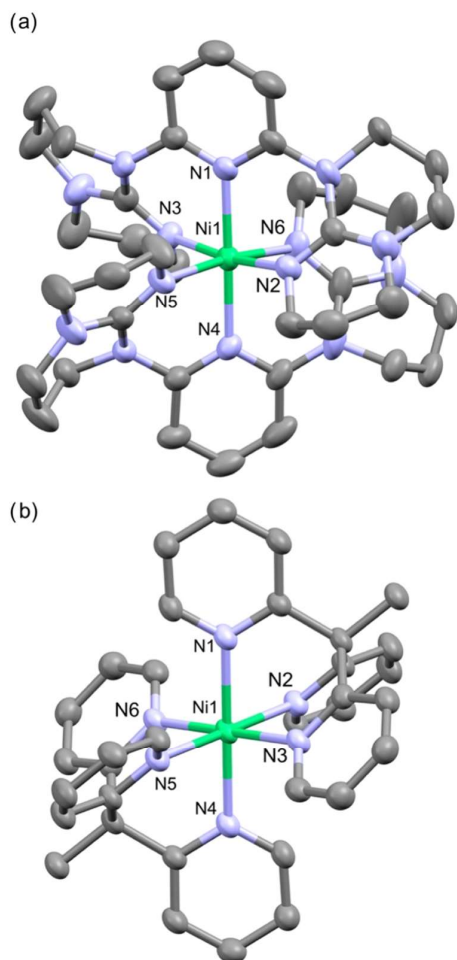


Figure 1. Molecular structures of the cations of (a) $1[\text{PF}_6]_2 \times \text{CH}_3\text{CN}$ and (b) $5[\text{BF}_4]_2 \times 4\text{CH}_3\text{CN}$ determined by XRD. Thermal ellipsoids are displayed at 50% probability. Hydrogen atoms, counterions, and solvent molecules are omitted for clarity.

splitting Δ_o . Both the ligand field splitting Δ_o and the Racah parameter B can be deduced from the measured ${}^3\text{A}_2 \rightarrow {}^3\text{T}_2$ and ${}^3\text{A}_2 \rightarrow {}^3\text{T}_1({}^3\text{F})$ band maxima (Table 1 and Figures S8–S12) using eqs 1 and 2.⁶¹

$$\Delta_o = E({}^3\text{A}_2 \rightarrow {}^3\text{T}_2) = \sigma_1 \quad (1)$$

$$15B = \frac{(\sigma_2 - 2\Delta_o)(\sigma_2 - \Delta_o)}{(\sigma_2 - 1.8\Delta_o)} \quad (2)$$

with

$$\sigma_2 = E({}^3\text{A}_2 \rightarrow {}^3\text{T}_1({}^3\text{F})) \quad (3)$$

The ${}^3\text{T}_1({}^3\text{P})$ band maximum can be calculated using the equation given for the ${}^3\text{T}_1$ state in Table III of ref 62, denoting its band maximum as σ_3 using the notation defined in ref 61:

$$\sigma_3 = \frac{15B}{2} + \frac{3\Delta_o}{2} + \frac{1}{2}\sqrt{(9B - \Delta_o)^2 + 144B^2} \quad (4)$$

These equations do not include spin–orbit coupling and, as always in ligand field analyses, are used for absorption band maxima of the complex in its fixed ground-state geometry.

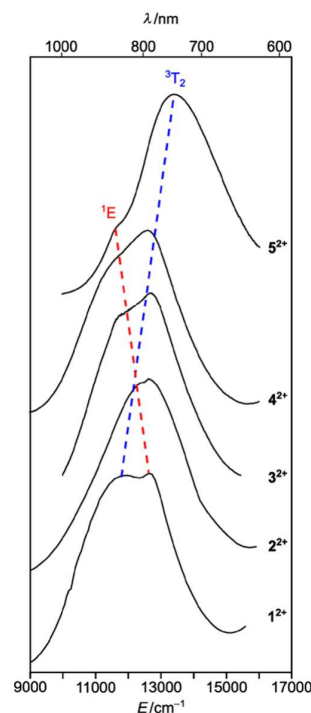


Figure 2. Normalized and vertically offset UV/Vis/NIR absorption spectra of 1^{2+} – 5^{2+} as $[\text{BF}_4]^-$ salts in CH_3CN with absorption band assignments and dotted lines approximating the positions of the ${}^3\text{T}_2$ (blue) and ${}^1\text{E}$ (red) band maxima as a guide to the eye.

Table 1. Energies of Band Maxima in Solution Absorption Spectra of Spin-Allowed and the Lowest Spin-Forbidden Bands^a

	${}^3\text{T}_2 = \Delta_o$	${}^1\text{E}$	ΔE	${}^3\text{T}_1({}^3\text{F})$	${}^3\text{T}_1({}^3\text{P})$	B
1^{2+}	11,990	12,600	−610	18,500	29,050	771
2^{2+}	12,420	12,630	−210	19,750	31,830	954
3^{2+}	12,680	11,650	1030	19,060	29,650	712
4^{2+}	12,700	11,300	1400	19,200	29,910	734
5^{2+}	13,380	11,650	1730	21,140	33,820	987

^aThe ${}^3\text{T}_1({}^3\text{P})$ band maximum was calculated using eq 4. Octahedral ligand field splitting and Racah parameter B (cm^{-1}) calculated from eqs 1 and 2 for 1^{2+} – 5^{2+} are given. All band maxima are rounded to the nearest 10 cm^{-1} .

Structural changes are expected to be very small for intraconfigurational spin-flip transitions and larger by orders of magnitude for interconfigurational transitions. The spectra in Figure 2 represent a situation where this distinction can no longer be made based on a qualitative analysis of either absorption intensities or band shapes. The formally spin-forbidden intraconfigurational ${}^3\text{A}_2 \rightarrow {}^1\text{E}$ band is observed as a weak shoulder on the ${}^3\text{A}_2 \rightarrow {}^3\text{T}_2$ band, either on the high-energy side (1^{2+}) or on the low-energy side (3^{2+} , 4^{2+} , and 5^{2+}). The displayed absorption spectrum of 3^{2+} is part of a pioneering body of work on the ${}^3\text{A}_2 \rightarrow {}^1\text{E}$ absorption band.⁶³ For 2^{2+} , two maxima of nearly equal intensity are observed. The intensity of the spin-flip band is rather high due to intensity borrowing, i.e., spin–orbit coupling induced perturbative interconfigurational interaction between the E spin–orbit components of the ${}^3\text{T}_2$ and ${}^1\text{E}$ states. The intensity increase therefore scales directly with the square of the spin–

orbit coupling parameter and inversely with the square of the energy difference between the coupled states ΔE ,^{32,34,63} defined here as the difference between the two observed maxima for each spectrum in Figure 2. All observed absorption band maxima, calculated Δ_0 , B , and ΔE values are collected in Table 1.

Table 1 shows that the energy differences ΔE are small. The two electronic states are therefore very close in energy, much closer than in strongly emitting Cr^{III} complexes. As an example, the lowest-energy spin-allowed band maximum for the d³ chromium(III) complex with the tpe ligand [Cr(tpe)₂]³⁺ is reported at 431 nm (23200 cm⁻¹), higher in energy by 9700 cm⁻¹ than the spin-flip luminescence maximum at 13500 cm⁻¹.¹⁶ The corresponding energy difference between the two lowest excited states in nickel(II) complexes $1^{2+}-5^{2+}$ is smaller by at least a factor of five, a very significant difference. The B values are lower than the free ion value of 1082 cm⁻¹ for nickel(II) in the gas phase,⁶⁴ with the complexes showing reduced values ranging from 65 to 90% of the free ion value.

Quantum Chemical Calculations. All complex cations $1^{2+}-5^{2+}$ were optimized by density functional theory methods (CPCM-(acetonitrile)-RJCOSX-UB3LYP-D3BJ-ZORA/def2-TZVPP). Average Ni–N distances and N–Ni–N angles of the experimental structure determinations are well reproduced by the DFT calculations (Supporting Information, Tables S2 and S3). These geometries were used for subsequent CASSCF-(12,7)-NEVPT2^{29,65–67} calculations to estimate the energies of the interconfigurational excited triplet state levels (lowest microstates of ³T₂ and ³T₁ origin) relative to the intra-configurational metal-centered spin-flip state levels (lowest microstates of ¹E origin) (Figure 3). The active space comprises two occupied Ni–N σ -bonding orbitals and the five 3d orbitals (Supporting Information, Tables S4–S8).

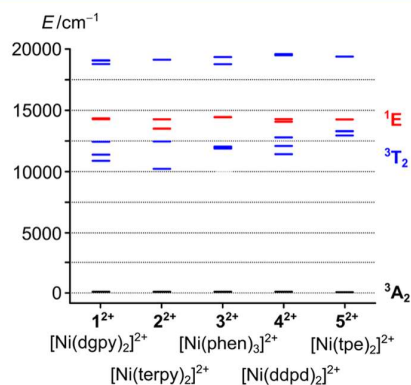


Figure 3. CASSCF(12,7)-NEVPT2-calculated energies of the lowest triplet (blue) and singlet (red) states of complex cations $1^{2+}-5^{2+}$ at the ground-state geometry.

The energies of the ³T₂ and ³T₁(³F) states are well reproduced by the calculations, ranging from 11,570 to 13,190 cm⁻¹ (exp. 119,90–13,380 cm⁻¹) and from 19,019 to 21,267 cm⁻¹ (exp. 185,00–21,140 cm⁻¹), respectively. Notably, the degeneracies of the ³T₂ and ³T₁ levels are significantly lifted for 1^{2+} , 2^{2+} , and 4^{2+} , reflecting the lower symmetry deviating from perfect octahedral coordination geometry. The ¹E levels are less strongly split, and their energies vary only from 13,902 to 14,461 cm⁻¹ (exp. 11,300 to 12,660 cm⁻¹). In all cases, the ¹E energies are calculated higher

than the ³T₂ energies. The calculated Δ_0 values in Table 2 are in very good agreement with those determined from the

Table 2. CASSCF(12,7)-NEVPT2-Calculated Energies of the Lowest Triplet (Blue) and Singlet (Red) States of Complex Cations $1^{2+}-5^{2+}$ (in cm⁻¹)^a

	³ T ₂ = Δ_0	¹ E	ΔE	³ T ₁ (³ F)	³ T ₁ (³ P)	B
1^{2+}	11,570	14,324	−2754	19,019	29,707	1178
2^{2+}	11,712	13,902	−2190	19,546	30,047	1189
3^{2+}	11,962	14,461	−2499	19,478	30,205	1188
4^{2+}	12,099	14,192	−2093	19,823	30,498	1196
5^{2+}	13,190	14,267	−1077	21,267	31,992	1213

^aThe term energies are given as average values of the split states. The Racah B parameters were calculated from an ab initio ligand field theory (AFLT) analysis^{57,58} with an active space comprising only the eight 3d electrons and the five 3d orbitals (CASSCF(8,5)).

absorption spectra in Table 1. The calculated B values (CASSCF(8,5)) in Table 2 show no reduction from the experimental free ion value, due to the overestimation of the spin-flip state energies in contrast to the values derived from experimental data in Table 1. The overestimation of spin-flip state energies by CASSCF-NEVPT2 methods has been noted before,^{19,29,68} preventing a quantitative comparison of calculated energy differences with those determined from absorption spectra. All ΔE values are graphically illustrated in Figure S13 (Supporting Information).

Calculated Absorption Spectra Based on Two Coupled Potential Energy Curves. The absorption spectra of nickel(II) complexes often show overlapping spin-allowed and spin-forbidden d–d bands (Figure 2), a situation extensively discussed and analyzed in the literature.^{31,33,34,69} We apply a straightforward model to the spectra in Figure 2. It has the advantage of being mathematically simple, yielding an analytical equation that can be fitted to the experimental spectra, and it has been applied to the absorption spectra of more than 15 nickel(II) complexes, leading to detailed trends of excited-state energies and other properties.³⁴ The model is illustrated in Figure 4 below. It contains two excited states, represented as harmonic potential energy curves along a single normal coordinate. The curve with its minimum at the same horizontal position as the ground state represents the singlet excited state, with the triplet curve being significantly offset along the horizontal coordinate. The two states are coupled by a single coupling constant, leading to the anharmonic adiabatic potentials with an avoided crossing, also shown in the figure. These are no longer harmonic and do not show minima at the same position as the ground state, illustrating that no pure spin-flip transition occurs. The singlet and triplet character of the adiabatic curves varies along the horizontal axis.

This model contains many simplifications, among them the neglect of all electronic states other than the two coupled levels in Figure 4, a drastic simplification especially in view of the significant calculated low-symmetry splittings of the ³T₂ state, and to a lesser extent, of the ¹E state (Figure 3). The spin-allowed spectrum is approximated by a Lorentzian profile in order to obtain an analytical equation. The low- and high-energy wings of the absorption bands are therefore not well reproduced. We use only the region around the band maxima for the fits in Figure 5, with calculated spectra shown for the wavenumber range analyzed. These assumptions have been shown to not significantly influence the parameters or quality

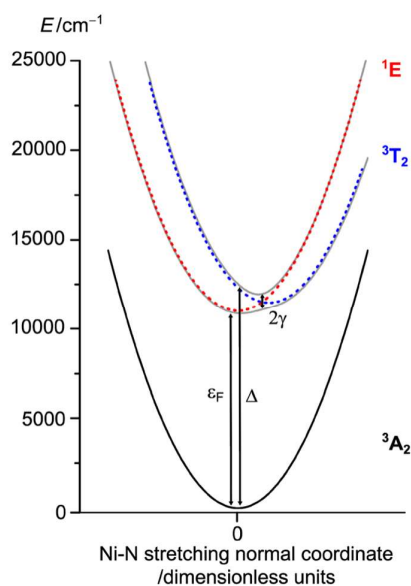


Figure 4. Model with two coupled excited states, showing the diabatic 3T_2 (blue) and 1E (red) states and the adiabatic potential energy surfaces (gray).

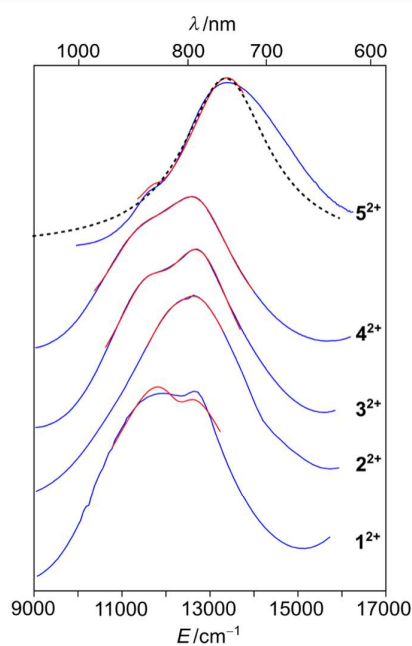


Figure 5. Experimental absorption spectra of 1^{2+} – 5^{2+} (blue traces), calculated absorption spectra (fit to eq 5, red traces) in the wavenumber range used for the fit, and an exemplary calculated absorption spectrum for the 3T_2 band of 5^{2+} neglecting coupling between the two excited states (dotted black trace).

of the calculated absorption spectrum for the $[\text{Ni}(\text{H}_2\text{O})_6]^{2+}$ complex in solution.³¹

The absorbance (ω) is given by

$$\sigma(\omega) = -\frac{1}{\pi} \text{Im} \left(\frac{\beta}{1 - \gamma^2 \alpha \beta} \right) \quad (5)$$

with

$$\alpha = \frac{1}{\omega - \varepsilon_F + i\Gamma} \quad (6)$$

and

$$\beta = \frac{1}{\omega - \Delta + i\sqrt{\omega_0\lambda}} \quad (7)$$

with the parameters ε_F and Δ denoting the energies of the spin-flip excited state and the absorption maximum to the excited state with a nonzero offset along the normal coordinate, respectively, i.e., at the Franck–Condon geometry. ω_0 is the vibrational frequency, identical for all three harmonic potential energy curves representing the electronic states in Figure 4 and set to 450 cm^{-1} , a typical value for metal–ligand stretching frequencies.^{32–34} γ is the coupling constant between the singlet and triplet components of identical symmetry. The width of the allowed absorption band in the absence of coupling is given by $\sqrt{\omega_0\lambda}$ with the parameter λ adjusted to reproduce the observed bandwidth. Γ is a phenomenological damping factor defining the width of individual vibronic transitions. The key parameters are illustrated in Figure 4. Figure 5 shows the comparison of absorption spectra calculated with eq 5. Overall, a good agreement is obtained with this simple model.

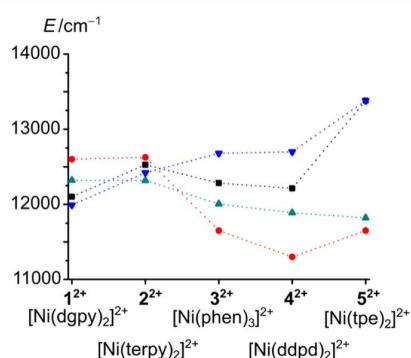
The calculations allow us to analyze a significant portion of the absorption band system, not limited to measured band maxima in Table 1 or the calculated energy differences for the complex frozen in the optimized ground-state geometry in Table 2. This is an important aspect, as the two excited states differ significantly in structure: the 3T_2 state with a higher d_σ antibonding population has longer metal–ligand bonds, leading to an offset of its potential energy minimum along the normal coordinate in Figure 4 and to a broad absorption band. The width of this band is higher (complexes 1^{2+} – 4^{2+}) or comparable (complex 5^{2+}) to the energy difference ΔE in Tables 1 and 2, meaning that it is very likely that the lowest-energy excited state (minimum of the lower adiabatic potential energy surface in Figure 4) has predominant 3T_2 character. This potentially emitting state is structurally distorted, leading to efficient nonradiative relaxation as generally observed for interconfigurational states. In addition to this qualitative discussion of the lowest-energy adiabatic potential energy minimum, the lowest calculated eigenfunction with its two diabatic components also has maximum amplitude at values significantly higher than zero on the normal coordinate axis of Figure 4. A representative example is illustrated in the Supporting Information (Figure S14).

The one-dimensional model in Figure 4 obviously does not include the influence of structural changes along additional normal coordinates. Resolved vibronic structure involving ligand-centered modes is clearly visible in low-temperature spectra of single crystalline $[\text{Ni}(\text{H}_2\text{O})_6]^{2+}$ and has been analyzed with a multidimensional model.⁷⁰ This is an experimental illustration of the strong structural distortions occurring for excitations with formal spin-flip character if the d_σ orbitals are involved. For all of these reasons, the expected emission spectrum would consist of a broad band, as, for example, observed in a hexacarbene cobalt(III) complex,⁷¹ unlike the narrow band shapes for typical spin-flip transitions with high quantum yield.^{13–20}

The values of ε_F and Δ in Table 3 are graphically compared in Figure 6. The comparison shows that the energy difference

Table 3. Values of Parameters Employed in the Model Described in the Main Text (Equations 3–5) in cm^{-1}

parameter	1 ²⁺	2 ²⁺	3 ²⁺	4 ²⁺	5 ²⁺
ω_0	450	450	450	450	450
λ	7440	5500	3022	2797	2860
Γ	380	400	797	1044	200
γ	290	144	545	638	220
ε_F	12,320	12,318	12,006	11,888	11,820
Δ	12,102	12,526	12,283	12,212	13,380
$\sqrt{\omega_0\lambda}$	1830	1573	1166	1122	1112
ΔE	-218	208	770	324	1560

**Figure 6.** Experimental transition energies from Table 1; red circles ¹E band, blue triangles ³T₂ band. Parameters ε_F (green triangles) and Δ (black squares) for complexes 1²⁺–5²⁺.

is lower than 800 cm^{-1} for complexes 1²⁺–4²⁺ and on the order of 1500 cm^{-1} for the tpe complex 5²⁺. The ΔE values in Table 3 are similar to those obtained from the experimental spectra in Table 1. All values are compared in the Supporting Information (Figure S12).

The values in Table 3 and Figure 6 allow us to predict wavelength ranges for potential luminescence spectra. If spin-flip luminescence is observed, its maximum should occur near ε_F , i.e., in the 11,500–12,500 cm^{-1} (870–800 nm) range, as the Stokes shift is expected to be very small for spin-flip transitions. If the lowest-energy potential energy minimum has a predominant ³T₂ character, a broad luminescence band should be observed with its high-wavenumber onset at the electronic origin, estimated to be lower than the band maximum Δ by approximately the bandwidth $\sqrt{\omega_0\lambda}$ in Table 3, leading to luminescence onsets between 820 nm for 5²⁺ and 980 nm for 1²⁺. Luminescence maxima are expected at wavelengths longer by at least 100 nm than the estimated onset, due to the significant Stokes shifts of interconfigurational transitions.

We were unable to observe any luminescence in the spin-flip region at temperatures between 80 and 280 K for complexes 3²⁺–5²⁺ in the solid state (Supporting Information, Figures S14–S17). Additionally, no onset was observed between 800 and 1000 nm, which would correspond to the high-energy edge of a broad luminescence band. Likewise, no luminescence was observed for 3²⁺ and 5²⁺ in frozen butyronitrile at 77 K with 450 and 340 nm excitation, respectively (Supporting Information, Figure S18).

In marked contrast, ref 72 reports luminescence traces observed for the phen complex 3²⁺ and the tpm analogue of 5²⁺ (tpm = tris(pyrid-2-yl)methane) at 150 K and at 80 K. The

reported emission features of the two complexes do not vary with temperature and are nearly superimposable (Supporting Information of ref 72, Figures S25 and S26; Supporting Information, Figure S19), which is unexpected, considering the distinct absorption spectra of 3²⁺ and 5²⁺ (Figure 2) and the strong intensity decrease at higher temperatures expected for d–d luminescence transitions from the distorted emitting states of 1²⁺–5²⁺ and related complexes. The reported features have characteristics only partially in agreement with the expectations for a broad luminescence band from the ³T₂ state: the onset at approximately 750 nm is at too short a wavelength, and the maximum is at approximately 920 nm, intermediate between the expected ranges for pure spin-flip and ³T₂ luminescence. More work to confidently assign luminescence from pseudooctahedral nickel(II) complexes is clearly needed.

One way to increase the energy difference between the two excited states is through the application of external hydrostatic pressure. A shift to a higher wavenumber on the order of +20 cm^{-1} kbar⁻¹ has been reported for the ³T₂ absorption band of several nickel(II) complexes.^{73,74} In contrast, a shift to a lower wavenumber is expected for spin-flip transitions in chromium(III) complexes, with the highest absolute value reported to date on the order of -15 cm^{-1} kbar⁻¹.⁶⁸ Overall, an external pressure should therefore lead to an increase of the energy difference ΔE that can be estimated to be on the order of 2000 cm^{-1} at 60 kbar, doubling the highest ΔE values in Tables 1 and 3 but still less than half that observed for chromium(III) complexes with intense spin-flip emission. External pressure can therefore push the emitting state closer to the ideal for “spin-flip” characteristics. Consequently, we applied external pressure to 4[BF₄]₂ and monitored the 800–1000 nm range, where onset of spin-flip luminescence is expected. Even under these extreme conditions, at pressures up to 62 kbar, no experimental evidence for spin-flip luminescence from 4²⁺ could be gathered (Supporting Information, Figure S20). The effect of pressure on the sample crystal is documented by the Raman spectra at variable pressure (Supporting Information, Figures S21 and S22). Small shifts of the Raman maxima on the order of 0.3 to 0.9 cm^{-1} kbar⁻¹ unambiguously indicate that the sample is under pressure (Figures S23 and S24). The Raman signals broaden by less than a factor of two between ambient pressure and 62 kbar, documenting that the crystal quality of the sample does not deteriorate dramatically.

CONCLUSIONS

Spin-flip luminescence from six-coordinate nickel(II) complexes is much more challenging to achieve than for chromium(III) complexes. One reason for this is the relatively small energy difference between the ¹E excited state from which spin-flip luminescence can originate and the strongly distorted ³T₂ excited state closest in energy. The strong-field pyridine ligands discussed in this study (terpy = 2,2':6',2''-terpyridine; phen = 1,10-phenanthroline; ddpd = N,N'-dimethyl-N,N'-dipyridine-2-ylpyridine-2,6-diamine; dgpy = 2,6-diguanidylpyridine, tpe = 1,1,1-tris(pyrid-2-yl)ethane)—even with additional external pressure—are too weak to induce a sufficient splitting in the respective nickel(II) complexes. Consequently, stronger ligand fields are required. Yet, too strong ligand fields favor a four-coordinate, square-planar nickel(II) complex with a diamagnetic ground state instead of the pseudooctahedral geometry with a paramagnetic ground

state required for spin-flip emission. This delicate balance will be further explored in the future.

■ ASSOCIATED CONTENT

SI Supporting Information

The Supporting Information is available free of charge at <https://pubs.acs.org/doi/10.1021/acs.inorgchem.3c00779>.

Detailed ESI⁺, spectroscopic and electrochemical data, and information on computational studies, including charge-transfer number analyses, difference densities, orbitals of the active space (PDF), and Cartesian coordinates of optimized geometries (PDF)

Accession Codes

CCDC 2125074–2125075 contain the supplementary crystallographic data for this paper. These data can be obtained free of charge via www.ccdc.cam.ac.uk/data_request/cif, or by emailing data_request@ccdc.cam.ac.uk, or by contacting The Cambridge Crystallographic Data Centre, 12 Union Road, Cambridge CB2 1EZ, UK; fax: +44 1223 336033.

■ AUTHOR INFORMATION

Corresponding Authors

Katja Heinze – Department of Chemistry, Johannes Gutenberg University, Mainz 55128, Germany; orcid.org/0000-0003-1483-4156; Email: katja.heinze@uni-mainz.de

Christian Reber – Département de chimie, Université de Montréal, Montréal, QC H3C 3J7, Canada; orcid.org/0000-0001-9350-7262; Email: christian.reber@umontreal.ca

Authors

Nathan R. East – Department of Chemistry, Johannes Gutenberg University, Mainz 55128, Germany

Chahinez Dab – Département de chimie, Université de Québec à Rimouski, Rimouski, QC G5L 3A1, Canada

Christoph Förster – Department of Chemistry, Johannes Gutenberg University, Mainz 55128, Germany

Complete contact information is available at: <https://pubs.acs.org/doi/10.1021/acs.inorgchem.3c00779>

Author Contributions

N.R.E. synthesized and characterized the nickel(II) complexes, measured the absorption and luminescence spectra in solution, and performed the DFT/CASSCF calculations. C.D. measured all Raman and luminescence spectra on crystalline samples at variable temperatures and pressures and analyzed the spectroscopic results. C.F. solved the single-crystal X-ray structures. C.R. analyzed and calculated the absorption spectra. K.H. and C.R. conceived the project. The manuscript was written through contributions of all authors. All authors have given approval to the final version of the manuscript.

Notes

The authors declare no competing financial interest.

■ ACKNOWLEDGMENTS

This work was financially supported by the Deutsche Forschungsgemeinschaft (DFG) under grant INST 247/1018-1 (K.H.). This work was supported by the Max Planck Graduate Center with the Johannes Gutenberg University Mainz (MPGC). N.R.E. is a recipient of a position through the DFG Excellence Initiative by the Graduate School Materials

Science in Mainz (GSC 266). Parts of this research were conducted using the supercomputer Mogon and advisory services offered by Johannes Gutenberg University Mainz (<http://www.hpc.uni-mainz.de>) and the supercomputer Elwertitsch and advisory services offered by the Rheinland-Pfälzische Technische Universität Kaiserslautern-Landau (<https://hpc.rz.rptu.de>), which are members of the AHRP and the Gauss Alliance e.V. The authors thank Dr. Dieter Schollmeyer for collecting the XRD data. Financial support from the Natural Sciences and Engineering Research Council (NSERC) of Canada and the Fonds de recherche du Québec—Nature et Technologies for a fellowship to C.D. is gratefully acknowledged.

■ REFERENCES

- (1) Dorn, M.; East, N. R.; Förster, C.; Kitzmann, W. R.; Moll, J.; Reichenauer, F.; Reuter, T.; Stein, L.; Heinze, K. d–d and Charge Transfer Photochemistry of 3d Metal Complexes. In *Comprehensive Inorganic Chemistry III*; Elsevier, 2023; Vol. 8, pp 707–788.
- (2) Wegeberg, C.; Wenger, O. S. Luminescent First-Row Transition Metal Complexes. *JACS Au* **2021**, *1*, 1860–1876.
- (3) Wenger, O. S. Photoactive Nickel Complexes in Cross-Coupling Catalysis. *Chem. - Eur. J.* **2021**, *27*, 2270–2278.
- (4) Chábera, P.; Lindh, L.; Rosemann, N. W.; Prakash, O.; Uhlig, J.; Yartsev, A.; Wärnmark, K.; Sundström, V.; Persson, P. Photo-functionality of iron(III) N-heterocyclic carbenes and related d⁵ transition metal complexes. *Coord. Chem. Rev.* **2021**, *426*, 213517.
- (5) Förster, C.; Heinze, K. Photophysics and photochemistry with Earth-abundant metals—fundamentals and concepts. *Chem. Soc. Rev.* **2020**, *49*, 1057–1070.
- (6) Wenger, O. S. Photoactive Complexes with Earth-Abundant Metals. *J. Am. Chem. Soc.* **2018**, *140*, 13522–13533.
- (7) Bizzarri, C.; Spuling, E.; Knoll, D. M.; Volz, D.; Bräse, S. Sustainable metal complexes for organic light-emitting diodes (OLEDs). *Coord. Chem. Rev.* **2018**, *373*, 49–82.
- (8) Arias-Rotondo, D. M. The fruit fly of photophysics. *Nat. Chem.* **2022**, *14*, 716.
- (9) Kitzmann, W. R.; Heinze, K. Charge-Transfer and Spin-Flip States: Thriving as Complements. *Angew. Chem., Int. Ed.* **2022**, *135*, e202213207.
- (10) Kitzmann, W. R.; Moll, J.; Heinze, K. Spin-flip luminescence. *Photochem. Photobiol. Sci.* **2022**, *21*, 1309–1331.
- (11) Dorn, M.; Kalmbach, J.; Boden, P.; Pöpcke, A.; Gómez, S.; Förster, C.; Kuczelinis, F.; Carrella, L. M.; Büldt, L. A.; Bings, N. H.; et al. A Vanadium(III) Complex with Blue and NIR-II Spin-Flip Luminescence in Solution. *J. Am. Chem. Soc.* **2020**, *142*, 7947–7955.
- (12) Dorn, M.; Kalmbach, J.; Boden, P.; Kruse, A.; Dab, C.; Reber, C.; Niedner-Schatteburg, G.; Lochbrunner, S.; Gerhards, M.; Seitz, M.; Heinze, K. Ultrafast and long-time excited state kinetics of an NIR-emissive vanadium(III) complex I: synthesis, spectroscopy and static quantum chemistry. *Chem. Sci.* **2021**, *12*, 10780–10790.
- (13) Otto, S.; Grabolle, M.; Förster, C.; Kreitner, C.; Resch-Genger, U.; Heinze, K. [Cr(ddpd)₂]³⁺: A Molecular, Water-Soluble, Highly NIR-Emissive Ruby Analogue. *Angew. Chem., Int. Ed.* **2015**, *54*, 11572–11576.
- (14) Wang, C.; Otto, S.; Dorn, M.; Kreidt, E.; Lebon, J.; Sršan, L.; Di Martino-Fumo, P.; Gerhards, M.; Resch-Genger, U.; Seitz, M.; Heinze, K. Deuterated Molecular Ruby with Record Luminescence Quantum Yield. *Angew. Chem., Int. Ed.* **2018**, *57*, 1112–1116.
- (15) Otto, S.; Förster, C.; Wang, C.; Resch-Genger, U.; Heinze, K. A Strongly Luminescent Chromium(III) Complex Acid. *Chem. - Eur. J.* **2018**, *24*, 12555–12563.
- (16) Treiling, S.; Wang, C.; Förster, C.; Reichenauer, F.; Kalmbach, J.; Boden, P.; Harris, J. P.; Carrella, L. M.; Rentschler, E.; Resch-Genger, U.; et al. Luminescence and Light-Driven Energy and Electron Transfer from an Exceptionally Long-Lived Excited State of a

Non-Innocent Chromium(III) Complex. *Angew. Chem., Int. Ed.* **2019**, *58*, 18075–18085.

(17) Jiménez, J.-R.; Doistau, B.; Cruz, C. M.; Besnard, C.; Cuerva, J. M.; Campaña, A. G.; Piguet, C. Chiral Molecular Ruby $[\text{Cr}(\text{dqp})_2]^{3+}$ with Long-Lived Circularly Polarized Luminescence. *J. Am. Chem. Soc.* **2019**, *141*, 13244–13252.

(18) Jiménez, J.-R.; Poncet, M.; Doistau, B.; Besnard, C.; Piguet, C. Luminescent polypyridyl heteroleptic Cr^{III} complexes with high quantum yields and long excited state lifetimes. *Dalton Trans.* **2020**, *49*, 13528–13532.

(19) Reichenauer, F.; Wang, C.; Förster, C.; Boden, P.; Ugur, N.; Báez-Cruz, R.; Kalmbach, J.; Carrella, L. M.; Rentschler, E.; Ramanan, C.; et al. Strongly Red-Emissive Molecular Ruby $[\text{Cr}(\text{bpmp})_2]^{3+}$ Surpasses $[\text{Ru}(\text{bpy})_3]^{2+}$. *J. Am. Chem. Soc.* **2021**, *143*, 11843–11855.

(20) Stein, L.; Wang, C.; Förster, C.; Resch-Genger, U.; Heinze, K. Bulky ligands protect molecular ruby from oxygen quenching. *Dalton Trans.* **2022**, *51*, 17664–17670.

(21) Harris, J. P.; Reber, C.; Colmer, H. E.; Jackson, T. A.; Forshaw, A. P.; Smith, J. M.; Kinney, R. A.; Telsler, J. Near-infrared ${}^2E_g \rightarrow {}^4A_{2g}$ and visible LMCT luminescence from a molecular bis-(tris(carbene)-borate) manganese(IV) complex. *Can. J. Chem.* **2017**, *95*, 547–552.

(22) Otto, S.; Dorn, M.; Förster, C.; Bauer, M.; Seitz, M.; Heinze, K. Understanding and exploiting long-lived near-infrared emission of a molecular ruby. *Coord. Chem. Rev.* **2018**, *359*, 102–111.

(23) Kitzmann, W. R.; Ramanan, C.; Naumann, R.; Heinze, K. Molecular ruby: exploring the excited state landscape. *Dalton Trans.* **2022**, *51*, 6519–6525.

(24) Wong, Y.-S.; Tang, M.-C.; Ng, M.; Yam, V. W.-W. Toward the Design of Phosphorescent Emitters of Cyclometalated Earth-Abundant Nickel(II) and Their Supramolecular Study. *J. Am. Chem. Soc.* **2020**, *142*, 7638–7646.

(25) Ogawa, T.; Sinha, N.; Pfund, B.; Prescimone, A.; Wenger, O. S. Molecular Design Principles to Elongate the Metal-to-Ligand Charge Transfer Excited-State Lifetimes of Square-Planar Nickel(II) Complexes. *J. Am. Chem. Soc.* **2022**, *144*, 21948–21960.

(26) Poirier, S.; Lynn, H.; Reber, C.; Tailleux, E.; Marchivie, M.; Guionneau, P.; Probert, M. R. Variation of M···H–C Interactions in Square-Planar Complexes of Nickel(II), Palladium(II), and Platinum(II) Probed by Luminescence Spectroscopy and X-ray Diffraction at Variable Pressure. *Inorg. Chem.* **2018**, *57*, 7713–7723.

(27) Arriortua, M. I.; Rojo, T.; Amigó, J. M.; Germain, G.; Declercq, J. P. Metal(II) Terpyridine Complex: $\text{Ni}(\text{Terpy})_2(\text{PF}_6)_2$. *Bull. Soc. Chim. Belg.* **1982**, *91*, 337–338.

(28) Vander Griend, D. A.; Bediako, D. K.; DeVries, M. J.; DeJong, N. A.; Heeringa, L. P. Detailed Spectroscopic, Thermodynamic, and Kinetic Characterization of Nickel(II) Complexes with 2,2'-Bipyridine and 1,10-Phenanthroline Attained via Equilibrium-Restricted Factor Analysis. *Inorg. Chem.* **2008**, *47*, 656–662.

(29) Dorn, M.; Mack, K.; Carrella, L. M.; Rentschler, E.; Förster, C.; Heinze, K. Structure and Electronic Properties of an Expanded Terpyridine Complex of Nickel(II) $[\text{Ni}(\text{ddpd})_2](\text{BF}_4)_2$. *Z. Anorg. Allg. Chem.* **2018**, *644*, 706–712.

(30) Neuhauser, D.; Park, T.-J.; Zink, J. I. Analytical Derivation of Interference Dips in Molecular Absorption Spectra: Molecular Properties and Relationships to Fano's Antiresonance. *Phys. Rev. Lett.* **2000**, *85*, 5304–5307.

(31) Bussiére, G.; Reber, C.; Neuhauser, D.; Walter, D. A.; Zink, J. I. Molecular Properties Obtained by Analysis of Electronic Spectra Containing Interference Dips. Comparisons of Analytical Equations and Exact Models Based on Coupled Potential Energy Surfaces. *J. Phys. Chem. A* **2003**, *107*, 1258–1267.

(32) Nolet, M.-C.; Beaulac, R.; Boulanger, A.-M.; Reber, C. Allowed and Forbidden d–d Bands in Octahedral Coordination Compounds: Intensity Borrowing and Interference Dips in Absorption Spectra. In *Optical Spectra and Chemical Bonding in Transition Metal Complexes*; Springer, 2004; Vol. 107, pp 145–158.

(33) Nolet, M.-C.; Michaud, A.; Bain, C.; Zargarian, D.; Reber, C. Allowed and Forbidden d–d Transitions in Poly(3,5-

dimethylpyrazolyl)methane Complexes of Nickel(II). *Photochem. Photobiol.* **2006**, *82*, 57–63.

(34) González, E.; Rodrigue-Witchel, A.; Reber, C. Absorption spectroscopy of octahedral nickel(II) complexes: A case study of interactions between multiple electronic excited states. *Coord. Chem. Rev.* **2007**, *251*, 351–363.

(35) Wang, C.; Kitzmann, W. R.; Weigert, F.; Förster, C.; Wang, X.; Heinze, K.; Resch-Genger, U. Matrix Effects on Photoluminescence and Oxygen Sensitivity of a Molecular Ruby. *ChemPhotoChem* **2022**, *6*, e202100296.

(36) Santoro, A.; Sambiagio, C.; McGowan, P. C.; Halcrow, M. A. Synthesis and coordination chemistry of 1,1,1-tris-(pyrid-2-yl)ethane. *Dalton Trans.* **2015**, *44*, 1060–1069.

(37) Pal, A. K.; Zaccaroni, N.; Campagna, S.; Hanan, G. S. Near infra-red emission from a mer-Ru(II) complex: consequences of strong σ -donation from a neutral, flexible ligand with dual binding modes. *Chem. Commun.* **2014**, *50*, 6846–6849.

(38) X-Area; STOE&GmbH: Darmstadt, Germany, 2022.

(39) Blessing, R. H. An empirical correction for absorption anisotropy. *Acta Crystallogr., Sect. A: Found. Crystallogr.* **1995**, *51*, 33–38.

(40) Spek, A. L. Structure validation in chemical crystallography. *Acta Crystallogr., Sect. D: Biol. Crystallogr.* **2009**, *65*, 148–155.

(41) Sheldrick, G. M. SHELXT—Integrated space-group and crystal-structure determination. *Acta Crystallogr., Sect. A: Found. Crystallogr.* **2015**, *71*, 3–8.

(42) Sheldrick, G. M. Crystal structure refinement with SHELXL. *Acta Crystallogr., Sect. C: Struct. Chem.* **2015**, *71*, 3–8.

(43) Sheldrick, G. M. A short history of SHELX. *Acta Crystallogr., Sect. A: Found. Crystallogr.* **2008**, *64*, 112–122.

(44) Hübschle, C. B.; Sheldrick, G. M.; Dittrich, B. ShelXle: a Qt graphical user interface for SHELXL. *J. Appl. Crystallogr.* **2011**, *44*, 1281–1284.

(45) Neese, F. The ORCA program system. *Wiley Interdiscip. Rev.: Comput. Mol. Sci.* **2012**, *2*, 73–78.

(46) Becke, A. D. Density-functional thermochemistry. III. The role of exact exchange. *J. Chem. Phys.* **1993**, *98*, S648–S652.

(47) Miehlich, B.; Savin, A.; Stoll, H.; Preuss, H. Results obtained with the correlation energy density functionals of Becke and Lee, Yang and Parr. *Chem. Phys. Lett.* **1989**, *157*, 200–206.

(48) Lee, C.; Yang, W.; Parr, R. G. Development of the Colle-Salvetti correlation-energy formula into a functional of the electron density. *Phys. Rev. B* **1988**, *37*, 785–789.

(49) Izsák, R.; Neese, F. An overlap fitted chain of spheres exchange method. *J. Chem. Phys.* **2011**, *135*, No. 144105.

(50) Neese, F.; Wennmohs, F.; Hansen, A.; Becker, U. Efficient, approximate and parallel Hartree–Fock and hybrid DFT calculations. A 'chain-of-spheres' algorithm for the Hartree–Fock exchange. *Chem. Phys.* **2009**, *356*, 98–109.

(51) Pantazis, D. A.; Chen, X.-Y.; Landis, C. R.; Neese, F. All-Electron Scalar Relativistic Basis Sets for Third-Row Transition Metal Atoms. *J. Chem. Theory Comput.* **2008**, *4*, 908–919.

(52) Miertuš, S.; Scrocco, E.; Tomasi, J. Electrostatic interaction of a solute with a continuum. A direct utilization of AB initio molecular potentials for the prevision of solvent effects. *Chem. Phys.* **1981**, *55*, 117–129.

(53) Weigend, F. Accurate Coulomb-fitting basis sets for H to Rn. *Phys. Chem. Chem. Phys.* **2006**, *8*, 1057–1065.

(54) Weigend, F.; Ahlrichs, R. Balanced basis sets of split valence, triple zeta valence and quadruple zeta valence quality for H to Rn: Design and assessment of accuracy. *Phys. Chem. Chem. Phys.* **2005**, *7*, 3297–3305.

(55) Angeli, C.; Cimiraglia, R.; Evangelisti, S.; Leininger, T.; Malrieu, J. P. Introduction of n-electron valence states for multi-reference perturbation theory. *J. Chem. Phys.* **2001**, *114*, 10252–10264.

(56) Angeli, C.; Cimiraglia, R.; Malrieu, J.-P. n-electron valence state perturbation theory: A spinless formulation and an efficient

implementation of the strongly contracted and of the partially contracted variants. *J. Chem. Phys.* **2002**, *117*, 9138–9153.

(57) Atanasov, M.; Ganyushin, D.; Sivalingam, K.; Neese, F. A Modern First-Principles View on Ligand Field Theory Through the Eyes of Correlated Multireference Wavefunctions. In *Structure and Bonding: Molecular Electronic Structures of Transition Metal Complexes II*; Springer: Berlin, Heidelberg, 2012; Vol. 143, pp 149–220.

(58) Singh, S. K.; Eng, J.; Atanasov, M.; Neese, F. Covalency and chemical bonding in transition metal complexes: An ab initio based ligand field perspective. *Coord. Chem. Rev.* **2017**, *344*, 2–25.

(59) Anderer, C.; Nather, C.; Bensch, W. Bis(2,2':6',2''-terpyridine- $\kappa^3\text{N,N',N''}$)nickel(II) bis(perchlorate) hemihydrate. *IUCrData* **2016**, *1*, No. x161009.

(60) Hanifepour, Y.; Mirtamizdoust, B.; Wang, R.; Anbarh, S.; Joo, S. W. A Nano Nickel(II) Metal–Organic Coordination Compound for Nano Nickel(II) Oxide: Sonochemical Synthesis and Characterization. *J. Inorg. Organomet. Polym.* **2017**, *27*, 1045–1052.

(61) Reedijk, J.; van Leeuwen, P. W. N. M.; Groeneveld, W. L. A semi-empirical energy-level diagram for octahedral, Nickel(II) Complexes. *Recl. Trav. Chim. Pays-Bas* **2010**, *87*, 129–143.

(62) Knox, K.; Shulman, R. G.; Sugano, S. Covalency Effects in KNiF_3 . II. Optical Studies. *Phys. Rev.* **1963**, *130*, 512–516.

(63) Jørgensen, C. K.; Smith, L. H.; Hanshoff, G.; et al. Comparative Crystal Field Studies of some Ligands and the Lowest Singlet State of Paramagnetic Nickel(II) Complexes. *Acta Chem. Scand.* **1955**, *9*, 1362–1377.

(64) Kettle, S. F. A. *Physical Inorganic Chemistry: a Coordination Chemistry Approach*; University Science Books, 1996; p 163.

(65) Radoń, M.; Drabik, G. Spin States and Other Ligand–Field States of Aqua Complexes Revisited with Multireference ab Initio Calculations Including Solvation Effects. *J. Chem. Theory Comput.* **2018**, *14*, 4010–4027.

(66) Landry-Hum, J.; Bussière, G.; Daniel, C.; Reber, C. Triplet Electronic States in d^2 and d^8 Complexes Probed by Absorption Spectroscopy: A CASSCF/CASPT2 Analysis of $[\text{V}(\text{H}_2\text{O})_6]^{3+}$ and $[\text{Ni}(\text{H}_2\text{O})_6]^{2+}$. *Inorg. Chem.* **2001**, *40*, 2595–2601.

(67) Vlahović, F.; Perić, M.; Gruden-Pavlović, M.; Zlatar, M. Assessment of TD-DFT and LF-DFT for study of d–d transitions in first row transition metal hexaaqua complexes. *J. Chem. Phys.* **2015**, *142*, No. 214111.

(68) Otto, S.; Harris, J. P.; Heinze, K.; Reber, C. Molecular Ruby under Pressure. *Angew. Chem., Int. Ed.* **2018**, *57*, 11069–11073.

(69) Wexler, D.; Zink, J. L.; Reber, C. Vibronic structure induced in spin-forbidden transitions in emission and absorption spectra by excited-state coupling. *J. Phys. Chem. A* **1992**, *96*, 8757–8765.

(70) Dobe, C.; González, E.; Tregenna-Piggott, P. L. W.; Reber, C. Spectroscopic effects resulting from interacting singlet and triplet excited states: vibronic structure involving the O–H stretching mode in d–d absorption bands of $[\text{Ni}(\text{H}_2\text{O})_6]^{2+}$. *Dalton Trans.* **2014**, *43*, 17864–17870.

(71) Kaufhold, S.; Rosemann, N. W.; Chábera, P.; Lindh, L.; Bolaño Losada, I.; Uhlig, J.; Pascher, T.; Strand, D.; Wärnmark, K.; Yartsev, A.; Persson, P. Microsecond Photoluminescence and Photoreactivity of a Metal-Centered Excited State in a Hexacarbene–Co(III) Complex. *J. Am. Chem. Soc.* **2021**, *143*, 1307–1312.

(72) Wojnar, M. K.; Laorenza, D. W.; Schaller, R. D.; Freedman, D. E. Nickel(II) Metal Complexes as Optically Addressable Qubit Candidates. *J. Am. Chem. Soc.* **2020**, *142*, 14826–14830.

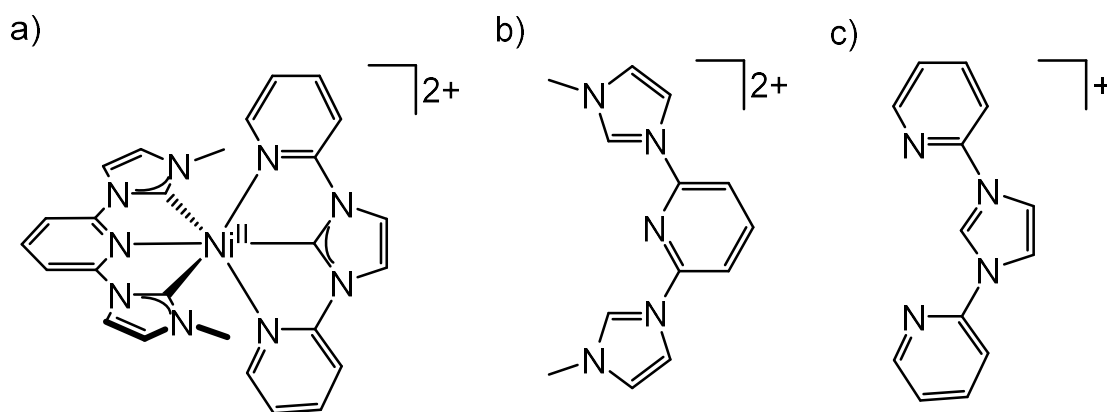
(73) Parsons, R. W.; Drickamer, H. G. Effect of Pressure on the Spectra of Certain Transition Metal Complexes. *J. Chem. Phys.* **1958**, *29*, 930–937.

(74) Zahner, J. C.; Drickamer, H. G. Effect of Pressure on Crystal-Field Energy and Covalency in Octahedral Complexes of Ni^{2+} , Co^{2+} , and Mn^{2+} . *J. Chem. Phys.* **1961**, *35*, 1483–1490.

3.4 Influencing Ligand Field States of Nickel(II) Complexes with Strongly σ -Donating and π -Accepting Ligands

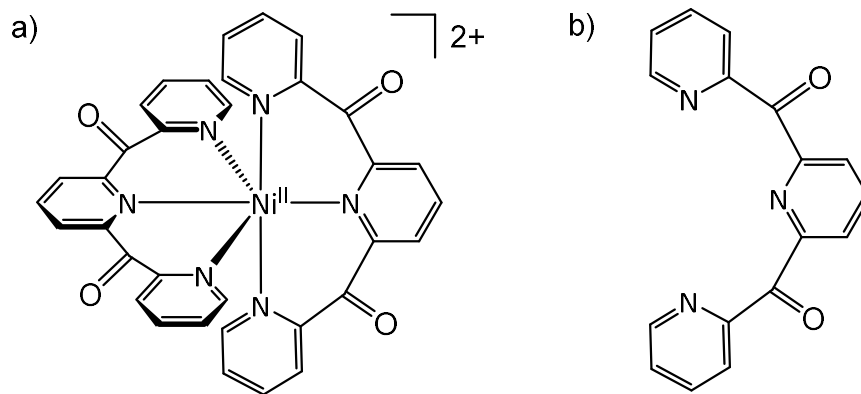
The prospect of SF emissive octahedral Ni^{II} complexes is attractive, however there are none reported to date. To achieve emission from Ni^{II} octahedral complexes the intra- and interconfigurational states must be separated, and intraconfigurational states must be lowest in energy.^[188] To do this a strong field σ -donating ligand is required, this will destabilize e_g^* orbitals. However, if the LF is too strong Ni^{II} will adopt a square planar or five-coordinate configuration, thus a balance is required.^[81] An alternative route is to use a more π -accepting ligand which can stabilize the t_{2g} orbitals. Both methods aim to increase Δ_o and the energy of the 3T_2 state.^[187] In principle this can better separate the LF states, however the effect of σ -donation and π -acceptance on the intraconfigurational 1E state is less clear.

Increasing the LF strength using σ -donors is not a new concept and has been used on Ni^{II} with strong field ligands such as phen or ddpd.^[190,191] These ligands however do not provide a strong enough LF for Ni^{II}, thus stronger σ -donating ligands such as carbenes are required. Detailed in this chapter is the synthesis along with structural characterization of a Ni^{II} heteroleptic carbene complex (scheme 3.1a) containing the literature known CNC ligand (1,1'-(pyridin-2,6-diyl)bis(3-methyl-1H-imidazol-3-ylidene)) (scheme 3.1b) and NCN ligand (1,3-bis(2-pyridyl)imidazolylidene) (scheme 3.1c).^[203,204]



Scheme 3.1: Molecular structures of a) [Ni(CNC)(NCN)]²⁺ and ligands b) CNC and c) NCN.

To investigate the effect of increased ligand π -accepting ability, the literature known dcpp (2,6-bis(2-carboxypyridyl)pyridine) (scheme 3.2b) ligand^[205] containing two electron-withdrawing carbonyl groups is used to make the homoleptic [Ni(dcpp)₂]²⁺ complex (scheme 3.2a). Detailed in this chapter is the synthesis along with structural and optical characterization of [Ni(dcpp)₂]²⁺ which contains a strong π -accepting ligands.



Scheme 3.2: Molecular structures of a) $[\text{Ni}(\text{dcpp})_2]^{2+}$ and ligand b) dcpp.

What will also further be discussed is the influence of the second coordination sphere on the LF parameters of $[\text{Ni}(\text{dcpp})_2]^{2+}$. This is carried out by coordinating the Lewis acid $\text{Sc}[\text{OTf}]_3$ to the ligand carbonyl groups and measuring changes to the LF states using absorption spectroscopy.

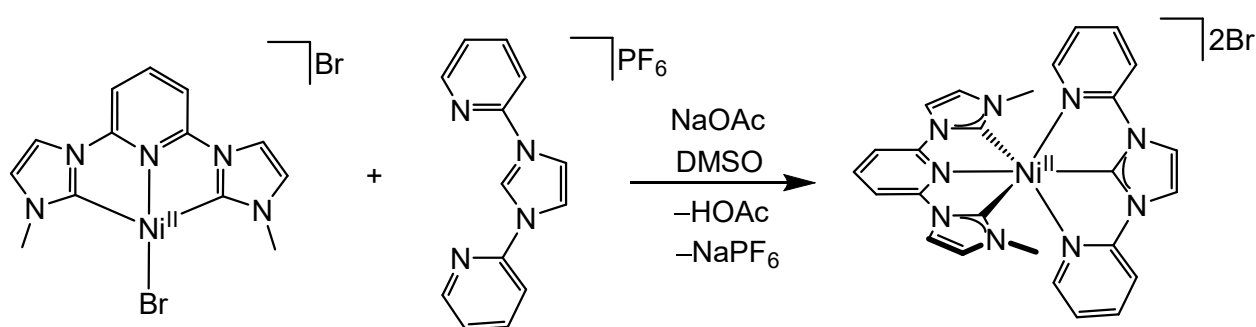
Supporting Information

Found on page 192

3.4.1 Increasing σ -Donation

It is well known that nickel(II) unlike its heavier analogues Pt^{II} and Pd^{II} can form octahedral complexes, this is a result of Ni^{II} containing a weaker intrinsic LF splitting.^[101] However, there is a boundary where this is not the case and it becomes more energetically favourable to adopt square planar coordination over octahedral. A strong ligand field is required for favourable separate ES ordering and so a balance is required. Few octahedral Ni^{II} complexes containing carbenes have been reported,^[198–200] but combination of CNC and NCN ligands can potentially provide a strong ligand field with three carbenes that is not too strong.

Synthesis



Scheme 3.3: Synthesis route of $[\text{Ni}(\text{CNC})(\text{NCN})]^{2+}$ from the known bromide CNC Ni^{II} complex $[\text{NiBr}(\text{CNC})]\text{Br}$,^[203] NaOAc acts as a weak base to deprotonate the H-NCN⁺ pro-ligand to the carbene (see section 6.4, pg 192 for details)

Structural Characterization

To further evaluate photophysical properties it was first required to verify if the complex was coordinated as octahedral or square planar via single-crystal XRD. The complex $[\text{Ni}(\text{CNC})(\text{NCN})][\text{PF}_6]_2$ crystallized in the monoclinic space group $P2_1/c$ with two independent cations in the asymmetric unit.

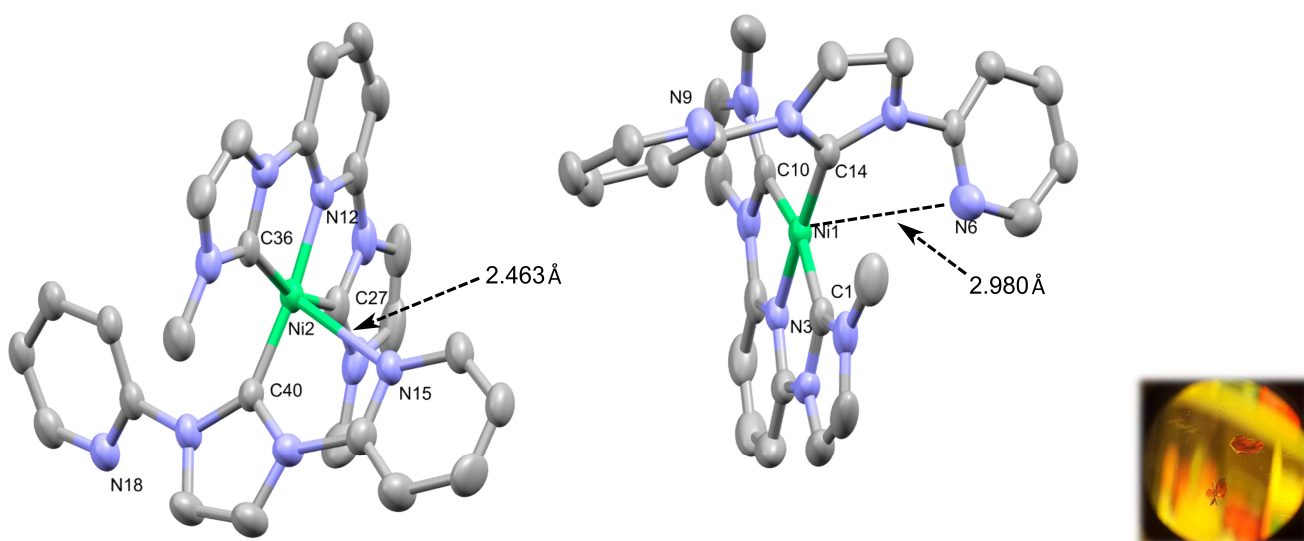


Figure 3.1: Molecular structures of cation $[\text{Ni}(\text{CNC})(\text{NCN})]^{2+}$ with photo of crystals. Structures show 4+1 coordination (left) and square planar coordination (right). Thermal ellipsoids are displayed at 50% probability. Hydrogen atoms, counterions, and solvent molecules are omitted for clarity.

Table 3.1: Selected bond lengths/Å and angles/deg of the two cations of $[\text{Ni}(\text{CNC})(\text{NCN})]^{2+}$, for comparison also obtained from DFT calculations.

	exp / Å	DFT / Å		exp / deg	DFT / deg
Ni(1) – C(14)	1.856(4)	2.003	C(14) – Ni(1) – N(3)	177.70(15)	173.00
Ni(1) – N(3)	1.862(3)	2.076	C(14) – Ni(1) – C(1)	98.01(17)	106.92
Ni(1) – C(1)	1.920(4)	2.084	N(3) – Ni(1) – C(1)	81.26(16)	76.40
Ni(1) – C(10)	1.924(4)	2.086	C(14) – Ni(1) – C(10)	99.61(19)	100.53
Ni(2) – C(36)	1.920(4)	2.092	N(3) – Ni(1) – C(10)	81.24(17)	76.52
Ni(2) – N(12)	1.883(3)	2.099	C(1) – Ni(1) – C(10)	162.17(18)	152.47
Ni(2) – C(27)	1.903(4)	2.093	C(40) – Ni(2) – N(12)	172.86(15)	171.44
Ni(2) – C(40)	1.860(4)	2.002	C(40) – Ni(2) – C(36)	99.95(17)	101.34
Ni(2) – C(15)	2.436(3)	2.066	N(12) – Ni(2) – C(36)	80.29(16)	75.93
			C(40) – Ni(2) – C(27)	98.31(18)	105.78
			N(12) – Ni(2) – C(27)	80.71(17)	75.74
			C(36) – Ni(2) – C(27)	160.39(18)	151.02

What is clear from the structural analysis of this complex is that the LF strength imposed on Ni^{II} with the CNC and NCN ligands is too strong and the complex adopts a square planar and 4+1 coordination. The bond angle C–Ni–C is a restrained 162.17° due to five-membered nature of the CNC ligand, bond lengths of the centrally coordinated atoms vary from 1.856 – 1.924 Å. The analysis also shows one cation with a 4+1 coordination, the bond length Ni(2) – N(15) is very long 2.436(3) Å, and can most likely be viewed as a weak interaction rather than a genuine single bond. In both cases (square planar (figure 3.2) and 4+1) the orbitals with z-components are lowered in energy (in particular d_{z^2}). This will lead to spin pairing i.e. a singlet ground state (figure 3.2).

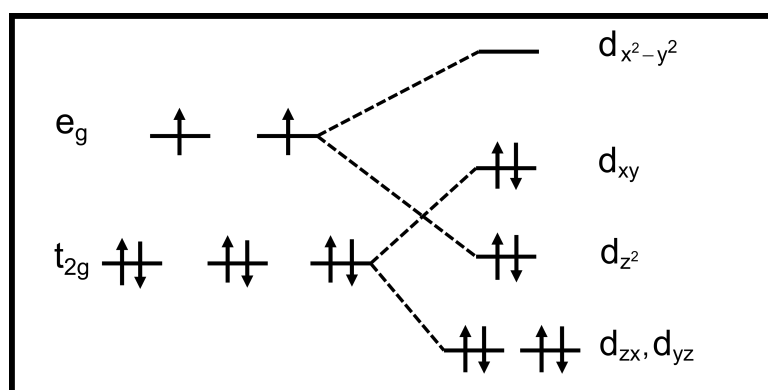


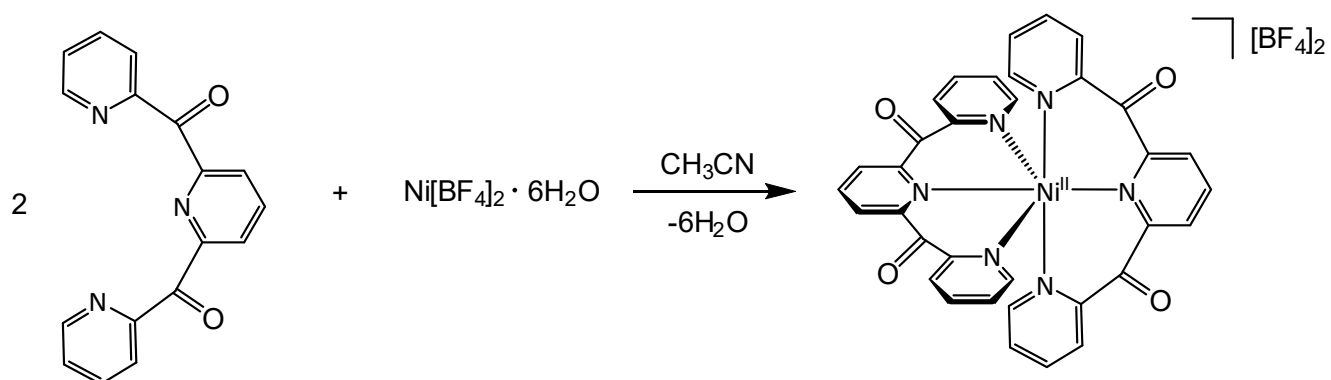
Figure 3.2: Ligand field splitting diagram for square planar coordinated complexes. Orbitals with z-components are lowered in energy. The effect is similar with 4+1 coordination but to a lesser extent.

The Tanabe-Sugano diagram for d^8 octahedrons no longer applies to this complex. It is clear that if strong σ -donors are used to increase the LF splitting for Ni^{II}, they would have to be used in conjunction with a more rigid or cage ligand to maintain an octahedral coordination.

3.4.2 Increasing π -Accepting

Introduction of π -accepting ligands to a TM is an alternative way to increase LF splitting. The dcpp ligand contains two carbonyl groups as strong π -acceptors, this ligand also offers additional potential to enhance its accepting capability via Lewis acid coordination. This can help further explore the effect of π -accepting ligand behavior on LF states. The method of Lewis acid coordination has been already successfully used with Mn^{IV} complex (**37²⁺**), where Lewis acid (Sc[OTf]₃) coordination significantly enhanced the GS oxidation potential of the complex.^[177]

Synthesis



Scheme 3.4: Synthesis route of $[\text{Ni}(\text{dcpp})_2]^{2+}$. (see section 6.4, pg 192 for details)

Structural Characterization

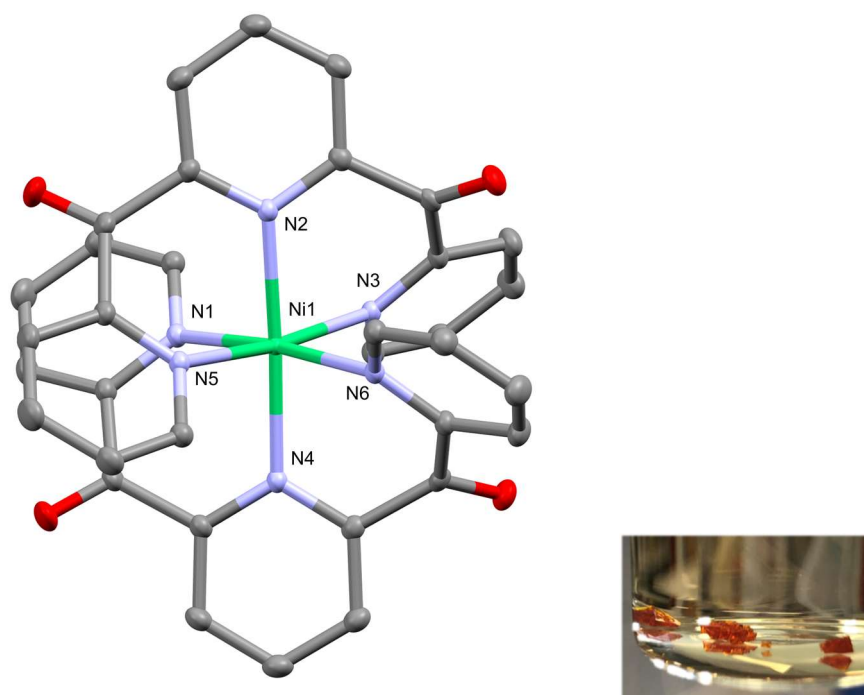


Figure 3.3: Molecular structure of the cation $[\text{Ni}(\text{dcpp})_2]^{2+}$ with photo of crystals. Thermal ellipsoids are displayed at 50% probability. Hydrogen atoms, counterions, and solvent molecules are omitted for clarity.

Table 3.2: Selected bond lengths/Å and angles/deg of the cation of $[\text{Ni}(\text{dcp})_2]^{2+}$, for comparison also obtained from DFT calculations.

	exp / Å	DFT / Å		exp / deg	DFT / deg
Ni(1) – N(2)	2.0819(11)	2.087	N(2) – Ni(1) – N(4)	177.48(6)	179.96
Ni(1) – N(1)	2.0939(11)	2.115	N(2) – Ni(1) – N(1)	92.07(4)	88.22
Ni(1) – N(3)	2.0967(11)	2.114	N(2) – Ni(1) – N(6)	94.83(4)	88.22
Ni(1) – N(4)	2.0819(11)	2.086	N(2) – Ni(1) – N(5)	86.16(4)	91.74
Ni(1) – N(5)	2.0939(11)	2.115	N(2) – Ni(1) – N(3)	86.94(4)	91.78
Ni(1) – N(6)	2.0967(11)	2.114	N(4) – Ni(1) – N(5)	92.07(4)	88.21
			N(4) – Ni(1) – N(1)	86.16(4)	91.77
			N(4) – Ni(1) – N(3)	94.83(4)	88.25
			N(4) – Ni(1) – N(6)	86.94(4)	91.76
			N(5) – Ni(1) – N(3)	173.10(4)	176.46

As seen from XRD analysis the homoleptic $[\text{Ni}(\text{dcp})_2]^{2+}$ complex is octahedral. With N–Ni–N bond angles close to 180° , the average Ni–N bond length ranges from 2.0819 – 2.0967 Å. With and octahedral coordination the position of LF states can be determined.

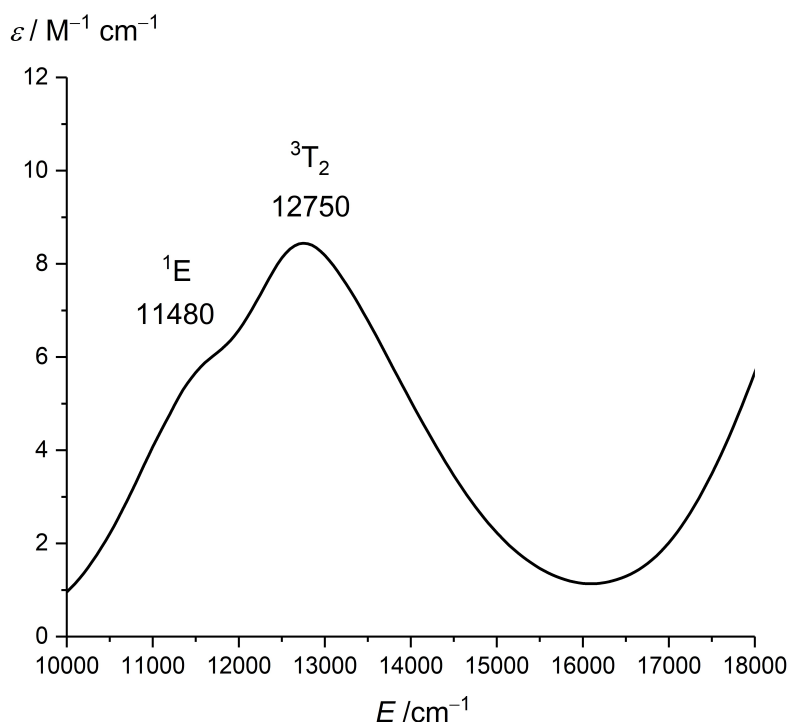


Figure 3.4: UV/Vis/NIR spectrum of [Ni(dcpp)₂][PF₆]₂ in acetonitrile with absorption band assignments.

The absorption spectrum of [Ni(dcpp)₂][PF₆]₂ shows LF states ³T₂ and ¹E are mixed. The ¹E state is seen as a lower energy shoulder (11 480 cm⁻¹) on the ³T₂ state (12 750 cm⁻¹), this lack of separation ($\Delta E = 1270 \text{ cm}^{-1}$) hinders any potential SF emission. The separation as seen in the absorption spectrum is comparable to [Ni(ddpd)₂]²⁺ (**43**²⁺) ($\Delta E = 1400 \text{ cm}^{-1}$) with the ¹E state also seen as a lower energy shoulder (11 300 cm⁻¹) on the ³T₂ state (12 700 cm⁻¹). The ³T₁ band is masked by CT bands and cannot be detected in the absorption spectrum preventing Racah *B* calculation. Increasing the π -accepting nature of the ligand to this extent does not have the desired effect of splitting the LF states sufficiently.

The dcpp ligand enables the possibility of further increase in the π -accepting effect, by coordinating a Lewis acid to the carbonyl groups on the ligand. Coordination of 2 eq of Sc[OTf]₃ gave an unexpected outcome (figure 3.5).

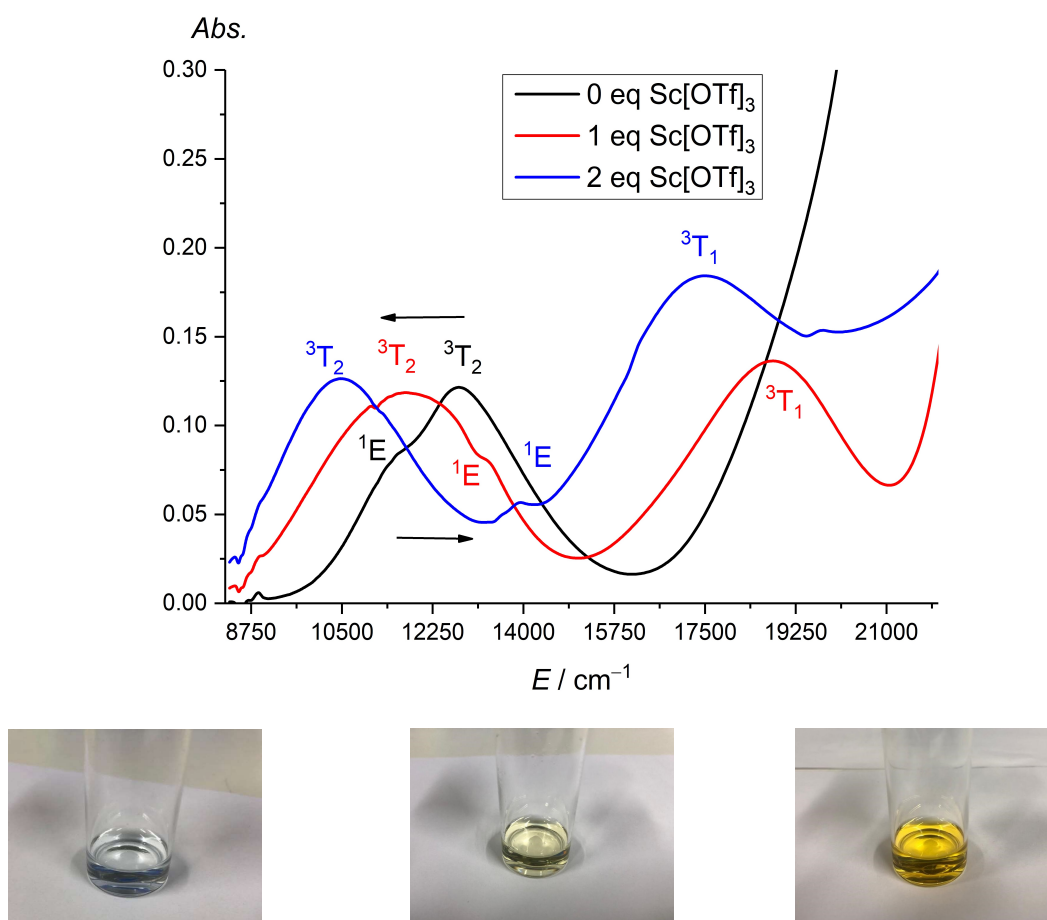


Figure 3.5: UV/Vis/NIR spectra of $[\text{Ni}(\text{dcpp})_2][\text{PF}_6]_2$ in acetonitrile following addition of 1–2 eq of $\text{Sc}[\text{OTf}]_3$. Photos of $[\text{Ni}(\text{dcpp})_2][\text{PF}_6]_2$ in acetonitrile (right) following addition of 1 eq of $\text{Sc}[\text{OTf}]_3$ (middle) and 2 eq of $\text{Sc}[\text{OTf}]_3$ (left).

It could be expected that with an increase in the π -accepting effect the energy of the t_{2g} orbitals would be more stabilized and Δ_o would increase, moving 3T_2 state to higher energy. Although the effects of increased π -acceptance on the 1E state are not clear, it could also be surmised that there would be an increase in the nephelauxetic effect resulting from increased electron delocalization and enhanced M-L covalency moving the 1E state to lower energy (however, the opposite occurred experimentally).^[82] As the equivalence of $\text{Sc}[\text{OTf}]_3$ increases (up to 2 eq) Δ_o decreases, with a shift of the 3T_2 state to lower energy (1 eq $\text{Sc}[\text{OTf}]_3 = 11\,730\text{ cm}^{-1}$ and 2 eq $\text{Sc}[\text{OTf}]_3 = 10\,430\text{ cm}^{-1}$). The energy of the 1E state moves to higher energies with increased $\text{Sc}[\text{OTf}]_3$ (1 eq $\text{Sc}[\text{OTf}]_3 = 13\,300\text{ cm}^{-1}$ and 2 eq $\text{Sc}[\text{OTf}]_3 = 13\,910\text{ cm}^{-1}$). The increase in Racah B parameter for the Lewis acid coordinated complexes of 954 cm^{-1} (1 eq $\text{Sc}[\text{OTf}]_3$) and 1205 cm^{-1} (2 eq $\text{Sc}[\text{OTf}]_3$) also reflects this change.

This unexpected shift of the 3T_2 state to lower energies could be the result of the Lewis acid coordination decreasing the σ -donation of the dcpp ligand, this would lead to a lowering of Δ_o in-line with experiment. The increase in energy of 1E state and increase in energy of the Racah B parameter implies a decrease in covalency of the M-L σ -bonds, this could be a result of

changes in coordination geometry upon addition of $\text{Sc}[\text{OTf}]_3$, which would alter the nephelauxetic effect.

3.4.3 Conclusion

SF luminescence from octahedral Ni^{II} complexes remains a challenge due to the close proximity of $^3\text{T}_2$ and ^1E LF states. This leads to mixing of states and deactivation of the ^1E state preventing SF emission. Increasing the LF splitting is a clear way to separate these states and this can be done by increasing the σ -donation or π -accepting natures of coordinating ligands.

A significant challenge with Ni^{II} is that it adopts a square planer geometry in strong LFs, and so a balance of LF strength is required. This study shows that as σ -donation increases with the combination of carbene ligands CNC and NCN, Ni^{II} adopts a square planar or 4+1 configuration i.e. dissociates one to two axial pyridine ligands. The LF strength accompanying ligands with three carbene moieties is too strong. If the strategy to separate LF states in Ni^{II} is by increasing LF splitting with σ -donors, it should be accompanied with a very rigid or cage strong field ligands, to ensure octahedral geometry is maintained.^[197–201]

Increasing the π -accepting natures of the ligands is another way to increase LF splitting with stabilization of the $\text{t}_{2\text{g}}$ orbitals. $[\text{Ni}(\text{dcpp})_2]^{2+}$ even with strongly π -accepting ligands still shows mixing of LF states demonstrating LF splitting is not high enough. To further enhance the π -accepting character, a second sphere coordination is introduced with the Lewis acid $\text{Sc}[\text{OTf}]_3$. What is seen is that increased ligand π -accepting has a more multifaceted effect on LF splitting and LF states. This is demonstrated by unanticipated shift of the $^3\text{T}_2$ state to lower energies and the ^1E state to higher energies. Further investigation is required to determine how the π -accepting nature of ligands affect Ni^{II} LF states, this will help understand ligand requirements needed in the pursuit of SF luminescence from octahedral Ni^{II} complexes.

4. Summary and Outlook

In recent years, there have been great advances made in the field of photoactive 3d transition metal complexes. However, little research has been devoted to octahedral Mn^{IV} and Ni^{II} compounds. It is evident from this thesis that the photophysical properties of octahedral Mn^{IV} complexes are of great interest fundamentally and for eventual use in applications.^[16,21]

Herein is the report of the successful preparation of the emissive strongly dual state photooxidative [Mn(dgpy)₂]⁴⁺ (dgpy = 2,6-diguanidylpyridine) complex. Synthesis, characterization and isolation of [Mn(dgpy)₂]ⁿ⁺ (n = 2–4) in three oxidative states aids with key understanding as to the importance of ligand design; this represents one of the very few octahedral Mn^{IV} complexes supported solely by nitrogen donors.^[127] The tridentate dgpy ligand combines accepting (pyridines) and strongly donating (guanidine) moieties capable of offering a strong LF that can stabilise the electron rich high-spin d⁵ [Mn(dgpy)₂]²⁺, a Jahn-Teller distorted high-spin d⁴ [Mn(dgpy)₂]³⁺, and an electron poor d³ [Mn(dgpy)₂]⁴⁺ complex. What is also apparent through CASSCF is that the dgpy ligand gives the desired excited state ligand field state ordering.

There is only one other known example of octahedral Mn^{IV} emission^[174] and so the photophysics of these compounds are not well understood. [Mn(dgpy)₂]⁴⁺ provides a second example of long lived phosphorescence ($\tau = 1.6$ ns) from a mixed ²MC/²LMCT state that is significantly red shifted to 1435 nm,^[21,174] highlighting the range at which emission can be achieved with octahedral Mn^{IV} complexes. An important finding (aided by DFT studies) is related to the bimolecular reactivity of this compound.^[62] [Mn(dgpy)₂]⁴⁺ photooxidises very challenging substrates ranging up to benzene and CH₃CN; such reactivity demonstrates the strongest practical photooxidative power possessed by a transition metal complex.^[60] Even more uniquely [Mn(dgpy)₂]⁴⁺ displays unconventional dual state reactivity upon NIR irradiation,^[2,62] oxidising a lower potential substrate (naphthalene) dynamically from a mixed ²LMCT/²MC state and high potential substrates (benzene) statically from a ⁴LMCT state via a pre-organised CH₃CN (solvent) intermediate. Unusually slow ISC (780 fs) enables this reactivity from the ⁴LMCT state.

These results add significant understanding to manganese transition metal (photo)chemistry, helping further understand the requirements for isolation of octahedral Mn^{IV} complexes. What is shown is the range at which emission can be found, the photooxidative potential and the possibility of accessing the full oxidising power of [Mn(dgpy)₂]⁴⁺ due to static quenching and slow ISC. It also shows how complex design can lead to panchromatic absorption and the possibility of using low energy NIR excitation for such photooxidative applications.^[206]

With such understanding, it can be concluded that strongly donating ligands are required to stabilise Mn^{IV} centres and low energy LMCT absorption bands should be pushed to higher energies to get higher energy emission. Thus, ligand design is paramount and using tridentate ligands containing carbene donors can offer these characteristics. It is clear that the range at

which Mn^{IV} emission can occur is large, thus more Mn^{IV} examples are required to further understand the nephelauxetic effect and CT state admixtures associated with Mn^{IV} complexes. The photooxidative capabilities of [Mn(dgpy)₂]⁴⁺ show how the utilization of both static and dynamic quenching can aid with photoredox reactions. Not much is understood regarding ISC rates of Mn^{IV} but it is apparent from this case that 'slower' ISC rates are not necessarily detrimental for photoreactivity.^[50] Lastly, future studies with such a compound class could focus on photoredox catalysis. To do this it would be important to make complexes such as [Mn(dgpy)₂]⁴⁺ water stable, and to reduce the GS oxidation potential. Lowering the GS oxidation potential is important to enhance GS stability and ensure the possibility of catalyst recovery with a stable sacrificial oxidant. This could be accomplished with bulky strongly donating ligands, which would both lower the GS potential and reduce complex substitutional lability.^[29]

The investigation of a series of five Ni^{II} octahedral complexes highlights the challenges associated with LF strength in d⁸ systems. In order to achieve MC SF emission from such compounds, strong LFs are required for MC states to be lowest in energy.^[187,189] However, a limit is reached when the d⁸ Ni^{II} system adopts a square planar geometry.^[186] The complexes described i.e. [Ni(dgpy)₂]²⁺, [Ni(terpy)₂]²⁺ (terpy = 2,2';6',2''-terpyridine), [Ni(phen)₂]²⁺ (phen = 1,10-phenanthroline), [Ni(ddpd)₂]²⁺ (ddpd = *N,N'*-dimethyl-*N,N'*-dipyridin-2-ylpyridine-2,6-diamine) and [Ni(tpe)₂]²⁺ (tpe = 1,1,1-tris(pyrid-2-yl)ethane), each contain medium to strong field ligands that have yielded emission with other metals, e.g. Cr^{III}, Co^{III}, Mn^{IV}.^[77,79,202] However, these Ni^{II} complexes do not show emission even at high hydrostatic pressures. It is clear from DFT and coupled surface studies that detrimental mixing of intra- and interconfigurational states leads to the non-radiative decay.^[188] This mixing can be seen as 'intensity borrowing' using absorption spectroscopy, with the spin forbidden states shown as shoulders on the spin allowed absorption bands. Evidently, it is important to separate these states with strong LF, so that mixing cannot occur while also maintaining an octahedral ligand environment. Attempts to further increase ligand field strength via σ -donation by *N*-heterocyclic carbenes resulted with the square planar [Ni(CNC)(NCN)][PF₆]₂ (CNC = (1,1'-(pyridin-2,6-diyl)bis(3-methyl-1H-imidazol-3-ylidene)) and (NCN = (1,3-bis(2-pyridyl)imidazolylidene). Attempts to do the same with a more π -accepting ligand gave octahedrally coordinated [Ni(dcpp)₂]²⁺ (dcpp = 2,6-bis(2-carboxypyridyl)pyridine), however the ligand field states were again mixed. Coordination of the Lewis acid Sc[OTf]₃ shows that a second sphere coordination can influence ligand field states. Coordination showed an unanticipated shift of the ³T₂ state to lower energies and ¹E state to higher energies.

Further investigation is required to determine how the π -accepting nature of ligands affect Ni^{II} LF states, and more careful ligand design is required in order to increase ligand field strength and maintain an octahedral ligand field. This could be overcome by using more sterically demanding strong field ligands such as cage ligands to impart a strong field and impose an octahedral coordination.^[201]

5. References

- [1] L. Li, J. Lin, N. Wu, S. Xie, C. Meng, Y. Zheng, X. Wang, Y. Zhao, *Energy Built Environ.* **2022**, *3*, 139–157.
- [2] D. M. Arias-Rotondo, J. K. McCusker, *Chem. Soc. Rev.* **2016**, *45*, 5803–5820.
- [3] A. Carella, F. Borbone, R. Centore, *Front. Chem.* **2018**, *6*, 481.
- [4] A. Hagfeldt, G. Boschloo, L. Sun, L. Kloo, H. Pettersson, *Chem. Rev.* **2010**, *110*, 6595–6663.
- [5] H. Xu, R. Chen, Q. Sun, W. Lai, Q. Su, W. Huang, X. Liu, *Chem. Soc. Rev.* **2014**, *43*, 3259–3302.
- [6] S. Aghazada, M. Nazeeruddin, *Inorganics* **2018**, *6*, 52.
- [7] J. M. R. Narayanam, C. R. J. Stephenson, *Chem. Soc. Rev.* **2011**, *40*, 102–113.
- [8] C. Förster, K. Heinze, *Chem. Soc. Rev.* **2020**, *49*, 1057–1070.
- [9] O. S. Wenger, *J. Am. Chem. Soc.* **2018**, *140*, 13522–13533.
- [10] N. Haque, A. Hughes, S. Lim, C. Vernon, *Resources* **2014**, *3*, 614–635.
- [11] A.W. Adamson, W.L. Waltz, E. Zinato, D.W. Watts, P.D. Fleischauer, R.D. Lindholm, *Chem. Rev.* **1968**, *68*, 541–585.
- [12] W. Zhang, R. Alonso-Mori, U. Bergmann, C. Bressler, M. Chollet, A. Galler, W. Gawelda, R. G. Hadt, R. W. Hartsock, T. Kroll, K. S. Kjær, K. Kubiček, H. T. Lemke, H. W. Liang, D. A. Meyer, M. M. Nielsen, C. Purser, J. S. Robinson, E. I. Solomon, Z. Sun, D. Sokaras, T. B. van Driel, G. Vankó, T.-C. Weng, D. Zhu, K. J. Gaffney, *Nature* **2014**, *509*, 345–348.
- [13] O. S. Wenger, *Chem. Eur. J.* **2019**, *25*, 6043–6052.
- [14] M. Kaupp, *J. Comput. Chem.* **2007**, *28*, 320–325.
- [15] A. Steffen, B. Hupp, *Comprehensive inorganic chemistry III*. Vol. 2, (Ed.: J. Reedijk), Elsevier, **2021**.
- [16] C. Wegeberg, O. S. Wenger, *JACS Au* **2021**, *1*, 1860–1876.
- [17] P. Chábera, Y. Liu, O. Prakash, E. Thyrhaug, A. E. Nahhas, A. Honarfar, S. Essén, L. A. Fredin, T. C. B. Harlang, K. S. Kjær, K. Handrup, F. Ericson, H. Tatsuno, K. Morgan, J. Schnadt, L. Häggström, T. Ericsson, A. Sobkowiak, S. Lidin, P. Huang, S. Styring, J. Uhlig, J. Bendix, R. Lomoth, V. Sundström, P. Persson, K. Wärnmark, *Nature* **2017**, *543*, 695–699.
- [18] W. Leis, M. A. Argüello Cordero, S. Lochbrunner, H. Schubert, A. Berkefeld, *J. Am. Chem. Soc.* **2022**, *144*, 1169–1173.
- [19] Y. Tanabe, S. Sugano, *J. Phys. Soc. Jpn.* **1954**, *9*, 753–766.
- [20] Y. Tanabe, S. Sugano, *J. Phys. Soc. Jpn.* **1954**, *9*, 766–799.
- [21] W. R. Kitzmann, J. Moll, K. Heinze, *Photochem. Photobiol. Sci.* **2022**, *21*, 1309–1331.
- [22] A. D. Kirk, *Chem. Rev.* **1999**, *99*, 1607–1640.
- [23] M. Maestri, F. Bolletta, L. Moggi, V. Balzani, M. S. Henry, and M. Z. Hoffman, *J. Am. Chem. Soc.* **1978**, *100*, 2694–2701.
- [24] Dorn, M. East, N. R. Förster, C. Kitzmann, W. R. Moll, J. Reichenauer, F. Reuter, T. Stein, L. Heinze, K. *Comprehensive inorganic chemistry III (Third Edition)*. Vol. 8, (Ed.: J. Reedijk), Elsevier, **2023**.
- [25] L. Stein, C. Wang, C. Förster, U. Resch-Genger, K. Heinze, *Dalton Trans.* **2022**, *51*, 17664–17670.

-
- [26] M. Dorn, J. Kalmbach, P. Boden, A. Pöpcke, S. Gómez, C. Förster, F. Kuczelinis, L. M. Carrella, L. A. Büldt, N. H. Bings, E. Rentschler, S. Lochbrunner, L. González, M. Gerhards, M. Seitz, K. Heinze, *J. Am. Chem. Soc.* **2020**, *142*, 7947–7955.
- [27] Robert O. C. Hart, Simon G. Bott, Jerry L. Atwood, Stephen R. Cooper, *J. Chem. Soc., Chem. Commun.* **1992**, *21*, 894–895.
- [28] M. K. Chan, W. H. Armstrong, *Inorg. Chem.* **1989**, *28*, 3777–3779.
- [29] B. Wittwer, N. Dickmann, S. Berg, D. Leitner, L. Tesi, D. Hunger, R. Gratzl, J. van Slageren, N. I. Neuman, D. Munz, S. Hohloch, *Chem. Commun.* **2022**, *58*, 6096–6099.
- [30] A. P. Forshaw, R. P. Bontchev, J. M. Smith, *Inorg. Chem.* **2007**, *46*, 3792–3794.
- [31] G. Das, P. K. Bharadwaj, D. Ghosh, B. Chaudhuri, R. Banerjee, *Chem. Commun.* **2001**, *37*, 323–324.
- [32] S. Romain, C. Baffert, C. Duboc, J.-C. Leprêtre, A. Deronzier, M.-N. Collomb, *Inorg. Chem.* **2009**, *48*, 3125–3131.
- [33] H. Yoon, Y. Morimoto, Y.-M. Lee, W. Nam, S. Fukuzumi, *Chem. Commun.* **2012**, *48*, 11187–11189.
- [34] S. I. Shylin, J. L. Pogrebetsky, A. O. Husak, D. Bykov, A. Mokhir, F. Hampel, S. Shova, A. Ozarowski, E. Gumienna-Kontecka, I. O. Fritsky, *Chem. Commun.* **2021**, *57*, 11060–11063.
- [35] O. S. Wenger, S. Bénard, H. U. Güdel, *Inorg. Chem.* **2002**, *41*, 5968–5977.
- [36] S. Campagna, F. Puntoriero, F. Nastasi, G. Bergamini, V. Balzani, *Top. Curr. Chem.* **2007**, *280*, 1–36.
- [37] P. W. Atkins, J. de Paula, *Physical Chemistry*. 9th ed., W.H Freeman and Company, New York, **2010**.
- [38] J. R. Lakowicz, *Principles of fluorescence spectroscopy*. 3rd ed., Springer, New York, **2006**.
- [39] T. J. Penfold, E. Gindensperger, C. Daniel, C. M. Marian, *Chem. Rev.* **2018**, *118*, 6975–7025.
- [40] R. Englman, J. Jortner, *Mol. Phys.* **1970**, *18*, 145–164.
- [41] W. R. Browne, J. G. Vos, *Coord. Chem. Rev.* **2001**, *219-221*, 761–787.
- [42] J. V. Caspar, E. M. Kober, B. P. Sullivan, T. J. Meyer, *J. Am. Chem. Soc.* **1982**, *104*, 630–632.
- [43] L. A. Büldt, X. Guo, A. Prescimone, O. S. Wenger, *Angew. Chem. Int. Ed.* **2016**, *55*, 11247–11250.
- [44] W. R. Kitzmann, K. Heinze, *Angew. Chem. Int. Ed.* **2022**, e202213207.
- [45] R. Englman, *J. Lumin.* **1970**, *1, 2*, 134–142.
- [46] A. Beeby, I. M. Clarkson, R. S. Dickins, S. Faulkner, D. Parker, *J. Chem. Soc., Perkin Trans. 2* **1999**, 493–503.
- [47] C. M. Marian, *WIREs Comput. Mol. Sci.* **2012**, *2*, 187–203.
- [48] J. K. McCusker, *Acc. Chem. Res.* **2003**, *36*, 876–887.
- [49] W. R. Kitzmann, C. Ramanan, R. Naumann, K. Heinze, *Dalton Trans.* **2022**, *51*, 6519–6525.
- [50] L. S. Forster, *Coord. Chem. Rev.* **2006**, *250*, 2023–2033.
- [51] E. V. Dose, M. A. Hoselton, N. Sutin, M. F. Tweedle, L. J. Wilson, *J. Am. Chem. Soc.* **1978**, *100*, 1141–1147.

-
- [52] P. J. Gonçalves, L. de Boni, I. E. Borissevitch, S. C. Zílio, *J. Phys. Chem. A* **2008**, *112*, 6522–6526.
- [53] C. Antolini, C. D. Spellman, C. J. Otolski, G. Doumy, A. M. March, D. A. Walko, C. Liu, X. Zhang, B. T. Young, J. E. Goodwill, D. Hayes, *J. Am. Chem. Soc.* **2022**, *144*, 22514–22527.
- [54] G. B. Shaw, C. D. Grant, H. Shirota, E. W. Castner, G. J. Meyer, L. X. Chen, *J. Am. Chem. Soc.* **2007**, *129*, 2147–2160.
- [55] L. Bergmann, G. J. Hedley, T. Baumann, S. Bräse, I. D. W. Samuel, *Sci. Adv.* **2016**, *2*, e1500889.
- [56] F. Strieth-Kalthoff, M. J. James, M. Teders, L. Pitzer, F. Glorius, *Chem. Soc. Rev.* **2018**, *47*, 7190–7202.
- [57] C. B. Larsen, O. S. Wenger, *Chem. Eur. J.* **2018**, *24*, 2039–2058.
- [58] D. Genovese, M. Cingolani, E. Rampazzo, L. Prodi, N. Zaccheroni, *Chem. Soc. Rev.* **2021**, *50*, 8414–8427.
- [59] V. Balzani, L. Moggi, M. F. Manfrin, F. Bolletta, *Coord. Chem. Rev.* **1975**, *15*, 321–433.
- [60] D. Kim, T. S. Teets, *Chem. Phys. Rev.* **2022**, *3*, 21302.
- [61] N. Sharma, J. Jung, K. Ohkubo, Y.-M. Lee, M. E. El-Khouly, W. Nam, S. Fukuzumi, *J. Am. Chem. Soc.* **2018**, *140*, 8405–8409.
- [62] C. Förster, K. Heinze, *Chem. Phys. Rev.* **2022**, *3*, 41302.
- [63] F. Reichenauer, C. Wang, C. Förster, P. Boden, N. Ugur, R. Báez-Cruz, J. Kalmbach, L. M. Carrella, E. Rentschler, C. Ramanan, G. Niedner-Schatteburg, M. Gerhards, M. Seitz, U. Resch-Genger, K. Heinze, *J. Am. Chem. Soc.* **2021**, *143*, 11843–11855.
- [64] S. Otto, A. M. Nauth, E. Ermilov, N. Scholz, A. Friedrich, U. Resch-Genger, S. Lochbrunner, T. Opatz, K. Heinze, *ChemPhotoChem* **2017**, *1*, 344–349.
- [65] R. A. Marcus, *Angew. Chem. Int. Ed. Engl.* **1993**, *32*, 1111–1121.
- [66] E. J. Piechota, G. J. Meyer, *J. Chem. Educ.* **2019**, *96*, 2450–2466.
- [67] R. A. Marcus, N. Sutin, *Biochim. Biophys. Acta, Bioenerg.* **1985**, *811*, 265–322.
- [68] A. Aydogan, R. E. Bangle, A. Cadranel, M. D. Turlington, D. T. Conroy, E. Cauët, M. L. Singleton, G. J. Meyer, R. N. Sampaio, B. Elias, L. Troian-Gautier, *J. Am. Chem. Soc.* **2021**, *143*, 15661–15673.
- [69] J. Olmsted, T. J. Meyer, *J. Phys. Chem.* **1987**, *91*, 1649–1655.
- [70] S. V. Rosokha, J. K. Kochi, *Acc. Chem. Res.* **2008**, *41*, 641–653.
- [71] S. Sittel, R. Naumann, K. Heinze, *Front. Chem.* **2022**, *10*, 887439.
- [72] J. P. Barham, B. König, *Angew. Chem. Int. Ed.* **2020**, *59*, 11732–11747.
- [73] S. Wu, J. Kaur, T. A. Karl, X. Tian, J. P. Barham, *Angew. Chem. Int. Ed.* **2022**, *61*, e202107811.
- [74] H. Huang, Z. M. Strater, M. Rauch, J. Shee, T. J. Sisto, C. Nuckolls, T. H. Lambert, *Angew. Chem. Int. Ed.* **2019**, *58*, 13318–13322.
- [75] K. S. Kjær, N. Kaul, O. Prakash, P. Chábera, N. W. Rosemann, A. Honarfar, O. Gordivska, L. A. Fredin, K.-E. Bergquist, L. Häggström, T. Ericsson, L. Lindh, A. Yartsev, S. Styring, P. Huang, J. Uhlig, J. Bendix, D. Strand, V. Sundström, P. Persson, R. Lomoth, K. Wärnmark, *Science* **2019**, *363*, 249–253.
- [76] P. Herr, C. Kerzig, C. B. Larsen, D. Häussinger, O. S. Wenger, *Nat. Chem.* **2021**, *13*, 956–962.

-
- [77] S. Treiling, C. Wang, C. Förster, F. Reichenauer, J. Kalmbach, P. Boden, J. P. Harris, L. M. Carrella, E. Rentschler, U. Resch-Genger, C. Reber, M. Seitz, M. Gerhards, K. Heinze, *Angew. Chem. Int. Ed.* **2019**, *58*, 18075–18085.
- [78] S. Otto, M. Grabolle, C. Förster, C. Kreitner, U. Resch-Genger, K. Heinze, *Angew. Chem. Int. Ed.* **2015**, *54*, 11572–11576.
- [79] S. Otto, M. Dorn, C. Förster, M. Bauer, M. Seitz, K. Heinze, *Coord. Chem. Rev.* **2018**, *359*, 102–111.
- [80] Oppenheim, J. Miller, J., *Tanabe-Sugano for Mathematica*.
<https://github.com/JulesOpp/Tanabe-Sugano>, Accessed 08 May 2023.
- [81] P. W. Atkins, T. L. Overton, J. P. Rourke, M. T. Weller, F. A. Armstrong, *Inorganic Chemistry*. 5th ed., W.H Freeman and Company, New York, **2010**.
- [82] N. Sinha, P. Yaltseva, O. S. Wenger, *Angew. Chem. Int. Ed.* **2023**, e202303864.
- [83] L. Stein, P. Boden, R. Naumann, C. Förster, G. Niedner-Schatteburg, K. Heinze, *Chem. Commun.* **2022**, *58*, 3701–3704.
- [84] N. Sinha, J.-R. Jiménez, B. Pfund, A. Prescimone, C. Piguet, O. S. Wenger, *Angew. Chem. Int. Ed.* **2021**, *60*, 23722–23728.
- [85] M. G. Brik, A. M. Srivastava, *ECS J. Solid State Sci. Technol.* **2018**, *7*, R3079-R3085.
- [86] S. Otto, N. Scholz, T. Behnke, U. Resch-Genger, K. Heinze, *Chem. Eur. J.* **2017**, *23*, 12131–12135.
- [87] S. Otto, J. P. Harris, K. Heinze, C. Reber, *Angew. Chem. Int. Ed.* **2018**, *57*, 11069–11073.
- [88] H. Xiang, J. Cheng, X. Ma, X. Zhou, J. J. Chruma, *Chem. Soc. Rev.* **2013**, *42*, 6128–6185.
- [89] T. M. Stonelake, K. A. Phillips, H. Y. Otaif, Z. C. Edwardson, P. N. Horton, S. J. Coles, J. M. Beames, S. J. A. Pope, *Inorg. Chem.* **2020**, *59*, 2266–2277.
- [90] J. A. Treadway, G. F. Strouse, R. R. Ruminski, T. J. Meyer, *Inorg. Chem.* **2001**, *40*, 4508–4509.
- [91] A. K. Pal, S. Nag, J. G. Ferreira, V. Brochery, G. La Ganga, A. Santoro, S. Serroni, S. Campagna, G. S. Hanan, *Inorg. Chem.* **2014**, *53*, 1679–1689.
- [92] M. J. Cook, A. P. Lewis, G. S. G. McAuliffe, V. Skarda, *J. Chem. Soc., Perkin Trans. 2* **1984**.
- [93] D. B. Nemez, I. B. Lozada, J. D. Braun, J. A. G. Williams, D. E. Herbert, *Inorg. Chem.* **2022**, *61*, 13386–13398.
- [94] J. T. Yarranton, J. K. McCusker, *J. Am. Chem. Soc.* **2022**, *144*, 12488–12500.
- [95] D. W. Thompson, A. Ito, T. J. Meyer, *Pure Appl. Chem.* **2013**, *85*, 1257–1305.
- [96] T. J. Meyer, *Pure Appl. Chem.* **1986**, *58*, 1193–1206.
- [97] P. Chen, T. J. Meyer, *Chem. Rev.* **1998**, *98*, 1439–1478.
- [98] J. M. Lang, Z. A. Dreger, H. G. Drickamer, *J. Phys. Chem.* **1993**, *97*, 2289–2294.
- [99] E. Krausz, J. Ferguson, *Progress in Inorganic Chemistry*. Vol. 37, Wiley, Chichester, **1989**.
- [100] P. S. Wagenknecht, P. C. Ford, *Coord. Chem. Rev.* **2011**, *255*, 591–616.
- [101] P. Pyykko, *Chem. Rev.* **1988**, *88*, 563–594.
- [102] J. K. McCusker, *Science* **2019**, *363*, 484–488.
- [103] P. Chábera, L. Lindh, N. W. Rosemann, O. Prakash, J. Uhlig, A. Yartsev, K. Wärnmark, V. Sundström, P. Persson, *Coord. Chem. Rev.* **2021**, *426*, 213517.
- [104] P. S. Wagenknecht, P. C. Ford, *Coord. Chem. Rev.* **2011**, *255*, 591–616.

-
- [105] T. Reuter, A. Kruse, R. Schoch, S. Lochbrunner, M. Bauer, K. Heinze, *Chem. Commun.* **2021**, 57, 7541–7544.
- [106] J. A. Treadway, B. Loeb, R. Lopez, P. A. Anderson, F. R. Keene, T. J. Meyer, *Inorg. Chem.* **1996**, 35, 2242–2246.
- [107] C. Wang, S. Otto, M. Dorn, E. Kreidt, J. Lebon, L. Sršan, P. Di Martino-Fumo, M. Gerhards, U. Resch-Genger, M. Seitz, K. Heinze, *Angew. Chem. Int. Ed.* **2018**, 57, 1112–1116.
- [108] S. Otto, C. Förster, C. Wang, U. Resch-Genger, K. Heinze, *Inorg. Chem.* **2018**, 24, 12555–12563.
- [109] S. F. McClanahan, J. R. Kincaid, *J. Am. Chem. Soc.* **1986**, 108, 3840–3841.
- [110] R. G. Lucchini, M. Aschner, Y. Kim, M. Šarić, *Handbook on the Toxicology of Metals*. 4th ed., Elsevier, London, **2015**.
- [111] R. L. M. Baric, *Handbook on the toxicology of metals*. 3rd ed., Elsevier, London, **2007**.
- [112] J-B. Sortais, *Manganese Catalysis in Organic Synthesis*, Wiley-VCH Weinheim, Germany, **2022**.
- [113] D. S. Avila, R. L. Puntel, M. Aschner, *Met. Ions life Sci.* **2013**, 13, 199–227.
- [114] N. Cox, M. Retegan, F. Nesse, D. A. Pantazis, A. Boussac, W. Lubitz, *Science* **2014**, 345, 804–808.
- [115] C. Herrero, A. Quaranta, W. Leibl, A. W. Rutherford, A. Aukauloo, *Energy Environ. Sci.* **2011**, 4, 2353.
- [116] J. C. Vites, M. M. Lynam, *Coord. Chem. Rev.* **1995**, 146, 167–189.
- [117] W. M. Haynes, D. R. Lide, T. J. Bruno, *CRC Handbook of Chemistry and Physics 95th Edition*, CRC Press, Boca Raton, Florida, **2014**.
- [118] L. Hung, C. Chen, *Mater. Sci. Eng., R* **2002**, 39, 143–222.
- [119] M. H. Du, *J. Mater. Chem. C* **2014**, 2, 2475–2481.
- [120] M. D. Dramićanin, Ł. Marciniak, S. Kuzman, W. Piotrowski, Z. Ristić, J. Periša, I. Evans, J. Mitrić, V. Đorđević, N. Romčević, M. G. Brik, C.-G. Ma, *Light Sci. Appl.* **2022**, 11, 279.
- [121] Y. Qin, P. She, X. Huang, W. Huang, Q. Zhao, *Coord. Chem. Rev.* **2020**, 416, 213331.
- [122] N. G. Connelly, W. E. Geiger, *Chem. Rev.* **1996**, 96, 877–910.
- [123] G. W. Brudvig, R. H. Crabtree, *Progress in Inorganic Chemistry*. Vol. 37, Wiley, Chichester, **1989**.
- [124] D. M. Eichhorn, W. H. Armstrong, *Inorg. Chem.* **1990**, 29, 3607–3612.
- [125] P. Cieslik, P. Comba, B. Dittmar, D. Ndiaye, É. Tóth, G. Velmurugan, H. Wadepohl, *Angew. Chem. Int. Ed.* **2022**, 61, e202115580.
- [126] S. Wang, T. D. Westmoreland, *Inorg. Chem.* **2009**, 48, 719–727.
- [127] A. D. M.-N. Collomb, *Encyclopedia of Inorganic Chemistry*. 1st Ed., Wiley, Chichester, **2006**.
- [128] F.A. Cotton, G. Wilkinson, P.L. Gaus, *Advanced Inorganic Chemistry*. 2nd Ed., John Wiley & Sons, Toronto, **1987**.
- [129] P. Tao, S.-J. Liu, W.-Y. Wong, *Adv. Optical Mater.* **2020**, 8, 2000985.
- [130] S. Zhang, Y. Zhao, J. Zhou, H. Ming, C.-H. Wang, X. Jing, S. Ye, Q. Zhang, *Chemical Engineering Journal* **2021**, 421, 129886.
- [131] J. J. Alexander, H. B. Gray, *J. Am. Chem. Soc.* **1968**, 90, 4260–4271.
- [132] I. Syiemlieh, A. Kumar, S. D. Kurbah, A. K. De, R. A. Lal, *J. Mol. Struct.* **2018**, 1151, 343–352.

-
- [133] A. Saha, P. Majumdar, S. Goswami, *J. Chem. Soc., Dalton Trans.* **2000**, 1703–1708.
- [134] C. P. Basu, *Inorg. Chem.* **1992**, *31*, 4980–4986.
- [135] R. A. Lal, D. Basumatary, A. K. De, A. Kumar, *Transit. Met. Chem.* **2007**, *32*, 481–493.
- [136] D. Basumatary, R. A. Lal, A. Kumar, *J. Mol. Struct.* **2015**, *1092*, 122–129.
- [137] M. Bortoluzzi, J. Castro, A. Gobbo, V. Ferraro, L. Pietrobon, S. Antoniutti, *New J. Chem.* **2020**, *44*, 571–579.
- [138] V. Morad, I. Cherniukh, L. Pöttschacher, Y. Shynkarenko, S. Yakunin, M. V. Kovalenko, *Chem. Mater.* **2019**, *31*, 10161–10169.
- [139] J. Chen, Q. Zhang, F.-K. Zheng, Z.-F. Liu, S.-H. Wang, A.-Q. Wu, G.-C. Guo, *Dalton Trans.* **2015**, *44*, 3289–3294.
- [140] Y. Suffren, N. O'Toole, A. Hauser, E. Jeanneau, A. Brioude, C. Desroches, *Dalton Trans.* **2015**, *44*, 7991–8000.
- [141] L.-J. Xu, C.-Z. Sun, H. Xiao, Y. Wu, Z.-N. Chen, *Adv. Mater.* **2017**, *29*.
- [142] D. G. M. Wrighton, *Chem. Phys.* **1974**, 295–299.
- [143] A. S. Berezin, K. A. Vinogradova, V. A. Nadolinny, T. S. Sukhikh, V. P. Krivopalov, E. B. Nikolaenkova, M. B. Bushuev, *Dalton Trans.* **2018**, *47*, 1657–1665.
- [144] G. E. Hardy, J. I. Zink, *Inorg. Chem.* **1976**, *15*, 3061–3065.
- [145] J. Steube, A. Kruse, O. S. Bokareva, T. Reuter, S. Demeshko, R. Schoch, M. A. Argüello Cordero, A. Krishna, S. Hohloch, F. Meyer, K. Heinze, O. Kühn, S. Lochbrunner, M. Bauer, *Nature chemistry* **2023**, *15*, 468–474.
- [146] N. Elgrishi, K. J. Rountree, B. D. McCarthy, E. S. Rountree, T. T. Eisenhart, J. L. Dempsey, *J. Chem. Educ.* **2018**, *95*, 197–206.
- [147] A. Saju, J. R. Griffiths, S. N. MacMillan, D. C. Lacy, *J. Am. Chem. Soc.* **2022**, *144*, 16761–16766.
- [148] A. W. Adamson, W. L. Waltz, E. Zinato, D. W. Watts, P. D. Fleischauer, R. D. Lindholm, *Chem. Rev.* **1968**, *68*, 541–585.
- [149] M. Drosou, G. Zahariou, D. A. Pantazis, *Angew. Chem. Int. Ed.* **2021**, *60*, 13493–13499.
- [150] H. Aghabozorg, G. J. Palenik, R. C. Stoufer, J. Summers, *Inorg. Chem.* **1982**, *21*, 3903–3907.
- [151] R. J. F. Berger, G. V. Girichev, N. I. Giricheva, A. A. Petrova, N. V. Tverdova, *Angew. Chem. Int. Ed.* **2017**, *56*, 15751–15754.
- [152] C. Mantel, A. K Hassan, J. Pecaut, A. Deronzier, M-N. Collomb, C. Duboc-Toia, *J. Am. Chem. Soc.* **2003**, *125*, 12337–12344.
- [153] G. A. Craig, M. Murrie, *Chem. Soc. Rev.* **2015**, *44*, 2135–2147.
- [154] J. Vallejo, A. Pascual-Álvarez, J. Cano, I. Castro, M. Julve, F. Lloret, J. Krzystek, G. de Munno, D. Armentano, W. Wernsdorfer, R. Ruiz-García, E. Pardo, *Angew. Chem. Int. Ed.* **2013**, *52*, 14075–14079.
- [155] J. M. Frost, K. L. M. Harriman, M. Murugesu, *Chem. Sci.* **2016**, *7*, 2470–2491.
- [156] Y. Garcia, P. Gütllich, *Top. Curr. Chem.* **2004**, *234*, 49–62.
- [157] P. Greig Sim and Ekk Sinn.
- [158] A. P. Forshaw, J. M. Smith, A. Ozarowski, J. Krzystek, D. Smirnov, S. A. Zvyagin, T. D. Harris, H. I. Karunadasa, J. M. Zadrozny, A. Schnegg, K. Holldack, T. A. Jackson, A. Alamiri, D. M. Barnes, J. Telser, *Inorg. Chem.* **2013**, *52*, 144–159.
- [159] F. Hossain, M. A. Rigsby, C. T. Duncan, P. L. Milligan, R. L. Lord, M.-H. Baik, F. A. Schultz, *Inorg. Chem.* **2007**, *46*, 2596–2603.

-
- [160] A. A. Alaimo, D. Takahashi, L. Cunha-Silva, G. Christou, T. C. Stamatatos, *Inorg. Chem.* **2015**, *54*, 2137–2151.
- [161] A. Majumder, S. Goswami, S. R. Batten, M. Salah El Fallah, J. Ribas, S. Mitra, *Inorg. Chim. Acta* **2006**, *359*, 2375–2382.
- [162] P. Pavacik, J. C. Huffman, G. Christou, *J. Chem. Soc., Chem. Commun.* **1986**, *1*, 43–44.
- [163] T. Weyhermüller, T. K Paine, E. Bothe, E. Bill, P. Chaudhuri, *Inorg. Chim. Acta* **2002**, *337*, 344–356.
- [164] S. K. Chandra, P. Basu, D. Ray, S. Pal, A. Chakravorty, *Inorg. Chem.* **1990**, *29*, 2423–2428.
- [165] D. F. Back, G. Manzoni de Oliveira, C. Mensch Canabarro, B. Almeida Iglesias, *Z. Anorg. Allg. Chem.* **2015**, *641*, 941–947.
- [166] N. Sarkar, K. Harms, A. Bauzá, A. Frontera, S. Chattopadhyay, *ChemistrySelect* **2017**, *2*, 2975–2984.
- [167] Michael K. Chan, William H. Armstrong, *Inorg. Chem.* **1989**, 3777–3779.
- [168] Y. Xu, C. Li, X. Wu, M.-X. Li, Y. Ma, H. Yang, Q. Zeng, J. L. Sessler, Z.-X. Wang, *J. Am. Chem. Soc.* **2022**, *144*, 18834–18843.
- [169] M. G. Brik, A. M. Srivastava, *J. Lumin.* **2013**, *133*, 69–72.
- [170] Y. Li, S. Qi, P. Li, Z. Wang, *RSC Adv.* **2017**, *7*, 38318–38334.
- [171] Q. Zhou, L. Dolgov, A. M. Srivastava, L. Zhou, Z. Wang, J. Shi, M. D. Dramićanin, M. G. Brik, M. Wu, *J. Mater. Chem. C* **2018**, *6*, 2652–2671.
- [172] S. Adachi, *Journal of Luminescence* **2018**, *202*, 263–281.
- [173] M. G. Brik, S. J. Camardello, A. M. Srivastava, N. M. Avram, A. Suchocki, *ECS J. Solid State Sci. Technol.* **2016**, *5*, R3067-R3077.
- [174] V. Baslon, J. P. Harris, C. Reber, H. E. Colmer, T. A. Jackson, A. P. Forshaw, J. M. Smith, R. A. Kinney, J. Telser, *Can. J. Chem.* **2017**, *95*, 547–552.
- [175] J. R. Mayfield, E. N. Grotemeyer, T. A. Jackson, *Chem. Commun.* **2020**, *56*, 9238–9255.
- [176] N. Sharma, Y.-M. Lee, W. Nam, S. Fukuzumi, *Isr. J. Chem.* **2020**, *60*, 1049–1056.
- [177] H. Yoon, Y.-M. Lee, X. Wu, K.-B. Cho, R. Sarangi, W. Nam, S. Fukuzumi, *J. Am. Chem. Soc.* **2013**, *135*, 9186–9194.
- [178] C. Saracini, S. Fukuzumi, Y.-M. Lee, W. Nam, *Dalton Trans.* **2018**, *47*, 16019–16026.
- [179] N. Sharma, J. Jung, Y.-M. Lee, M. S. Seo, W. Nam, S. Fukuzumi, *Chem. Eur. J.* **2017**, *23*, 7125–7131.
- [180] N. Sharma, Y.-M. Lee, X.-X. Li, W. Nam, S. Fukuzumi, *Inorg. Chem.* **2019**, *58*, 14299–14303.
- [181] D. G. Karmalkar, M. S. Seo, Y.-M. Lee, Y. Kim, E. Lee, R. Sarangi, S. Fukuzumi, W. Nam, *Inorg. Chem.* **2021**, *60*, 16996–17007.
- [182] J. Chen, H. Yoon, Y.-M. Lee, M. S. Seo, R. Sarangi, S. Fukuzumi, W. Nam, *Chem. Sci.* **2015**, *6*, 3624–3632.
- [183] L. A. Büldt, C. B. Larsen, O. S. Wenger, *Chem. Eur. J.* **2017**, *23*, 8577–8580.
- [184] L. A. Büldt, O. S. Wenger, *Dalton Trans.* **2017**, *46*, 15175–15177.
- [185] Y.-S. Wong, M.-C. Tang, M. Ng, V. W.-W. Yam, *J. Am. Chem. Soc.* **2020**, *142*, 7638–7646.
- [186] T. Ogawa, N. Sinha, B. Pfund, A. Prescimone, O. S. Wenger, *J. Am. Chem. Soc.* **2022**, *144*, 21948–21960.
- [187] E. González, A. Rodrigue-Witchel, C. Reber, *Coord. Chem. Rev.* **2007**, *251*, 351–363.

-
- [188] M.-C. Nolet, A. Michaud, C. Bain, D. Zargarian, C. Reber, *Photochem. Photobiol.* **2006**, *82*, 57–63.
- [189] C. R. G. Bussiere, *J. Am. Chem. Soc.* **1998**, *120*, 6306–6315.
- [190] M. Dorn, K. Mack, L. M. Carrella, E. Rentschler, C. Förster, K. Heinze, *Z. Anorg. Allg. Chem.* **2018**, *644*, 706–712.
- [191] D. A. V. Griend, D. K. Bediako, M. J. DeVries, N. A. DeJong, L. P. Heeringa, *Inorg. Chem.* **2008**, *47*, 656–662.
- [192] M.-C. Nolet, R. Beaulac, A.-M. Boulanger, C. Reber, *Struct. Bond.* **2004**, *107*, 145–158.
- [193] R. W. Parsons, H. G. Drickamer, *J. Chem. Phys.* **1958**, *29*, 930–937.
- [194] J. C. Zahner, H. G. Drickamer, *J. Chem. Phys.* **1961**, *35*, 1483–1490.
- [195] S. Poirier, H. Lynn, C. Reber, E. Tailleux, M. Marchivie, P. Guionneau, M. R. Probert, *Inorg. Chem.* **2018**, *57*, 7713–7723.
- [196] A. Mrutu, K. I. Goldberg, R. A. Kemp, *Inorg. Chim. Acta* **2010**, *364*, 115–119.
- [197] X. Zhang, B. Liu, A. Liu, W. Xie, W. Chen, *Organometallics* **2009**, *28*, 1336–1349.
- [198] S. Gu, W. Chen, *Organometallics* **2009**, *28*, 909–914.
- [199] S. Gu, J. Du, J. Huang, Y. Guo, L. Yang, W. Xu, W. Chen, *Dalton Trans.* **2017**, *46*, 586–594.
- [200] S. Gu, D. Xu, W. Chen, *Dalton Trans.* **2011**, *40*, 1576–1583.
- [201] N. Takeda, D. Shimizu, N. Tokitoh, *Inorg. Chem.* **2005**, *44*, 8561–8568.
- [202] A. K. Pal, C. Li, G. S. Hanan, E. Zysman-Colman, *Angew. Chem. Int. Ed.* **2018**, *57*, 8027–8031.
- [203] K. Inamoto, J.-I. Kuroda, K. Hiroya, Y. Noda, T. S. M. Watanabe, *Organometallics* **2006**, *25*, 3095–3098.
- [204] J. C. C. Chen, I. J. B. Lin, *Organometallics* **2000**, *19*, 5113–5121.
- [205] C. R. Goldsmith, T. D. P. Stack, *Inorg. Chem.* **2006**, *45*, 6048–6055.
- [206] T. Jiang, N. F. Polizzi, J. Rawson, M. J. Therien, *J. Am. Chem. Soc.* **2017**, *139*, 8412–8415.
- [207] X-Area; STOE & Cie GmbH, Darmstadt, Germany.
- [208] R. H. Blessing, *Acta Crystallogr., Sect. A: Found. Crystallogr.* **1995**, *51*, 33–38.
- [209] A. L. Spek, *Acta Crystallogr., Sect. D: Biol. Crystallogr.* **2009**, *65*, 148–155.
- [210] G. M. Sheldrick, *Acta Crystallogr., Sect. A: Found. Crystallogr.* **2015**, *71*, 3–8.
- [211] G. M. Sheldrick, *Acta Crystallogr., Sect. C: Struct. Chem* **2015**, *71*, 3–8.
- [212] G. M. Sheldrick, *Acta Crystallogr., Sect. A: Found. Crystallogr.* **2008**, *64*, 112–122.
- [213] C. B. Hübschle, G. M. Sheldrick, B. Dittrich, *J. Appl. Crystallogr.* **2011**, *44*, 1281–1284.
- [214] F. Neese, *WIREs Comput. Mol. Sci.* **2012**, *2*, 73–78.
- [215] A. D. Becke, *J. Chem. Phys.* **1993**, *98*, 5648–5652.
- [216] B. Miehlich, A. Savin, H. Stoll, H. Preuss, *Chem. Phys. Lett.* **1989**, *157*, 200–206.
- [217] C. Lee, W. Yang, and R. G. Parr, *Phys. Rev. B.* **1988**, *37*, 785–789.
- [218] R. Izsák, F. Neese, *J. Chem. Phys.* **2011**, *135*, 144105.
- [219] F. Neese, F. Wennmohs, A. Hansen, U. Becker, *Chem. Phys.* **2009**, *356*, 98–109.
- [220] D. A. Pantazis, X.-Y. Chen, C. R. Landis, F. Neese, *J. Chem. Theory Comput.* **2008**, *4*, 908–919.
- [221] S. Miertus, E. Scrocco, J. Tomasi, *Chem. Phys.* **1981**, *55*, 117–129.
- [222] F. Weigend, *Phys. Chem. Chem. Phys.* **2006**, *8*, 1057–1065.
- [223] F. Weigend, R. Ahlrichs, *Phys. Chem. Chem. Phys.* **2005**, *7*, 3297–3305.

6. Appendix

6.1 Supporting Information to Chapter 3.1. (“The Full d^3 – d^5 Redox Series of Mononuclear Manganese Complexes: Geometries and Electronic Structures of $[\text{Mn}(\text{dgpy})_2]^{n+}$ ”)

The Full d^3 – d^5 Redox Series of Mononuclear Manganese Complexes: Geometries and Electronic Structures of $[\text{Mn}(\text{dgpy})_2]^{n+}$

Nathan R. East,[†] Christoph Förster,[†] Luca M. Carrella,[†] Eva Rentschler,[†] and Katja Heinze^{†}*

[†] Department of Chemistry, Johannes Gutenberg University, Duesbergweg 10-14, 55128 Mainz, Germany

Crystallographic Data of *cis-fac-1*[PF₆]₂×0.5C₂H₅OC₂H₅×CH₃CN. C₃₈H₅₄F₁₂MnN₁₄P₂×0.5C₂H₅OC₂H₅×CH₃CN (1129.94); triclinic; $P\bar{1}$; $a = 12.517(3)$ Å, $b = 12.772(3)$ Å, $c = 17.096(3)$ Å; $\alpha = 96.91(3)^\circ$; $\beta = 92.32(3)^\circ$; $\gamma = 115.73(3)^\circ$; $V = 2431.2(10)$ Å³; $Z = 2$; density, calcd. = 1.544 g cm⁻³, $T = 120(2)$ K, $\mu = 0.435$ mm⁻¹; $F(000) = 1172$; crystal size 0.180 × 0.173 × 0.170 mm³; $\theta = 2.282$ to 27.949 deg.; $-16 \leq h \leq 16$, $-16 \leq k \leq 16$, $-22 \leq l \leq 22$; rfln collected = 107028; rfln unique = 11616 [$R(\text{int}) = 0.0884$]; completeness to $\theta = 25.242$ deg. = 99.9 %; semi empirical absorption correction from equivalents; max. and min. transmission 1.0756 and 0.9157; data 11616; restraints 24, parameters 744; goodness-of-fit on $F^2 = 1.008$; final indices [$I > 2\sigma(I)$] $R_1 = 0.0414$, $wR_2 = 0.1103$; R indices (all data) $R_1 = 0.0554$, $wR_2 = 0.1218$; largest diff. peak and hole 0.410 and -0.435 e Å⁻³.

Crystallographic Data of *mer-1*[BF₄]₂. C₃₈H₅₄FB₂F₈MnN₁₄ (935.51); triclinic; $P\bar{1}$; $a = 9.2829(19)$ Å, $b = 12.056(2)$ Å, $c = 18.156(4)$ Å; $\alpha = 74.24(3)^\circ$; $\beta = 80.11(3)^\circ$; $\gamma = 77.07(3)^\circ$; $V = 1892.5(8)$ Å³; $Z = 2$; density, calcd. = 1.642 g cm⁻³, $T = 120(2)$ K, $\mu = 0.443$ mm⁻¹; $F(000) = 974$; crystal size 0.170 × 0.103 × 0.050 mm³; $\theta = 2.426$ to 30.369 deg.; $-12 \leq h \leq 12$, $-17 \leq k \leq 17$, $-23 \leq l \leq 23$; rfln collected = 20301; rfln unique = 9690 [$R(\text{int}) = 0.0707$]; completeness to $\theta = 25.242$ deg. = 99.7 %; semi empirical absorption correction from equivalents; max. and min. transmission 1.16520 and 0.91631; data 9690; restraints 58, parameters 615; goodness-of-fit on $F^2 = 1.013$; final indices [$I > 2\sigma(I)$] $R_1 = 0.0541$, $wR_2 = 0.1187$; R indices (all data) $R_1 = 0.0973$, $wR_2 = 0.1385$; largest diff. peak and hole 0.487 and -0.931 e Å⁻³.

Crystallographic Data of *mer-1*[PF₆]₃×1.5CH₃CN. C₃₈H₅₄F₁₈MnN₁₄P₃×1.5CH₃CN (1258.38); monoclinic; Ia ; $a = 16.680(3)$ Å, $b = 35.592(7)$ Å, $c = 17.206(3)$ Å, $\beta = 92.43(3)^\circ$; $V = 10206(4)$ Å³; $Z = 8$; density, calcd. = 1.638 g cm⁻³, $T = 120(2)$ K, $\mu = 0.469$ mm⁻¹; $F(000) = 5160$; crystal size 0.270 × 0.200 × 0.160 mm³; $\theta = 2.444$ to 27.923 deg.; $-19 \leq h \leq 21$, $-46 \leq k \leq 46$, $-22 \leq l \leq 22$; rfln collected = 51022; rfln unique = 21221 [$R(\text{int}) = 0.0895$]; completeness to $\theta = 26.000$ deg. = 99.9 %; semi empirical absorption correction from equivalents; max. and min. transmission 1.15787 and 0.93046; data 21221; restraints 101, parameters 1492; goodness-of-fit on $F^2 = 1.038$; final indices [$I > 2\sigma(I)$] $R_1 = 0.0740$, $wR_2 = 0.1751$; R indices (all data) $R_1 = 0.1138$, $wR_2 = 0.2004$; largest diff. peak and hole 1.060 and -0.639 e Å⁻³.

Crystallographic Data of *mer-1*[PF₆]₄×3CH₃CN. C₃₈H₅₄F₂₄MnN₁₄P₄×3CH₃CN (1464.93); monoclinic; $P2_1/c$; $a = 21.344(4)$ Å, $b = 12.739(3)$ Å, $c = 21.674(4)$ Å, $\beta = 102.16(3)^\circ$; $V = 5761(2)$ Å³; $Z = 4$; density, calcd. = 1.689 g cm⁻³, $T = 120(2)$ K, $\mu = 0.470$ mm⁻¹; $F(000) = 2988$; crystal size 0.210 × 0.147 × 0.030 mm³; $\theta = 2.523$ to 25.999 deg.; $-26 \leq h \leq 26$, $-13 \leq k \leq 15$, $-26 \leq l \leq 25$; rfln collected = 28998; rfln unique = 11281 [$R(\text{int}) = 0.0940$]; completeness to $\theta = 25.242$ deg. = 99.7 %; semi empirical absorption correction from equivalents; max. and min. transmission 1.17966 and 0.91491; data 11281; restraints 146, parameters 935; goodness-of-fit on $F^2 = 1.099$; final indices [$I > 2\sigma(I)$] $R_1 = 0.0834$, $wR_2 = 0.1791$; R indices (all data) $R_1 = 0.1298$, $wR_2 = 0.2071$; largest diff. peak and hole 1.735 and -0.597 e Å⁻³.

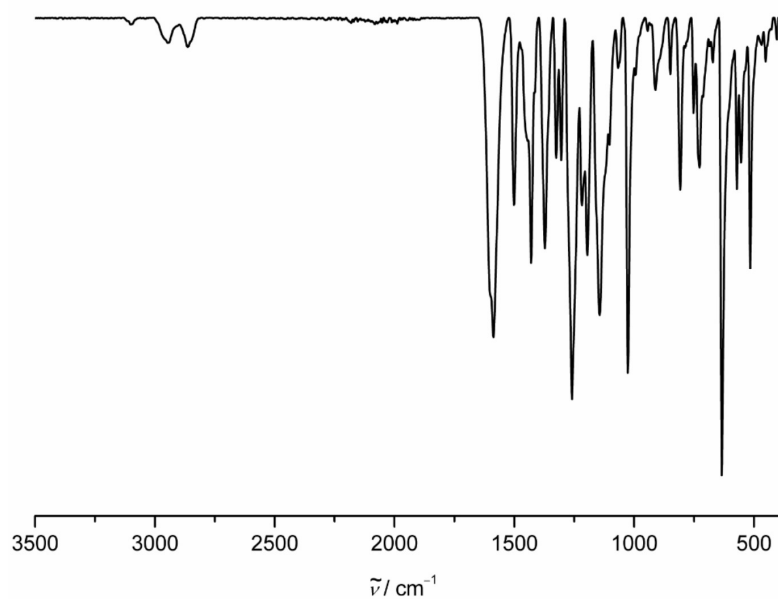


Figure S1. ATR-IR spectrum of *mer-1*[OTf]₂.

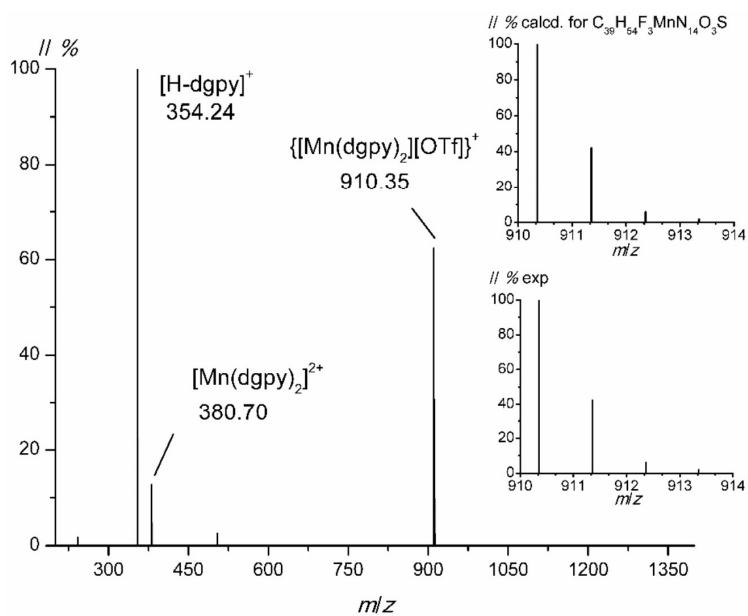


Figure S2. ESI⁺ mass spectrum of *mer-1*[OTf]₂ in dry acetonitrile.

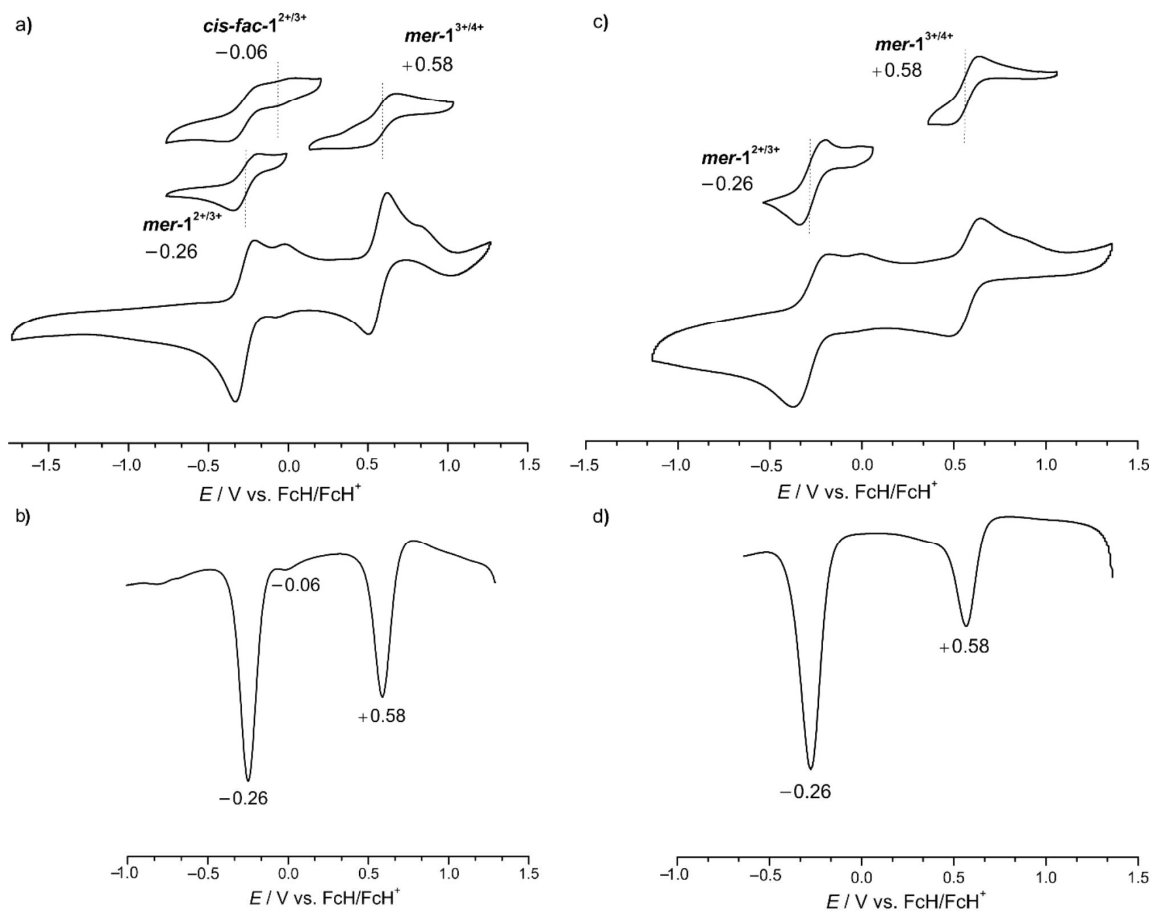


Figure S3. a) Cyclic voltammograms and b) square-wave voltammogram of **1**[PF₆]₃, c) cyclic voltammograms and d) square-wave voltammogram of **mer-1**[PF₆]₄, 1 mM in acetonitrile containing 0.1 M [ⁿBu₄N][B(C₆F₅)₄] as supporting electrolyte.

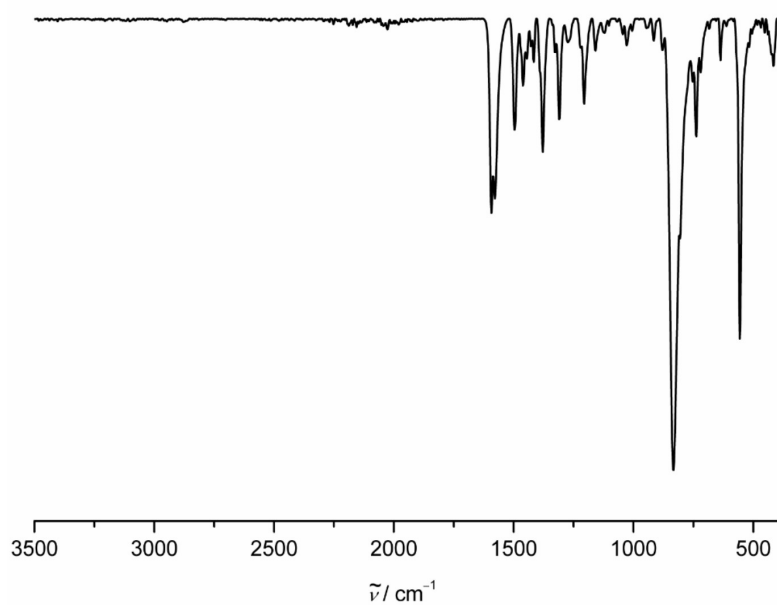


Figure S4. ATR-IR spectrum of *mer-1*[PF₆]₃.

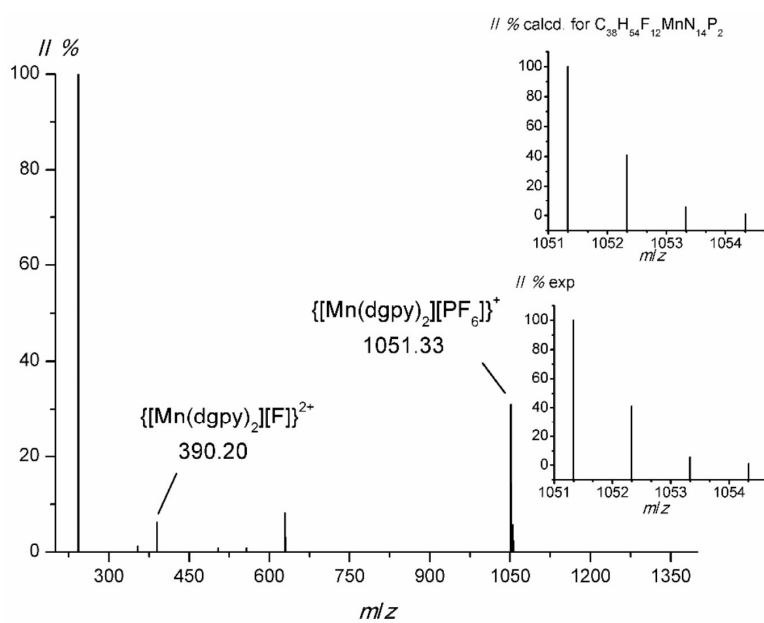


Figure S5. ESI⁺ mass spectrum of *mer-1*[PF₆]₃ in dry acetonitrile.

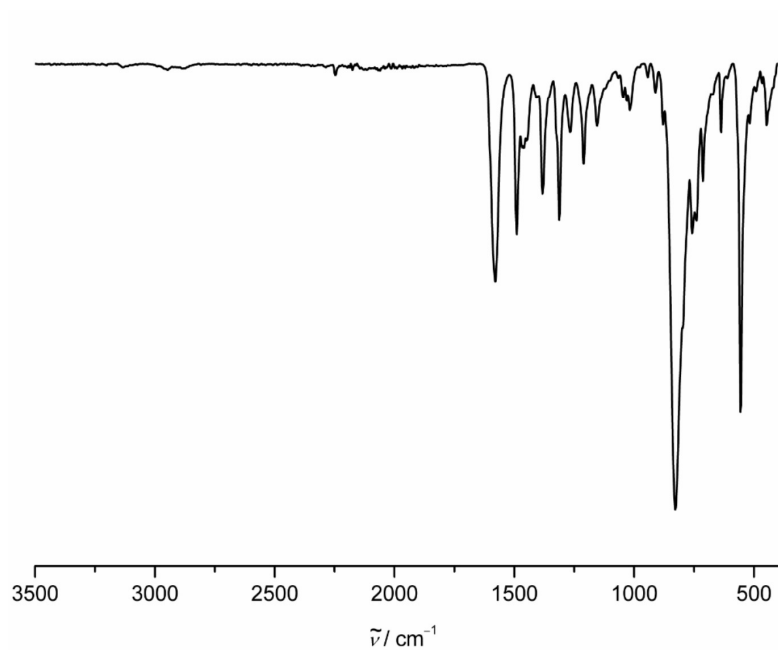


Figure S6. ATR-IR spectrum of *mer-1*[PF₆]₄.

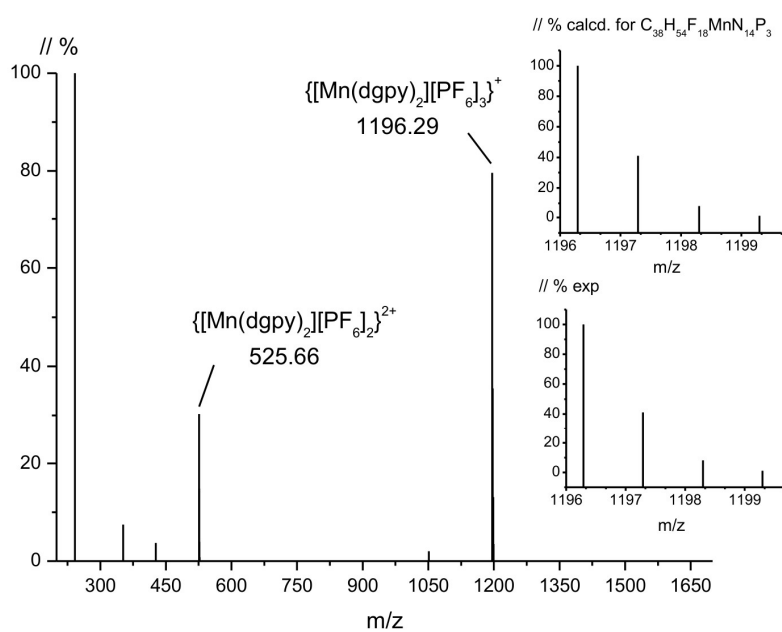


Figure S7. ESI⁺ mass spectrum of *mer-1*[PF₆]₄ in dry acetonitrile.

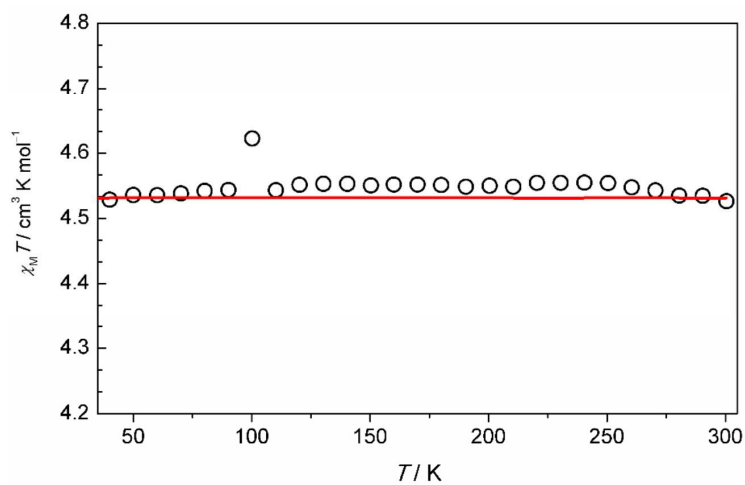


Figure S8. Temperature dependence of the magnetic susceptibility in $\chi_M T$ vs. T for *mer-1*[OTf]₂ (circles), with fit (solid red line, $g = 2.056(2)$).

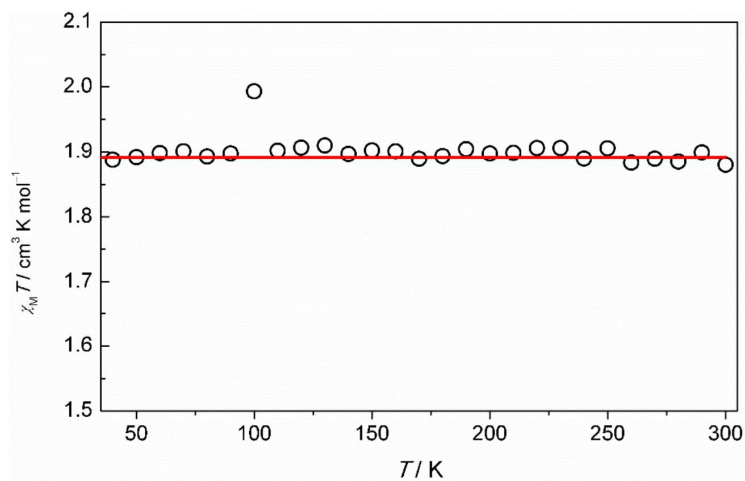


Figure S9. Temperature dependence of the magnetic susceptibility in $\chi_M T$ vs. T for *mer-1*[PF₆]₄ (circles), with fit (solid red line, $g = 2.025(1)$).

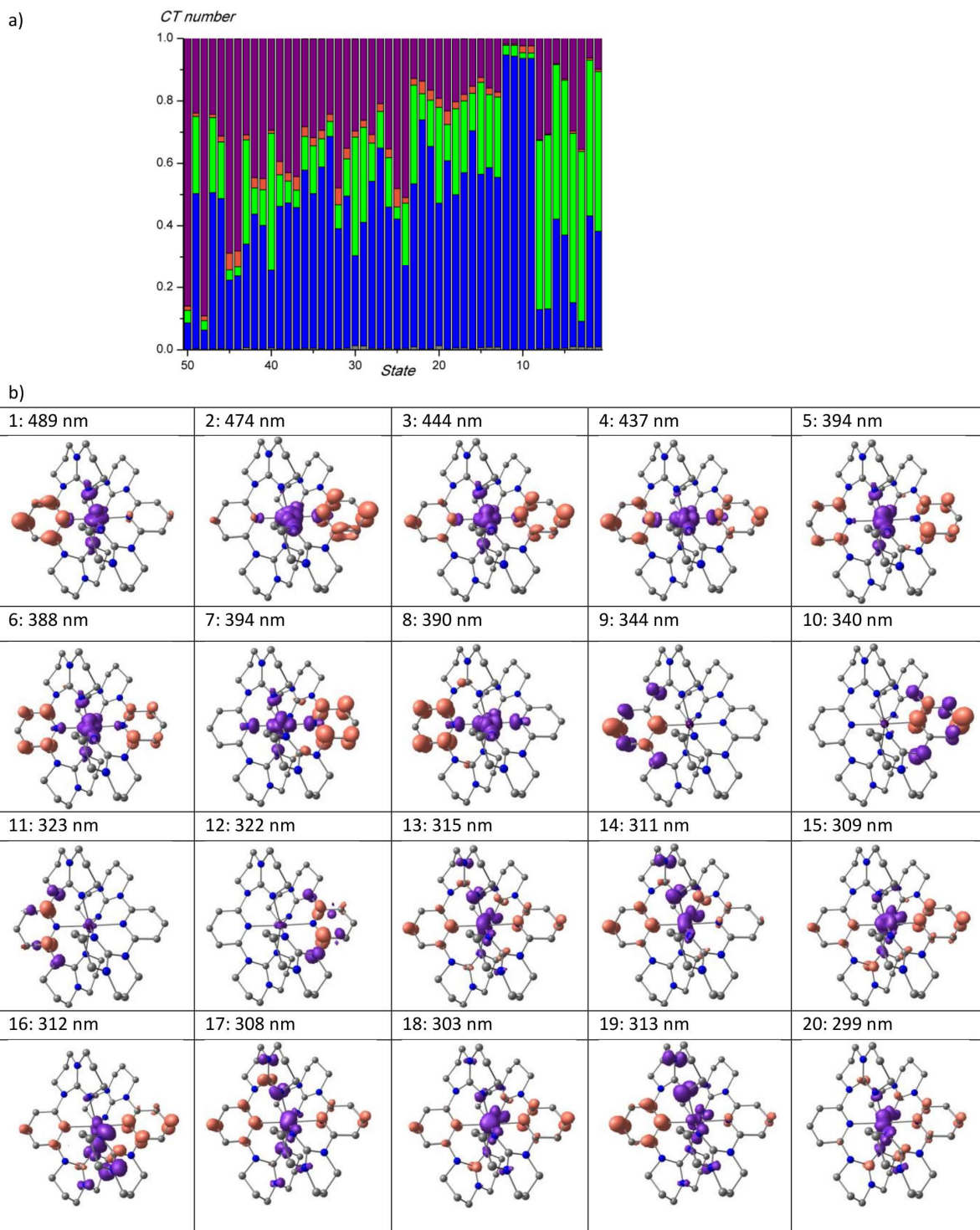


Figure S10. a) Charge transfer analysis of the 50 lowest spin-allowed transitions of *mer-1*²⁺ (green: MLCT, blue: ILCT/LC, purple: LL'CT, orange: LMCT, gray: MC) and b) difference densities of the 20 lowest spin-allowed transitions of *mer-1*²⁺ with the respective wavelength (purple = electron loss; orange = electron gain) displayed at an isosurface value of 0.006 a.u..

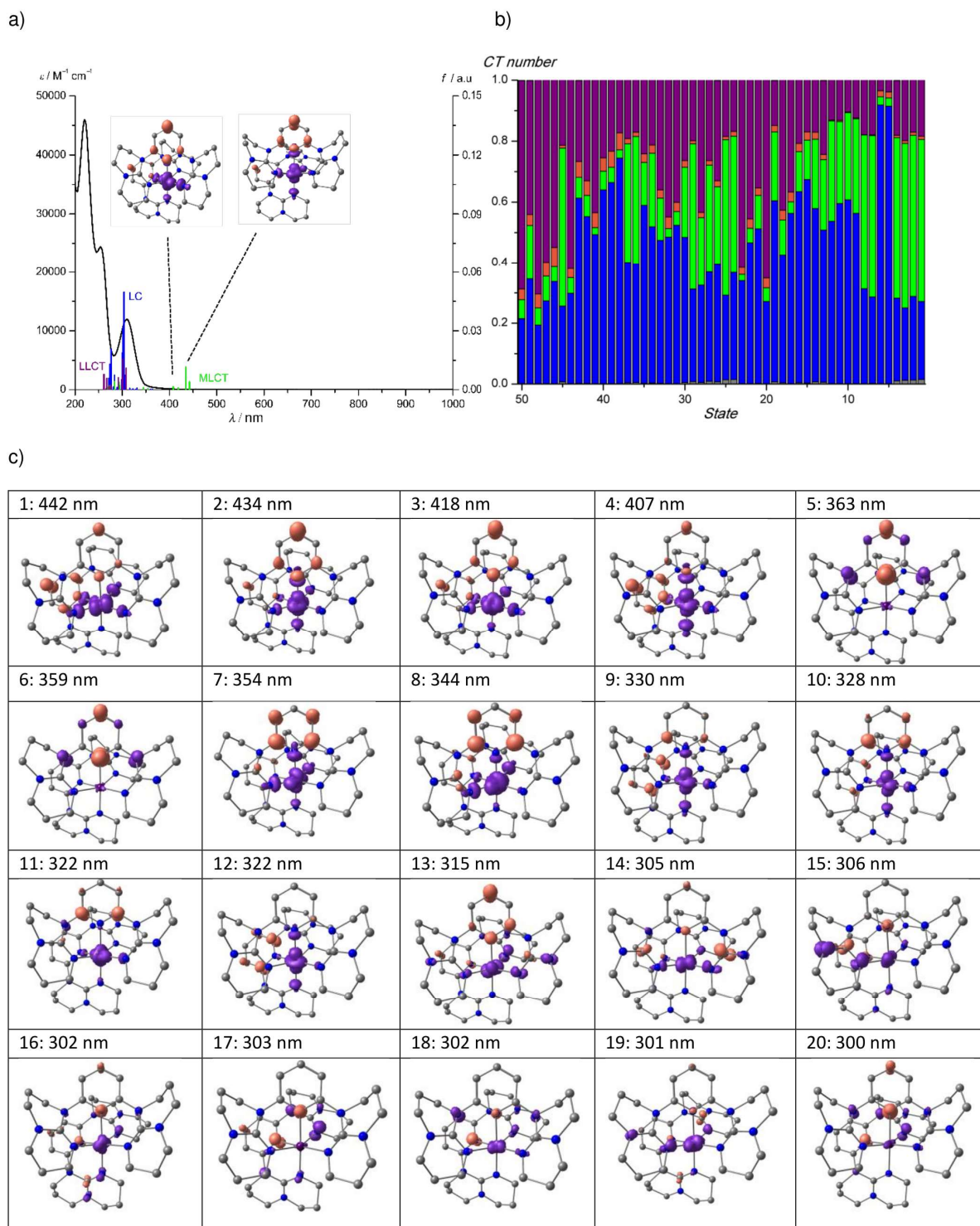


Figure S11. a) UV/Vis/NIR spectra of $1[\text{OTf}]_2$ in CH_3CN and *cis-fac-1*²⁺ TDDFT calculated transitions with the color code indicating the character of the transition according to charge transfer analyses (green: MLCT, purple: LLCT, orange: LMCT, blue: LC, gray: MC). Exemplary difference electron densities of significant low-energy spin-allowed transitions are displayed at an isosurface value of 0.006 a.u., b) Charge transfer analysis of the 50 lowest spin-allowed transitions of

*cis-fac-1*²⁺ (green: MLCT, blue: ILCT/LC, purple: LL'CT, orange: LMCT, gray: MC) and c) difference densities of the 20 lowest spin-allowed transitions of *cis-fac-1*²⁺ with the respective wavelength (purple = electron loss; orange = electron gain) displayed at an isosurface value of 0.006 a.u..

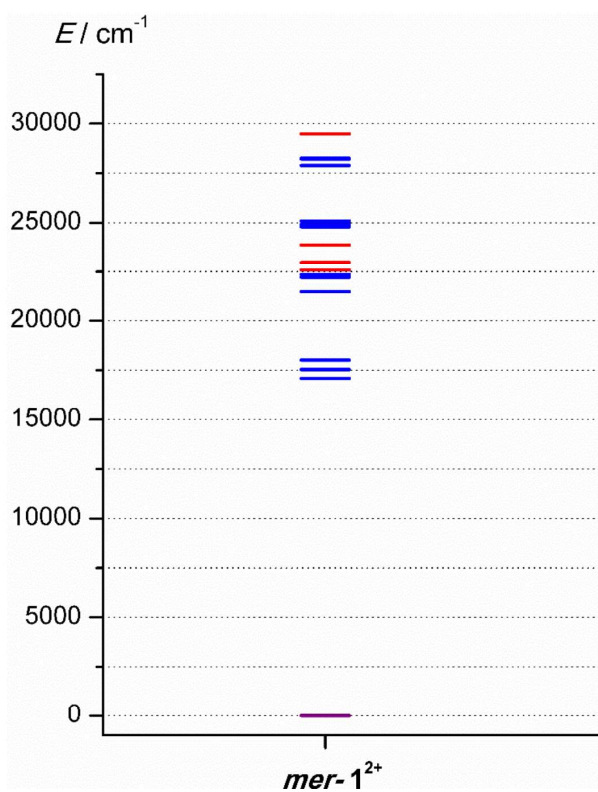
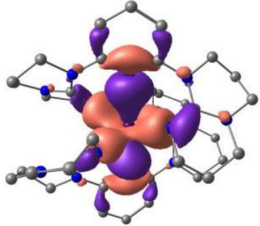
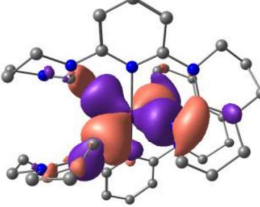
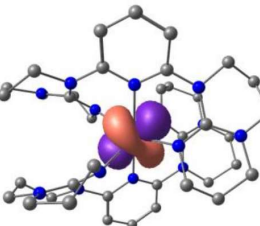
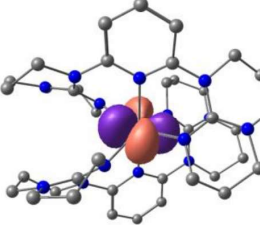
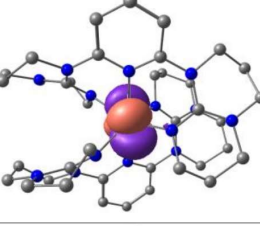
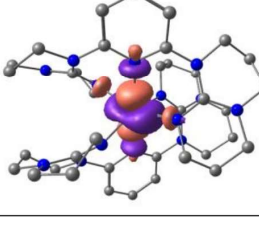
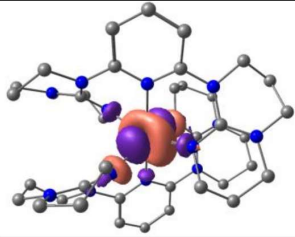
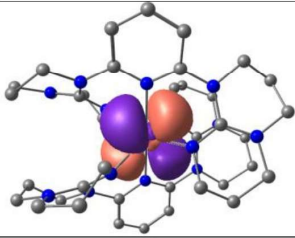
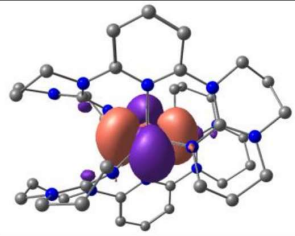
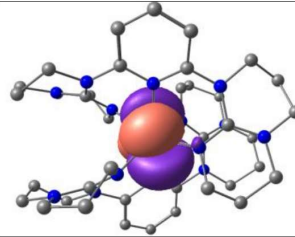
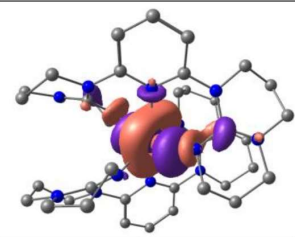
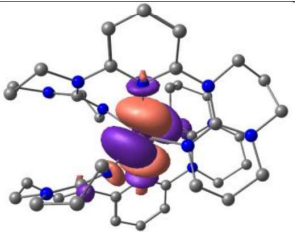
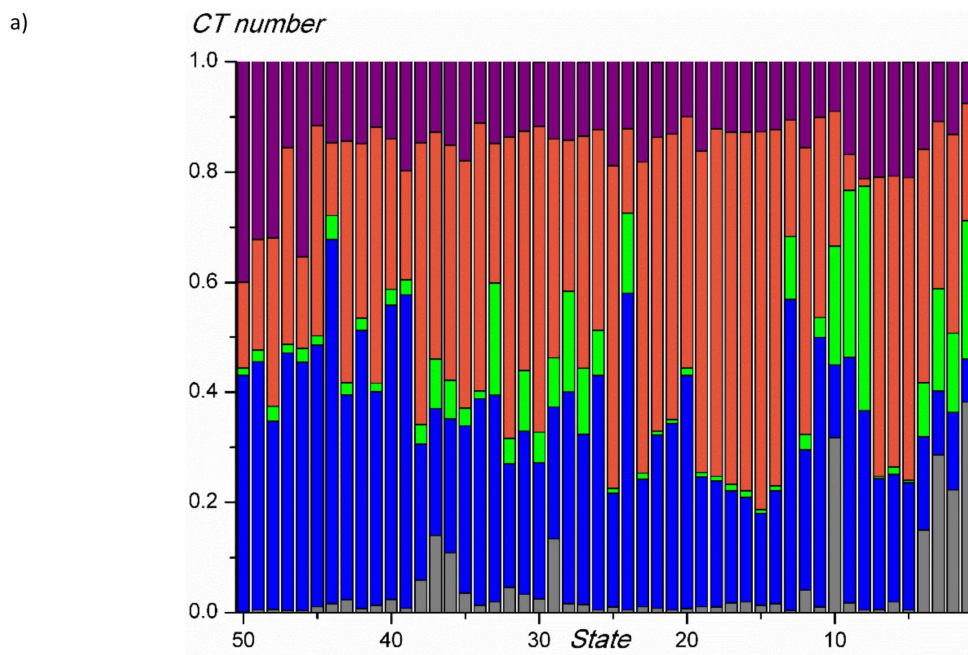


Figure S12. Energies of sextet (purple), quartet (blue) and doublet (red) states of $mer-1^{2+}$ calculated by CASSCF(9,12)-SC-NEVPT2.

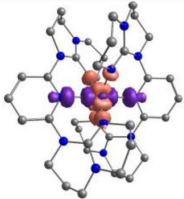
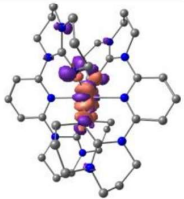
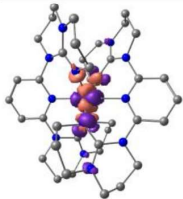
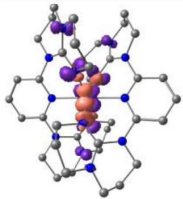
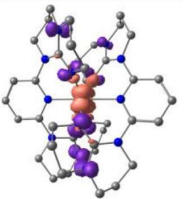
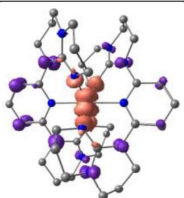
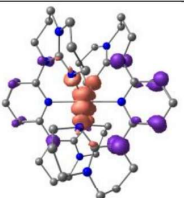
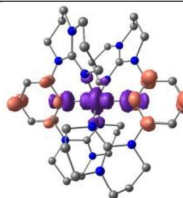
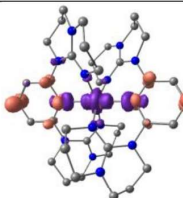
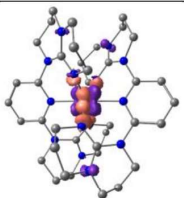
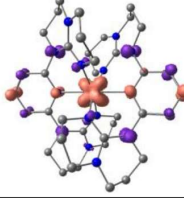
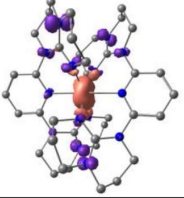
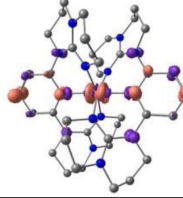
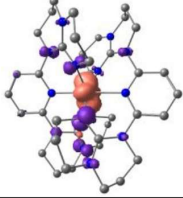
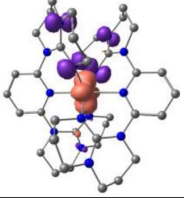





Table S1. Orbital energies/Hartree of the canonical orbitals used in the active space of the CASSCF(9,12)-SC-NEVPT2 calculations of *mer-1*²⁺ depicted at a contour value of 0.030 a.u.. Hydrogen atoms omitted for clarity.

#	<i>E</i> /H	orbital
198	-0.4891	
199	-0.4758	
200	-0.1234	
201	-0.1114	
202	-0.0900	
203	0.0642	

204	0.0773	
205	1.4644	
206	1.5277	
207	1.5258	
208	1.8152	
209	1.8954	



b)

1: 1334 nm	2: 531 nm	3: 499 nm	4: 457 nm	5: 421 nm
				
6: 409 nm	7: 395 nm	8: 379 nm	9: 364 nm	10: 357 nm
				
11: 356 nm	12: 355 nm	13: 350 nm	14: 349 nm	15: 351 nm
				
16: 345 nm	17: 344 nm	18: 341 nm	19: 339 nm	20: 330 nm
				

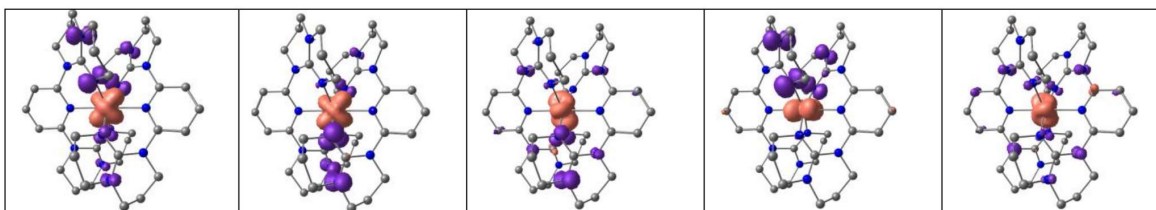


Figure S13. a) Charge transfer analysis of the 50 lowest spin-allowed transitions of $mer-1^{3+}$ (green: MLCT, blue: ILCT/LC, purple: LL'CT, orange: LMCT, gray: MC) and b) difference densities of the 20 lowest spin-allowed transitions of $mer-1^{3+}$ with the respective wavelength (purple = electron loss; orange = electron gain) displayed at an isosurface value of 0.006 a.u..

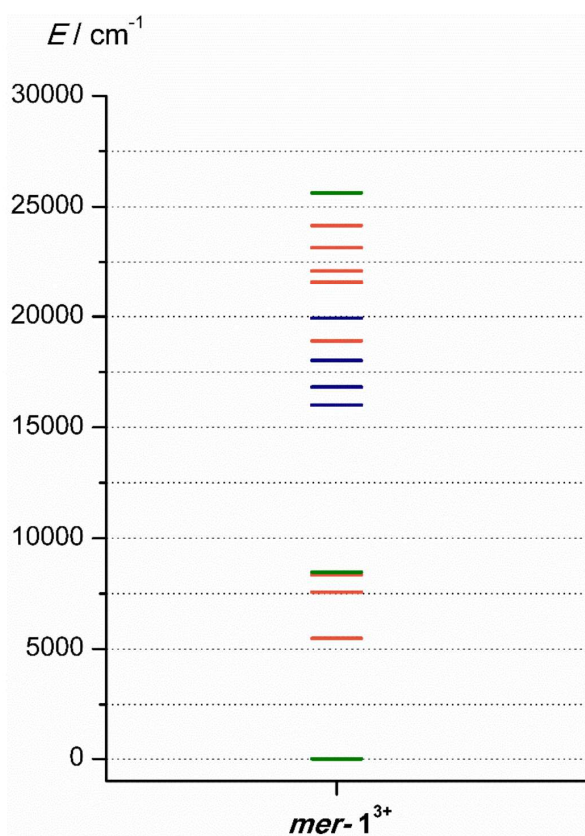
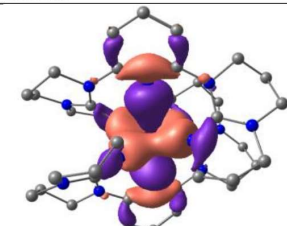
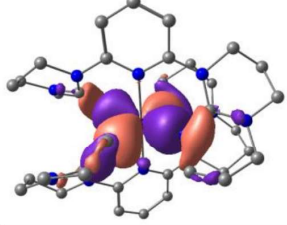
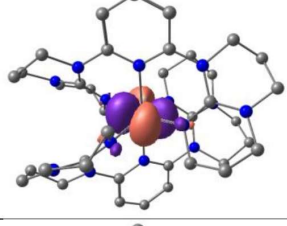
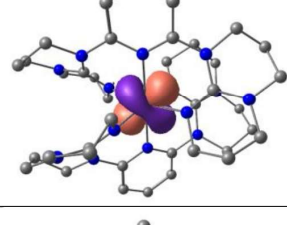
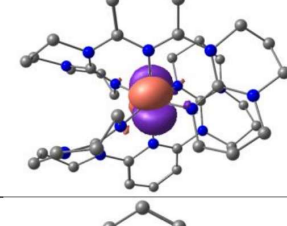
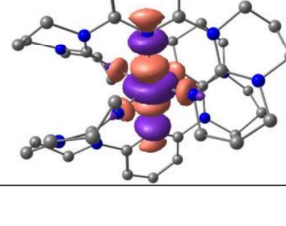
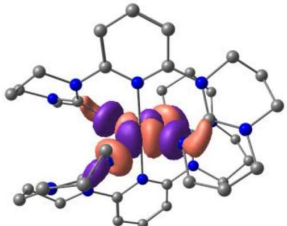
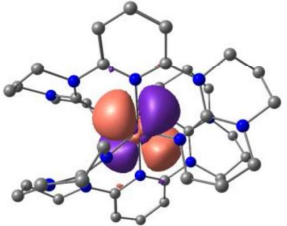
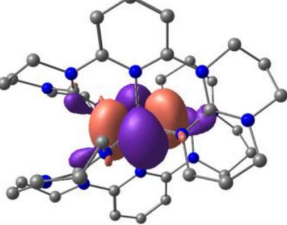
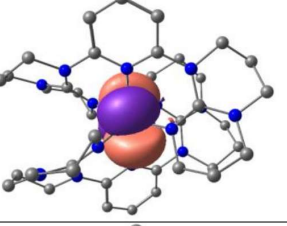
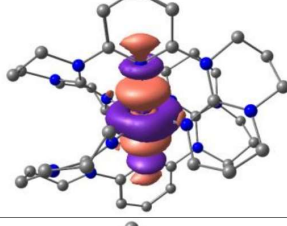
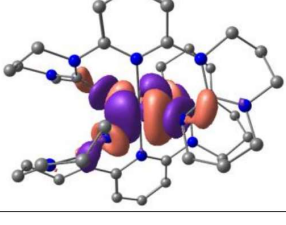


Figure S14. Energies of quintet (green), triplet (orange) and singlet (blue) states of $mer-1^{3+}$ calculated by CASSCF(8,12)-SC-NEVPT2.

Table S2. Orbital energies/Hartree of the canonical orbitals used in the active space of the CASSCF(8,12)-SC-NEVPT2 calculations of *mer-1*³⁺ depicted at a contour value of 0.030 a.u.. Hydrogen atoms omitted for clarity.

#	E/H	orbital
198	-0.5549	
199	-0.5573	
200	-0.2215	
201	-0.2234	
202	-0.1904	
203	-0.0206	

204	0.0725	
205	1.3128	
206	1.3678	
207	1.3734	
208	1.7869	
209	1.8475	

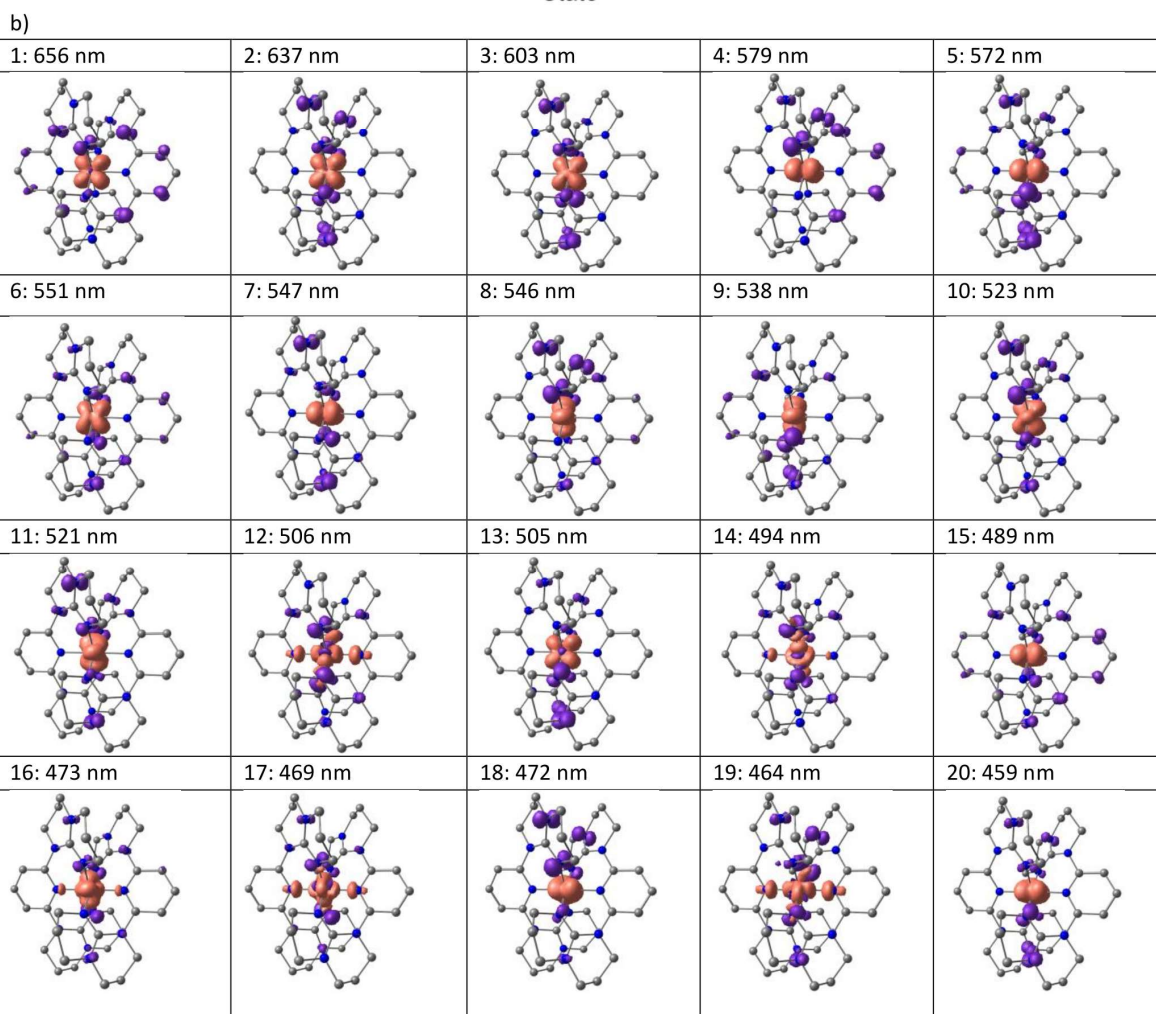
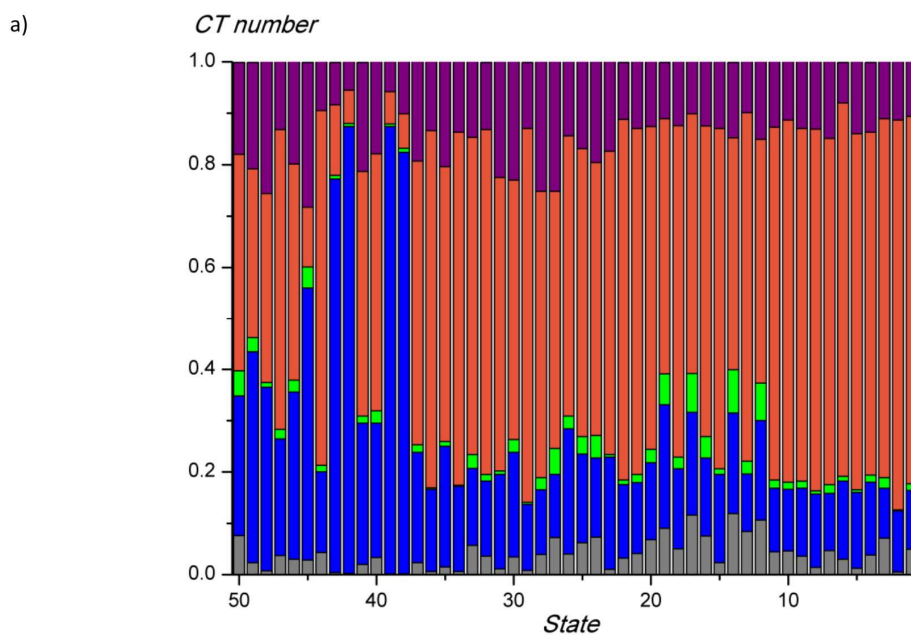


Figure S15. a) Charge transfer analysis of the 50 lowest spin-allowed transitions of $mer-1^{4+}$ (green: MLCT, blue: ILCT/LC, purple: LL'CT, orange: LMCT, gray: MC) and b) difference densities of the 20 lowest spin-allowed transitions of $mer-1^{4+}$ with the respective wavelength (purple = electron loss; orange = electron gain) displayed at an isosurface value of 0.006 a.u..

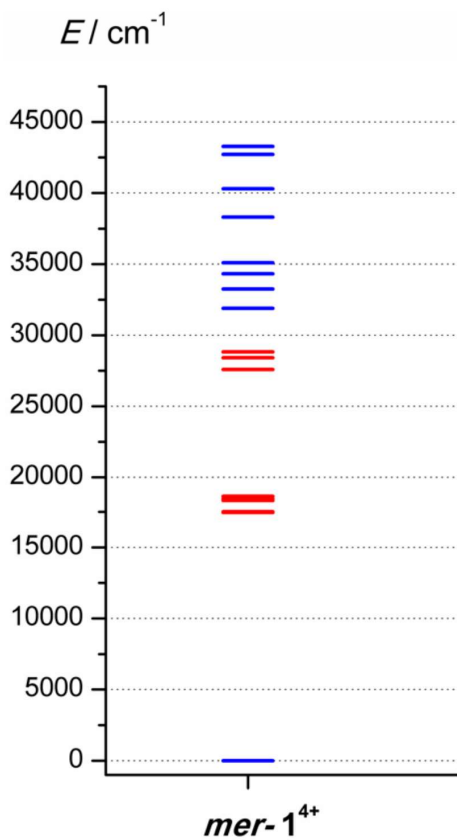
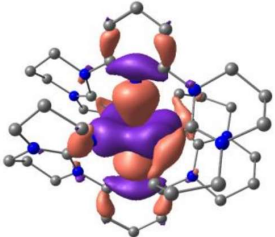
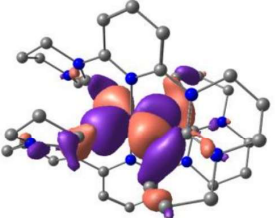
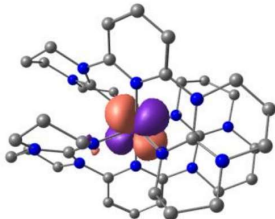
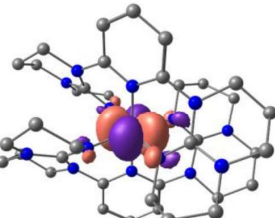
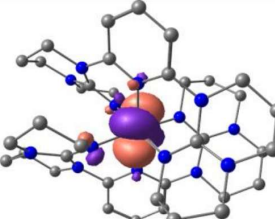
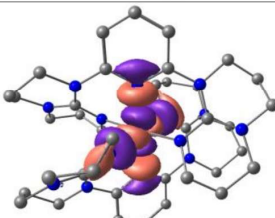


Figure S16. Energies of quartet (blue) and doublet (red) states of $mer-1^{4+}$ calculated by CASSCF(7,12)-SC-NEVPT2.

Table S3. Orbital energies/Hartree of the canonical orbitals used in the active space of the CASSCF(7,12)-SC-NEVPT2 calculations of *mer-1*⁴⁺ depicted at a contour value of 0.030 a.u.. Hydrogen atoms omitted for clarity.

#	<i>E</i> /H	orbital
198	-0.6109	
199	-0.5762	
200	-0.2820	
201	-0.2483	
202	-0.2450	
203	0.0200	

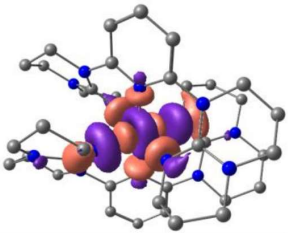
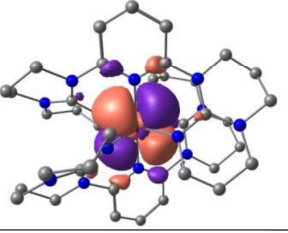
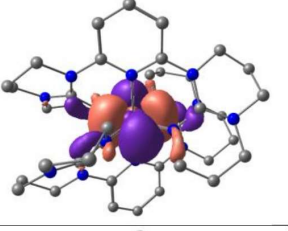
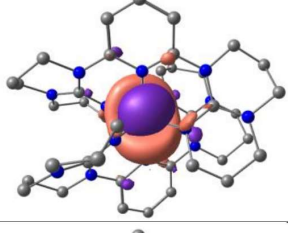
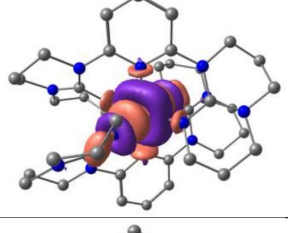
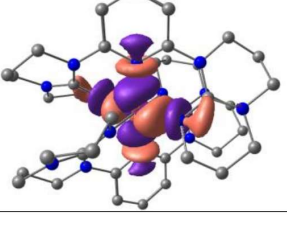
204	0.0290	
205	1.1918	
206	1.2704	
207	1.2499	
208	1.9906	
209	2.0059	

Table S4. Cartesian Coordinates of the DFT-UKS calculated ground state geometry *cis-fac-1²⁺*.

25	4.457920000	3.166517000	12.335040000
7	5.934908000	2.167948000	13.614839000
7	6.651562000	0.310223000	14.868735000
7	4.452002000	0.416027000	14.062116000
7	3.177728000	2.390085000	14.094061000
7	2.074383000	4.465716000	14.123512000
7	3.154850000	6.272716000	15.164046000
7	4.291144000	4.970881000	13.566244000
7	2.566139000	3.336149000	11.202255000
7	0.699050000	2.316371000	10.166277000
7	2.258921000	1.002438000	11.237127000
7	4.550211000	1.303587000	10.911876000
7	6.801237000	1.805879000	10.495685000
7	7.222186000	3.488121000	8.925340000
7	5.754024000	3.896609000	10.719902000
6	7.244123000	2.787085000	13.797754000
1	7.393579000	3.489610000	12.980438000
1	7.255752000	3.363651000	14.728173000
6	8.351836000	1.750226000	13.824875000
1	9.317507000	2.219178000	14.013210000
1	8.403928000	1.242786000	12.862248000
6	8.051126000	0.744779000	14.914114000
1	8.256107000	1.171640000	15.900495000
1	8.674253000	-0.144388000	14.806979000
6	5.720967000	1.023804000	14.181125000
6	6.420946000	-0.928884000	15.619212000
1	7.079225000	-1.685705000	15.183224000
6	4.983213000	-1.409427000	15.550943000
1	4.943109000	-2.481853000	15.738299000
1	4.367715000	-0.913358000	16.301090000
6	4.478017000	-1.045131000	14.167623000
1	3.495785000	-1.438564000	13.940537000
1	5.154697000	-1.418027000	13.398790000
6	3.261378000	1.085440000	14.382054000
6	2.183878000	0.396787000	14.948185000
1	2.240027000	-0.643527000	15.213150000
6	1.024607000	1.107121000	15.200456000
1	0.177671000	0.602267000	15.645099000
6	0.948029000	2.463037000	14.936237000
1	0.053893000	3.003366000	15.189436000
6	2.074985000	3.089561000	14.394027000
6	0.829161000	5.216969000	14.313929000
1	0.832867000	6.048420000	13.607320000
1	-0.011625000	4.584971000	14.054675000
6	0.783221000	5.731523000	15.739945000
1	0.848203000	4.890640000	16.430065000
6	1.958777000	6.674637000	15.916220000
1	2.238391000	6.770496000	16.966773000
1	1.683095000	7.670804000	15.558900000
6	3.242913000	5.249966000	14.276727000
6	4.284268000	7.187475000	15.357106000
1	3.874513000	8.178460000	15.553215000
1	4.837808000	6.876748000	16.247694000
6	5.193572000	7.191558000	14.146748000
1	4.702184000	7.683466000	13.304864000
1	6.105089000	7.742642000	14.375640000
6	5.507026000	5.750828000	13.793336000
1	6.086765000	5.292937000	14.598892000
1	6.118448000	5.688589000	12.895780000
6	2.112001000	4.647426000	10.735329000
1	2.488932000	5.390755000	11.434635000
1	2.558633000	4.866914000	9.761862000
6	0.597702000	4.712977000	10.630480000
1	0.280957000	5.668268000	10.212292000
1	0.154657000	4.620676000	11.622845000
6	1.875569000	2.305131000	10.852621000
6	0.285960000	-0.138674000	10.280450000
1	0.687590000	-0.978349000	9.714239000
6	1.116416000	0.129572000	11.533294000
1	1.475690000	-0.778480000	12.003505000
1	0.513122000	0.654445000	12.271413000
6	3.510877000	0.462235000	10.952309000
6	3.668838000	-0.910312000	10.740043000
1	2.832001000	-1.587191000	10.729198000
6	4.951762000	-1.377739000	10.521014000
1	5.113739000	-2.435032000	10.359272000
6	6.030256000	-0.509905000	10.460203000

1	7.009325000	-0.896490000	10.242584000
6	5.778591000	0.857294000	10.619673000
6	8.152400000	1.338767000	10.163856000
1	8.856154000	2.079611000	10.542457000
1	8.356708000	0.408684000	10.680895000
6	8.252764000	1.217608000	8.655449000
1	9.225701000	0.839297000	8.344417000
1	7.496292000	0.517056000	8.302594000
6	8.026805000	2.605500000	8.068246000
1	7.549803000	2.550911000	7.087305000
1	8.987051000	3.106269000	7.931926000
6	6.545200000	3.123402000	10.041743000
6	7.180356000	4.869899000	8.439349000
1	8.180596000	5.127282000	8.088774000
1	6.510969000	4.919728000	7.576175000
6	6.721593000	5.818675000	9.527127000
1	7.509890000	5.946327000	10.271719000
1	6.506095000	6.794591000	9.092862000
6	5.487466000	5.233005000	10.185823000
1	4.672187000	5.188790000	9.458502000
1	5.140523000	5.858800000	11.005393000
6	0.313404000	1.123087000	9.401619000
6	0.110557000	3.584090000	9.742644000
1	-0.730285000	-0.396080000	10.577617000
1	-0.663903000	1.322861000	8.970127000
1	1.013966000	0.989792000	8.572985000
1	-0.974226000	3.481863000	9.791176000
1	0.384413000	3.779687000	8.700620000
1	-0.142225000	6.267532000	15.948787000
1	6.744037000	-0.770340000	16.650412000

Table S5. Cartesian Coordinates of the DFT-UKS calculated ground state geometry *mer-1*²⁺.

25	0.375339000	-0.243808000	0.544855000
6	1.762753000	-3.059877000	0.237409000
6	1.931048000	-4.445878000	0.328507000
6	0.847025000	-5.225067000	0.679289000
6	-0.379383000	-4.634356000	0.925272000
6	-0.483535000	-3.249979000	0.813252000
7	0.571204000	-2.490362000	0.477655000
1	2.873768000	-4.913340000	0.107044000
1	-1.221899000	-5.237408000	1.216221000
6	1.759361000	0.498927000	-2.191563000
6	2.483745000	0.002665000	-3.430216000
6	3.919057000	-0.285381000	-3.037480000
7	3.982989000	-0.988560000	-1.750196000
6	2.852706000	-1.215243000	-1.015076000
7	1.767752000	-0.522283000	-1.150144000
1	4.417436000	-0.917393000	-3.777333000
1	2.247701000	1.407627000	-1.824634000
1	2.457217000	0.741660000	-4.230021000
6	-1.936916000	-1.588997000	1.908087000
7	-3.201950000	-1.332757000	2.345128000
6	-3.440934000	-0.336752000	3.395217000
6	-2.349401000	0.713126000	3.429098000
6	-1.006331000	0.015683000	3.389687000
7	-0.890458000	-0.895926000	2.254401000
1	-3.516437000	-0.848835000	4.359594000
1	-0.856984000	-0.548380000	4.316953000
6	1.261216000	2.774734000	0.623797000
6	1.184615000	4.167235000	0.649246000
6	-0.043924000	4.766005000	0.453076000
6	-1.161112000	3.986213000	0.236974000
6	-1.026035000	2.593518000	0.234848000
7	0.170711000	2.010293000	0.434542000
1	2.054457000	4.771171000	0.836698000
1	-2.105933000	4.461314000	0.048221000
6	2.276222000	-0.686705000	2.993768000
6	3.153407000	-0.092988000	4.081776000
6	4.411729000	0.433186000	3.423029000
7	4.113435000	1.105823000	2.152960000
6	2.838993000	1.167820000	1.666287000
7	1.907157000	0.333341000	2.014203000
1	4.924346000	1.155957000	4.063292000
1	2.818008000	-1.499349000	2.496952000
1	3.418488000	-0.838806000	4.830325000
6	-2.244195000	0.711703000	-0.832720000
7	-3.413239000	0.500012000	-1.509820000

6	-3.434525000	-0.267341000	-2.761410000
6	-2.030303000	-0.626422000	-3.202227000
6	-1.272097000	-1.097414000	-1.975269000
7	-1.196934000	-0.034722000	-0.976986000
1	-3.946108000	0.345649000	-3.508380000
1	-2.065165000	-1.401159000	-3.967093000
1	-0.257560000	-1.404257000	-2.215901000
7	2.889457000	-2.267636000	-0.079688000
7	-1.755423000	-2.649418000	1.008795000
6	-2.896329000	-3.499086000	0.617966000
1	-3.022053000	-4.322599000	1.325085000
1	-2.669136000	-3.925639000	-0.356926000
1	0.958056000	-6.297813000	0.759757000
1	-0.131540000	5.843885000	0.463479000
7	-2.194185000	1.817585000	0.041376000
7	2.545904000	2.188503000	0.746691000
6	3.655768000	3.025569000	0.250714000
6	-3.458131000	2.525519000	0.324759000
1	-3.641282000	3.306384000	-0.417400000
1	-3.356267000	3.002890000	1.296435000
6	5.319129000	-1.423377000	-1.362718000
6	5.301037000	-1.871536000	0.079070000
6	4.192927000	-2.886043000	0.224628000
1	4.140671000	-3.275341000	1.239183000
1	5.126708000	-1.020803000	0.738613000
1	5.658153000	-2.235068000	-2.014377000
1	5.998467000	-0.580782000	-1.511191000
6	-4.376355000	-2.113790000	1.967737000
6	-4.175760000	-2.699119000	0.590145000
1	-5.004222000	-3.355450000	0.327768000
1	-4.121636000	-1.902605000	-0.152521000
1	-4.564271000	-2.906287000	2.699695000
1	-5.232484000	-1.440200000	1.990596000
1	-4.411229000	0.120050000	3.198211000
1	4.490202000	0.644084000	-2.964339000
1	1.998116000	-0.904396000	-3.795181000
1	0.724402000	0.759653000	-2.398082000
1	4.396774000	-3.721065000	-0.450062000
1	6.251500000	-2.326961000	0.351499000
1	-0.195525000	0.737239000	3.319118000
1	-2.453184000	1.322072000	4.327303000
1	-2.437786000	1.369689000	2.565572000
1	1.363724000	-1.116524000	3.395960000
1	2.613629000	0.712633000	4.583330000
1	5.111179000	-0.384235000	3.228796000
6	4.919074000	2.204093000	0.146798000
6	5.268497000	1.756335000	1.544793000
1	6.090449000	1.037067000	1.544604000
1	5.720118000	2.809389000	-0.272980000
1	4.761474000	1.342828000	-0.503295000
1	3.845196000	3.865600000	0.924186000
1	3.354617000	3.426061000	-0.714519000
1	5.583530000	2.610265000	2.152955000
6	-4.623557000	1.567465000	0.300441000
6	-4.717674000	1.001442000	-1.095650000
1	-5.536828000	2.100167000	0.560061000
1	-4.480635000	0.768897000	1.027505000
1	-5.425351000	0.169881000	-1.146019000
1	-5.063341000	1.767622000	-1.796718000
1	-4.034301000	-1.169940000	-2.613726000
1	-1.529461000	0.244164000	-3.629943000
1	-1.776812000	-1.970620000	-1.552191000

Table S6. Cartesian Coordinates of the DFT-UKS calculated ground state geometry of *mer-1*³⁺.

25	0.383227000	-0.222053000	0.339033000
6	1.724579000	-2.991375000	0.097939000
6	1.873696000	-4.374682000	0.224909000
6	0.796139000	-5.116912000	0.670579000
6	-0.409862000	-4.495693000	0.946821000
6	-0.510094000	-3.128391000	0.736524000
7	0.543658000	-2.407038000	0.333992000
1	2.798513000	-4.867349000	-0.015745000
1	-1.233293000	-5.060100000	1.352416000
6	1.679330000	0.693798000	-2.188187000
6	2.457343000	0.276959000	-3.416565000
6	3.884487000	0.034653000	-2.986933000
7	3.924212000	-0.815406000	-1.788587000

6	2.810848000	-1.094134000	-1.075858000
7	1.718409000	-0.359299000	-1.162320000
1	4.455059000	-0.486069000	-3.757353000
1	2.105559000	1.616094000	-1.790836000
1	2.420902000	1.058636000	-4.173100000
6	-1.877815000	-1.390769000	1.790245000
7	-2.999865000	-1.293249000	2.519317000
6	-3.211224000	-0.250558000	3.532549000
6	-2.241560000	0.903500000	3.386637000
6	-0.866122000	0.365982000	3.041418000
7	-0.894558000	-0.511979000	1.860356000
1	-3.097170000	-0.719661000	4.512864000
1	-0.472149000	-0.201718000	3.888082000
6	1.370787000	2.705092000	0.478209000
6	1.339243000	4.095341000	0.359929000
6	0.135363000	4.705123000	0.068133000
6	-1.008365000	3.947926000	-0.097575000
6	-0.914493000	2.565776000	0.041769000
7	0.256928000	1.973398000	0.320305000
1	2.214748000	4.697821000	0.514071000
1	-1.934427000	4.429422000	-0.353077000
6	2.049188000	-0.969168000	2.722886000
6	2.613582000	-0.352879000	3.987609000
6	3.967048000	0.220212000	3.632845000
7	3.898092000	0.955105000	2.358476000
6	2.767108000	0.999987000	1.615524000
7	1.840746000	0.071703000	1.706039000
1	4.319411000	0.927301000	4.386226000
1	2.751791000	-1.717483000	2.347360000
1	2.714539000	-1.102229000	4.770238000
6	-2.172903000	0.632515000	-0.853323000
7	-3.371625000	0.313771000	-1.394068000
6	-3.475456000	-0.693400000	-2.452997000
6	-2.141321000	-0.913650000	-3.119840000
6	-1.115930000	-1.177278000	-2.040598000
7	-1.093382000	-0.102443000	-1.037459000
1	-4.220614000	-0.339157000	-3.163774000
1	-2.201961000	-1.762680000	-3.798309000
1	-0.116756000	-1.261430000	-2.459742000
7	2.847388000	-2.206341000	-0.233006000
7	-1.758579000	-2.479667000	0.935079000
6	-2.944344000	-3.210203000	0.419470000
1	-2.898622000	-4.255656000	0.723285000
1	-2.902708000	-3.188814000	-0.669614000
1	0.900411000	-6.183294000	0.815263000
1	0.088962000	5.780043000	-0.036678000
7	-2.095807000	1.791206000	-0.083440000
7	2.610653000	2.071077000	0.727782000
6	3.796891000	2.889213000	0.383998000
6	-3.343648000	2.539038000	0.189732000
1	-3.557861000	3.237380000	-0.620579000
1	-3.178107000	3.110158000	1.095077000
6	5.258319000	-1.326489000	-1.471042000
6	5.272082000	-1.855084000	-0.059906000
6	4.148414000	-2.851514000	0.055266000
1	4.086259000	-3.266580000	1.058236000
1	5.145415000	-1.044435000	0.659696000
1	5.539638000	-2.105585000	-2.183856000
1	5.953153000	-0.495243000	-1.597665000
6	-4.045619000	-2.312409000	2.408222000
6	-4.232422000	-2.611211000	0.936020000
1	-5.045028000	-3.314215000	0.764770000
1	-4.472091000	-1.685644000	0.411339000
1	-3.759724000	-3.211059000	2.959307000
1	-4.946555000	-1.901307000	2.853929000
1	-4.242760000	0.086193000	3.448219000
1	4.395123000	0.977201000	-2.773231000
1	2.027074000	-0.629736000	-3.845166000
1	0.638569000	0.898195000	-2.419360000
1	4.326926000	-3.668606000	-0.644818000
1	6.216875000	-2.350330000	0.154984000
1	-0.176970000	1.178417000	2.844651000
1	-2.202189000	1.455504000	4.328261000
1	-2.574298000	1.606781000	2.621322000
1	1.105833000	-1.471061000	2.900992000
1	1.945199000	0.428956000	4.350432000
1	4.715543000	-0.570229000	3.544079000
6	5.067195000	2.098995000	0.571403000
6	5.121303000	1.681964000	2.020341000

1	5.955008000	1.006398000	2.216551000
1	5.918429000	2.728884000	0.321021000
1	5.094229000	1.226979000	-0.083271000
1	3.849837000	3.769376000	1.024983000
1	3.672995000	3.221027000	-0.644786000
1	5.235737000	2.552976000	2.670542000
6	-4.498685000	1.580651000	0.343478000
6	-4.661887000	0.882095000	-0.983326000
1	-5.404001000	2.121711000	0.619618000
1	-4.259109000	0.865855000	1.128374000
1	-5.372790000	0.054990000	-0.932071000
1	-5.021803000	1.582612000	-1.741898000
1	-3.863071000	-1.626829000	-2.030602000
1	-1.861609000	-0.032632000	-3.702500000
1	-1.326014000	-2.130937000	-1.557647000

Table S7. Cartesian Coordinates of the DFT-UKS calculated ground state geometry of *mer-1*⁴⁺.

25	-0.089767000	-0.595322000	-0.093908000
6	0.793990000	-3.122292000	-1.221706000
6	0.677685000	-4.446338000	-1.625940000
6	-0.518903000	-5.105611000	-1.439479000
6	-1.594411000	-4.445407000	-0.878267000
6	-1.460981000	-3.110711000	-0.531811000
7	-0.272687000	-2.471064000	-0.692262000
1	1.502521000	-4.954604000	-2.089122000
1	-2.515595000	-4.971210000	-0.705877000
6	1.239397000	0.982954000	-2.225994000
6	2.057382000	0.908998000	-3.493481000
6	3.437059000	0.431928000	-3.114805000
7	3.329282000	-0.838314000	-2.378917000
6	2.198260000	-1.184768000	-1.757050000
7	1.213504000	-0.319725000	-1.532557000
1	4.051803000	0.230115000	-3.989666000
1	1.667344000	1.741093000	-1.569767000
1	2.108866000	1.894343000	-3.951876000
6	-2.537959000	-1.567773000	1.024507000
7	-3.637306000	-1.341569000	1.741998000
6	-3.620945000	-0.591489000	3.013892000
6	-2.384635000	0.260844000	3.164305000
6	-1.176447000	-0.513973000	2.693965000
7	-1.371036000	-0.996148000	1.311176000
1	-3.689944000	-1.327485000	3.818347000
1	-1.009171000	-1.380337000	3.335832000
6	1.267787000	1.748829000	0.927971000
6	1.406647000	3.061014000	1.359018000
6	0.308619000	3.894794000	1.338909000
6	-0.909608000	3.426262000	0.896147000
6	-1.022411000	2.108086000	0.475481000
7	0.062303000	1.286056000	0.498576000
1	2.345817000	3.427995000	1.727743000
1	-1.751541000	4.090636000	0.856237000
6	1.228838000	-2.421228000	1.841602000
6	2.087419000	-2.455703000	3.083661000
6	3.501240000	-2.138296000	2.662998000
7	3.521262000	-0.891017000	1.879615000
6	2.409816000	-0.384842000	1.334461000
7	1.297170000	-1.096560000	1.194898000
1	4.150633000	-1.970296000	3.520513000
1	1.575781000	-3.187096000	1.147429000
1	2.041912000	-3.444926000	3.534833000
6	-2.457685000	0.812463000	-1.034370000
7	-3.614002000	0.853620000	-1.719229000
6	-3.733401000	0.256144000	-3.060321000
6	-2.366364000	0.050541000	-3.659405000
6	-1.542665000	-0.721269000	-2.658364000
7	-1.471832000	-0.011963000	-1.366804000
1	-4.315300000	0.950014000	-3.663194000
1	-2.444200000	-0.513240000	-4.586151000
1	-0.530182000	-0.877641000	-3.012180000
7	2.045533000	-2.494897000	-1.325129000
7	-2.595379000	-2.412778000	-0.068437000
6	-3.896047000	-2.934184000	-0.565309000
1	-4.053966000	-3.941051000	-0.184139000
1	-3.839355000	-2.974111000	-1.651975000
1	-0.616955000	-6.139191000	-1.737436000
1	0.402724000	4.917797000	1.672319000
7	-2.288524000	1.656988000	0.050704000

6.2 Supporting Information to Chapter 3.2. (“Oxidative Two-State Photoreactivity of a Manganese(IV) Complex using NIR Light”)

Oxidative Two-State Photoreactivity of a Manganese(IV) Complex using NIR Light

Nathan R. East¹, Robert Naumann¹, Christoph Förster¹, Charusheela Ramanan^{2,3}, Gregor Diezemann¹ and Katja Heinze^{1*}

¹ Department of Chemistry, Johannes Gutenberg University, Duesbergweg 10-14, 55128 Mainz, Germany

² Department of Physics and Astronomy, Vrije Universiteit Amsterdam, Amsterdam, Netherlands

³ Max-Planck-Institute for Polymer Research, Mainz, Germany

Supplementary Information

Table of Contents

1. Methods and Materials
2. Analytical and Spectroscopic Data
3. Cartesian coordinates of DFT-UKS calculated geometries
4. References

1. Methods and Materials

General Procedures. Acetonitrile CH_3CN was distilled under argon atmosphere from CaH_2 . Butyronitrile $\text{CH}_3\text{CH}_2\text{CH}_2\text{CN}$ was dried according to a previously reported procedure.¹ Nitromethane CH_3NO_2 , γ -valerolactone $\text{C}_5\text{H}_8\text{O}_2$ and 1,2-butylene carbonate $\text{C}_5\text{H}_8\text{O}_3$ were dried by storing over 25% v/v pre-activated 3 Å molecular sieves for two days, distillation under reduced pressure at 30°C under argon and by three freeze pump thaw cycles to remove oxygen. The arene substrates (from commercial suppliers Acros, Alfa Aesar, Fischer and Sigma-Aldrich) were distilled prior to use. The complex $[\text{Mn}(\text{dgpy})_2][\text{PF}_6]_4$ was prepared according to a literature procedure.²

UV/Vis/NIR spectra were recorded on a Jasco V770 spectrometer using 1.0 cm cells (Hellma, Suprasil) under inert atmosphere.

NMR spectra were recorded on a Bruker Avance DRX 400 spectrometer. The measurements were performed at 400.31 MHz (^1H), 100.05 MHz ($^{13}\text{C}\{^1\text{H}\}$), 162.04 MHz ($^{31}\text{P}\{^1\text{H}\}$) and 376.67 MHz (^{19}F); [CD_3CN (^1H , $\delta = 1.94$)].³

ATR-IR spectra were recorded with a Bruker ALPHA II FT-IR spectrometer with a platinum Di-ATR module inside an argon-filled glovebox.

ESI mass spectra were recorded on a Micromass Q-TOF-Ultima spectrometer in CH_3CN .

High performance liquid chromatography was performed on a Jasco 2000 series HPLC containing a UV-2075plus detector and a repositil 100, C18 5 μm reversed phase column (250 x 4.6 mm). Measurements were carried out at 40°C and pH 7 using a CH_3CN /water gradient eluent and the product retention time was compared with an authentic sample. The yield was determined by comparing peak areas.

Conductivities were measured with a Greisinger conductivity cell, model 6MH 3431 LFE-210 with platinum electrodes in dry acetonitrile under inert atmosphere. The equivalent conductivity Λ_e was plotted as a function of $c^{0.5}$. To determine Λ_0 , Λ_e was linearly extrapolated to infinite dilution.

Variable temperature steady-state emission spectra were recorded with a FLS1000 spectrometer from *Edinburgh Instruments* equipped with the cooled, red and NIR sensitive photomultiplier detectors PMT-980 and N-G09 PMT-1700. The CW lasers RLMDL-730-1W-3 and RLMDL-635-1W-3 from *Roithner Lasertechnik* were employed for excitation. For the sample preparation, a small amount of the solid was pressed to the inner wall of a self-made low temperature quartz cuvette with a spatula until the glass was covered with a thin layer of the sample. The measurements were carried out in a liquid nitrogen cooled cryostat Optistat DN from *Oxford Instruments*.

fs-Transient absorption experiments were conducted using a Helios-Fire pump-probe setup from *Ultrafast Systems* paired with a regeneratively amplified 1030 nm laser (*Pharos, Light Conversion*, 1030 nm, 200 fs, 200 μJ). The effective laser repetition rate of 1 kHz was set via an internal pulse picker. A small portion of the 1030 nm fundamental was directed to the optical delay line and was subsequently used to generate broadband probe light by focusing the beam onto a sapphire (Vis/NIR range) or CaF_2 (UV/Vis range) crystal. The pump pulse was generated with an optical parametric amplifier (*Orpheus-F, Light Conversion*). The samples were measured in a 1 mm quartz cuvette under argon. To cover the whole spectral region from 350 nm to 900 nm, the UV/Vis and Vis/NIR part of the transient absorption spectra were recorded separately under identical conditions and were combined using the overlap of both datasets in the vis region (500 nm – 550 nm). The software Glotaran 1.5.1 was employed for the global analysis of the TA data.⁴

Photolysis experiments were conducted under argon in airtight quartz cuvettes (1 cm) with $[\text{Mn}(\text{dgy})_2][\text{PF}_6]_4$ (50 μM) in dry solvents and in the absence or presence of the substrates given. The high-power LEDs UHP-T-730-LA34 (730 nm, 2.6 W) and UHP-T-850-LA33 (850 nm, 5.1 W) from *Prizmatix* were employed as collimated light sources (for emission spectra, see Supplementary Figs. 2 and 3).⁵ The temperature of the solution was kept constant at 25 °C using an *Agilent* Cary single cell peltier. To monitor the reaction progress, UV/Vis/NIR absorption spectra were recorded at regular time intervals. Supplementary Fig. 1 shows a representative photolysis experiment with irradiation at 730 nm.

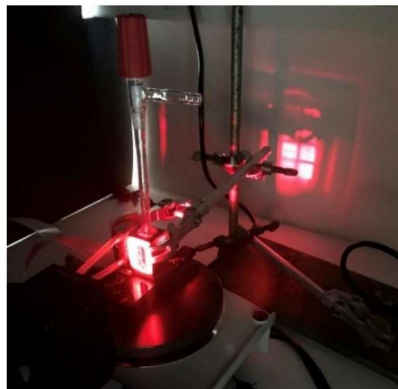


Figure 1. Photolysis experiment with the 730 LED.

ESI mass spectra were recorded directly from the photolysis reaction without further workup. Samples for HPLC quantification were treated with water (1 ml) and left to stand for 12 h at ambient conditions to give a brown precipitate (likely MnO_2). After filtration, the solvents were removed under reduced pressure and the yellow residue was dissolved in CH_3CN and subjected to HPLC.

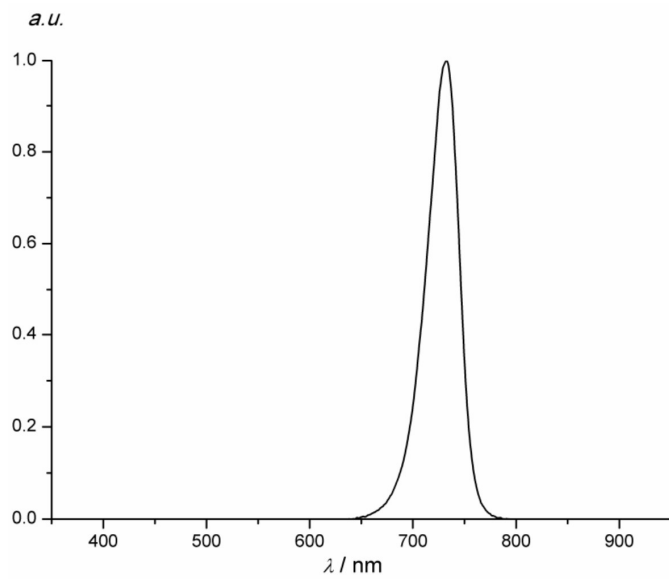


Figure 2. Normalized emission spectrum of the Prizmatix UHP-T-LA-730 LED series Ultra High Power LED (730 nm).⁵

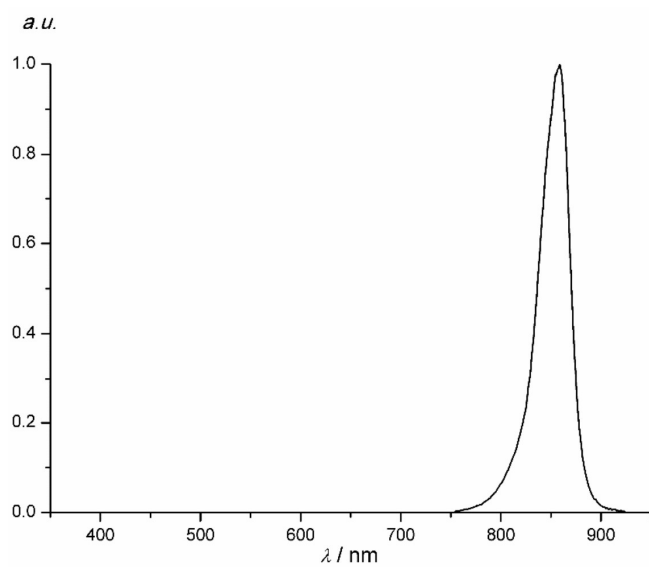


Figure 3. Normalized emission spectrum of the Prizmatix UHP-T-LA-850 LED series Ultra High Power LED (850 nm).⁵

Density Functional Theory (DFT) calculations were carried out using the ORCA program package⁶ (version 5.0.1). Tight convergence criteria were chosen for all calculations (keywords *tightscf* and *tightopt*). All calculations were performed using the B3LYP functional^{7–9} employing the RIJCOSX approximation (keyword *RIJCOSX*).^{10,11} Relativistic effects were calculated at the zeroth order regular approximation (keyword *ZORA*) level.¹² The *ZORA* keyword automatically invokes relativistically adjusted basis sets. To account for solvent effects, a conductor-like screening model (keyword *CPCM*) modeling acetonitrile was used in all calculations.^{13,14} Geometry optimizations were performed using Ahlrichs' polarized valence triple-zeta basis set (def2-TZVPP).^{15,16} Atom-pairwise dispersion correction was performed with the Becke-Johnson damping scheme (D3BJ).^{17,18} The energy of the electronic states and presence of energy minima were checked by numerical frequency calculations. Explicit counter ions and/or solvent molecules were not taken into account. The charge transfer number analyses of the time-dependent DFT (TDDFT)-calculated transitions were done using TheoDORE 2.2.^{19,20}

Molecular dynamics simulations were performed using the GROMACS 2018.4 program package employing the (optimized potentials for liquid simulations - all atom) OPLS-AA force field.^{21,22} All topologies were generated by hand. The geometry of the $[\text{Mn}(\text{dgp})_2]^{4+}$ ion was used as computed quantum chemically.² Mulliken charges were generated from a single point UHF calculation with a 6-31G basis using the Q-Chem 5.3.2 program package.²³ For the short-range interactions a cut-off of 1.2 nm was used and the long-range Coulomb interaction was treated using the particle-mesh Ewald method,²⁴ while for the van der Waals interaction a dispersion correction was applied.⁵ Periodic boundary conditions were used and the time step was 2 fs, which was possible because all bonds including a hydrogen atom were restrained to their equilibrium value using the LINCS algorithm.²⁶ The production run was prepared according to the following protocol. After an energy minimization of the solvated system, consisting of the complex, four $[\text{PF}_6]^-$ ions and 1760 acetonitrile molecules, an equilibration of 1 ns in the NVT ensemble at $T = 298$ K was performed using a velocity rescaling thermostat²⁷ with a time constant of 0.1 ps. Afterwards, the system was simulated for 1 ns in the NPT ensemble at a pressure of 1 bar using a Berendsen barostat²⁸ with a time constant of 2 ps and an isothermal compressibility of $1.26 \times 10^{-4} \text{ bar}^{-1}$ yielding a box size of $(5.43 \text{ nm})^3$. The system was then simulated at equilibrium for 1 μs and the resulting trajectory was analyzed using the tools provided by the GROMACS program package.

Synthesis of $[\text{Mn}(\text{dgpy})_2][\text{ClO}_4]_4$: A solution of 50 mg (0.034 mmol, 1.0 eq) $[\text{Mn}(\text{dgpy})_2][\text{PF}_6]_4$ in dry CH_3CN (3 mL) was added to a solution of 116 mg (0.34 mmol, 10 eq) $[\text{nBu}_4\text{N}][\text{ClO}_4]$ in dry CH_3CN (2 mL). The reaction was stirred at ambient temperature for 5 min. The product was purified by crystallization via slow diffusion of dry diethyl ether into a concentrated solution in acetonitrile to yield dark crystals. To ensure complete anion exchange, this procedure was repeated with another 10 eq of $[\text{nBu}_4\text{N}][\text{ClO}_4]$ to yield dark crystals of $[\text{Mn}(\text{dgpy})_2][\text{ClO}_4]_4$. The absence of $[\text{PF}_6]^-$ (831 and 558 cm^{-1}) and the presence of $[\text{ClO}_4]^-$ (1075 , 1042 and 1010 cm^{-1}) was confirmed by IR spectroscopy (Figure 4). IR (ATR): $\tilde{\nu} / \text{cm}^{-1} = 1576$ (s), 1486 (m), 1460 (m, sh), 1435 (m, sh), 1407 (w), 1380 (s), 1153 (w), 1075 (s), 1042 (s, sh), 1010 (s, sh), 938 (w, sh), 910 (m), 880 (m, sh), 848 (w), 800 (m), 749 (w, sh), 735 (m), 707 (m).

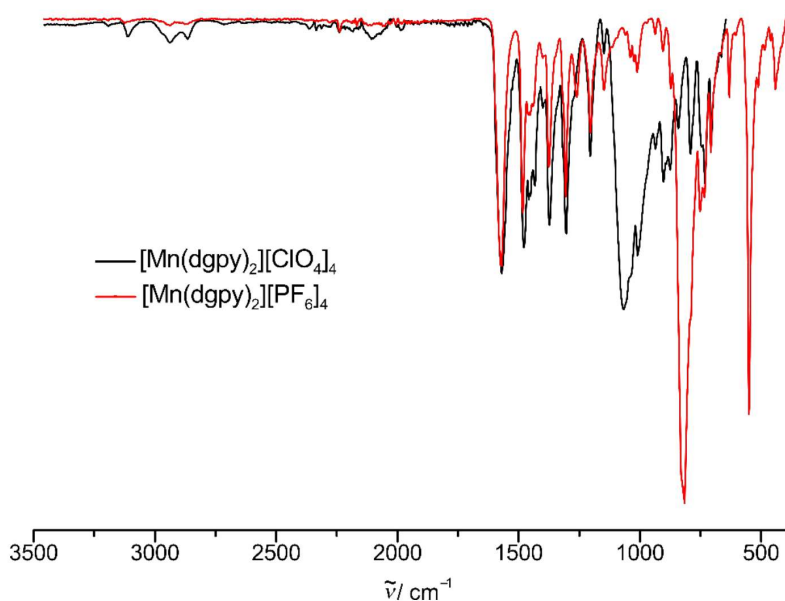


Figure 4. ATR-IR spectra of $[\text{Mn}(\text{dgpy})_2][\text{PF}_6]_4$ (red) and $[\text{Mn}(\text{dgpy})_2][\text{ClO}_4]_4$ (black) showing the successful $[\text{PF}_6]^-$ to $[\text{ClO}_4]^-$ counter ion exchange.

2. Analytical and Spectroscopic Data

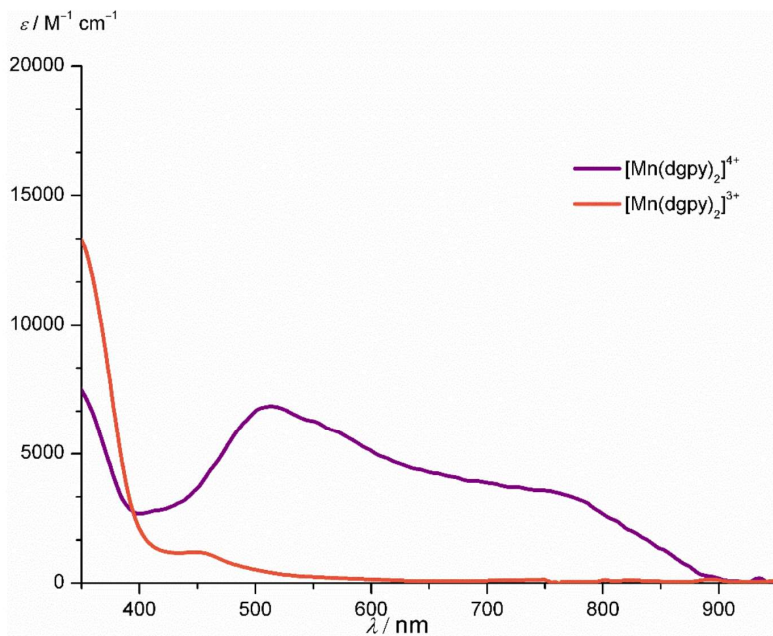


Figure 5. Absorption spectra of $[\text{Mn}(\text{dgpy})_2][\text{PF}_6]_4$ (purple) and $[\text{Mn}(\text{dgpy})_2][\text{PF}_6]_3$ (orange) in CH_3CN .¹

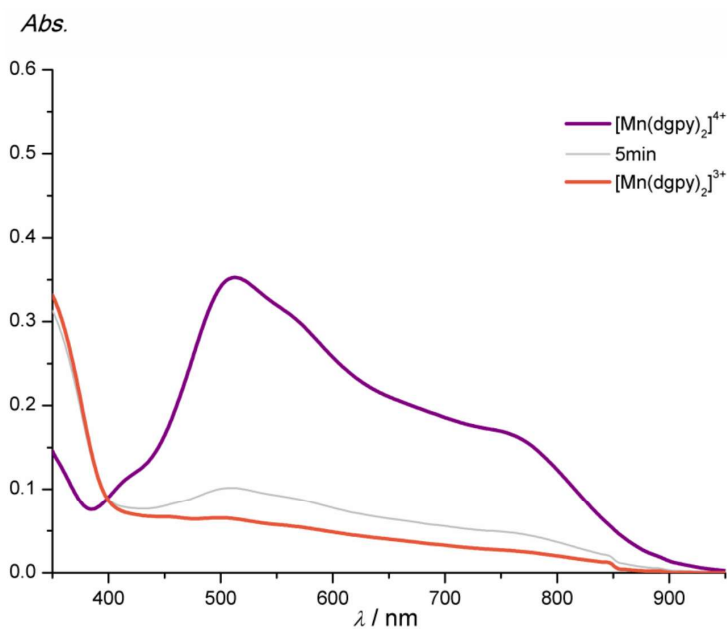


Figure 6. Absorption spectra of $[\text{Mn}(\text{dgpy})_2][\text{PF}_6]_4$ (purple) and after addition of 1 eq $[\text{n-Bu}_4\text{N}]\text{Cl}$ in CH_3CN after 5 min (grey) and 10 min (orange) in the dark.

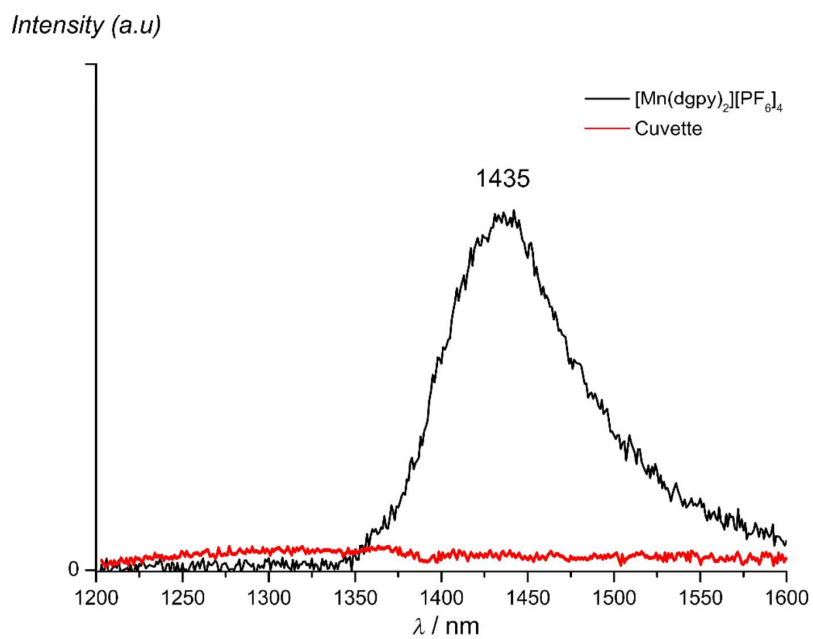


Figure 7. Luminescence spectra of $[\text{Mn}(\text{dgpy})_2][\text{PF}_6]_4$ after laser excitation with 635 nm at 77 K with control measurement at 77 K (empty cuvette).

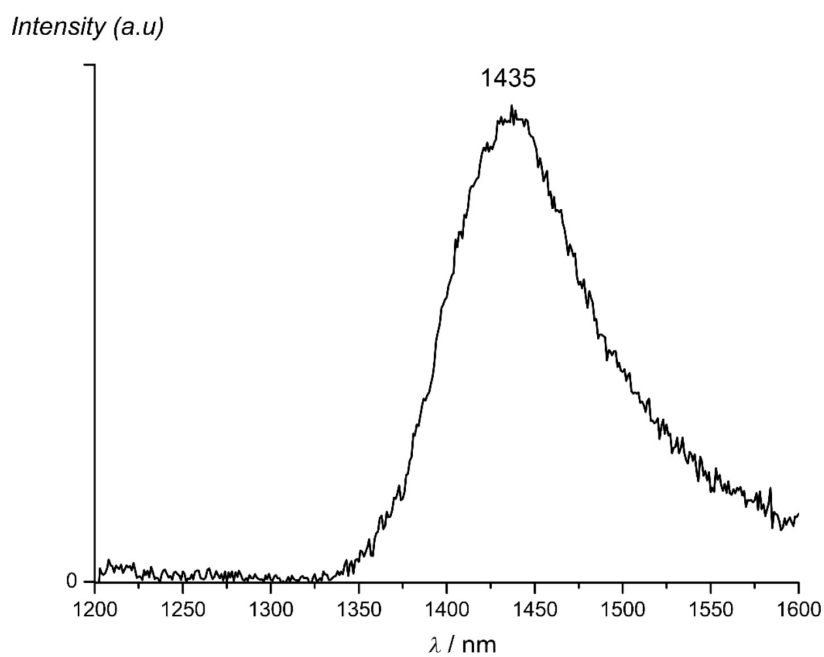


Figure 8. Luminescence spectra of $[\text{Mn}(\text{dgpy})_2][\text{PF}_6]_4$ after laser excitation with 730 nm at 77 K.

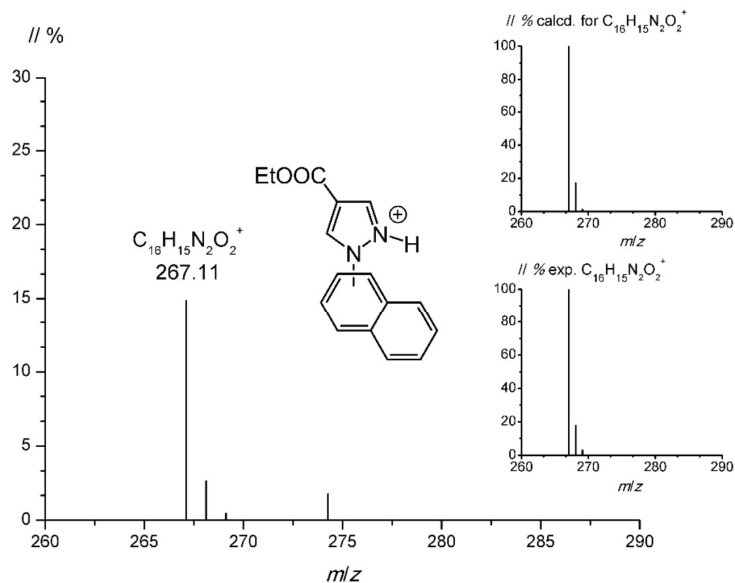


Figure 9. ESI⁺ mass spectrum of the product generated from the oxidation of naphthalene $C_{10}H_8$ (0.3 M) in CH_3CN with $[Mn(dgpy)_2][PF_6]_4$ (2 mM) under 730 nm irradiation in the presence of 1H-pyrazole-4-carboxylic acid ethyl ester (30 mM). The inset shows the experimental and calculated isotopic patterns of the $m/z = 267$ ($[C_{16}H_{15}N_2O_2]^+$) peak.

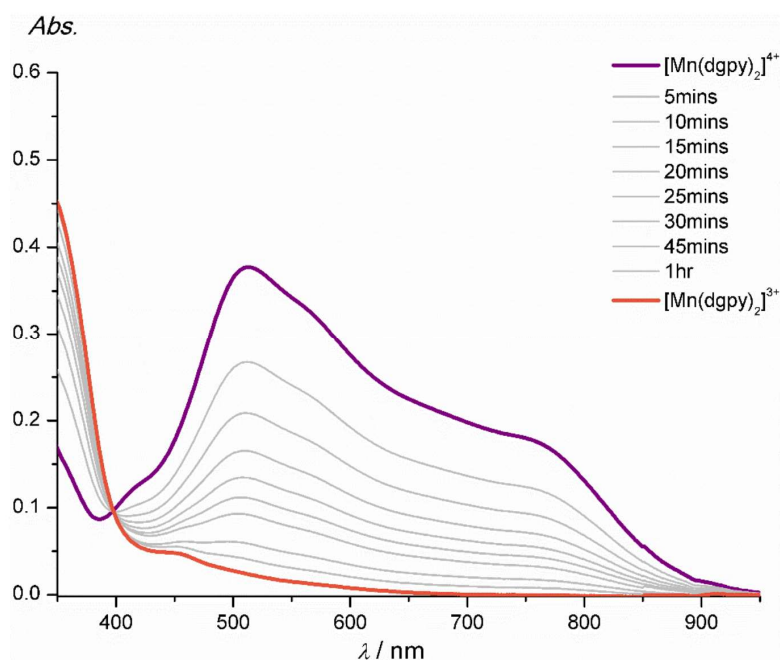


Figure 10. Absorption spectra of $[Mn(dgpy)_2][PF_6]_4$ (purple: before irradiation; orange: $[Mn(dgpy)_2][PF_6]_3$) during irradiation with the 730 nm LED in 0.3 M mesitylene in CH_3CN for 75 min.

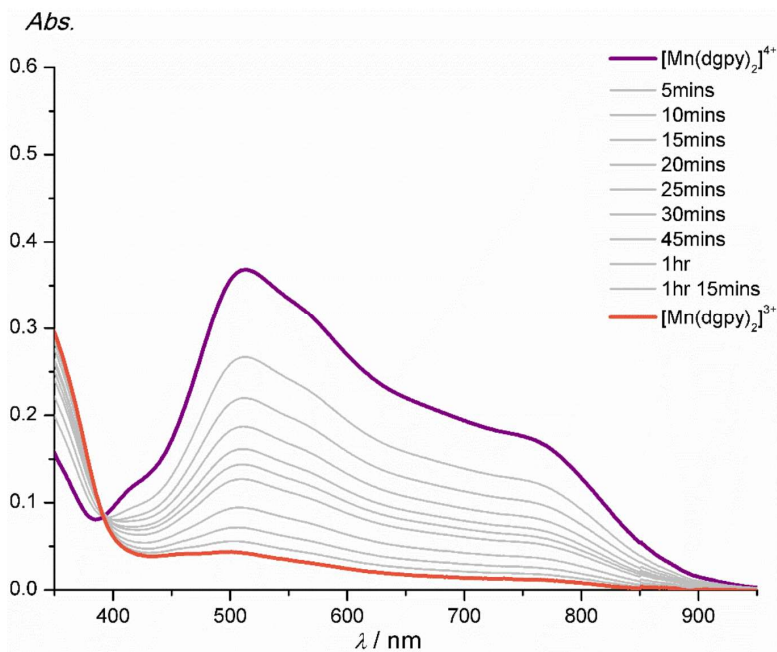


Figure 11. Absorption spectra of $[\text{Mn}(\text{dgpy})_2][\text{PF}_6]_4$ (purple: before irradiation; orange: $[\text{Mn}(\text{dgpy})_2][\text{PF}_6]_3$) during irradiation with the 730 nm LED in 0.3 M toluene in CH_3CN for 90 min.

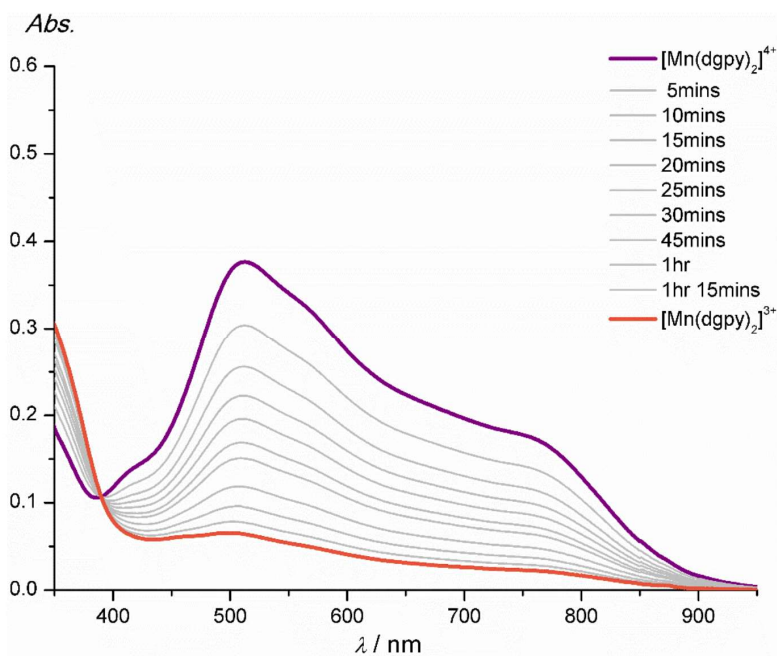


Figure 12. Absorption spectra of $[\text{Mn}(\text{dgpy})_2][\text{PF}_6]_4$ (purple: before irradiation; orange: $[\text{Mn}(\text{dgpy})_2][\text{PF}_6]_3$) during irradiation with the 730 nm LED in 0.3 M benzene in CH_3CN for 90 min.

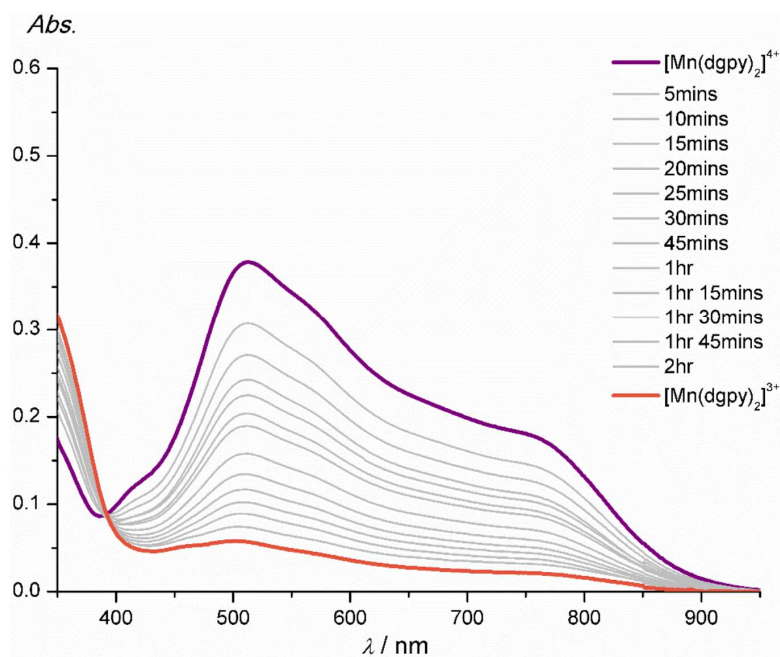


Figure 13. Absorption spectra of $[\text{Mn}(\text{dgpy})_2][\text{PF}_6]_4$ (purple: before irradiation; orange: $[\text{Mn}(\text{dgpy})_2][\text{PF}_6]_3$) during irradiation with the 730 nm LED in CH_3CN for 135 min.

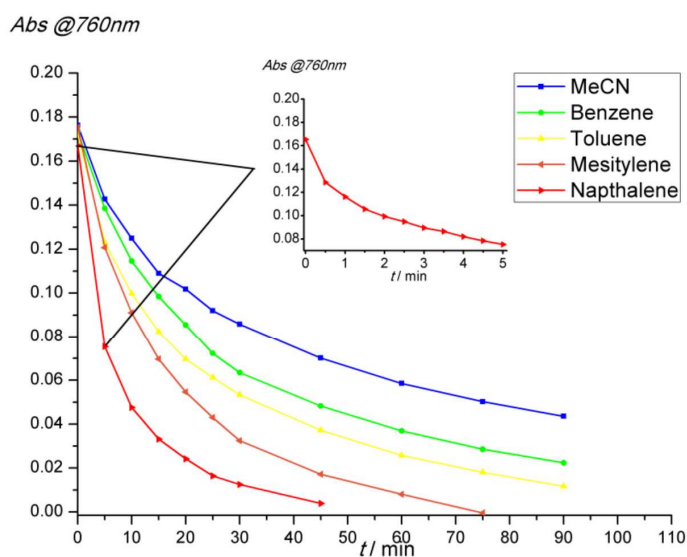


Figure 14. Kinetic traces observed at 760 nm of $[\text{Mn}(\text{dgpy})_2][\text{PF}_6]_4$ under irradiation with 730 nm in CH_3CN (blue), 0.3 M benzene in CH_3CN (green), 0.3 M toluene in CH_3CN (yellow), 0.3 M mesitylene in CH_3CN (orange) and 0.3 M naphthalene in CH_3CN (red). The inset shows the reaction with naphthalene over a minute time scale, measured in a separate experiment, demonstrating the high initial rate of this reaction.

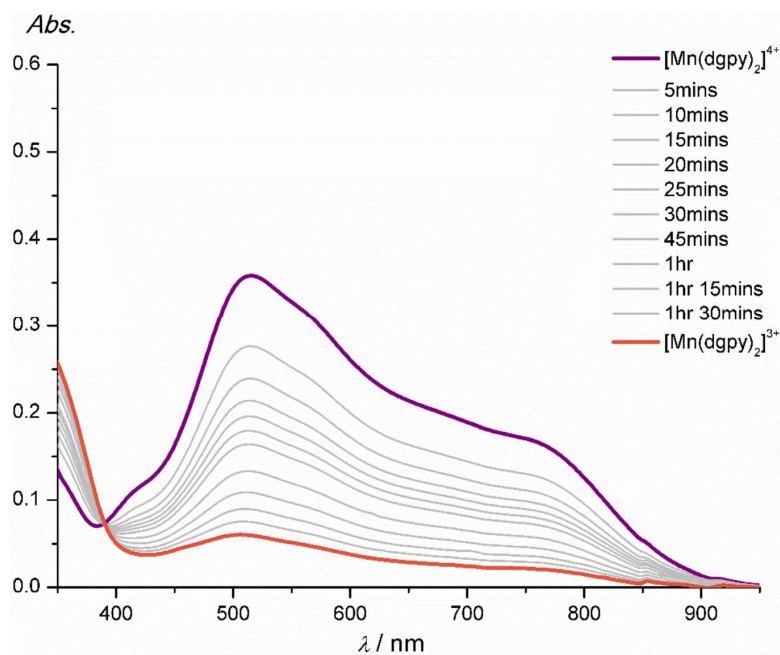


Figure 15. Absorption spectra of $[\text{Mn}(\text{dgpy})_2][\text{PF}_6]_4$ (purple: before irradiation; orange: $[\text{Mn}(\text{dgpy})_2][\text{PF}_6]_3$) during irradiation with the 730 nm LED in $\text{CH}_3\text{CH}_2\text{CH}_2\text{CN}$ for 105 min.

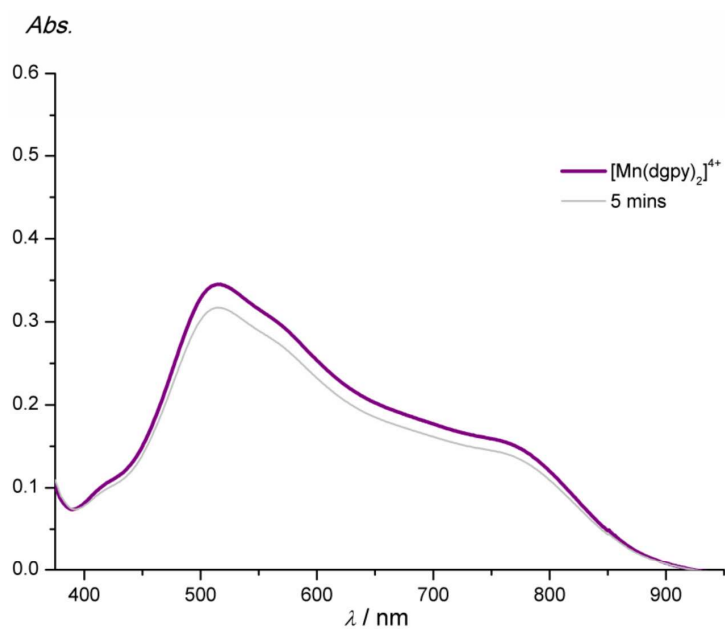


Figure 16. Absorption spectra of $[\text{Mn}(\text{dgpy})_2][\text{PF}_6]_4$ (purple: before irradiation; grey: after 5 min irradiation) during irradiation with the 730 nm LED in CH_3NO_2 .

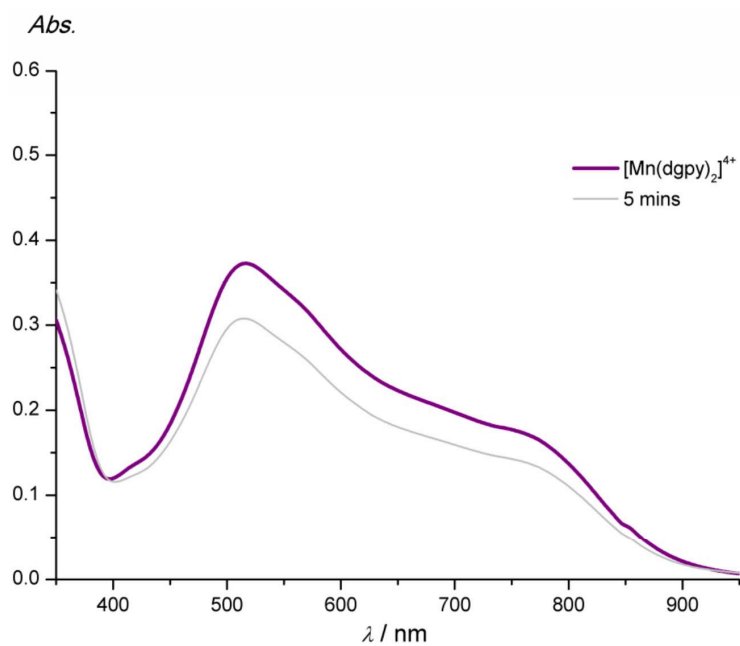


Figure 17. Absorption spectra of $[\text{Mn}(\text{dgpy})_2][\text{PF}_6]_4$ (purple: before irradiation; grey: after 5 min irradiation) during irradiation with the 730 nm LED in 1,2-butylene carbonate.

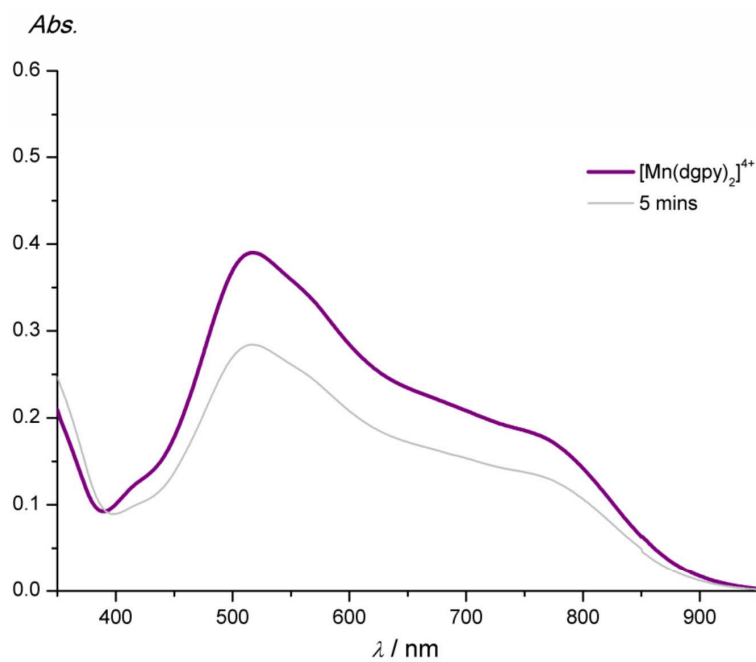


Figure 18. Absorption spectra of $[\text{Mn}(\text{dgpy})_2][\text{PF}_6]_4$ (purple: before irradiation; orange: grey 5 min irradiation) during irradiation with the 730 nm LED in γ -valerolactone.

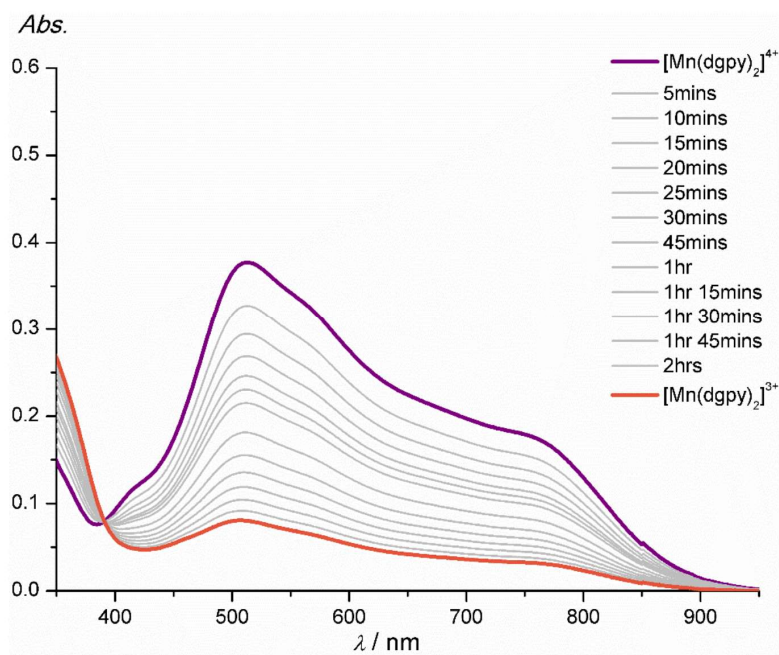


Figure 19. Absorption spectra of $[\text{Mn}(\text{dgpy})_2][\text{PF}_6]_4$ (purple: before irradiation; orange: $[\text{Mn}(\text{dgpy})_2][\text{PF}_6]_3$) during irradiation with the 850 nm LED in CH_3CN for 135 min.

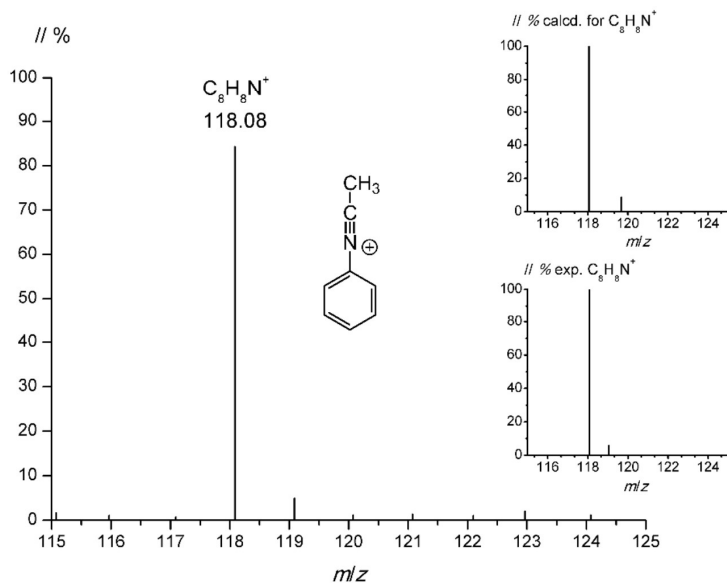


Figure 20. ESI⁺ mass spectrum of the nitrilium product generated from the oxidation of benzene C₆H₆ (0.3 M) in CH₃CN with [Mn(dgpy)₂][PF₆]₄ (1 mM) under 730 nm irradiation. The inset shows the experimental and calculated isotopic pattern of the *m/z* = 118 peak ([C₈H₈N]⁺).

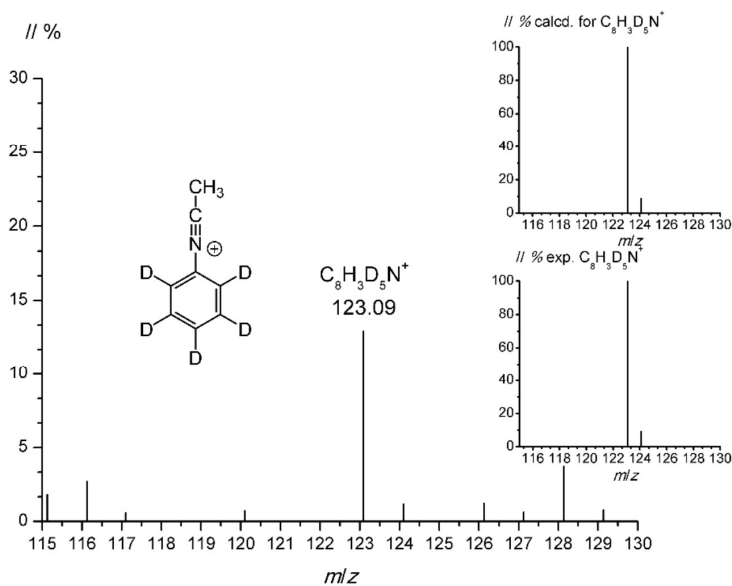


Figure 21. ESI⁺ mass spectrum of the nitrilium product generated from the oxidation of deuterated benzene C₆D₆ (0.3 M) in CH₃CN with [Mn(dgpy)₂][PF₆]₄ (1 mM) under 730 nm irradiation. The inset shows the experimental and calculated isotopic pattern of the *m/z* = 123 peak ([C₈H₅D₅N]⁺).

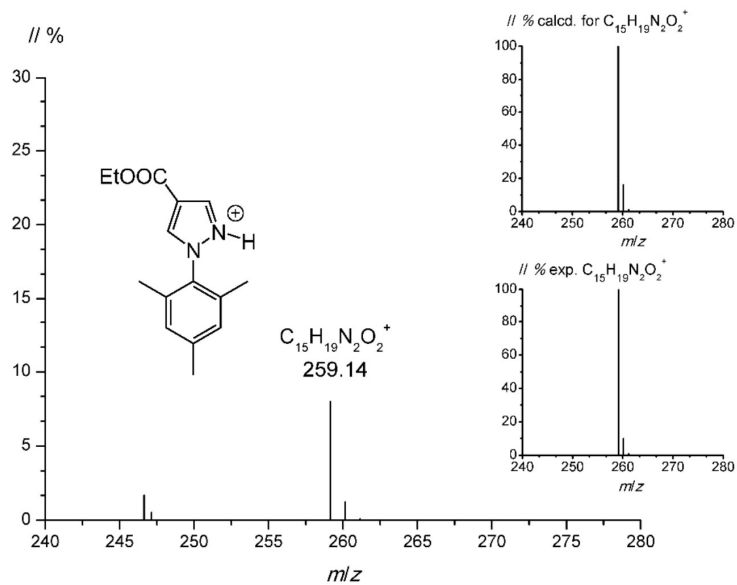


Figure 22. ESI⁺ mass spectrum of the product generated from the oxidation of mesitylene (15 mM) in CH₃CN with [Mn(dgpy)₂][PF₆]₄ (4.5 mM) under 730 nm irradiation in the presence of 1H-pyrazole-4-carboxylic acid ethyl ester (15 mM). The inset shows the experimental and calculated isotopic pattern of the *m/z* = 259 peak ([C₁₅H₁₉N₂O₂]⁺).

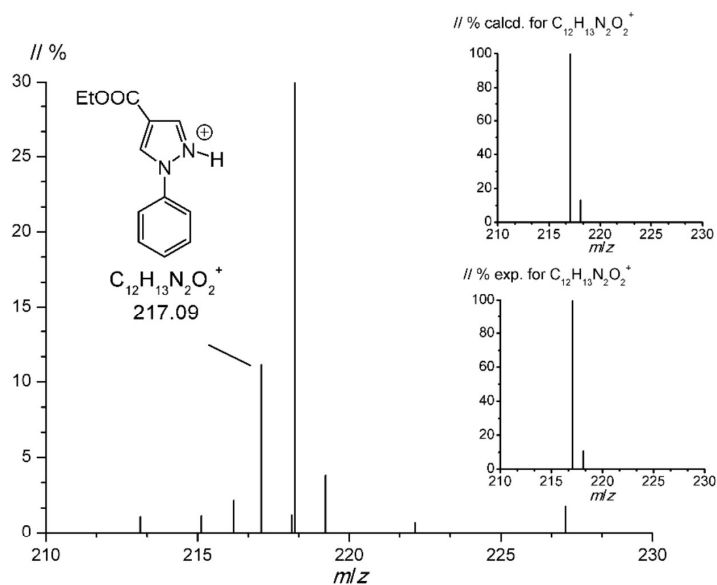


Figure 23. ESI⁺ mass spectrum of the product generated from the oxidation of benzene C₆H₆ (1.3 M) in CH₃CN with [Mn(dgpy)₂][PF₆]₄ (2 mM) under 730 nm irradiation in the presence of 1H-pyrazole-4-carboxylic acid ethyl ester (30 mM). The inset shows the experimental and calculated isotopic patterns of the *m/z* = 217 ([C₁₂H₁₃N₂O₂]⁺) peak.

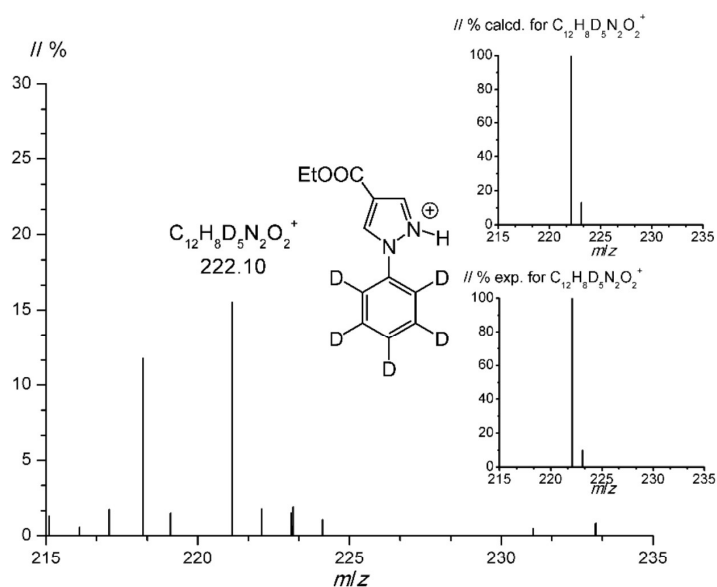


Figure 24. ESI⁺ mass spectrum of the product generated from the oxidation of deuterated benzene C₆D₆ (1.3 M) in CH₃CN with [Mn(dgpy)₂][PF₆]₄ (2 mM) under 730 nm irradiation in the presence of 1H-pyrazole-4-carboxylic acid ethyl ester (30 mM). The inset shows the experimental and calculated isotopic patterns of the *m/z* = 222 ([C₁₂H₈D₅N₂O₂]⁺) peak.

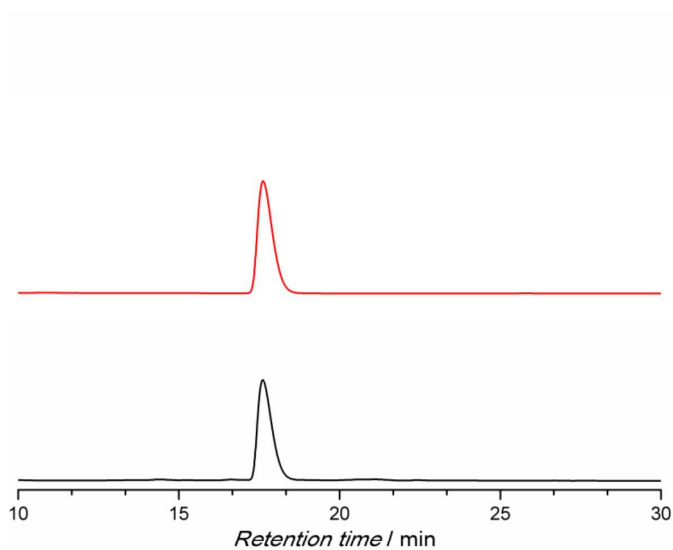


Figure 25. HPLC chromatogram of an authentic sample of ethyl 1-phenyl-1H-pyrazole-4-carboxylate as reference in CH₃CN/H₂O (red) and of the product of the 730 nm photolysis of benzene (1.3 M), 1H-pyrazole-4-carboxylic acid ethyl ester (30 mM) and [Mn(dgpy)₂][PF₄]₄ (4.5 mM) as limiting reagent in CH₃CN. Yield (11 %) determined by comparison of peak areas.

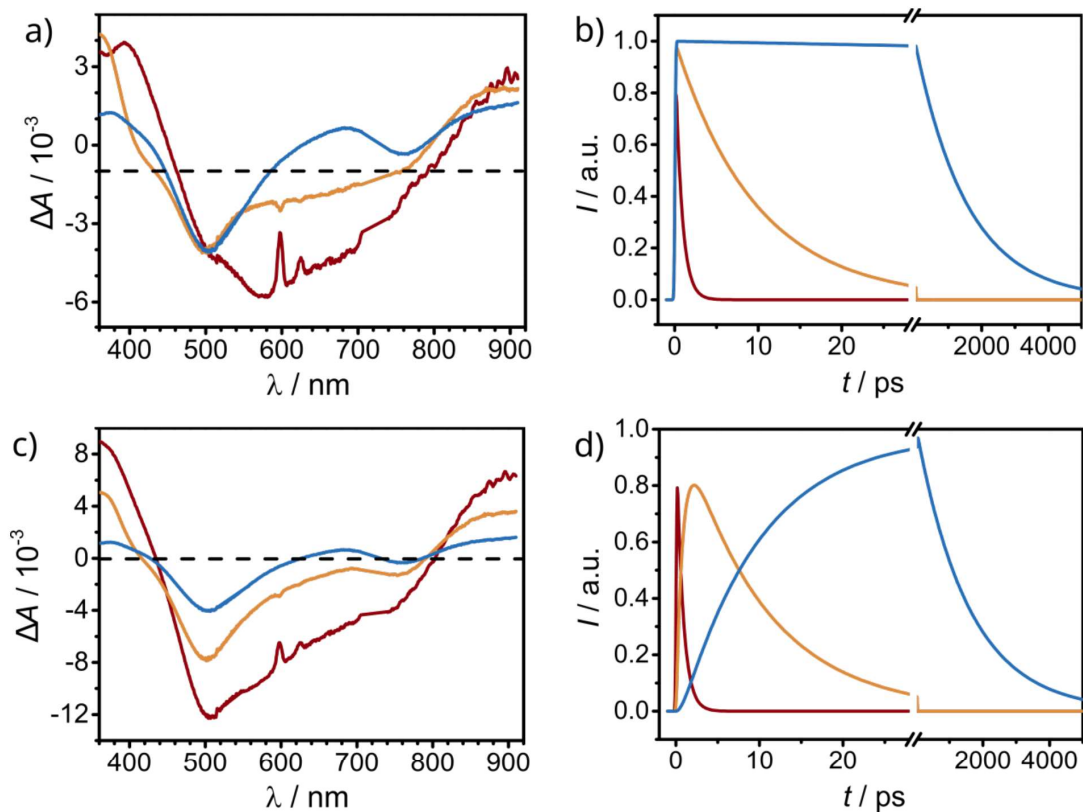


Figure 26. a) Decay associated difference spectra and c) evolution associated difference spectra and corresponding decay traces b) and d) of the global fit of the TA spectra obtained upon 730 nm excitation (800 nJ / pulse) of $[\text{Mn}(\text{dgpy})_2][\text{PF}_6]_4$ in CH_3CN (Fig. 2a of the main article). Lifetimes: 780 fs (red), 9.7 ps (orange), 1.6 ns (blue).

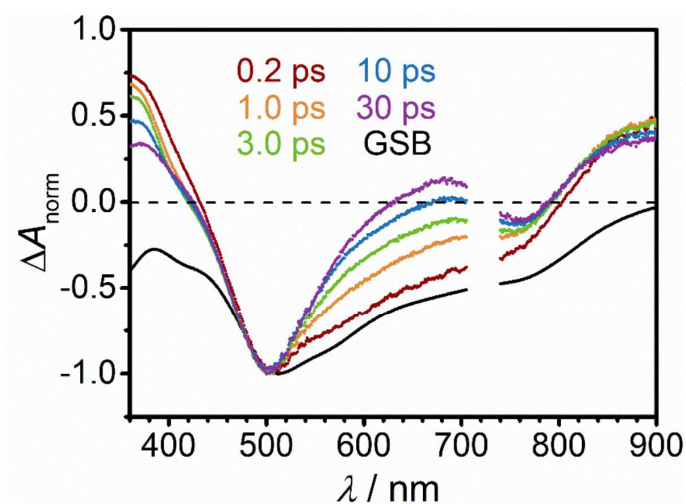


Figure 27. Normalized fs-transient absorption spectra of $[\text{Mn}(\text{dgpy})_2][\text{PF}_6]_4$ in CH_3CN after laser excitation at 730 nm (800 nJ / pulse) and hypothetical ground state bleach spectrum obtained from the normalized negative ground state spectrum of $[\text{Mn}(\text{dgpy})_2][\text{PF}_6]_4$ in CH_3CN (black).

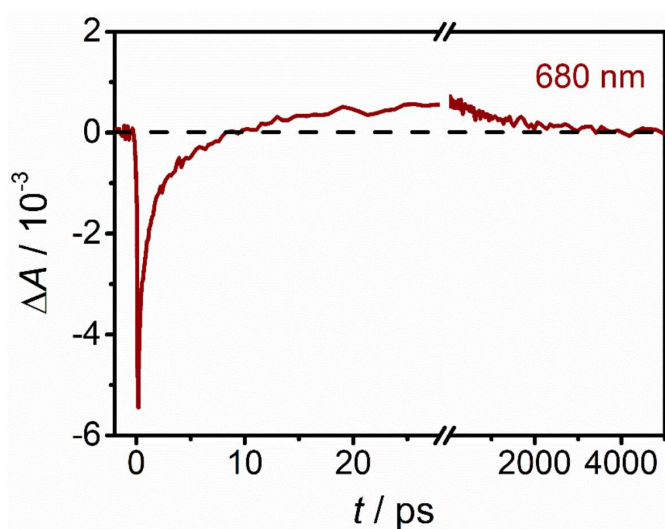


Figure 28. Decay trace at 680 nm from the transient absorption spectra of $[\text{Mn}(\text{dgpy})_2][\text{PF}_6]_4$ in CH_3CN after excitation with 730 nm laser pulses (800 nJ / pulse)

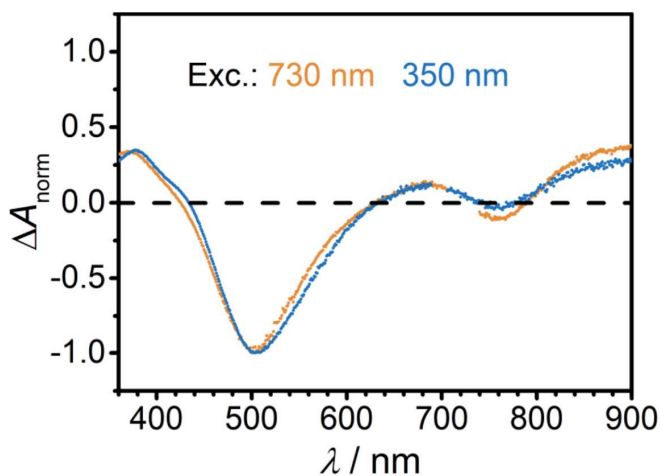


Figure 29. Normalized fs-transient absorption spectra of $[\text{Mn}(\text{dgpy})_2][\text{PF}_6]_4$ in CH_3CN 30 ps after laser excitation at 350 nm (400 nJ / pulse, blue) and 730 nm (800 nJ / pulse, orange), respectively.

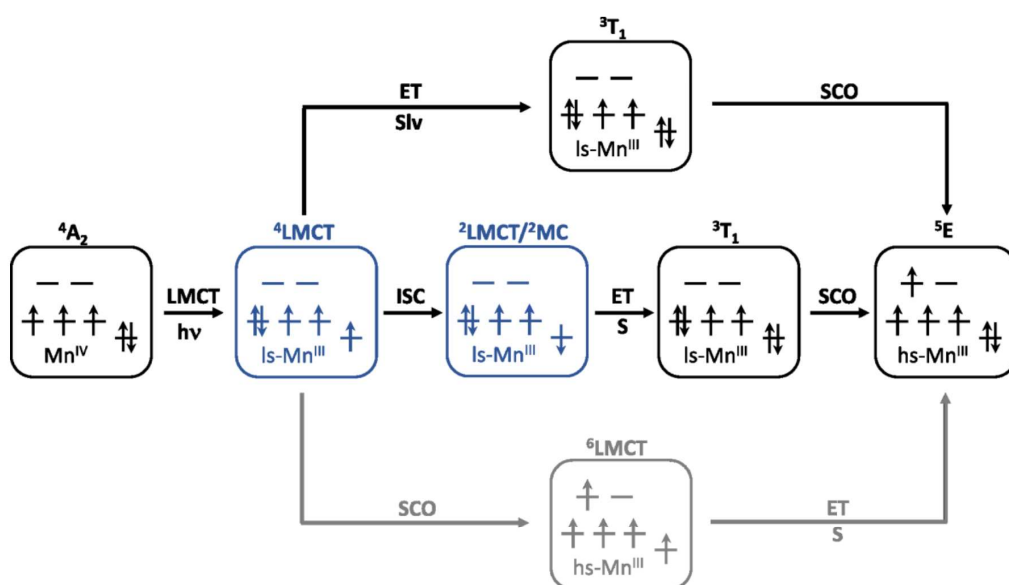


Figure 30. Possible mechanistic scenarios of the dynamics of the ${}^4\text{LMCT}$ excited state by static quenching by hole transfer to a solvent molecule Slv (top), by ISC to the ${}^2\text{LMCT}/{}^2\text{MC}$ state followed by hole transfer to a substrate (e.g. naphthalene as shown in the main text) to give the low-spin manganese(III) complex (${}^3\text{T}_1$) and SCO to the high-spin manganese(III) complex (${}^5\text{E}$) (center) and SCO to give a ${}^6\text{LMCT}$ state followed by hole transfer to a substrate S (bottom) to give the high-spin manganese(III) complex (${}^5\text{E}$). For details, see main article.

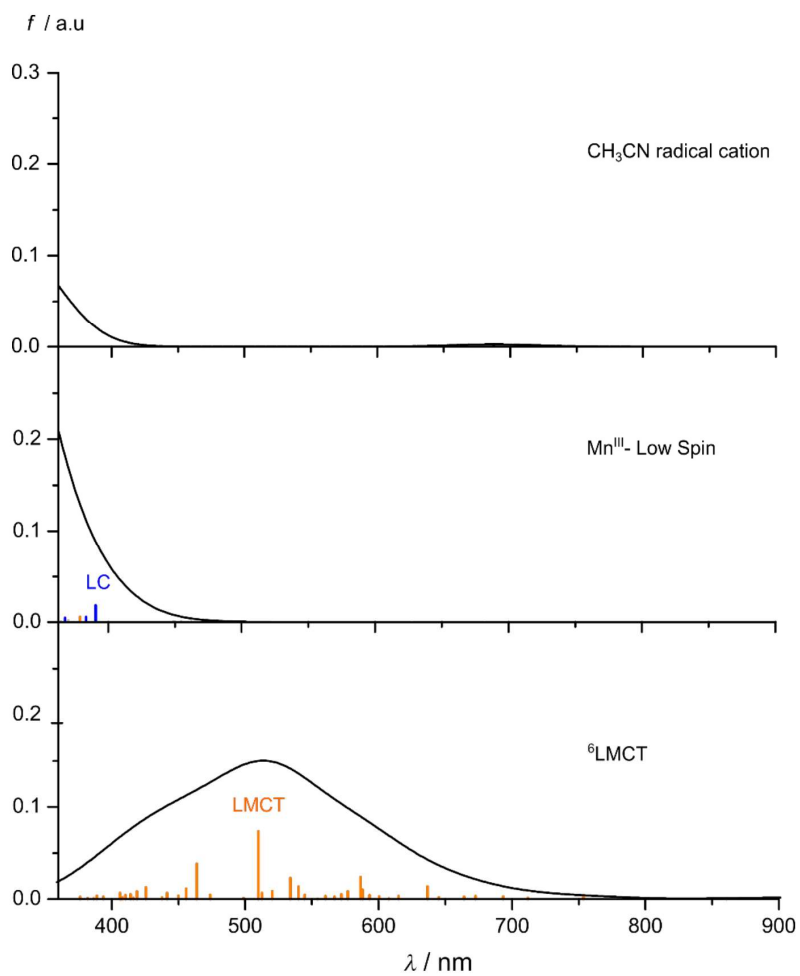


Figure 31. Time-dependent DFT calculated spin-allowed transitions of the CH_3CN radical cation in CH_3CN (top) of low-spin $[\text{Mn}(\text{dgy})_2]^{3+}$ (${}^3\text{T}_1$) in CH_3CN (center) and of the ${}^6\text{LMCT}$ excited state of $[\text{Mn}(\text{dgy})_2]^{4+}$ (bottom). Color code of the stick spectra according to charge transfer number analysis (green: MLCT, purple: LLCT, orange: LMCT, blue: LC, gray: MC). Gaussian bands broadened with FWHM = 80 nm.

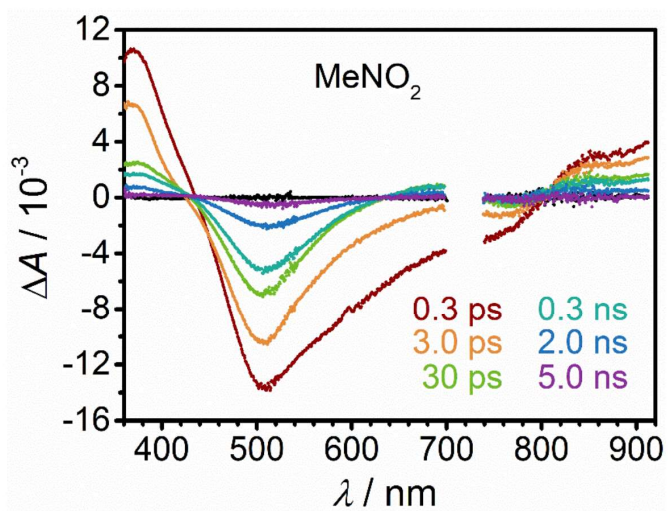


Figure 32. Transient absorption spectra of $[\text{Mn}(\text{dgpy})_2][\text{PF}_6]_4$ in CH_3NO_2 after laser excitation at 730 nm (800 nJ / pulse).

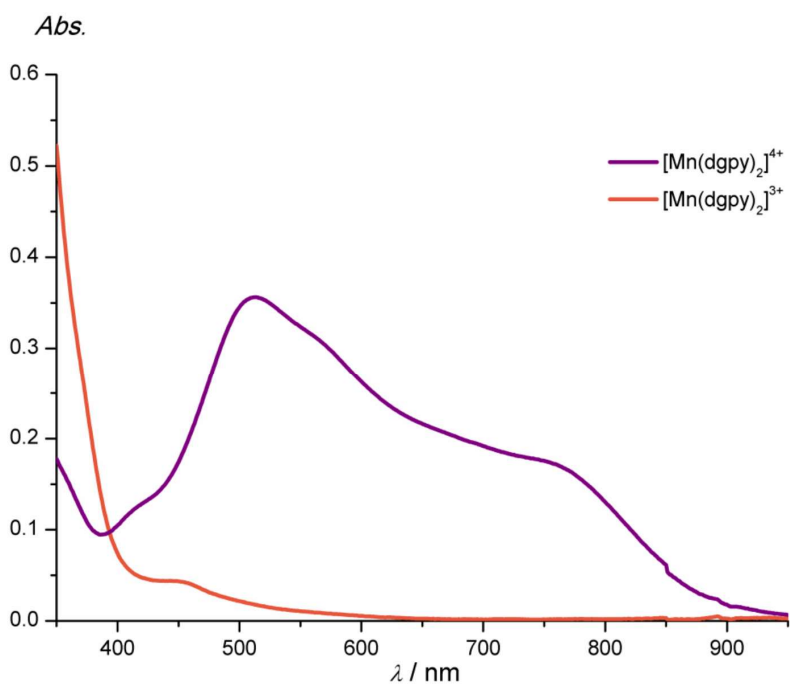


Figure 33. Absorption spectra of $[\text{Mn}(\text{dgpy})_2][\text{PF}_6]_4$ (purple) and after addition of 1 eq dgpy (orange) in CH_3CN in the dark.

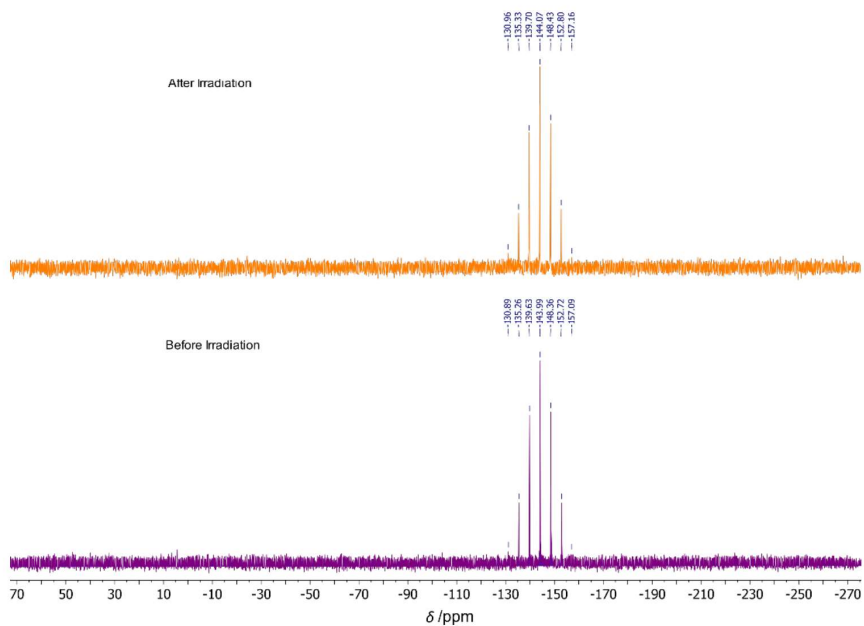


Figure 34. ^{31}P NMR spectra of $[\text{Mn}(\text{dgpy})_2][\text{PF}_6]_4$ (top, purple: before irradiation; bottom, orange: after 120 min irradiation) during irradiation with the 730 nm LED in CD_3CN .

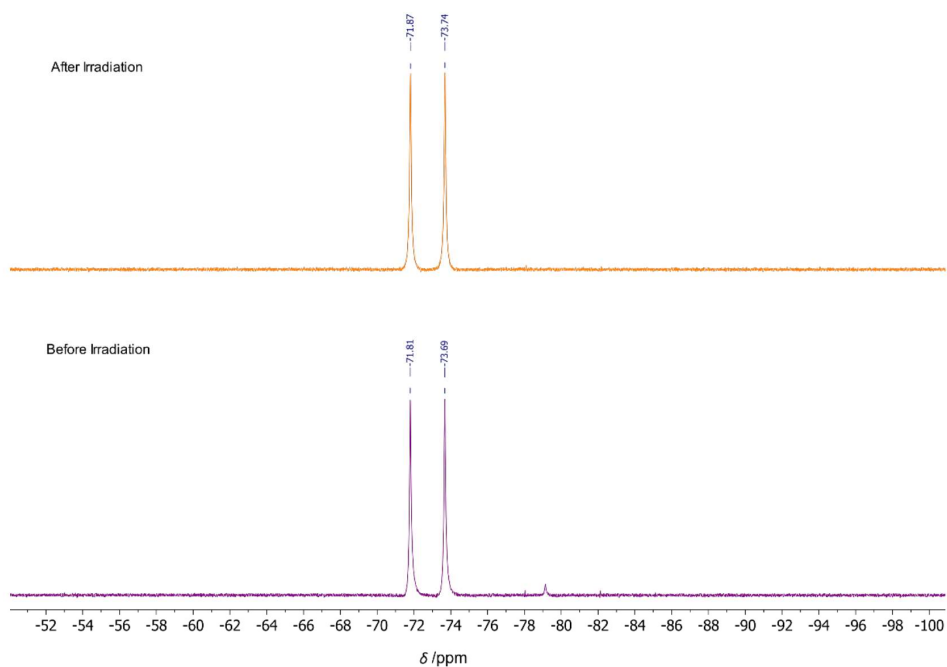


Figure 35. ^{19}F NMR spectra of $[\text{Mn}(\text{dgpy})_2][\text{PF}_6]_4$ (top, purple: before irradiation; bottom, orange: after 120 min irradiation) during irradiation with the 730 nm LED in CD_3CN .

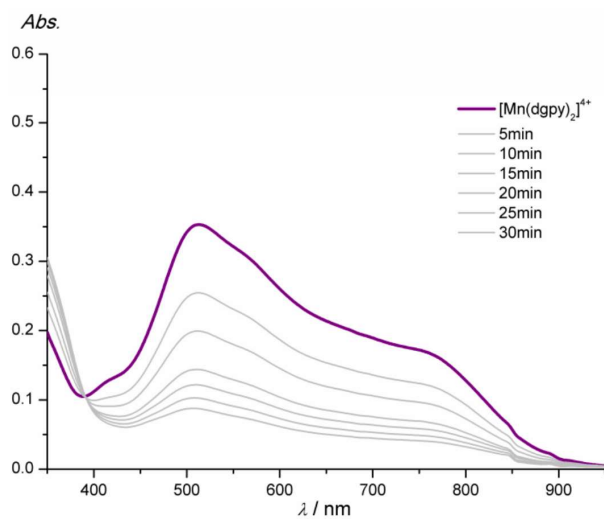


Figure 36. Absorption spectra of $[\text{Mn}(\text{dgpy})_2][\text{ClO}_4]_4$ (purple: before irradiation) during 30 min irradiation with the 730 nm LED in CH_3CN .

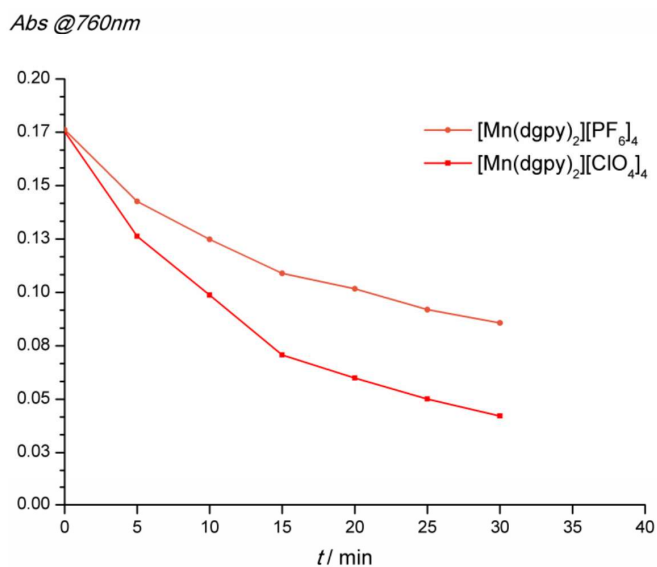


Figure 37. Kinetic traces observed at 760 nm of $[\text{Mn}(\text{dgpy})_2][\text{PF}_6]_4$ (orange) and $[\text{Mn}(\text{dgpy})_2][\text{ClO}_4]_4$ (red) under irradiation with 730 nm in CH_3CN .

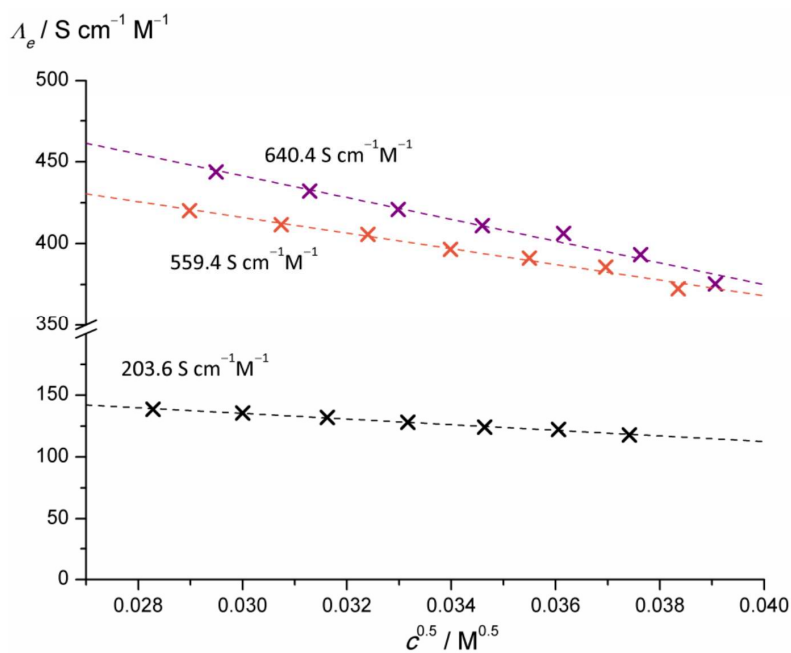


Figure 38. Equivalent conductivity Λ_e vs. $c^{1/2}$ plots of $[\text{Mn}(\text{dgy})_2][\text{PF}_6]_4$ (purple) $[\text{Mn}(\text{dgy})_2][\text{PF}_6]_4$ (orange) and $[\text{n-Bu}_4\text{N}][\text{PF}_6]$ (black) in CH_3CN at 293 K.

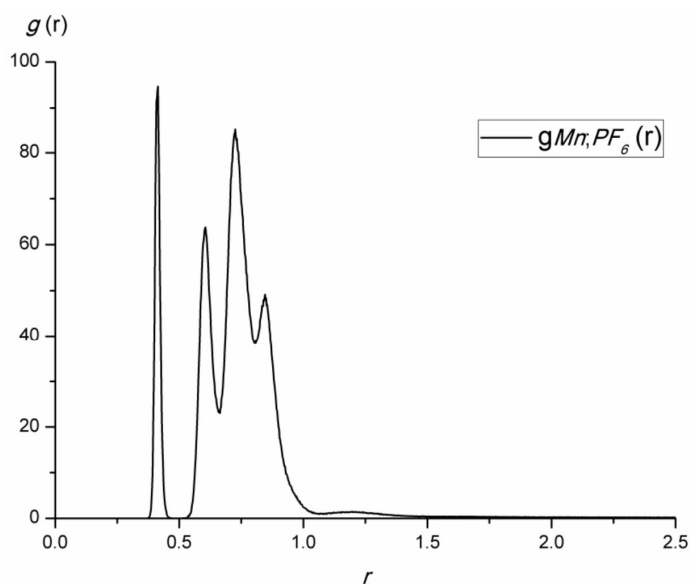


Figure 39. Radial distribution $g(r)$ of the four $[\text{PF}_6]^-$ counter ions (center of mass) from the Mn center in a molecular dynamics simulation of $[\text{Mn}(\text{dgy})_2][\text{PF}_6]_4$ in CH_3CN with maxima at 0.41, 0.61, 0.73 and 0.85 nm (sampling time 1 μs). The low number of $[\text{PF}_6]^-$ counter ions precludes a meaningful statistical analysis.

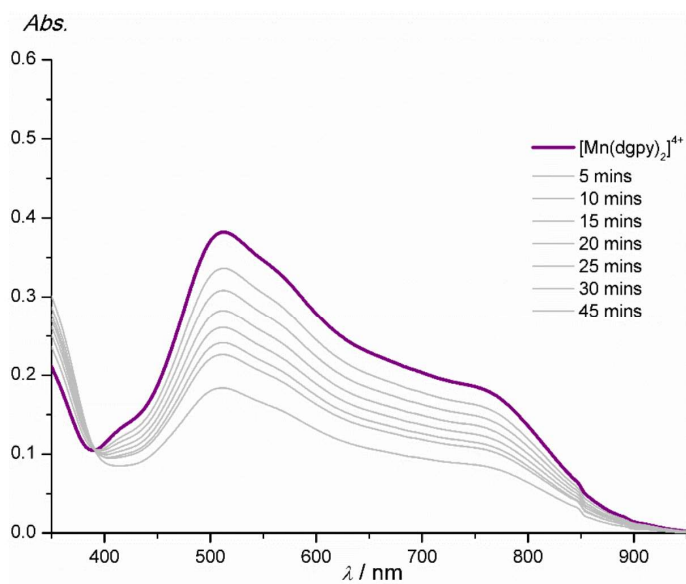


Figure 40. Absorption spectra of $[\text{Mn}(\text{dgpy})_2][\text{PF}_6]_4$ in the presence of 50 mM $[\text{n-Bu}_4\text{N}][\text{PF}_6]$ (purple: before irradiation) during irradiation with the 730 nm LED in CH_3CN .

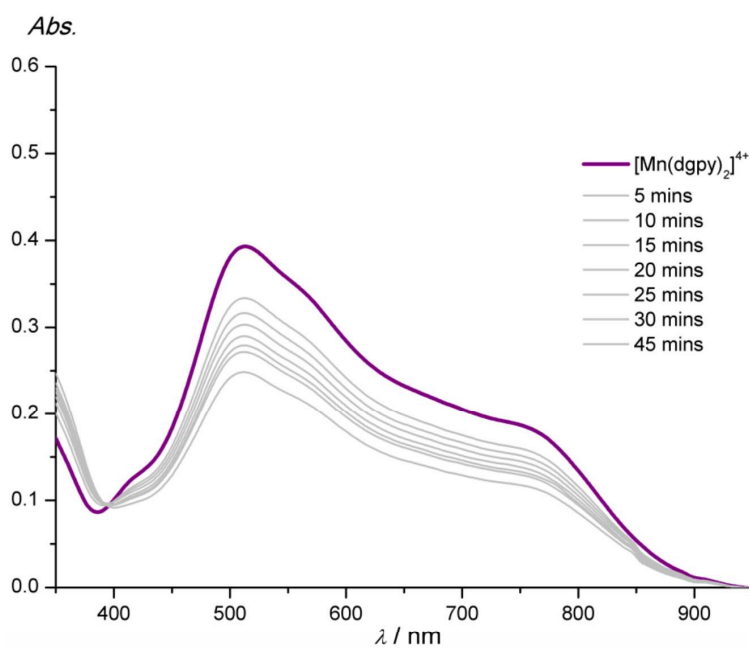


Figure 41. Absorption spectra of $[\text{Mn}(\text{dgpy})_2][\text{PF}_6]_4$ in the presence of 100 mM $[\text{n-Bu}_4\text{N}][\text{PF}_6]$ (purple: before irradiation) during irradiation with the 730 nm LED in CH_3CN .

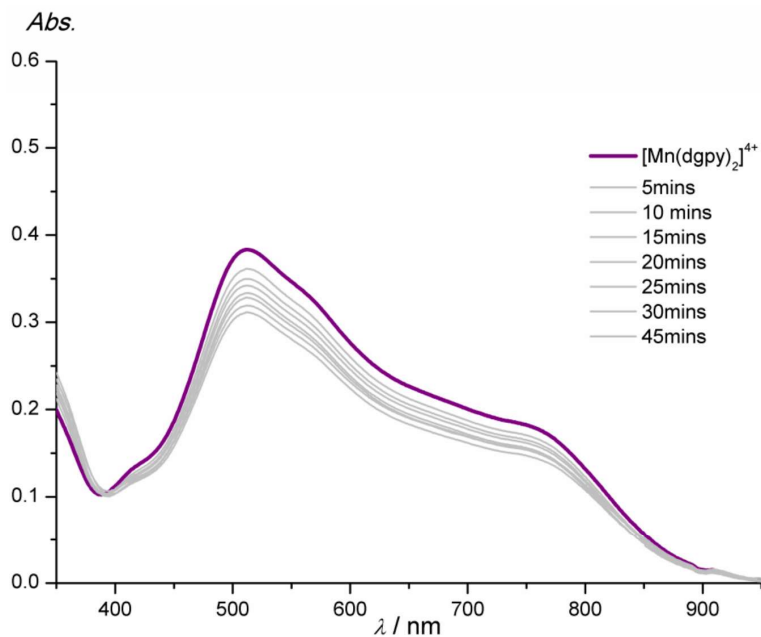


Figure 42. Absorption spectra of $[\text{Mn}(\text{dgpy})_2][\text{PF}_6]_4$ in the presence of 200 mM $[\text{n-Bu}_4\text{N}][\text{PF}_6]$ (purple: before irradiation) during irradiation with the 730 nm LED in CH_3CN .

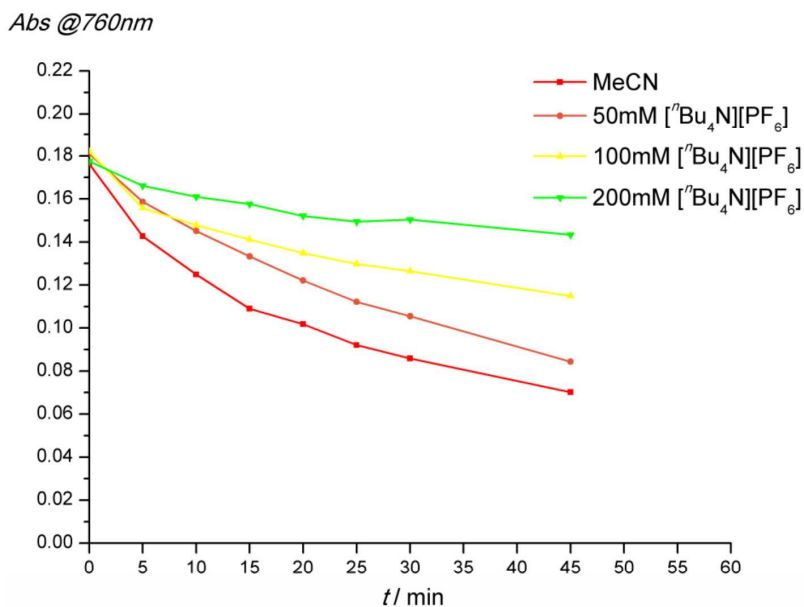


Figure 43. Kinetic traces observed at 760 nm of $[\text{Mn}(\text{dgpy})_2][\text{PF}_6]_4$ in the presence of 0, 50, 100 and 200 mM $[\text{n-Bu}_4\text{N}][\text{PF}_6]$ (in red, orange, yellow and green) under irradiation with 730 nm in CH_3CN .

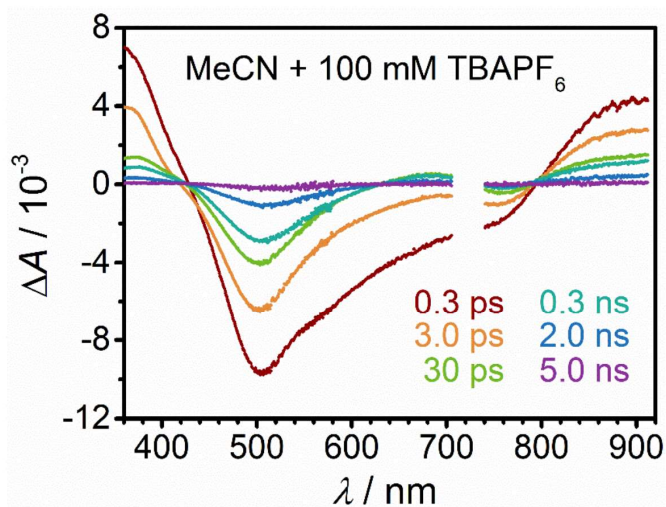


Figure 44. Transient absorption spectra of $[\text{Mn}(\text{dgpy})_2][\text{PF}_6]_4$ in CH_3CN in the presence of 100 mM $[\text{n-Bu}_4\text{N}][\text{PF}_6]_4$ after excitation with 730 nm laser pulses of ca. 200 fs duration (800 nJ / pulse).

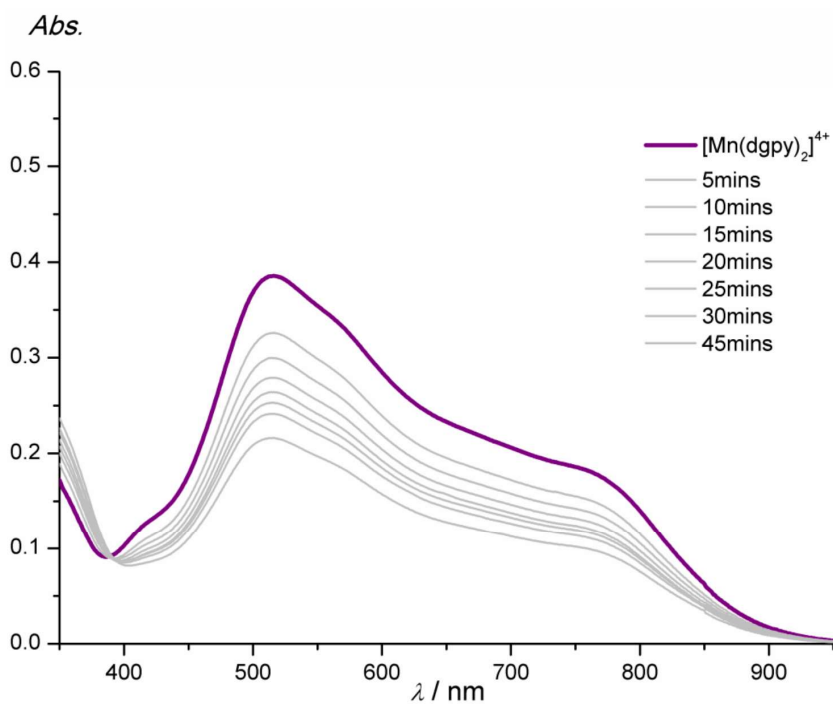


Figure 45. Absorption spectra of $[\text{Mn}(\text{dgpy})_2][\text{PF}_6]_4$ (purple: before irradiation; orange: after 45 min irradiation) during irradiation with the 730 nm LED in $\text{CH}_3\text{CN}/o\text{-dichlorobenzene}$ 1:1 v/v.

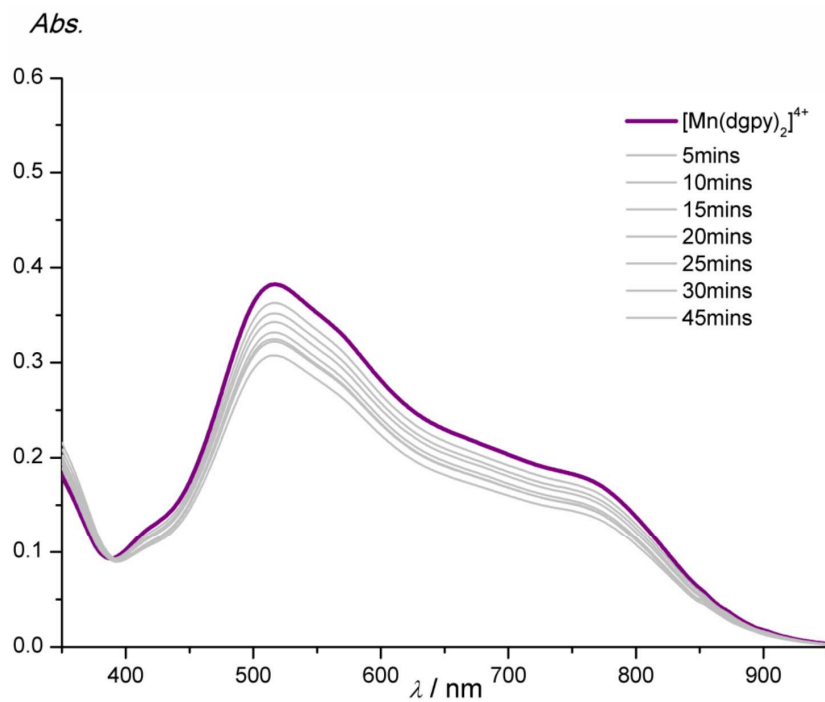


Figure 46. Absorption spectra of $[\text{Mn}(\text{dgpy})_2][\text{PF}_6]_4$ (purple: before irradiation; orange: after 45 min irradiation) during irradiation with the 730 nm LED in $\text{CH}_3\text{CN}/o\text{-dichlorobenzene}$ 1:2 v/v.

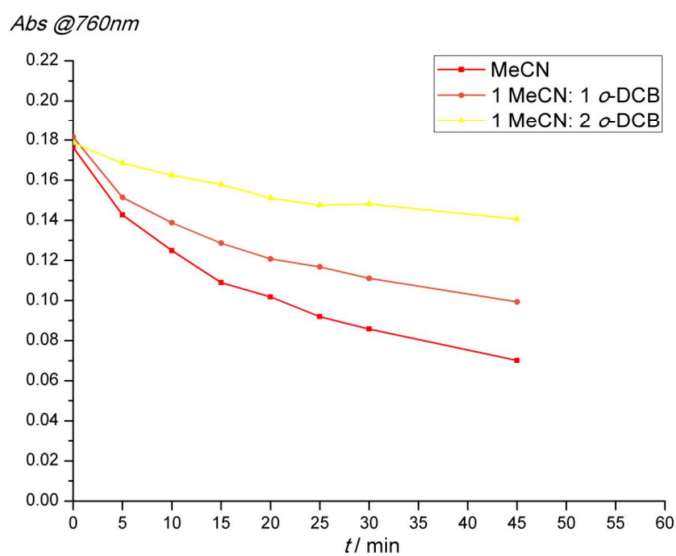


Figure 47. Kinetic traces observed at 760 nm of $[\text{Mn}(\text{dgpy})_2][\text{PF}_6]_4$ under irradiation with 730 nm in CH_3CN (red), $\text{CH}_3\text{CN}/o\text{-dichlorobenzene}$ 1:1 v/v (orange) and $\text{CH}_3\text{CN}/o\text{-dichlorobenzene}$ 1:2 v/v (yellow).

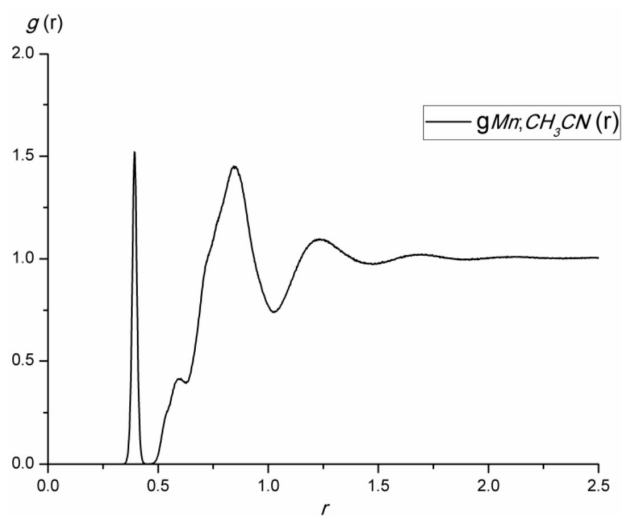


Figure 48. Radial distribution $g(r)$ of CH_3CN molecules (center of mass) from the Mn center in a molecular dynamics simulation of $[\text{Mn}(\text{dgy})_2][\text{PF}_6]_4$ in CH_3CN with maxima at 0.39, 0.60, 0.85, 1.23 and 1.68 nm (sampling time 1 μs). The number of CH_3CN molecules $n(r)$ up to a distance r is given by

$$n(r) = \rho \cdot (4\pi) \cdot \int_0^r dr' (r')^2 g(r'), \text{ with the particle density } \rho = 1761/160.1 \text{ nm}^{-3} = 11 \text{ nm}^{-3},$$

giving $n(4.25 \text{ \AA}) = 0.9$; $n(6.28 \text{ \AA}) = 2.7$ and $n(10.20 \text{ \AA}) = 41.6$.

3. Cartesian coordinates of DFT-UKS calculated geometries

[Mn(dgpy)₂]⁴⁺ (quartet ground state)²

25	-0.089767000	-0.595322000	-0.093908000
6	0.793990000	-3.122292000	-1.221706000
6	0.677685000	-4.446338000	-1.625940000
6	-0.518903000	-5.105611000	-1.439479000
6	-1.594411000	-4.445407000	-0.878267000
6	-1.460981000	-3.110711000	-0.531811000
7	-0.272687000	-2.471064000	-0.692262000
1	1.502521000	-4.954604000	-2.089122000
1	-2.515595000	-4.971210000	-0.705877000
6	1.239397000	0.982954000	-2.225994000
6	2.057382000	0.908998000	-3.493481000
6	3.437059000	0.431928000	-3.114805000
7	3.329282000	-0.838314000	-2.378917000
6	2.198260000	-1.184768000	-1.757050000
7	1.213504000	-0.319725000	-1.532557000
1	4.051803000	0.230115000	-3.989666000
1	1.667344000	1.741093000	-1.569767000
1	2.108866000	1.894343000	-3.951876000
6	-2.537959000	-1.567773000	1.024507000
7	-3.637306000	-1.341569000	1.741998000
6	-3.620945000	-0.591489000	3.013892000
6	-2.384635000	0.260844000	3.164305000
6	-1.176447000	-0.513973000	2.693965000
7	-1.371036000	-0.996148000	1.311176000
1	-3.689944000	-1.327485000	3.818347000
1	-1.009171000	-1.380337000	3.335832000
6	1.267787000	1.748829000	0.927971000
6	1.406647000	3.061014000	1.359018000
6	0.308619000	3.894794000	1.338909000
6	-0.909608000	3.426262000	0.896147000
6	-1.022411000	2.108086000	0.475481000
7	0.062303000	1.286056000	0.498576000
1	2.345817000	3.427995000	1.727743000
1	-1.751541000	4.090636000	0.856237000
6	1.228838000	-2.421228000	1.841602000
6	2.087419000	-2.455703000	3.083661000
6	3.501240000	-2.138296000	2.662998000
7	3.521262000	-0.891017000	1.879615000
6	2.409816000	-0.384842000	1.334461000
7	1.297170000	-1.096560000	1.194898000
1	4.150633000	-1.970296000	3.520513000
1	1.575781000	-3.187096000	1.147429000
1	2.041912000	-3.444926000	3.534833000
6	-2.457685000	0.812463000	-1.034370000
7	-3.614002000	0.853620000	-1.719229000
6	-3.733401000	0.256144000	-3.060321000
6	-2.366364000	0.050541000	-3.659405000
6	-1.542665000	-0.721269000	-2.658364000
7	-1.471832000	-0.011963000	-1.366804000
1	-4.315300000	0.950014000	-3.663194000
1	-2.444200000	-0.513240000	-4.586151000
1	-0.530182000	-0.877641000	-3.012180000
7	2.045533000	-2.494897000	-1.325129000
7	-2.595379000	-2.412778000	-0.068437000
6	-3.896047000	-2.934184000	-0.565309000
1	-4.053966000	-3.941051000	-0.184139000
1	-3.839355000	-2.974111000	-1.651975000
1	-0.616955000	-6.139191000	-1.737436000
1	0.402724000	4.917797000	1.672319000
7	-2.288524000	1.656988000	0.050704000
7	2.414269000	0.931841000	0.891682000
6	3.701828000	1.672791000	0.822053000
6	-3.445028000	2.470747000	0.529068000
1	-3.449415000	3.445955000	0.054052000
1	-3.334393000	2.612557000	1.603762000
6	4.524246000	-1.686215000	-2.440438000
6	4.506386000	-2.649162000	-1.281296000
6	3.212527000	-3.418264000	-1.347430000
1	3.098704000	-4.098566000	-0.507059000
1	4.602518000	-2.116240000	-0.336276000
1	4.554261000	-2.212129000	-3.396627000
1	5.381399000	-1.016212000	-2.397112000

6	-4.940181000	-1.921578000	1.405914000
6	-5.046279000	-2.085369000	-0.088466000
1	-5.976019000	-2.587734000	-0.346499000
1	-5.055094000	-1.110504000	-0.580714000
1	-5.067837000	-2.884522000	1.912298000
1	-5.690521000	-1.238874000	1.804404000
1	-4.532142000	-0.001571000	3.046419000
1	3.959128000	1.167763000	-2.498962000
1	1.602590000	0.218828000	-4.206406000
1	0.215861000	1.278726000	-2.430273000
1	3.203708000	-3.998925000	-2.268156000
1	5.334681000	-3.349723000	-1.357913000
1	-0.284247000	0.094640000	2.724752000
1	-2.263216000	0.540901000	4.209377000
1	-2.484103000	1.177038000	2.596133000
1	0.192726000	-2.642942000	2.065151000
1	1.733564000	-1.725726000	3.813079000
1	3.932376000	-2.945537000	2.067110000
6	4.860451000	0.725325000	0.656617000
6	4.832193000	-0.236149000	1.817065000
1	5.569892000	-1.028856000	1.700957000
1	5.783923000	1.300166000	0.667054000
1	4.809459000	0.192385000	-0.292669000
1	3.852558000	2.235214000	1.741508000
1	3.621005000	2.373648000	-0.004714000
1	5.032172000	0.273757000	2.761356000
6	-4.762384000	1.809632000	0.197036000
6	-4.796618000	1.618961000	-1.299734000
1	-5.565964000	2.471453000	0.512504000
1	-4.893823000	0.866074000	0.729763000
1	-5.685069000	1.070422000	-1.648016000
1	-4.810741000	2.587762000	-1.811251000
1	-4.284897000	-0.685982000	-3.005936000
1	-1.905910000	1.014112000	-3.881004000
1	-1.986093000	-1.705703000	-2.514812000

[Mn(dgpy)₂]⁴⁺ (²LMCT state)

25	-0.105301000	-0.570224000	-0.114788000
6	0.760718000	-3.103144000	-1.257871000
6	0.635014000	-4.409808000	-1.712963000
6	-0.570809000	-5.059857000	-1.562967000
6	-1.636055000	-4.407720000	-0.980355000
6	-1.483904000	-3.090573000	-0.561708000
7	-0.291391000	-2.455081000	-0.698771000
1	1.456078000	-4.910899000	-2.190735000
1	-2.563895000	-4.930516000	-0.846559000
6	1.267214000	1.004862000	-2.206924000
6	2.103383000	0.960357000	-3.464518000
6	3.467840000	0.442216000	-3.086946000
7	3.329466000	-0.842507000	-2.388553000
6	2.192264000	-1.180707000	-1.770654000
7	1.217958000	-0.304358000	-1.536046000
1	4.084499000	0.251110000	-3.963485000
1	1.684440000	1.749236000	-1.529786000
1	2.182705000	1.960425000	-3.886633000
6	-2.535857000	-1.586688000	1.065549000
7	-3.609121000	-1.463181000	1.852793000
6	-3.606044000	-0.681215000	3.101185000
6	-2.436865000	0.270270000	3.179622000
6	-1.196872000	-0.428103000	2.669262000
7	-1.396362000	-0.940662000	1.300228000
1	-3.584936000	-1.393545000	3.928573000
1	-0.951842000	-1.268704000	3.322064000
6	1.278889000	1.774047000	0.919039000
6	1.428164000	3.096532000	1.326252000
6	0.357902000	3.957529000	1.231596000
6	-0.851795000	3.500587000	0.752783000
6	-0.976257000	2.164565000	0.394103000
7	0.079974000	1.316551000	0.472092000
1	2.360852000	3.450878000	1.722445000
1	-1.673097000	4.183801000	0.645319000
6	1.196025000	-2.409675000	1.824185000
6	2.031540000	-2.474116000	3.082174000
6	3.450161000	-2.141804000	2.697287000
7	3.480462000	-0.878577000	1.948123000
6	2.382064000	-0.373890000	1.368632000

7	1.274167000	-1.079282000	1.192335000
1	4.083741000	-1.997435000	3.571762000
1	1.552848000	-3.169729000	1.129545000
1	1.982930000	-3.474838000	3.507815000
6	-2.430165000	0.852754000	-1.088878000
7	-3.582986000	0.886198000	-1.762132000
6	-3.739145000	0.204037000	-3.053623000
6	-2.386604000	0.028701000	-3.693154000
6	-1.506117000	-0.694215000	-2.702666000
7	-1.451951000	-0.008136000	-1.401145000
1	-4.393259000	0.834249000	-3.653586000
1	-2.471300000	-0.561436000	-4.603516000
1	-0.486824000	-0.793946000	-3.065193000
7	2.022120000	-2.489364000	-1.352568000
7	-2.606854000	-2.419418000	-0.041562000
6	-3.916536000	-2.957925000	-0.504777000
1	-4.021566000	-3.986664000	-0.169424000
1	-3.901623000	-2.941840000	-1.592201000
1	-0.681621000	-6.080085000	-1.901621000
1	0.465733000	4.990670000	1.529492000
7	-2.243152000	1.714011000	-0.026510000
7	2.412022000	0.947363000	0.936991000
6	3.709274000	1.672319000	0.894138000
6	-3.382979000	2.568180000	0.399653000
1	-3.381348000	3.494689000	-0.175091000
1	-3.231742000	2.808247000	1.446781000
6	4.528395000	-1.686258000	-2.420936000
6	4.475871000	-2.684342000	-1.292939000
6	3.172153000	-3.429913000	-1.403779000
1	3.041556000	-4.137268000	-0.589002000
1	4.557901000	-2.184309000	-0.329617000
1	4.594701000	-2.184205000	-3.390759000
1	5.382556000	-1.016966000	-2.326341000
6	-4.882469000	-2.133067000	1.561108000
6	-5.070347000	-2.178176000	0.064675000
1	-5.995167000	-2.691397000	-0.191928000
1	-5.118120000	-1.169671000	-0.341032000
1	-4.885657000	-3.135473000	1.994901000
1	-5.661953000	-1.551571000	2.045339000
1	-4.551496000	-0.144411000	3.146503000
1	4.000047000	1.147202000	-2.444116000
1	1.643175000	0.308630000	-4.209215000
1	0.245660000	1.308945000	-2.418642000
1	3.163097000	-3.972360000	-2.348352000
1	5.296833000	-3.393360000	-1.377455000
1	-0.348477000	0.240708000	2.672200000
1	-2.290235000	0.579742000	4.213249000
1	-2.633406000	1.164769000	2.595413000
1	0.154172000	-2.625719000	2.026007000
1	1.660249000	-1.766514000	3.825196000
1	3.892224000	-2.931668000	2.085326000
6	4.855447000	0.711218000	0.729246000
6	4.806801000	-0.258035000	1.881344000
1	5.522932000	-1.069256000	1.752481000
1	5.789304000	1.269454000	0.743980000
1	4.791758000	0.185687000	-0.221309000
1	3.855801000	2.223952000	1.822054000
1	3.650070000	2.376877000	0.068285000
1	5.025827000	0.238968000	2.829151000
6	-4.687920000	1.850066000	0.179709000
6	-4.800671000	1.556726000	-1.292102000
1	-5.506085000	2.492324000	0.498253000
1	-4.726846000	0.933170000	0.766146000
1	-5.628657000	0.883102000	-1.510849000
1	-4.945387000	2.470295000	-1.872285000
1	-4.240772000	-0.752958000	-2.895360000
1	-1.961176000	0.999879000	-3.951399000
1	-1.885533000	-1.705819000	-2.561262000

[Mn(dgpy)₂]⁴⁺ (⁶LMCT state)

25	0.393339000	-0.308526000	0.353453000
6	1.680699000	-3.024355000	0.042295000
6	1.791418000	-4.411546000	0.008249000
6	0.690080000	-5.168392000	0.360387000
6	-0.495059000	-4.554435000	0.719844000
6	-0.556457000	-3.164829000	0.701061000

7	0.522227000	-2.435038000	0.373377000
6	1.605201000	0.627933000	-2.205272000
6	2.525711000	0.308965000	-3.361318000
6	3.923116000	0.174181000	-2.808482000
7	3.930030000	-0.807718000	-1.718243000
6	2.808511000	-1.112978000	-1.045526000
7	1.700685000	-0.386848000	-1.141347000
6	-1.845642000	-1.418398000	1.860130000
7	-2.911490000	-1.333416000	2.666995000
6	-3.129806000	-0.227271000	3.610485000
6	-2.195890000	0.931435000	3.348977000
6	-0.819301000	0.395531000	3.017829000
7	-0.867165000	-0.524613000	1.868530000
6	1.373221000	2.670361000	0.413725000
6	1.345579000	4.072180000	0.154806000
6	0.135283000	4.687683000	-0.067445000
6	-1.015490000	3.933515000	-0.090101000
6	-0.916999000	2.520118000	0.058775000
7	0.251908000	1.932199000	0.332582000
6	2.108022000	-0.975534000	2.735052000
6	2.647240000	-0.358920000	4.009993000
6	3.963464000	0.295644000	3.671249000
7	3.859862000	1.081724000	2.433405000
6	2.765508000	1.016894000	1.646994000
7	1.884980000	0.064180000	1.713944000
6	-2.168100000	0.598782000	-0.881078000
7	-3.351310000	0.346461000	-1.469983000
6	-3.455240000	-0.625470000	-2.566200000
6	-2.095346000	-0.892940000	-3.163023000
6	-1.153374000	-1.231219000	-2.028745000
7	-1.106203000	-0.146353000	-1.032975000
7	2.822250000	-2.237063000	-0.226860000
7	-1.775566000	-2.510826000	1.000771000
6	-3.004532000	-3.235458000	0.572469000
7	-2.083743000	1.796807000	-0.121475000
7	2.587737000	2.119182000	0.754066000
6	3.797104000	2.888081000	0.323269000
6	-3.345489000	2.531492000	0.186601000
6	5.250312000	-1.363639000	-1.410976000
6	5.248930000	-1.927364000	-0.012839000
6	4.109667000	-2.908499000	0.075037000
6	-3.983814000	-2.329587000	2.598495000
6	-4.254994000	-2.605528000	1.135544000
6	5.060596000	2.130479000	0.623166000
6	5.066799000	1.837923000	2.100082000
6	-4.496114000	1.564783000	0.288853000
6	-4.639095000	0.908241000	-1.057521000

[[Mn(dgpy)₂] / naphthalene]⁴⁺ (lowest energy doublet state)

25	-0.316098000	-0.534445000	-0.322094000
6	0.673825000	-3.159204000	-1.160652000
6	0.627909000	-4.529715000	-1.405905000
6	-0.515635000	-5.230574000	-1.089894000
6	-1.604552000	-4.565383000	-0.566231000
6	-1.535607000	-3.188325000	-0.384868000
7	-0.401521000	-2.501426000	-0.666082000
1	1.464076000	-5.042682000	-1.843882000
1	-2.485154000	-5.117609000	-0.295248000
6	0.933490000	0.816599000	-2.683617000
6	1.683414000	0.622269000	-3.983710000
6	3.089330000	0.192473000	-3.645538000
7	3.058248000	-0.950002000	-2.728818000
6	1.955079000	-1.237423000	-2.006028000
7	0.950945000	-0.402824000	-1.865816000
1	3.632542000	-0.131570000	-4.533474000
1	1.383241000	1.641961000	-2.130119000
1	1.710675000	1.550367000	-4.550505000
6	-2.655813000	-1.550336000	1.054465000
7	-3.747713000	-1.387362000	1.824773000
6	-3.779407000	-0.463733000	2.967218000
6	-2.655235000	0.546810000	2.918662000
6	-1.380342000	-0.146258000	2.486774000
7	-1.554371000	-0.847025000	1.206835000
1	-3.721911000	-1.060481000	3.880796000
1	-1.080279000	-0.872663000	3.246841000
6	0.908563000	2.020123000	0.384869000

6	0.970374000	3.369167000	0.718647000
6	-0.177353000	4.129484000	0.652142000
6	-1.362121000	3.548781000	0.257296000
6	-1.386329000	2.189770000	-0.053303000
7	-0.260875000	1.436944000	0.020032000
1	1.890212000	3.817364000	1.045911000
1	-2.243158000	4.155812000	0.172192000
6	1.247908000	-1.999961000	1.778541000
6	2.156813000	-1.833602000	2.977552000
6	3.520457000	-1.438755000	2.462990000
7	3.402389000	-0.307541000	1.536987000
6	2.216075000	0.029247000	0.986379000
7	1.169618000	-0.761232000	0.993470000
1	4.177054000	-1.116038000	3.271774000
1	1.631115000	-2.811836000	1.159360000
1	2.224031000	-2.767003000	3.534284000
6	-2.758844000	0.662455000	-1.417755000
7	-3.915531000	0.661841000	-2.128491000
6	-4.048839000	-0.122351000	-3.354639000
6	-2.689146000	-0.442445000	-3.919295000
6	-1.869406000	-1.063525000	-2.813180000
7	-1.783319000	-0.182122000	-1.640821000
1	-4.648021000	0.473743000	-4.045404000
1	-2.781852000	-1.130181000	-4.757639000
1	-0.856755000	-1.271673000	-3.142238000
7	1.885314000	-2.489350000	-1.397169000
7	-2.694470000	-2.516253000	0.053809000
6	-3.972971000	-3.149498000	-0.360058000
1	-4.041445000	-4.148304000	0.064700000
1	-3.957776000	-3.235787000	-1.445039000
1	-0.559440000	-6.298232000	-1.252984000
1	-0.148306000	5.180228000	0.903967000
7	-2.620244000	1.628083000	-0.420775000
7	2.108178000	1.287465000	0.393927000
6	3.331614000	2.091493000	0.169880000
6	-3.813933000	2.417841000	-0.039953000
1	-3.899277000	3.303334000	-0.670831000
1	-3.678571000	2.742195000	0.986850000
6	4.309306000	-1.704797000	-2.663904000
6	4.344142000	-2.519155000	-1.396307000
6	3.089897000	-3.351298000	-1.357775000
1	3.030475000	-3.944179000	-0.448122000
1	4.407244000	-1.872347000	-0.522653000
1	4.403940000	-2.344779000	-3.545326000
1	5.120453000	-0.976807000	-2.691419000
6	-4.976972000	-2.154445000	1.614699000
6	-5.164174000	-2.369612000	0.131219000
1	-6.064891000	-2.948883000	-0.064629000
1	-5.257052000	-1.413717000	-0.380720000
1	-4.930574000	-3.108421000	2.146638000
1	-5.791323000	-1.572729000	2.039043000
1	-4.748736000	0.033172000	2.957278000
1	3.651160000	1.012419000	-3.190082000
1	1.189648000	-0.134933000	-4.595797000
1	-0.104122000	1.079473000	-2.861665000
1	3.097176000	-4.027086000	-2.213867000
1	5.209766000	-3.178802000	-1.392975000
1	-0.567810000	0.562092000	2.386475000
1	-2.529712000	0.995822000	3.903088000
1	-2.894534000	1.344904000	2.222606000
1	0.240704000	-2.272199000	2.073974000
1	1.764360000	-1.065078000	3.646106000
1	4.004135000	-2.275812000	1.952496000
6	4.526787000	1.191700000	-0.007812000
6	4.665026000	0.373158000	1.251166000
1	5.426772000	-0.400111000	1.142721000
1	5.415051000	1.800739000	-0.163696000
1	4.398146000	0.547723000	-0.876476000
1	3.520797000	2.745727000	1.021668000
1	3.153568000	2.706657000	-0.709008000
1	4.947375000	1.003826000	2.098474000
6	-5.059991000	1.585282000	-0.188007000
6	-5.184997000	1.208853000	-1.640977000
1	-5.923474000	2.167703000	0.126517000
1	-4.999320000	0.699106000	0.442153000
1	-5.943426000	0.439415000	-1.792139000
1	-5.464005000	2.072678000	-2.247091000
1	-4.610445000	-1.036536000	-3.139903000
1	-2.198701000	0.462221000	-4.274641000

1	-2.315782000	-2.015117000	-2.524407000
6	-1.104922000	4.361931000	-3.240686000
6	-2.470587000	4.433566000	-3.007430000
6	-0.618362000	3.647908000	-4.336693000
1	-2.847911000	4.996585000	-2.166264000
1	0.445464000	3.605003000	-4.524838000
6	-3.365829000	3.780851000	-3.856517000
6	-1.497983000	2.979896000	-5.208074000
1	-4.429522000	3.834419000	-3.668222000
6	-2.900712000	3.049485000	-4.964233000
1	-0.413437000	4.859853000	-2.576650000
6	-3.781944000	2.382611000	-5.834786000
1	-4.847321000	2.445745000	-5.658207000
6	-1.031597000	2.237328000	-6.309171000
6	-3.292221000	1.646355000	-6.916377000
1	0.032665000	2.179385000	-6.493508000
1	-3.983376000	1.132964000	-7.569311000
6	-1.926118000	1.574104000	-7.151321000
1	-1.549144000	1.003961000	-7.988272000

[Mn(dgpy)₂]³⁺ (lowest energy triplet state, low-spin)

25	0.386304000	-0.211860000	0.410843000
6	1.684373000	-2.814635000	0.097648000
6	1.792162000	-4.203104000	0.090437000
6	0.713011000	-4.961717000	0.489789000
6	-0.460361000	-4.341405000	0.864501000
6	-0.542071000	-2.953316000	0.812845000
7	0.526424000	-2.204534000	0.445514000
1	2.695427000	-4.687169000	-0.232438000
1	-1.291181000	-4.934089000	1.198964000
6	1.590663000	0.816944000	-2.131136000
6	2.420041000	0.476749000	-3.350537000
6	3.846901000	0.285590000	-2.896456000
7	3.893052000	-0.676463000	-1.791541000
6	2.794395000	-0.946109000	-1.053632000
7	1.704577000	-0.217320000	-1.093916000
1	4.470378000	-0.120538000	-3.693199000
1	1.919383000	1.777755000	-1.733986000
1	2.362722000	1.282077000	-4.081236000
6	-1.889800000	-1.217511000	1.907430000
7	-3.020641000	-1.050369000	2.621672000
6	-3.187718000	0.046459000	3.584725000
6	-2.209693000	1.172250000	3.337252000
6	-0.843464000	0.586181000	3.053527000
7	-0.885270000	-0.371378000	1.939174000
1	-3.057537000	-0.363207000	4.589629000
1	-0.469733000	0.074014000	3.944338000
6	1.307095000	2.553394000	0.621893000
6	1.217387000	3.942246000	0.634795000
6	0.017043000	4.540079000	0.316626000
6	-1.077633000	3.759983000	0.014566000
6	-0.962344000	2.371577000	0.069752000
7	0.222659000	1.780800000	0.362478000
1	2.064836000	4.549582000	0.893148000
1	-1.999341000	4.230130000	-0.272575000
6	1.988006000	-1.066691000	2.797277000
6	2.822550000	-0.589021000	3.965564000
6	4.159311000	-0.150040000	3.417809000
7	3.964728000	0.783555000	2.303305000
6	2.778616000	0.876279000	1.662340000
7	1.821816000	-0.010570000	1.790796000
1	4.749100000	0.374658000	4.169939000
1	2.475753000	-1.933434000	2.349967000
1	2.959613000	-1.393234000	4.686782000
6	-2.133548000	0.442509000	-0.918455000
7	-3.276487000	0.124117000	-1.565615000
6	-3.294779000	-0.907912000	-2.606118000
6	-1.903011000	-1.108224000	-3.153529000
6	-0.985192000	-1.367596000	-1.979849000
7	-1.043016000	-0.282283000	-0.990643000
1	-3.984376000	-0.563454000	-3.376871000
1	-1.885268000	-1.954704000	-3.838421000
1	0.047557000	-1.464565000	-2.299977000
7	2.828880000	-2.065043000	-0.221654000
7	-1.781287000	-2.350445000	1.104574000
6	-2.967357000	-3.186652000	0.789606000

1	-2.951849000	-4.091846000	1.392703000
1	-2.898302000	-3.469106000	-0.259195000
1	0.785426000	-6.040108000	0.507964000
1	-0.064986000	5.617820000	0.299611000
7	-2.123256000	1.612128000	-0.154492000
7	2.572348000	1.980260000	0.835309000
6	3.716559000	2.851271000	0.478581000
6	-3.393407000	2.353940000	0.021551000
1	-3.533673000	3.060533000	-0.798686000
1	-3.316487000	2.916589000	0.947206000
6	5.213904000	-1.253533000	-1.543521000
6	5.270082000	-1.806928000	-0.142182000
6	4.114940000	-2.760741000	0.014593000
1	4.075262000	-3.180313000	1.016998000
1	5.209576000	-1.006386000	0.594232000
1	5.425556000	-2.031891000	-2.281662000
1	5.941712000	-0.454193000	-1.684933000
6	-4.153324000	-1.972085000	2.524391000
6	-4.251338000	-2.463674000	1.099575000
1	-5.081142000	-3.158724000	0.984110000
1	-4.410467000	-1.625656000	0.423694000
1	-4.032320000	-2.806478000	3.220769000
1	-5.041313000	-1.417287000	2.816776000
1	-4.215037000	0.398428000	3.502505000
1	4.287487000	1.233569000	-2.575918000
1	2.047164000	-0.436210000	-3.819037000
1	0.539441000	0.916795000	-2.384202000
1	4.241625000	-3.576484000	-0.698096000
1	6.202744000	-2.344898000	0.016266000
1	-0.130532000	1.364273000	2.813859000
1	-2.171737000	1.819014000	4.212996000
1	-2.533877000	1.777027000	2.494784000
1	1.000660000	-1.384413000	3.113647000
1	2.326502000	0.242289000	4.470392000
1	4.741390000	-1.008583000	3.072339000
6	5.011807000	2.085239000	0.543118000
6	5.154905000	1.555192000	1.947239000
1	6.008412000	0.881973000	2.033495000
1	5.835197000	2.755620000	0.304264000
1	5.016178000	1.270504000	-0.179039000
1	3.784107000	3.692825000	1.168609000
1	3.525994000	3.237017000	-0.520153000
1	5.298722000	2.371035000	2.660921000
6	-4.562097000	1.404925000	0.051512000
6	-4.592621000	0.691535000	-1.274270000
1	-5.480364000	1.970321000	0.198259000
1	-4.463287000	0.697590000	0.874845000
1	-5.303420000	-0.135738000	-1.267677000
1	-4.882342000	1.374227000	-2.077468000
1	-3.692545000	-1.837702000	-2.190380000
1	-1.580883000	-0.220181000	-3.701296000
1	-1.266219000	-2.312507000	-1.515329000

[Mn(dgpy)₂]³⁺ (lowest energy quintet state, high-spin)²

25	0.383227000	-0.222053000	0.339033000
6	1.724579000	-2.991375000	0.097939000
6	1.873696000	-4.374682000	0.224909000
6	0.796139000	-5.116912000	0.670579000
6	-0.409862000	-4.495693000	0.946821000
6	-0.510094000	-3.128391000	0.736524000
7	0.543658000	-2.407038000	0.333992000
1	2.798513000	-4.867349000	-0.015745000
1	-1.233293000	-5.060100000	1.352416000
6	1.679330000	0.693798000	-2.188187000
6	2.457343000	0.276959000	-3.416565000
6	3.884487000	0.034653000	-2.986933000
7	3.924212000	-0.815406000	-1.788587000
6	2.810848000	-1.094134000	-1.075858000
7	1.718409000	-0.359299000	-1.162320000
1	4.455059000	-0.486069000	-3.757353000
1	2.105559000	1.616094000	-1.790836000
1	2.420902000	1.058636000	-4.173100000
6	-1.877815000	-1.390769000	1.790245000
7	-2.999865000	-1.293249000	2.519317000
6	-3.211224000	-0.250558000	3.532549000
6	-2.241560000	0.903500000	3.386637000

6	-0.866122000	0.365982000	3.041418000
7	-0.894558000	-0.511979000	1.860356000
1	-3.097170000	-0.719661000	4.512864000
1	-0.472149000	-0.201718000	3.888082000
6	1.370787000	2.705092000	0.478209000
6	1.339243000	4.095341000	0.359929000
6	0.135363000	4.705123000	0.068133000
6	-1.008365000	3.947926000	-0.097575000
6	-0.914493000	2.565776000	0.041769000
7	0.256928000	1.973398000	0.320305000
1	2.214748000	4.697821000	0.514071000
1	-1.934427000	4.429422000	-0.353077000
6	2.049188000	-0.969168000	2.722886000
6	2.613582000	-0.352879000	3.987609000
6	3.967048000	0.220212000	3.632845000
7	3.898092000	0.955105000	2.358476000
6	2.767108000	0.999987000	1.615524000
7	1.840746000	0.071703000	1.706039000
1	4.319411000	0.927301000	4.386226000
1	2.751791000	-1.717483000	2.347360000
1	2.714539000	-1.102229000	4.770238000
6	-2.172903000	0.632515000	-0.853323000
7	-3.371625000	0.313771000	-1.394068000
6	-3.475456000	-0.693400000	-2.452997000
6	-2.141321000	-0.913650000	-3.119840000
6	-1.115930000	-1.177278000	-2.040598000
7	-1.093382000	-0.102443000	-1.037459000
1	-4.220614000	-0.339157000	-3.163774000
1	-2.201961000	-1.762680000	-3.798309000
1	-0.116756000	-1.261430000	-2.459742000
7	2.847388000	-2.206341000	-0.233006000
7	-1.758579000	-2.479667000	0.935079000
6	-2.944344000	-3.210203000	0.419470000
1	-2.898622000	-4.255656000	0.723285000
1	-2.902708000	-3.188814000	-0.669614000
1	0.900411000	-6.183294000	0.815263000
1	0.088962000	5.780043000	-0.036678000
7	-2.095807000	1.791206000	-0.083440000
7	2.610653000	2.071077000	0.727782000
6	3.796891000	2.889213000	0.383998000
6	-3.343648000	2.539038000	0.189732000
1	-3.557861000	3.237380000	-0.620579000
1	-3.178107000	3.110158000	1.095077000
6	5.258319000	-1.326489000	-1.471042000
6	5.272082000	-1.855084000	-0.059906000
6	4.148414000	-2.851514000	0.055266000
1	4.086259000	-3.266580000	1.058236000
1	5.145415000	-1.044435000	0.659696000
1	5.539638000	-2.105585000	-2.183856000
1	5.953153000	-0.495243000	-1.597665000
6	-4.045619000	-2.312409000	2.408222000
6	-4.232422000	-2.611211000	0.936020000
1	-5.045028000	-3.314215000	0.764770000
1	-4.472091000	-1.685644000	0.411339000
1	-3.759724000	-3.211059000	2.959307000
1	-4.946555000	-1.901307000	2.853929000
1	-4.242760000	0.086193000	3.448219000
1	4.395123000	0.977201000	-2.773231000
1	2.027074000	-0.629736000	-3.845166000
1	0.638569000	0.898195000	-2.419360000
1	4.326926000	-3.668606000	-0.644818000
1	6.216875000	-2.350330000	0.154984000
1	-0.176970000	1.178417000	2.844651000
1	-2.202189000	1.455504000	4.328261000
1	-2.574298000	1.606781000	2.621322000
1	1.105833000	-1.471061000	2.900992000
1	1.945199000	0.428956000	4.350432000
1	4.715543000	-0.570229000	3.544079000
6	5.067195000	2.098995000	0.571403000
6	5.121303000	1.681964000	2.020341000
1	5.955008000	1.006398000	2.216551000
1	5.918429000	2.728884000	0.321021000
1	5.094229000	1.226979000	-0.083271000
1	3.849837000	3.769376000	1.024983000
1	3.672995000	3.221027000	-0.644786000
1	5.235737000	2.552976000	2.670542000
6	-4.498685000	1.580651000	0.343478000
6	-4.661887000	0.882095000	-0.983326000
1	-5.404001000	2.121711000	0.619618000

1	-4.259109000	0.865855000	1.128374000
1	-5.372790000	0.054990000	-0.932071000
1	-5.021803000	1.582612000	-1.741898000
1	-3.863071000	-1.626829000	-2.030602000
1	-1.861609000	-0.032632000	-3.702500000
1	-1.326014000	-2.130937000	-1.557647000

4. References

1. Van Duyne, R. P. & Reilly, C. N. Low-temperature electrochemistry. I. Characteristics of electrode reactions in the absence of coupled chemical kinetics. *Anal. Chem.* **44**, 142–152 (1972).
2. East, N. R., Förster, C., Carrella, L. M., Rentschler, E. & Heinze, K. The full d³–d⁵ Redox Series of Mononuclear Manganese Complexes: Geometries and Electronic Structures of [Mn(dgpy)₂]ⁿ⁺. *Inorg. Chem.* **61**, 14616–14625 (2022).
3. Fulmer, G. R., Miller, A. J. M., Sherden, N. H., Gottlieb, H. E., Nudelman, A., Stoltz, B. M., Bercaw, J. E. & Goldberg, K. I. NMR Chemical Shifts of Trace Impurities: Common Laboratory Solvents, Organics, and Gases in Deuterated Solvents Relevant to the Organometallic Chemist. *Organometallics* **29**, 2176–2179 (2010).
4. Snellenburg, J. J., Laptinok, S., Seger, R., Mullen, K. M. & van Stokkum, I. H. M. Glotaran: A Java-Based Graphical User Interface for the R Package TIMP. *J. Stat. Softw.* **49**, 1–22 (2012).
5. <https://www.prizmatix.com/LEDUHP/LED-UHP-TLA.aspx> (accessed Feb. 21st 2023).
6. Neese, F. Software update: The ORCA program system, version 4.0. *WIREs Comput. Mol. Sci.* **8**, e1327 (2018).
7. Becke, A. D. Density-functional thermochemistry. III. The role of exact exchange. *J. Chem. Phys.* **98**, 5648–5652 (1993).
8. Miehlich, B., Savin, A., Stoll, H. & Preuss, H. Results obtained with the correlation energy density functionals of Becke and Lee, Yang and Parr. *Chem. Phys. Lett.* **157**, 200–206 (1989).
9. Lee, C., Yang, W. & Parr, R. G. Development of the Colle-Salvetti correlation-energy formula into a functional of the electron density. *Phys. Rev. B* **37**, 785–789 (1988).
10. Neese, F., Wennmohs, F., Hansen, A. & Becker, U. Efficient, approximate and parallel Hartree–Fock and hybrid DFT calculations. A ‘chain-of-spheres’ algorithm for the Hartree–Fock exchange. *Chem. Phys.* **356**, 98–109 (2009).
11. Izsák, R. & Neese, F. An overlap fitted chain of spheres exchange method. *J. Chem. Phys.* **135**, 144105 (2011).
12. Pantazis, D. A., Chen, X.-Y., Landis, C. R. & Neese, F. All-Electron Scalar Relativistic Basis Sets for Third-Row Transition Metal Atoms. *J. Chem. Theory Comput.* **4**, 908–919 (2008).
13. Miertus, S., Scrocco, E. & Tomasi, J. Electrostatic interaction of a solute with a continuum: A direct utilization of ab initio molecular potentials for the prevision of solvent effects. *Chem. Phys.* **55**, 117–129 (1981).
14. Barone, V. & Cossi, M. Quantum Calculation of Molecular Energies and Energy Gradients in Solution by a Conductor Solvent Model. *J. Phys. Chem. A* **102**, 1995–2001 (1998).
15. Weigend, F. Accurate Coulomb-fitting basis sets for H to Rn. *Phys. Chem. Chem. Phys.* **8**, 1057–1065 (2006).
16. Weigend, F. & Ahlrichs, R. Balanced basis sets of split valence, triple zeta valence and quadruple zeta valence quality for H to Rn: Design and assessment of accuracy. *Phys. Chem. Chem. Phys.* **7**, 3297–3305 (2005).

-
17. Grimme, S., Antony, J., Ehrlich, S. & Krieg, H. A consistent and accurate ab initio parametrization of density functional dispersion correction (DFT-D) for the 94 elements H-Pu. *J. Chem. Phys.* **132**, 154104 (2010).
 18. Grimme, S., Ehrlich, S. & Goerigk, L. Effect of the damping function in dispersion corrected density functional theory. *J. Comput. Chem.* **32**, 1456–1465 (2011).
 19. Plasser, F. TheoDORE; at <http://theodore-gc.sourceforge.net> (accessed Feb. 21st 2023).
 20. Plasser & F. TheoDORE: A toolbox for a detailed and automated analysis of electronic excited state computations. *J. Chem. Phys.* **152**, 84108 (2020).
 21. Hess, B., Kutzner, C., van der Spoel, D. & Lindahl, E. GROMACS 4: Algorithms for Highly Efficient, Load-Balanced, and Scalable Molecular Simulation. *J. Chem. Theory Comput.* **4**, 435–447 (2008).
 22. Jorgensen, W. L., Maxwell, D. S. & Tirado-Rives, J. Development and Testing of the OPLS All-Atom Force Field on Conformational Energetics and Properties of Organic Liquids. *J. Am. Chem. Soc.* **118**, 11225–11236 (1996).
 23. Shao, Y. et al., Advances in molecular quantum chemistry contained in the Q-Chem 4 program package. *Mol. Phys.* **113**, 184-215 (2015).
 24. Darden, T., York, D. & Pedersen, L. Particle mesh Ewald: An N-log(N) method for Ewald sums in large systems. *J. Chem. Phys.* **98**, 10089 (1993).
 25. Allen, M. & Tildesley, D. *Computer Simulations of Liquids*, 2nd edition Oxford Academic (2017).
 26. Hess, B., Bekker, H., Berendsen, H. J., Fraaije, J. G. LINCS: A Linear Constraint Solver for Molecular Simulations. *J. Comput. Phys.* **18**, 1463–1472 (1997).
 27. Bussi, G., Donadio, D. & Parrinello, M. Canonical sampling through velocity rescaling. *J. Chem. Phys.* **126**, 014101 (2007).
 28. Berendsen, H. J. C., Postma, J. P. M., DiNola, A. & Haak, J. R. Molecular dynamics with coupling to an external bath. *J. Chem. Phys.* **81**, 3684 (1984).

6.3 Supporting Information to Chapter 3.3. (“Coupled Potential Energy Surfaces Strongly Impact the Lowest-Energy Spin-Flip Transition in Six-Coordinate Nickel(II) Complexes”)

Supporting Information

Coupled Potential Energy Surfaces Strongly Impact the Lowest-Energy Spin-Flip Transition in Six-Coordinate Nickel(II) Complexes

Nathan R. East,[†] Chahinez Dab,^{††},^{†††} Christoph Förster,[†] Katja Heinze[†] and Christian Reber*^{††}*

[†] Department of Chemistry, Johannes Gutenberg University, Duesbergweg 10-14, 55128 Mainz, Germany

^{††} Université de Montréal, Département de chimie, C.P. 6128, Succursale Centre-ville, Montréal QC H3C 3J7, Canada

^{†††} Université du Québec à Rimouski, 300 allée des Ursulines, Rimouski QC G5L 3A1, Canada

e-mail for corresponding authors:

Katja Heinze: katja.heinze@uni-mainz.de

Christian Reber: christian.reber@umontreal.ca

Table of contents

Figure S1. ATR-IR spectrum of 1 [BF ₄] ₂	4
Figure S2. ESI ⁺ mass spectrum of 1 [BF ₄] ₂ in acetonitrile.....	4
Figure S3. ATR-IR spectrum of 5 [BF ₄] ₂	5
Figure S4. ESI ⁺ mass spectrum of 5 [BF ₄] ₂ in acetonitrile.....	5
Figure S5. Cyclic voltammogram of 1 [BF ₄] ₂ in dry, deaerated acetonitrile with [nBu ₄ N][PF ₆] as supporting electrolyte.....	6
Figure S6. Cyclic voltammogram of 5 [BF ₄] ₂ in dry, deaerated acetonitrile with [nBu ₄ N][PF ₆] as supporting electrolyte.....	7
Table S1. Electrochemical data for complexes 1 ²⁺ – 5 ²⁺	Error! Bookmark not defined.
Table S2. Selected bond lengths / Å and bond angles / deg of the cations of 1 [PF ₆] ₂ ×CH ₃ CN, 2 [ClO ₄] ₂ ×0.5H ₂ O, 3 [BF ₄] ₂ ×H ₂ O, 4 [BF ₄] ₂ ×2CH ₃ CN and 5 [BF ₄] ₂ ×4CH ₃ CN obtained from single crystal XRD.	8
Table S3. Selected bond lengths / Å and angles / deg of 1 ²⁺ , 2 ²⁺ , 3 ²⁺ , 4 ²⁺ and 5 ²⁺ obtained by DFT calculations.	8
Figure S7. Tanabe-Sugano diagram with all triplet states (blue) and the lowest-energy singlet state (red).....	9
Figure S8. UV/Vis/NIR spectrum of 1 [BF ₄] ₂ in acetonitrile with absorption band assignments.	10
Figure S9. UV/Vis/NIR spectrum of 2 [BF ₄] ₂ in acetonitrile with absorption band assignments.	10
Figure S10. UV/Vis/NIR spectrum of 3 [BF ₄] ₂ in acetonitrile with absorption band assignments.	11
Figure S11. UV/Vis/NIR spectrum of 4 [BF ₄] ₂ in acetonitrile with absorption band assignments.	11
Figure S12. UV/Vis/NIR spectrum of 5 [BF ₄] ₂ in acetonitrile with absorption band assignments.	12
Table S4. Active orbitals of the CASSCF(12,7)-NEVPT2 calculation on 1 ²⁺ , depicted at a contour value of 0.035 a.u. (hydrogen atoms omitted for clarity).	13
Table S5. Active orbitals of the CASSCF(12,7)-NEVPT2 calculation on 2 ²⁺ , depicted at a contour value of 0.035 a.u. (hydrogen atoms omitted for clarity).	14
Table S6. Active orbitals of the CASSCF(12,7)-NEVPT2 calculation on 3 ²⁺ , depicted at a contour value of 0.035 a.u. (hydrogen atoms omitted for clarity).	15
Table S7. Active orbitals of the CASSCF(12,7)-NEVPT2 calculation on 4 ²⁺ , depicted at a contour value of 0.035 a.u. (hydrogen atoms omitted for clarity).	16
Table S8. Active orbitals of the CASSCF(12,7)-NEVPT2 calculation on 5 ²⁺ , depicted at a contour value of 0.035 a.u. (hydrogen atoms omitted for clarity).	17
Figure S13. Comparison of energy differences between the ¹ E and ³ T ₂ states	18

Figure S14. Illustrative examples of coupled potential energy surfaces with lowest-energy eigenfunctions and calculated absorption spectra	19
Figure S15. Variable-temperature luminescence spectra of solid 3 [BF ₄] ₂	20
Figure S16. Variable-temperature luminescence spectra of solid 4 [BF ₄] ₂	20
Figure S17. Variable-temperature luminescence spectra of solid 5 [BF ₄] ₂	21
Figure S18. Luminescence spectra of 3 [BF ₄] ₂ (red, $\lambda_{\text{exc}} = 450$ nm) and 5 [BF ₄] ₂ (blue, $\lambda_{\text{exc}} = 340$ nm) in frozen butyronitrile at 77 K.	21
Figure S19. Reported photoluminescence spectra (normalized) of 3 [BF ₄] ₂ (orange) and [Ni(tpm) ₂][BF ₄] ₂ (green) as powders at 80 K and 150 K.....	22
Figure S20. Variable-pressure luminescence measurements for 4 [BF ₄] ₂	23
Figure S21. Variable pressure Raman spectra of 4 [BF ₄] ₂ ($\lambda_{\text{exc}} = 785$ nm), low-frequency region.....	23
Figure S22. Variable pressure Raman spectra of 4 [BF ₄] ₂ ($\lambda_{\text{exc}} = 488$ nm and 785 nm),	24
Figure S23. Selected Raman peak positions of 4 [BF ₄] ₂ ($\lambda_{\text{exc}} = 488$ nm) at variable pressure	25
Figure S24. Selected Raman peak positions of 4 [BF ₄] ₂ ($\lambda_{\text{exc}} = 785$ nm) at variable pressure	26
References	27

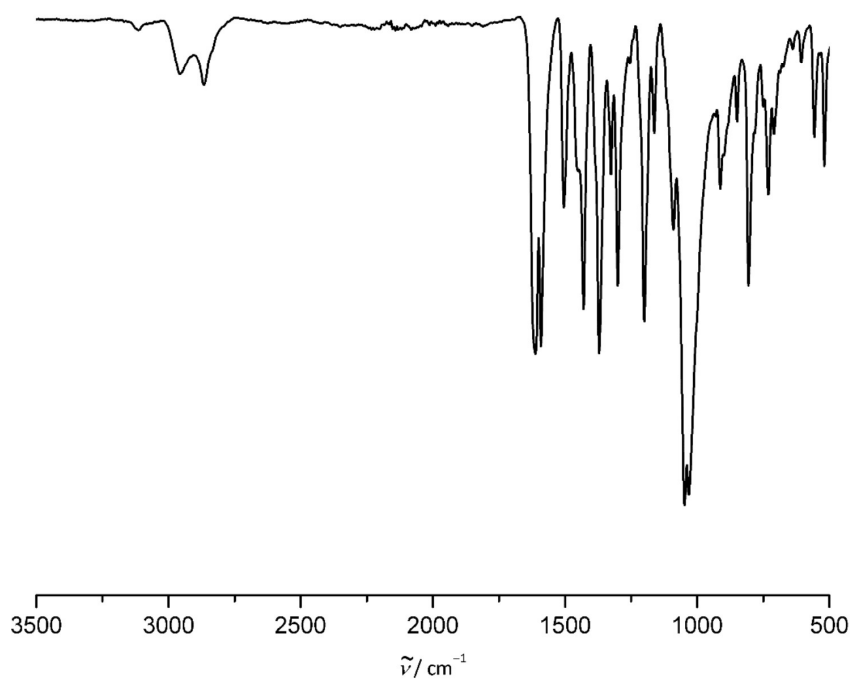


Figure S1. ATR-IR spectrum of **1**[BF₄]₂.

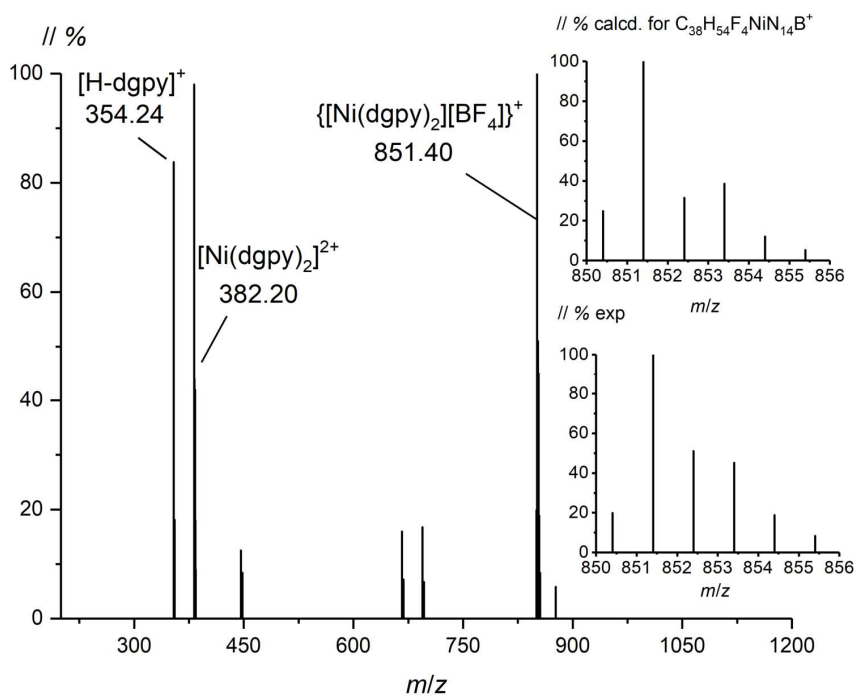


Figure S2. ESI⁺ mass spectrum of **1**[BF₄]₂ in acetonitrile.

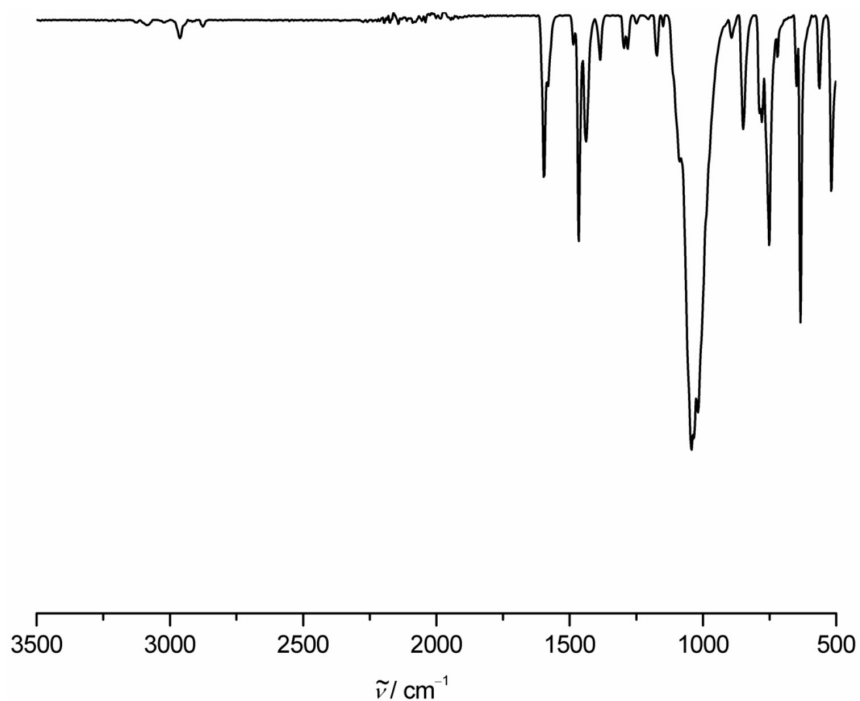


Figure S3. ATR-IR spectrum of $5[BF_4]_2$.

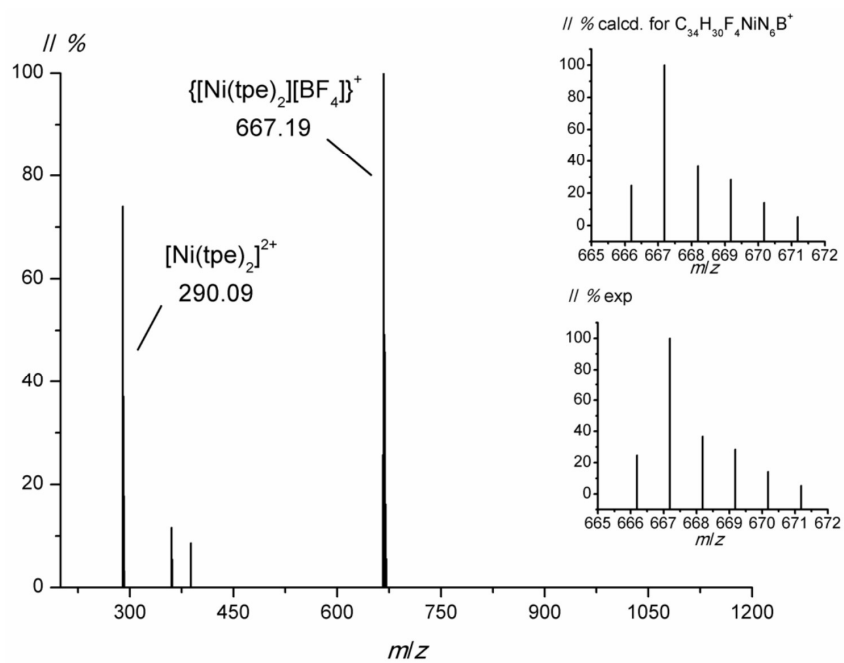


Figure S4. ESI⁺ mass spectrum of $5[BF_4]_2$ in acetonitrile.

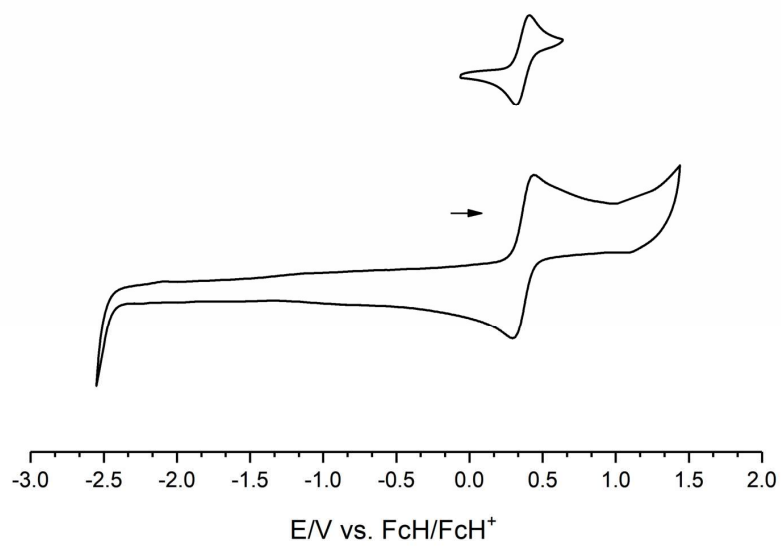


Figure S5. Cyclic voltammogram of $1[BF_4]_2$ in dry, deaerated acetonitrile with $[nBu_4N][PF_6]$ as supporting electrolyte.

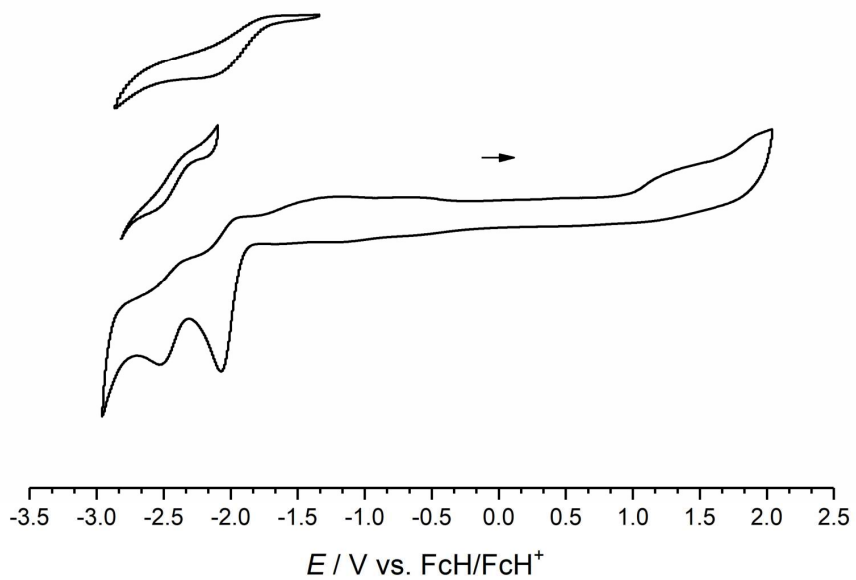


Figure S6. Cyclic voltammogram of $5[\text{BF}_4]_2$ in dry, deaerated acetonitrile with $[\text{nBu}_4\text{N}][\text{PF}_6]$ as supporting electrolyte.

Table S1. Electrochemical data for complexes $1^{2+} - 5^{2+}$.

Complex	$E_{1/2}$ / V vs. ferrocene			
	4+/3+	3+/2+	2+/1+	1+/0
1^{2+}		+0.39 (rev)		
2^{2+} ^[1,2]		+1.27 (rev)	-1.58 (qrev)	-1.76
3^{2+} ^[3]			-1.70	-2.40
4^{2+} ^[4]	+1.71 (irrev)	+1.22 (qrev)	-2.03	
5^{2+}			-1.92	-2.31

1^{2+} , 4^{2+} , 5^{2+} as $[\text{BF}_4]^-$ salts, in CH_3CN , 0.1 M $[\text{nBu}_4\text{N}][\text{PF}_6]$
 2^{2+} , 3^{2+} as $[\text{PF}_6]^-$ salts, in CH_3CN , 0.1 M $[\text{nBu}_4\text{N}][\text{PF}_6]$, SCE electrode, converted to ferrocene/ferrocenium couple.

Table S2. Selected bond lengths / Å and bond angles / deg of the cations of $1[\text{PF}_6]_2 \times \text{CH}_3\text{CN}$, $2[\text{ClO}_4]_2 \times 0.5\text{H}_2\text{O}$, $3[\text{BF}_4]_2 \times \text{H}_2\text{O}$, $4[\text{BF}_4]_2 \times 2\text{CH}_3\text{CN}$ and $5[\text{BF}_4]_2 \times 4\text{CH}_3\text{CN}$ obtained from single crystal XRD.

	$1[\text{PF}_6]_2$ (dgpy) this work	$2[\text{ClO}_4]_2$ (terpy) ref. 5	$3[\text{BF}_4]_2$ (phen) ref. 6	$4[\text{BF}_4]_2$ (ddpd) ref. 3	$5[\text{BF}_4]_2$ (tpe) this work
Ni1–N1	2.067(3)	2.000(2)	2.085(3)	2.058(2)	2.107(3)
Ni1–N2	2.075(3)	2.117(2)	2.070(13)	2.0922(15)	2.074(3)
Ni1–N3	2.065(3)	2.120(2)	2.089(3)	2.0922(15)	2.068(3)
Ni1–N4	2.060(3)	1.999(2)	2.121(13)	2.058(2)	2.107(3)
Ni1–N5	2.082(3)	2.110(2)	2.086(3)	2.0922(15)	2.074(3)
Ni1–N6	2.089(3)	2.119(2)	2.079(3)	2.0923(15)	2.068(3)
N1–Ni1–N2	86.06(13)	78.06(8)	91.20(3)	84.64(4)	85.37(12)
N2–Ni1–N3	86.78(11)	77.40(8)	90.62(13)	84.64(4)	85.20(12)
N4–Ni1–N5	86.49(12)	78.00(8)	89.60(3)	84.64(4)	85.37(12)
N5–Ni1–N6	85.97(12)	77.50(8)	96.70(4)	84.64(4)	85.20(12)

Table S3. Selected bond lengths / Å and angles / deg of 1^{2+} , 2^{2+} , 3^{2+} , 4^{2+} and 5^{2+} obtained by DFT calculations.

	1^{2+} (dgpy)	2^{2+} (terpy)	3^{2+} (phen)	4^{2+} (ddpd)	5^{2+} (tpe)
Ni1–N1	2.088	2.006	2.107	2.068	2.087
Ni1–N2	2.085	2.122	2.121	2.103	2.088
Ni1–N3	2.083	2.122	2.099	2.103	2.088
Ni1–N4	2.079	2.006	2.098	2.068	2.087
Ni1–N5	2.095	2.122	2.082	2.103	2.088
Ni1–N6	2.118	2.122	2.121	2.103	2.089
N1–Ni1–N2	84.93	78.03	95.51	85.45	86.12
N2–Ni1–N3	85.53	78.03	90.90	87.46	85.96
N4–Ni1–N5	84.62	78.03	93.72	85.45	86.09
N5–Ni1–N6	84.49	78.04	94.47	87.45	85.97

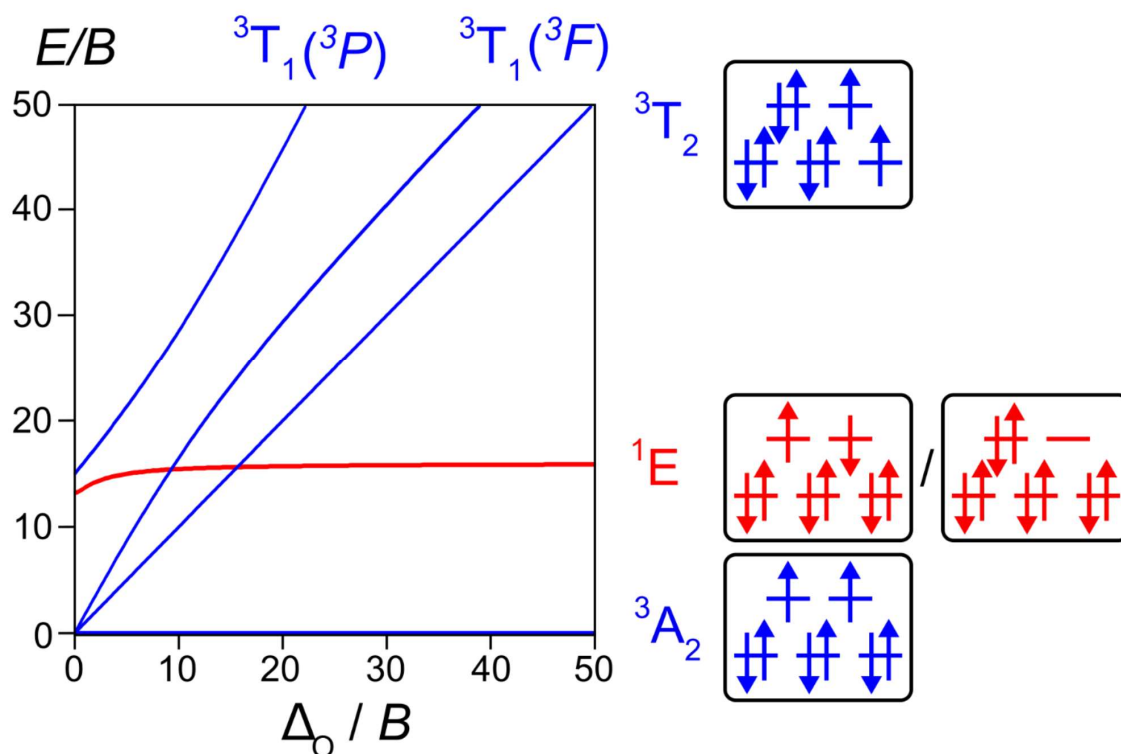


Figure S7. Tanabe-Sugano diagram with all triplet states (blue) and the lowest-energy singlet state (red). This diagram is used to assign absorption bands in Figures S8 to S12 and Figure 2. The broad d-d band at higher wavenumber is unambiguously assigned as the spin-allowed ${}^3T_1({}^3F)$ band, with the ${}^3T_1({}^3P)$ band hidden beneath more intense bands involving the ligands. The broad band with two maxima at lower wavenumber is analyzed as follows: for complexes $3^{2+} - 5^{2+}$, the more intense of the two maxima is assigned as the spin-allowed 3T_2 band, with the weaker shoulder assigned to the spin-forbidden 1E transition. For complexes 1^{2+} and 2^{2+} , the intensities of the two maxima are similar and the energy difference is small. The model calculation illustrated in Figure 5 was used to label absorption bands in these two complexes.

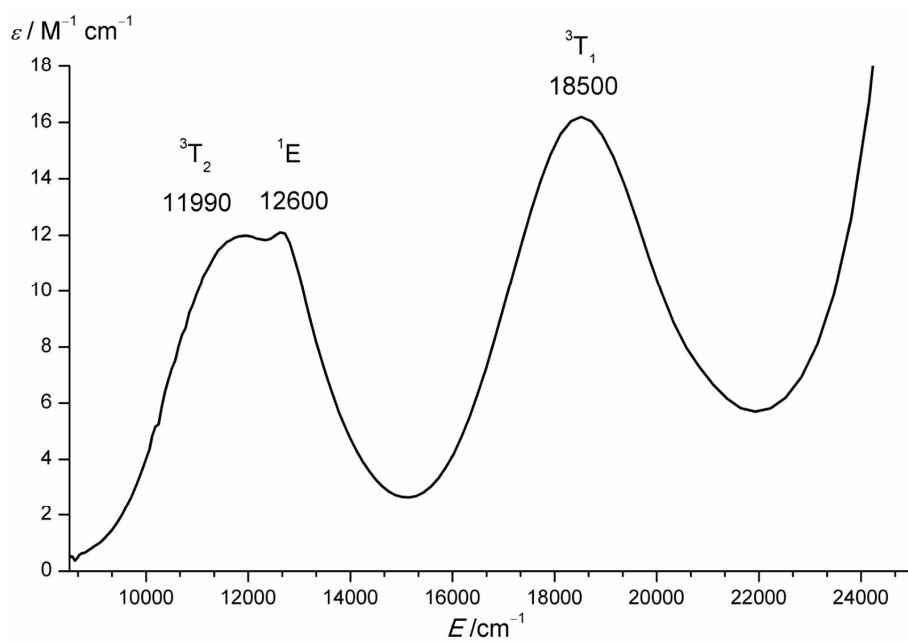


Figure S8. UV/Vis/NIR spectrum of $1[BF_4]_2$ in acetonitrile with absorption band assignments.

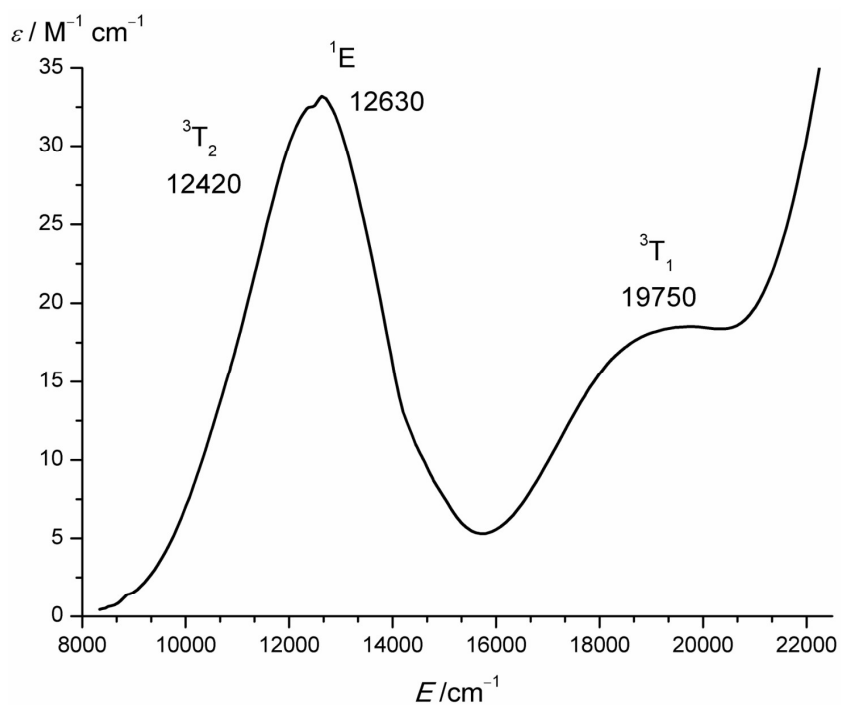


Figure S9. UV/Vis/NIR spectrum of $2[BF_4]_2$ in acetonitrile with absorption band assignments.

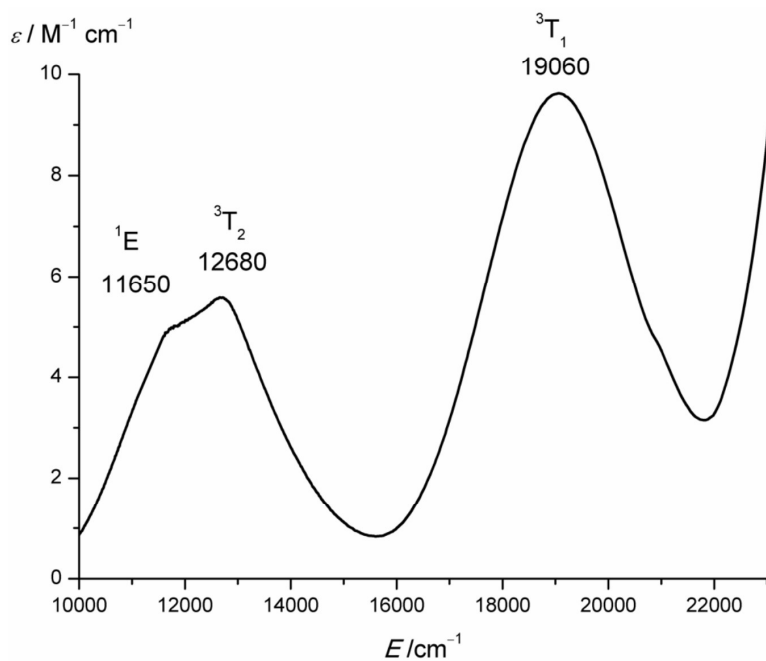


Figure S10. UV/Vis/NIR spectrum of $3[\text{BF}_4]_2$ in acetonitrile with absorption band assignments.

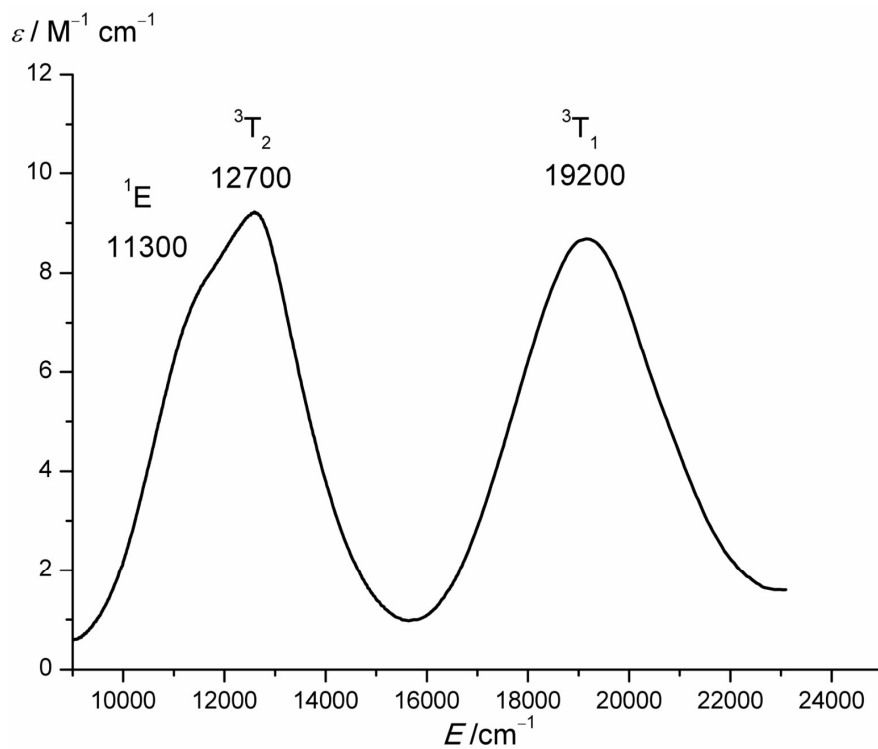


Figure S11. UV/Vis/NIR spectrum of $4[\text{BF}_4]_2$ in acetonitrile with absorption band assignments.

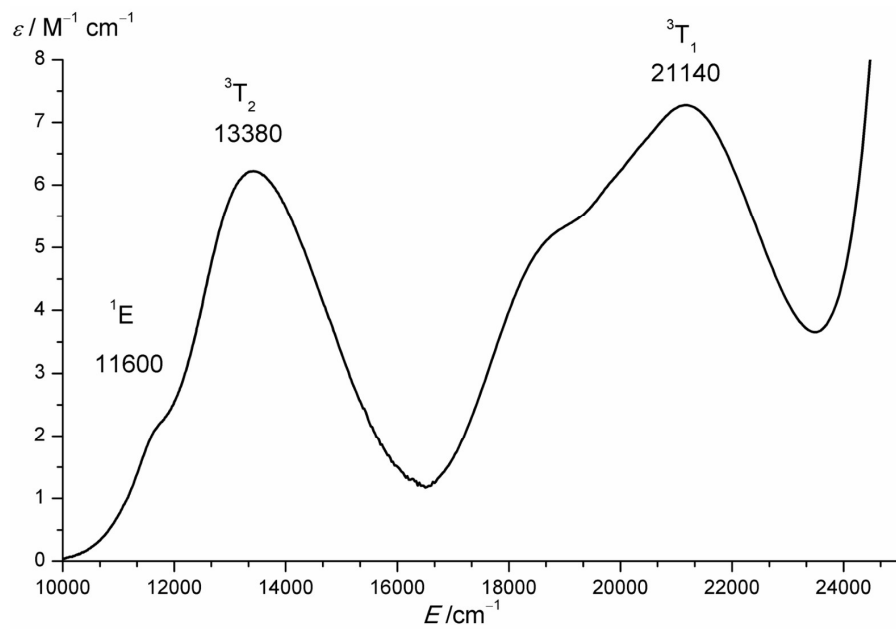


Figure S12. UV/Vis/NIR spectrum of 5[BF₄]₂ in acetonitrile with absorption band assignments.

Table S4. Active orbitals of the CASSCF(12,7)-NEVPT2 calculation on $\mathbf{1}^{2+}$, depicted at a contour value of 0.035 a.u. (hydrogen atoms omitted for clarity).

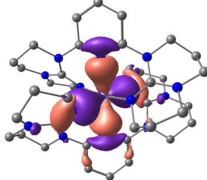
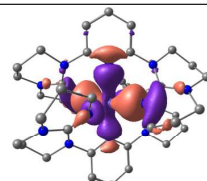
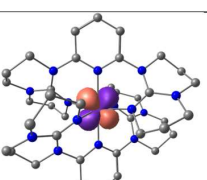
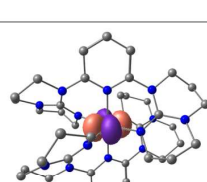
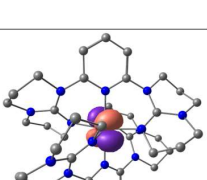
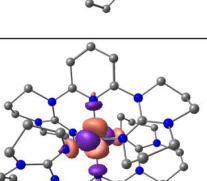
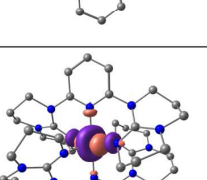
$\mathbf{1}^{2+}$ (d _{gpy})	E/H	orbital
	-0.5103	
	-0.5098	
	-0.4134	
	-0.4090	
	-0.4076	
	-0.3686	
	-0.3664	

Table S5. Active orbitals of the CASSCF(12,7)-NEVPT2 calculation on 2^{2+} , depicted at a contour value of 0.035 a.u. (hydrogen atoms omitted for clarity).

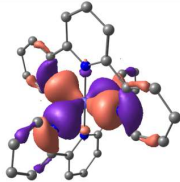
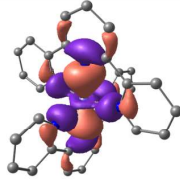
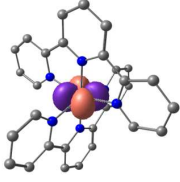
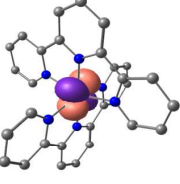
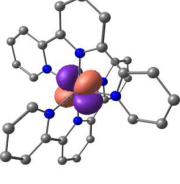
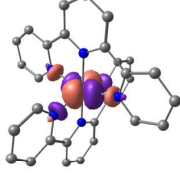
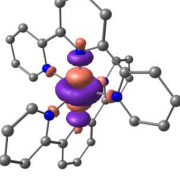
2^{2+} (terpy)	E/H	orbital
	-0.5291	
	-0.5555	
	-0.4387	
	-0.4371	
	-0.4371	
	-0.4326	
	-0.3877	

Table S6. Active orbitals of the CASSCF(12,7)-NEVPT2 calculation on 3^{2+} , depicted at a contour value of 0.035 a.u. (hydrogen atoms omitted for clarity).

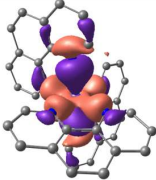
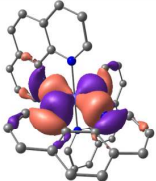
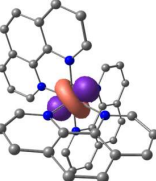
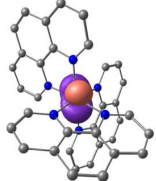
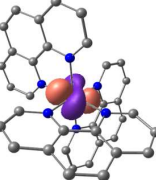
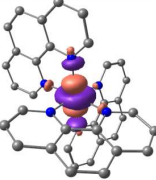
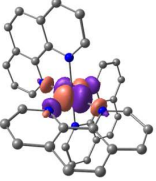
3^{2+} (phen)	E/H	orbital
	-0.5401	
	-0.5407	
	-0.4446	
	-0.4435	
	-0.4437	
	-0.4022	
	-0.4010	

Table S7. Active orbitals of the CASSCF(12,7)-NEVPT2 calculation on 4^{2+} , depicted at a contour value of 0.035 a.u. (hydrogen atoms omitted for clarity).

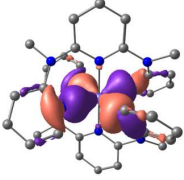
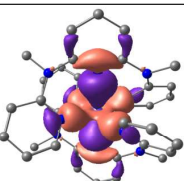
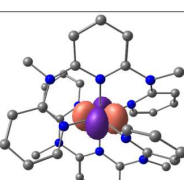
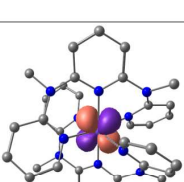
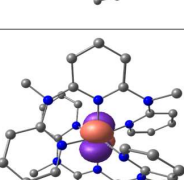
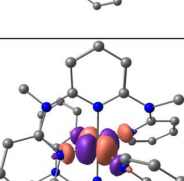
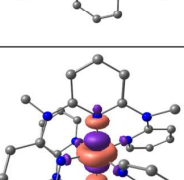
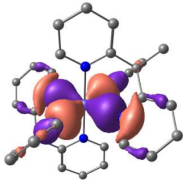
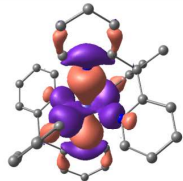
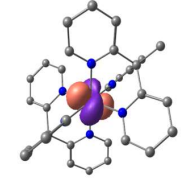
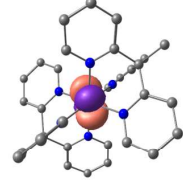
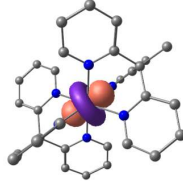
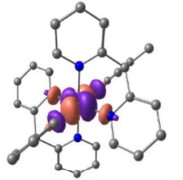
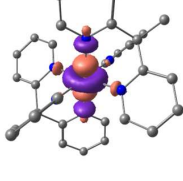
4^{2+} (ddpd)	E/H	orbital
	-0.5301	
	-0.5360	
	-0.4352	
	-0.4375	
	-0.4312	
	-0.3931	
	-0.3874	

Table S8. Active orbitals of the CASSCF(12,7)-NEVPT2 calculation on 5^{2+} , depicted at a contour value of 0.035 a.u. (hydrogen atoms omitted for clarity).

5^{2+} (tpe)	E/H	orbital
	-0.5348	
	-0.5346	
	-0.4352	
	-0.4351	
	-0.4381	
	-0.3894	
	-0.3892	

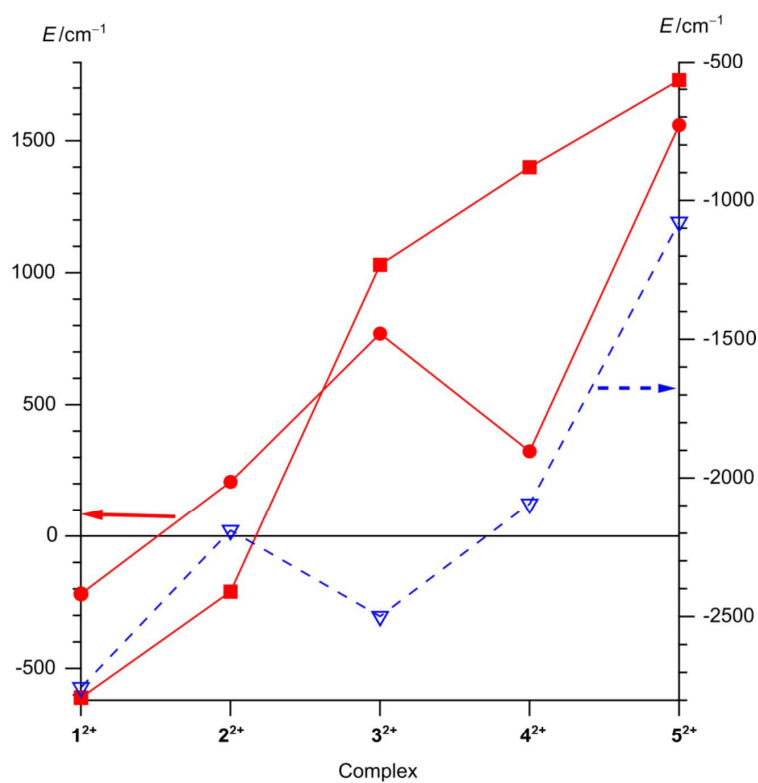


Figure S13. Comparison of energy differences between the 1E and 3T_2 states given as ΔE values from the three models (Tables 1 to 3). Full red squares and circles denote ΔE values determined from experimental absorption spectra and the fits to the absorption bands, respectively. They are shown on the lefthand ordinate scale. Open blue triangles denote ΔE values from CASSCF(12,7)-NEVPT2 calculations, shown on the righthand ordinate scale. Both E axes cover a range of 2300 cm^{-1} . The righthand axis shows a range lower by 2300 cm^{-1} than the lefthand axis.

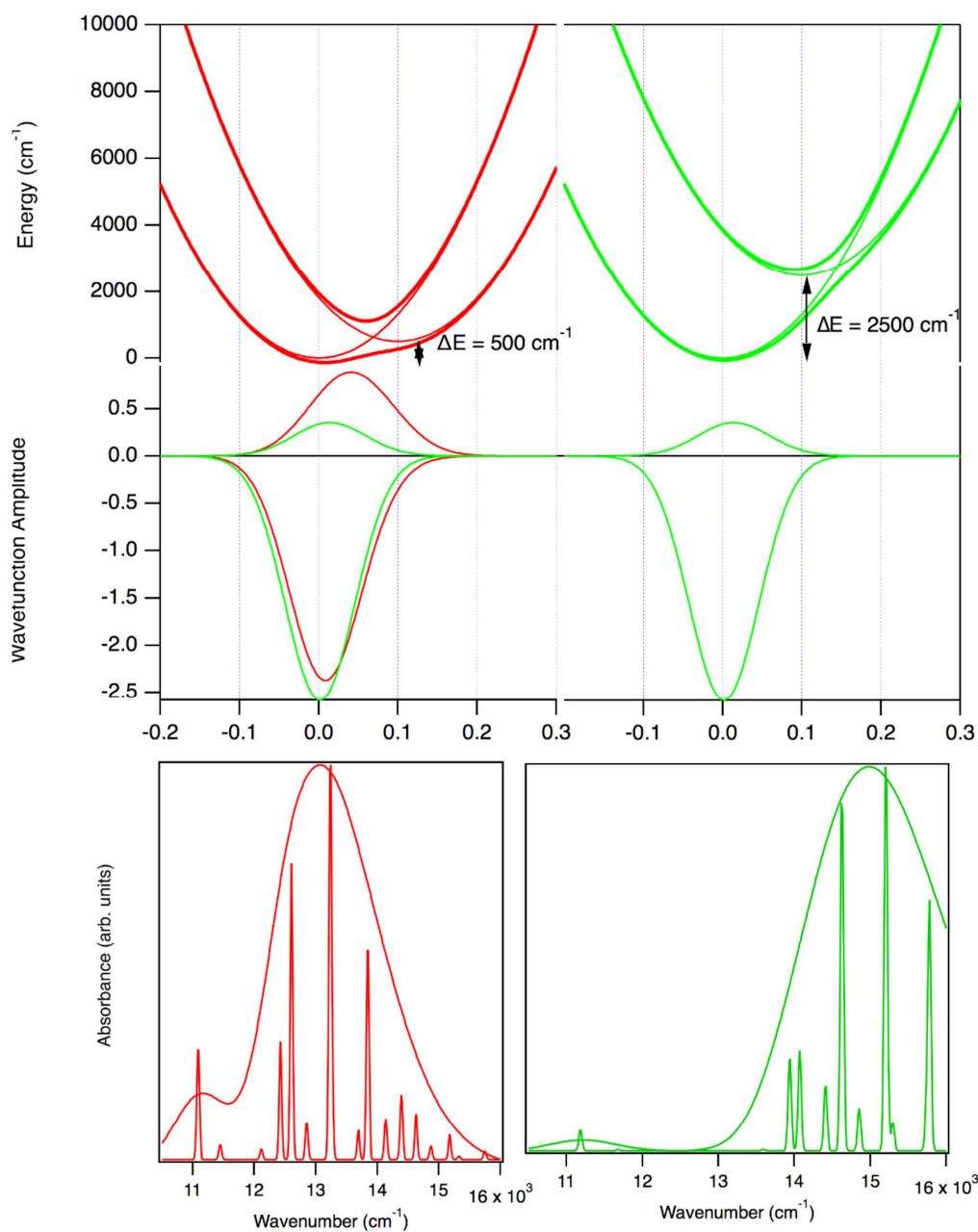


Figure S14. Illustrative examples of coupled potential energy surfaces with lowest-energy eigenfunctions and calculated absorption spectra. Lefthand column: energy difference between diabatic minima is 500 cm^{-1} . Righthand column: energy difference between diabatic minima is 2500 cm^{-1} . All other parameters are identical. Red eigenfunction: diabatic component from the displaced (3T_1) state has more amplitude than for the green eigenfunction and its maximum is at a higher value along the normal coordinate. The calculated absorption spectra show the higher intensity of the 1E band for the red potential energy curves, a consequence of the smaller ΔE value, and the differences of both the overall bandshapes and individual vibronic transitions induced by the coupling. The numerical method used is described in references 7, 8.

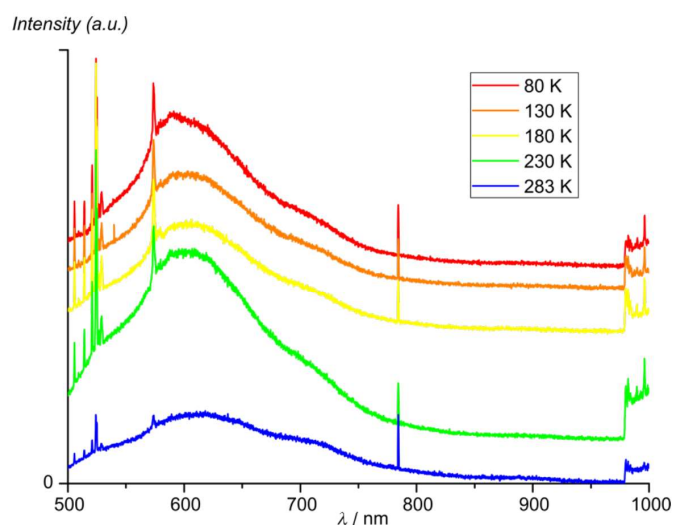


Figure S15. Variable-temperature luminescence spectra of solid $3[\text{BF}_4]_2$ ($\lambda_{\text{exc}} = 488 \text{ nm}$). Based on the absorption spectra, spin-flip luminescence is expected between 900 nm and 1000 nm and the onset of a possible broadband luminescence between 950 nm and 1000 nm. No such signals are observed, with Raman scattering signals (in first and second order diffraction) dominating the intensity.

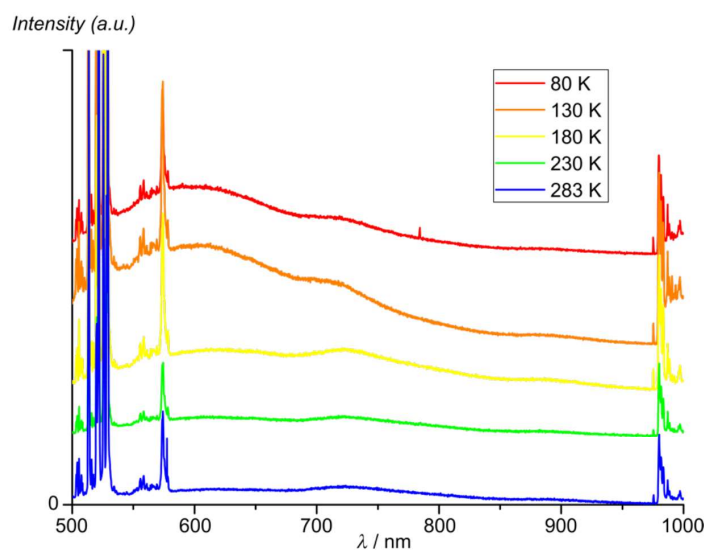


Figure S16. Variable-temperature luminescence spectra of solid $4[\text{BF}_4]_2$ ($\lambda_{\text{exc}} = 488 \text{ nm}$). Based on the absorption spectra, spin-flip luminescence is expected between 900 nm and 1000 nm. The onset of a possible broadband luminescence is expected between 950 nm and 1000 nm. No such signals are observed, with Raman scattering signals (in first and second order diffraction) dominating the measured intensity.

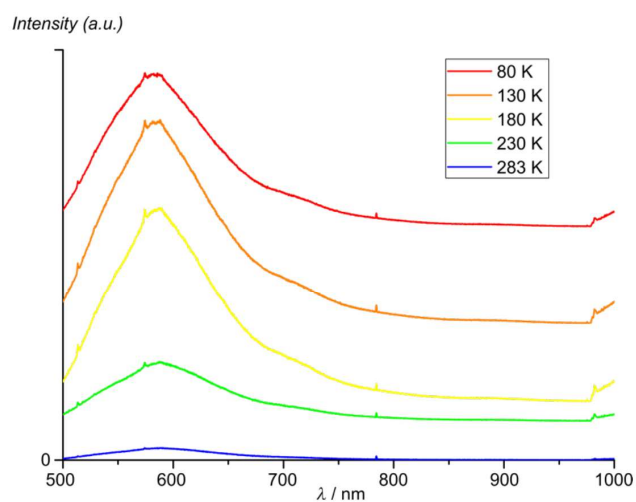


Figure S17. Variable-temperature luminescence spectra of solid $5[\text{BF}_4]_2$ ($\lambda_{\text{exc}} = 488 \text{ nm}$).

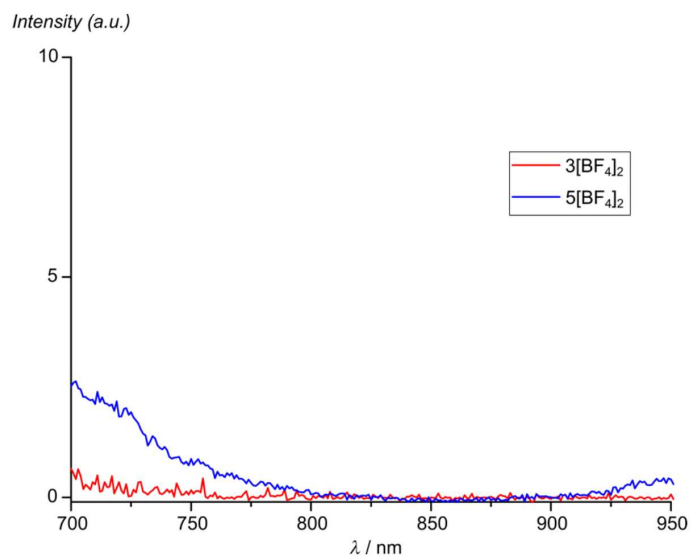


Figure S18. Luminescence spectra of $3[\text{BF}_4]_2$ (red, $\lambda_{\text{exc}} = 450 \text{ nm}$) and $5[\text{BF}_4]_2$ (blue, $\lambda_{\text{exc}} = 340 \text{ nm}$) in frozen butyronitrile at 77 K.

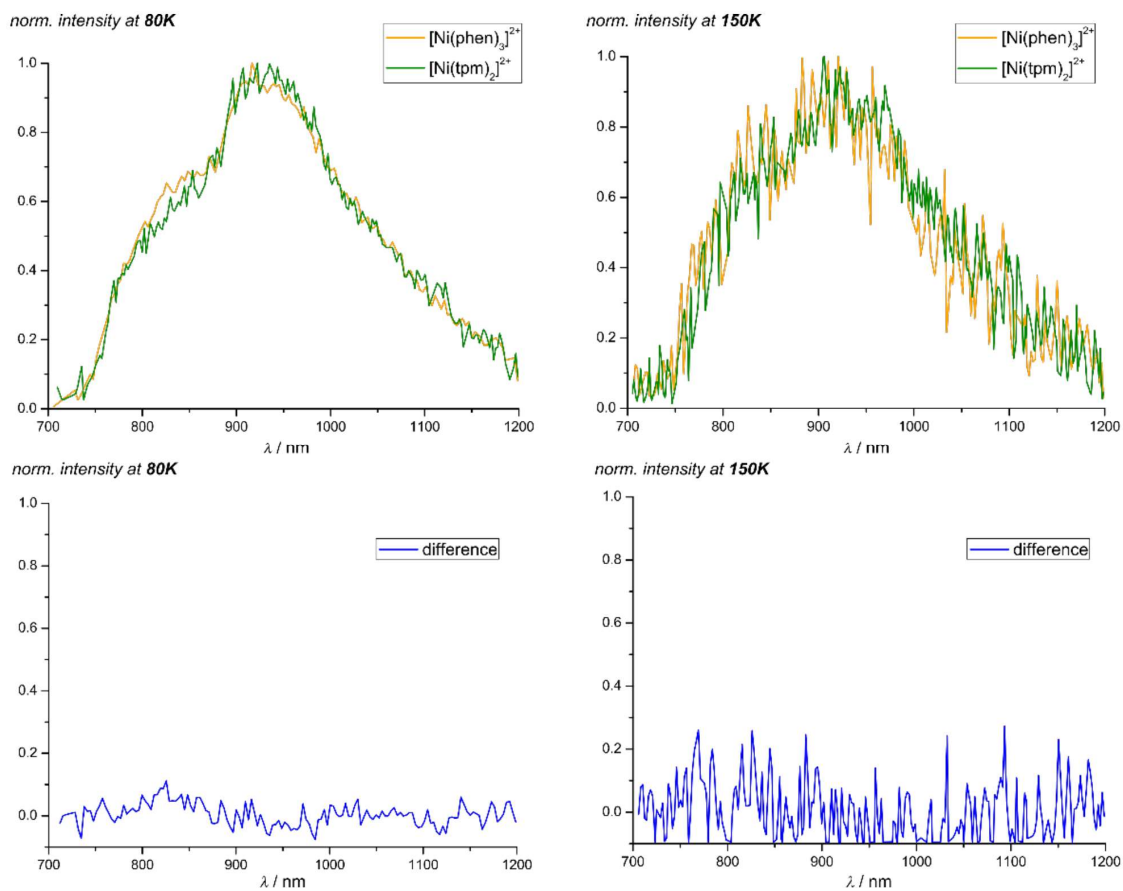


Figure S19. Reported photoluminescence spectra (normalized) of $3[\text{BF}_4]_2$ (orange) and $[\text{Ni}(\text{tpm})_2][\text{BF}_4]_2$ (green) as powders at 80 K and 150 K (data digitized from Figures S25 and S26 of ref. 72, as discussed in the manuscript) and the calculated difference spectra (tpm = tris(pyrid-2-yl)methane).

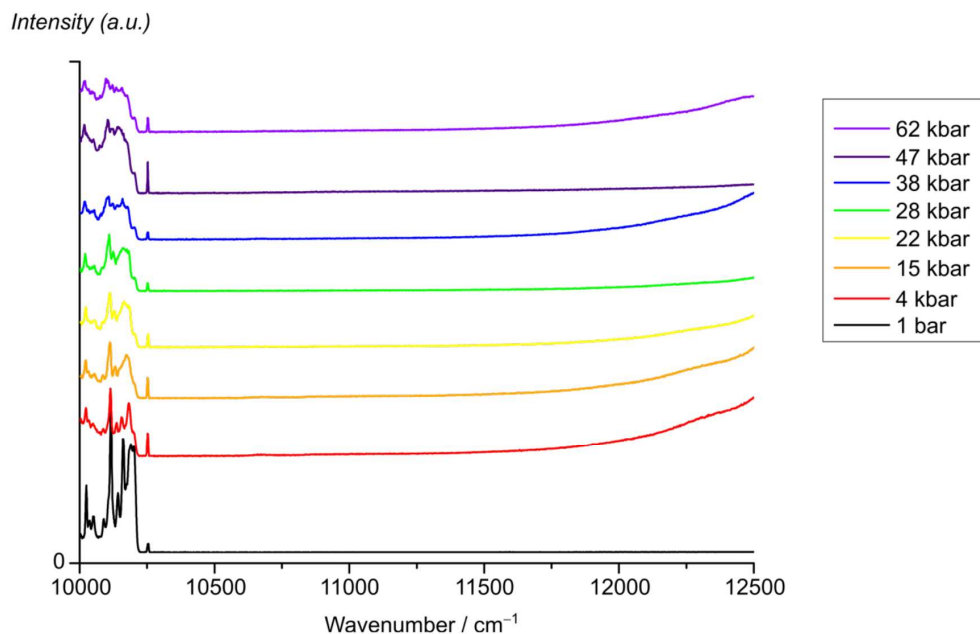


Figure S20. Variable-pressure luminescence measurements for $4[\text{BF}_4]_2$ ($\lambda_{\text{exc}} = 488 \text{ nm}$). The region where luminescence is expected at high pressure is shown.

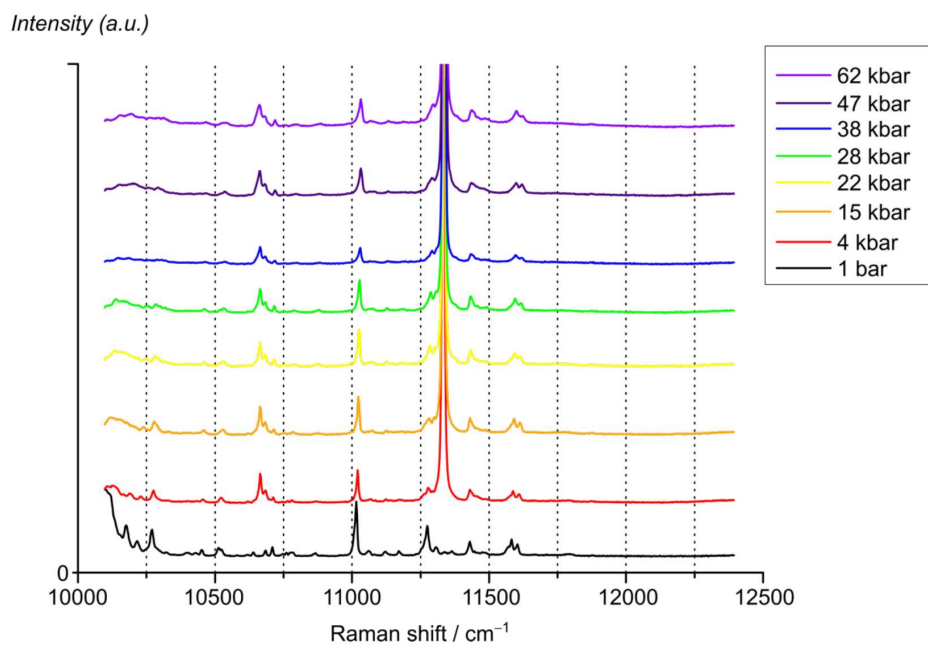


Figure S21. Variable pressure Raman spectra of $4[\text{BF}_4]_2$ ($\lambda_{\text{exc}} = 785 \text{ nm}$), low-frequency region. The vertical lines are drawn as guides for the eye to show the pressure-induced shifts. The Raman peak of the diamond anvils is observed at 1330 cm^{-1} for all measurements with the sample in the diamond anvil cell.

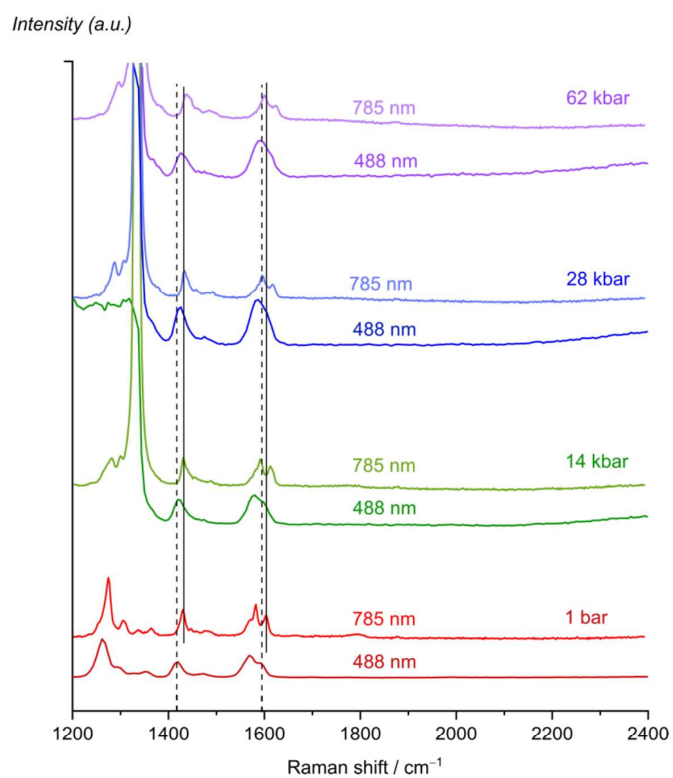


Figure S22. Variable pressure Raman spectra of $4[\text{BF}_4]_2$ ($\lambda_{\text{exc}} = 488 \text{ nm}$ and 785 nm), given for each spectrum, higher frequency region. The vertical lines are drawn as guides for the eye to show the pressure-induced shifts.

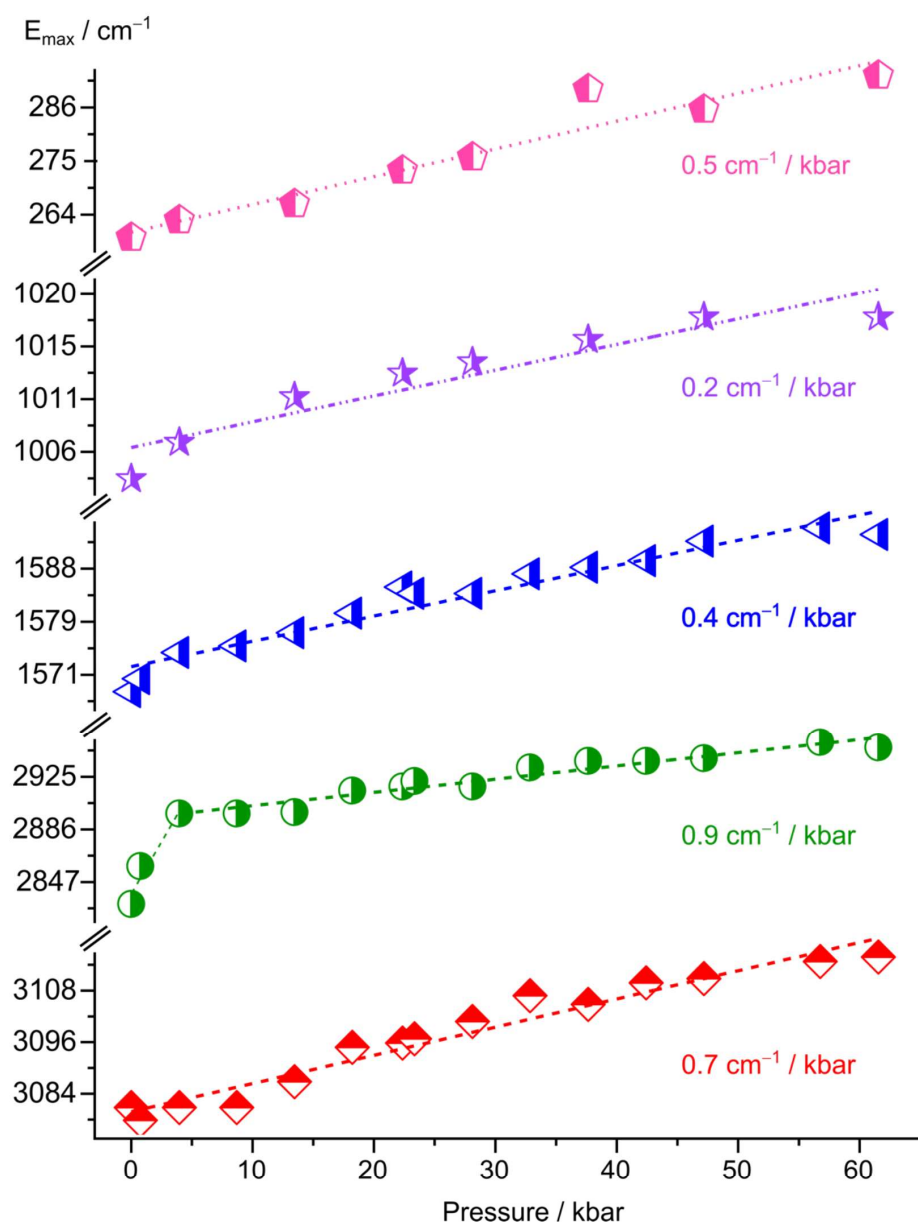


Figure S23. Selected Raman peak positions of $4[\text{BF}_4]_2$ ($\lambda_{\text{exc}} = 488 \text{ nm}$) at variable pressure.

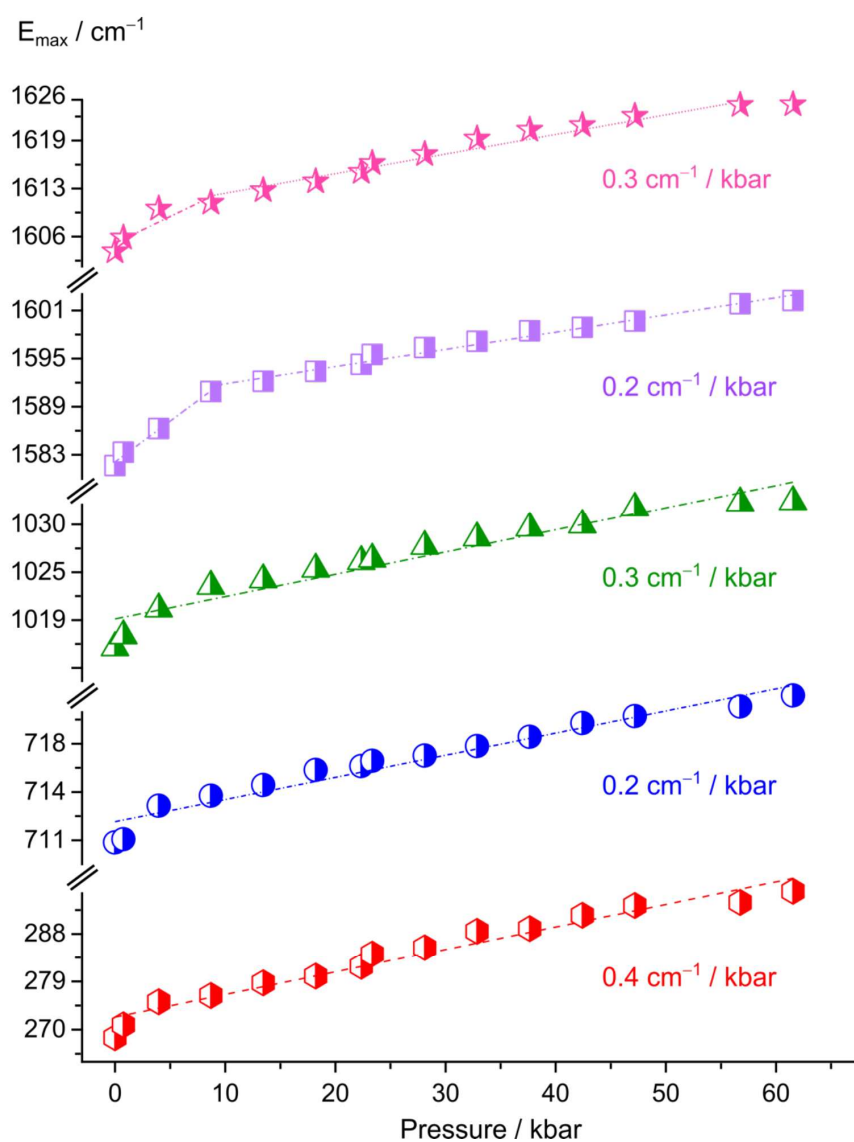


Figure S24. Selected Raman peak positions of $4[\text{BF}_4]_2$ ($\lambda_{\text{exc}} = 785 \text{ nm}$) at variable pressure.

References

- 1 Arana, C.; Keshavarz, M.; Potts, K. T.; Abruña, H. D.
Electrocatalytic reduction of CO₂ and O₂ with electropolymerized films of vinyl-terpyridine complexes of Fe, Ni and Co.
Inorg. Chim. Acta **1994**, *225*, 285-295.
- 2 Drew, M. G.; Foreman, M. R.; Geist, A.; Hudson, M. J.; Marken, F.; Norman, V.; Weigl, M.
Synthesis, structure, and redox states of homoleptic d-block metal complexes with bis-1,2,4-triazin-3-yl-pyridine and 1,2,4-triazin-3-yl-bipyridine extractants
Polyhedron **2006**, *25*, 888–900.
- 3 Arounagui, S.; Easwaramoorthy, D.; Ashokkumar, A.; Dattagupta, A.; Maiya, B. G.
Cobalt(III), nickel(II) and ruthenium(II) complexes of 1,10-phenanthroline family of ligands: DNA binding and photocleavage studies.
J. Chem. Sci. (publ. by the Indian Academy of Sciences) **2000**, *112*, 1-17.
- 4 Dorn, M.; Mack, K.; Carrella, L. M.; Rentschler, E.; Förster, C.; Heinze, K.
Structure and Electronic Properties of an Expanded Terpyridine Complex of Nickel(II) [Ni(ddpd)₂](BF₄)₂.
Z. Anorg. Allg. Chem. **2018**, *644*, 706–712.
- 5 Anderer, C.; Näther, C.; Bensch, W.
Bis(2,2':6',2''-terpyridine-κ³N,N',N'')nickel(II) bis(perchlorate) hemihydrate
IUCrData. **2016**, *1*, x161009.
- 6 Hanifehpour, Y.; Mirtamizdoust, B.; Wang, R.; Anbardeh, S.; Joo, S. W.
A Nano Nickel (II) Metal–Organic Coordination Compound for Nano Nickel (II) Oxide: Sonochemical Synthesis and Characterization.
J. Inorg. Organomet. Polym. **2017**, *27*, 1045–1052.
- 7 Bussièrè, G.; Reber, C.; Neuhauser, D.; Walter, D. A.; Zink, J. I.
Molecular Properties Obtained by Analysis of Electronic Spectra Containing Interference Dips. Comparisons of Analytical Equations and Exact Models Based on Coupled Potential Energy Surfaces.
J. Phys. Chem. A **2003**, *107*, 1258–1267.
- 8 Reber, C.; Zink J. I.
Interference Dips in Molecular Absorption Spectra Calculated for Coupled Electronic State Potential Surfaces.
J. Chem. Phys. **1992**, *96*, 2681–2691.

6.4 Supporting Information to Chapter 3.4. (“Influencing Ligand field states of Nickel(II) Complexes with Strongly σ -Donating and π -Accepting Ligands”)

Experimental section

General procedures. All reactions were performed under an argon atmosphere. The literature known $[\text{NiBr}(\text{CNC})]\text{Br}$ precursor^[203] was received from TCI chemicals. NaOAc, dry DMSO (>97%), $\text{Ni}[\text{BF}_4]_2 \cdot 6\text{H}_2\text{O}$ and $[\text{nBuN}_4][\text{PF}_6]$ were received from Sigma-Aldrich. The H-NCN ^[204] pro-ligand and dcp ^[205] ligand were prepared according to literature known procedures. Solvents CH_3CN and Et_2O were received from Alfa Aesar and distilled from calcium hydride and sodium respectively. The reagents were used as received from commercial suppliers. Gloveboxes (UniLab/Mbraun – Ar 4.8, $\text{O}_2 < 0.1$ ppm) were used to store and weigh sensitive compounds for synthesis as well as to prepare any measurement sample that required the absence of oxygen and water.

Intensity data for crystal structure determinations were collected with a STOE IPDS-2T diffractometer from STOE & CIE GmbH and an Oxford cooling system and corrected for absorption and other effects using Mo $\text{K}\alpha$ radiation ($\lambda = 0.71073 \text{ \AA}$). The diffraction frames were integrated using the STOE X-Area^[207] package, and most were corrected for absorption with MULABS^[208] of the PLATON software package.^[209] The structures were solved with SHELXT^[210] refined by the full-matrix method based on F^2 using SHELXL^[211] of the SHELX^[212] software package and the ShelXle^[213] graphical interface. All non-hydrogen atoms were refined anisotropically, while the positions of all hydrogen atoms were generated with appropriate geometric constraints and allowed to ride on their respective parent carbon atoms with fixed isotropic thermal parameters.

UV/Vis/NIR spectra were recorded on a Jasco V-770 spectrometer using 1.0 cm cells (Hellma, Suprasil).

Electrospray ionization mass spectra were recorded on an Agilent 6545 QTOF-MS spectrometer.

Elemental analyses were performed by the microanalytical laboratory of the Department of Chemistry of the University of Mainz using an Elementar vario EL Cube

Density functional theory calculations on the nickel(II) complex cations ($[\text{Ni}(\text{CNC})(\text{NCN})]^{2+}$ and $[\text{Ni}(\text{dcp})_2]^{2+}$) were carried out using the ORCA program package (version 4.2.1).^[214] Tight convergence criteria were chosen for all calculations (keywords tightscf and tightopt). All calculations were performed using the B3LYP functional^[215–217] employing the RIJCOSX approximation.^[218,219] Relativistic effects were calculated at the zeroth order regular approximation (ZORA) level.^[220] The ZORA keyword automatically invokes relativistically adjusted basis sets. To account for solvent effects, a conductor-like screening model (CPCM) modeling acetonitrile was used in all calculations.^[221] Geometry optimizations were

performed using Ahlrichs' polarized valence triple- ζ basis set (def2-TZVPP).^[222,223] Atom-pairwise dispersion correction was performed with the Becke-Johnson damping scheme (D3BJ). The energy of the electronic states and presence of energy minima were checked by numerical frequency calculations. Explicit counterions and/or solvent molecules were not taken into account.

Synthesis of [Ni(CNC)(NCN)][PF₆]. A solution of 52 mg (0.627 mmol, 3.0 eq) of NaOAc in dry DMSO (2 mL) was added to a solution of 96 mg (0.209 mmol, 1.0 eq) [NiBr(CNC)]Br^[203] and 100 mg (0.272 mmol, 1.3 eq) [H-NCN][PF₆] in dry DMSO (4 mL). The solution turned light orange and was stirred and heated to 100°C for 24 h. The DMSO was removed at 80°C under reduced pressure, leaving an orange powder, which was purified by crystallization via slow diffusion of dry diethyl ether into a concentrated dry acetonitrile solution to yield 155 mg (0.191 mmol, 91%) of [Ni(CNC)(NCN)][PF₆]₂ as orange crystals. Mass spectrometry confirmed composition (ESI⁺, CH₃CN): m/z (%) = 259.57 (37, [Ni(CNC)(NCN)]²⁺), 664.10 (91, [Ni(CNC)(NCN)]²⁺ + PF₆⁺).

For single-crystal X-ray diffraction (XRD) analysis, a solution of 334 mg of [ⁿBu₄N][PF₆] (0.586 mmol, 5 eq) in dry CH₃CN (4 mL) was added to 140 mg of [Ni(CNC)(NCN)][PF₆]₂. Crystallization via slow diffusion of dry diethyl ether into this solution gave orange crystals of [Ni(CNC)(NCN)][PF₆]₂, suitable for single-crystal XRD analysis. The PF₆ salt crystallizes in the P2₁/c space group.

Synthesis of [Ni(dcpp)₂][PF₆]₂. A solution of 100 mg (0.345 mmol, 2.0 eq) of dcpp in CH₃CN (1.5 mL) was added to a solution of 59 mg (0.173 mmol, 1.0 eq) Ni[BF₄]₂·6H₂O in CH₃CN (1.5 mL). The solution turned dark orange and was stirred at room temperature for 30 mins. The complex was precipitated from solution with Et₂O (7 ml) and the solution was filtered, leaving an orange powder, which was purified by crystallization via slow diffusion of diethyl ether into a concentrated dry acetonitrile solution to yield 129 mg (0.159 mmol, 92%) of [Ni(dcpp)₂][BF₄]₂ as orange crystals. Elemental analysis and mass spectrometry confirmed the composition and purity. Elem. anal. calcd. (%) for C₃₄H₂₂NiF₁₂NO₄P₂ (927.21): C 44.04 H 2.39, N 9.06; found C 44.35, H 2.08 N 9.35. MS (ESI⁺, CH₃CN): m/z (%) = 318.05 (14, [Ni(dcpp)₂]²⁺), 655.10 (76, [Ni(dcpp)₂ + F]⁺).

For single-crystal X-ray diffraction (XRD) analysis and further characterization, a solution of 239 mg of [ⁿBu₄N][PF₆] (0.616 mmol, 5 eq) in CH₃CN (3 mL) was added to 100 mg of [Ni(dcpp)₂][BF₄]₂. Crystallization via slow diffusion of diethyl ether into this solution gave orange crystals of [Ni(dcpp)₂][PF₆]₂, suitable for single-crystal XRD analysis. The PF₆ salt crystallizes in the Pbcn space group.

Structural Characterization

Table 6.1: Crystallographic data structure refinement for [Ni(CNC)(NCN)][PF₆]₂.

Empirical formula	C ₂₆ H ₂₃ F ₁₂ N ₉ Ni P ₂
Formula weight	810.18
Temperature	120(2) K
Wavelength	0.71073 Å
Crystal system	Monoclinic
Space group	P2 ₁ /c
Unit cell dimensions	a = 17.1436(9) Å a = 90° b = 17.7956(6) Å b = 99.907(4)° c = 20.2978(11) Å g = 90°
Volume	6100.1(5) Å ³
Z	8
Density (calculated)	1.764 Mg/m ³
Absorption coefficient	0.852 mm ⁻¹
F(000)	3264
Crystal size	0.200 x 0.143 x 0.050 mm ³
Theta range for data collection	2.464 to 30.964°.
Index ranges	-24<=h<=23, -24<=k<=25, -27<=l<=29
Reflections collected	43127
Independent reflections	17138 [R(int) = 0.0758]
Completeness to theta = 25.242°	99.4 %
Absorption correction	Semi-empirical from equivalents
Max. and min. transmission	0.8519 and 0.3829
Refinement method	Full-matrix least-squares on F ²
Data / restraints / parameters	17138 / 414 / 1033
Goodness-of-fit on F ²	0.899
Final R indices [I > 2sigma(I)]	R1 = 0.0728, wR2 = 0.1764
R indices (all data)	R1 = 0.1178, wR2 = 0.1928
Extinction coefficient	n/a
Largest diff. peak and hole	1.446 and -1.334 e.Å ⁻³

Table 6.2: Crystallographic data structure refinement for [Ni(dcpp)₂][PF₆]₂.

Empirical formula	C ₃₄ H ₂₂ F ₁₂ N ₆ Ni O ₄ P ₂	
Formula weight	927.22	
Temperature	120(2) K	
Wavelength	0.71073 Å	
Crystal system	Orthorhombic	
Space group	Pbcn	
Unit cell dimensions	a = 14.5984(6) Å	a = 90°
	b = 15.6099(5) Å	b = 90°
	c = 14.9803(4) Å	g = 90°
Volume	3413.7(2) Å ³	
Z	4	
Density (calculated)	1.804 Mg/m ³	
Absorption coefficient	0.780 mm ⁻¹	
F(000)	1864	
Crystal size	0.750 x 0.683 x 0.640 mm ³	
Theta range for data collection	2.610 to 31.044°.	
Index ranges	-19<=h<=20, -21<=k<=21, -21<=l<=16	
Reflections collected	18065	
Independent reflections	4901 [R(int) = 0.0247]	
Completeness to theta = 25.242°	99.8 %	
Absorption correction	Semi-empirical from equivalents	
Max. and min. transmission	0.2168 and 0.1860	
Refinement method	Full-matrix least-squares on F ²	
Data / restraints / parameters	4901 / 0 / 267	
Goodness-of-fit on F ²	1.022	
Final R indices [I > 2sigma(I)]	R1 = 0.0319, wR2 = 0.0883	
R indices (all data)	R1 = 0.0377, wR2 = 0.0901	
Extinction coefficient	n/a	
Largest diff. peak and hole	0.462 and -0.622 e.Å ⁻³	

Mass spectra

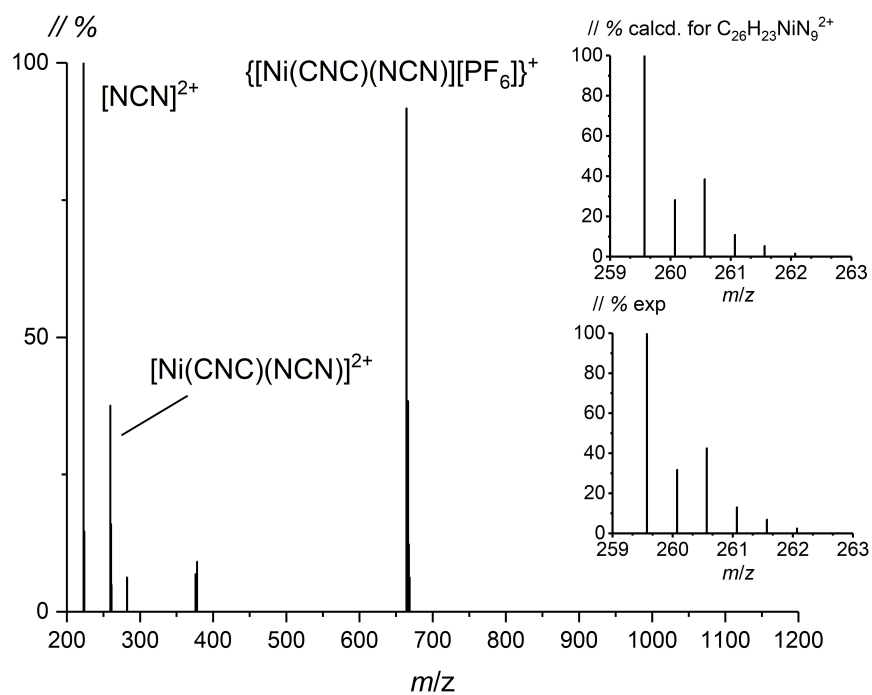


Figure 6.1: ESI⁺ mass spectrum of $[\text{Ni}(\text{CNC})(\text{NCN})][\text{PF}_6]_2$ in acetonitrile.

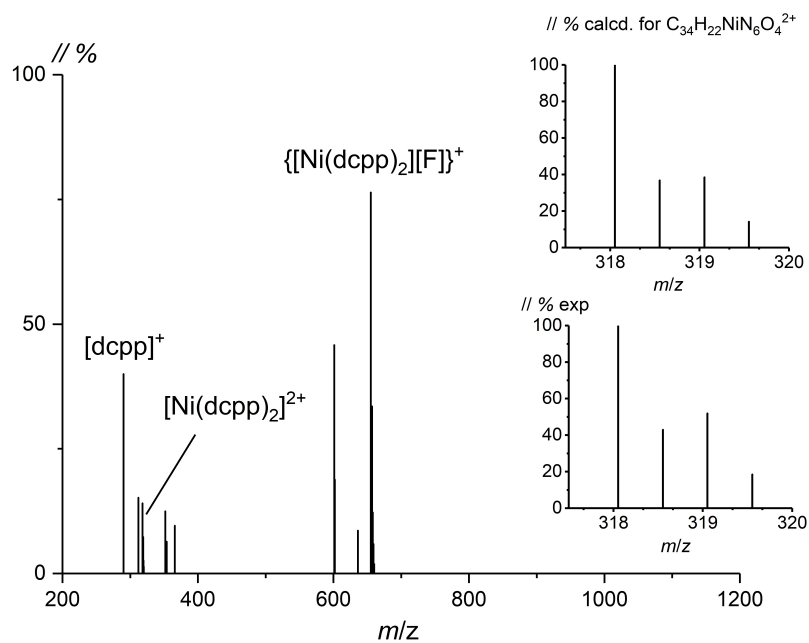


Figure 6.2: ESI⁺ mass spectrum of $[\text{Ni}(\text{dcpp})_2][\text{PF}_6]_2$ in acetonitrile.

7. Acknowledgements

[Redacted text block]

[Redacted text block]

[Redacted text block]

[Redacted text block]

[Redacted text block]

[Redacted text block]

[Redacted text block]

[Redacted text block]

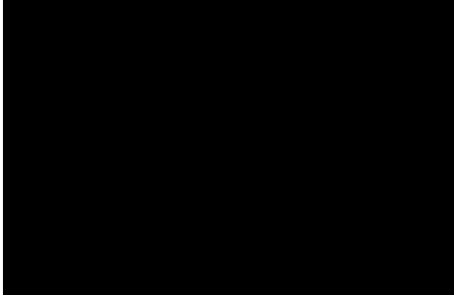
[Redacted text block]

[Redacted text block]

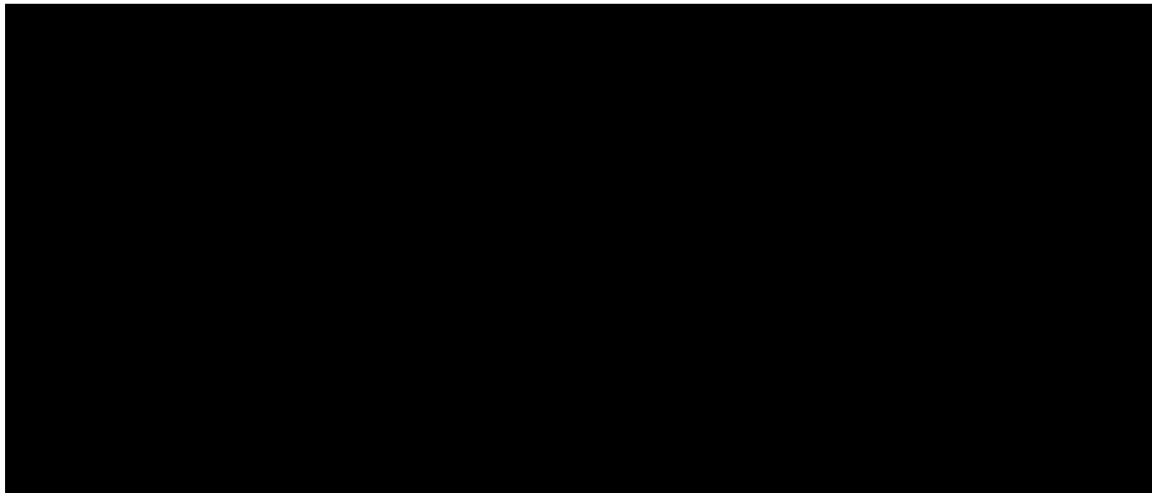
[Redacted text block]

8. Curriculum Vitae

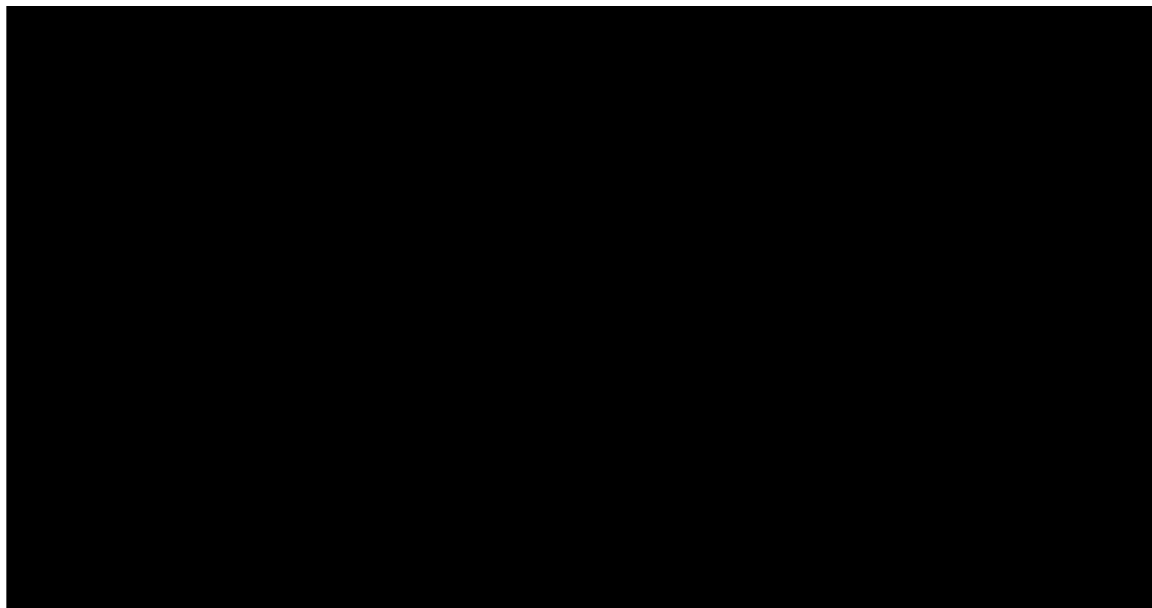
Nathan East



Education

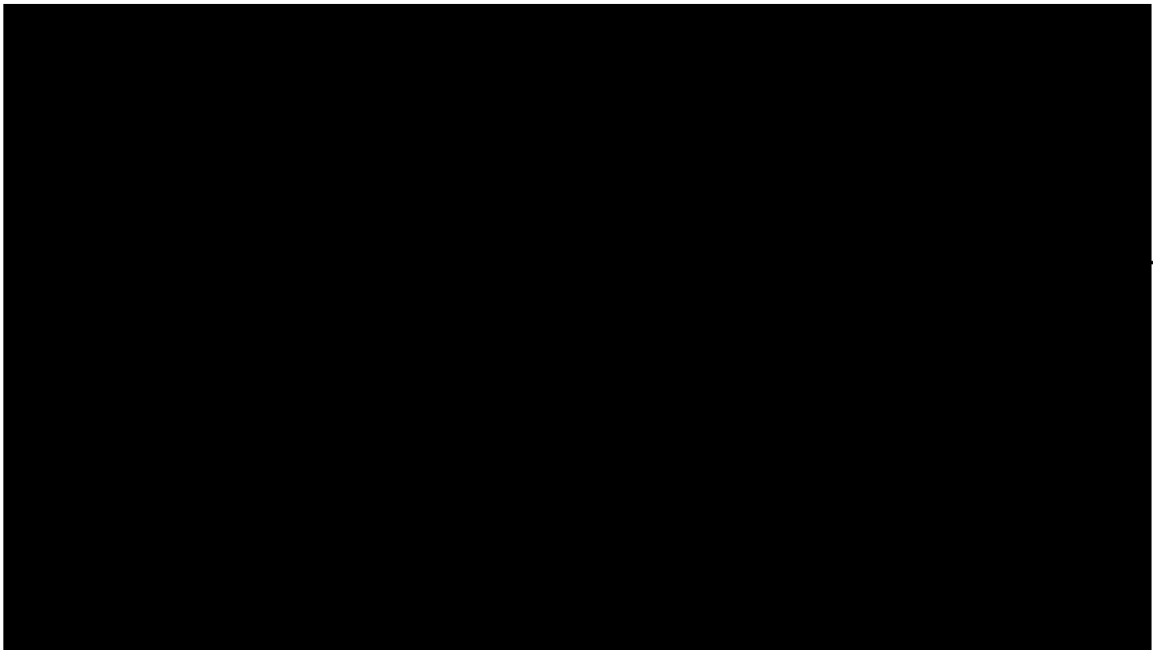


Publications

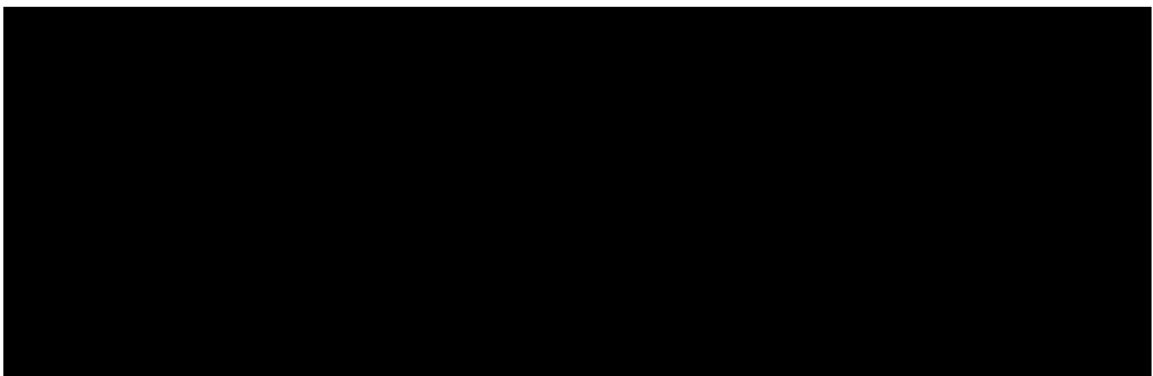




Awards



Conference Contributions



Skills



Further Experience

